

POLITECNICO DI MILANO

Facoltà di Ingegneria Industriale

Dipartimento di Energia

Corso di Dottorato in Scienze e Tecnologie Energetiche e Nucleari



Transient effects in linear concentrating solar thermal
power plant

Supervisor: Prof. Ennio Macchi

Tutor: Prof. Stefano Campanari

Coordinator: Prof. Carlo Enrico Bottani

PhD candidate

Andrea Giostri

XXVI ciclo

*“...Cont tütta i danè che ü spendü per fàrti stüdià...”
...”Prometto...stavolta ho smesso veramente...”*
(Cit. Struggente dialogo tra padre e figlio)

Alla mia famiglia

Acronyms

BOP	Balance Of Plant
CFD	Computational Fluid Dynamic
CLFR	Compact Linear Fresnel Reflectors
CMV	Cloud Movement Vector
COE	Cost of Energy
CPC	Compound Parabolic Concentrator
CSP	Concentrating Solar
DHI	Diffuse Horizontal Irradiation
DLR	Deutsches Zentrum für Luft- und Raumfahrt
DNI	Direct Normal Irradiance
DOY	Day Of the Year
DSG	Direct Steam Generation
ECO	Economizer
EDNI	Effective Direct Normal Irradiance
EVA	Evaporator
FCR	Fixed Charge Rate
GHI	Global Horizontal Irradiation
guiSmo	Guidelines CSP Performance Modeling
HCE	Heat Collector Element
HP	High Pressure
HTF	Heat Transfer Fluid
IAM	Incidence Angle Modifier
IP	Intermediate Pressure
IR	InfraRed
LCE	Linear Cloud Edge
LCoE	Levelised Cost of Electricity
LFR	Linear Fresnel Reflector
LP	Low Pressure
LST	Local Standard Time
MCP	Most Correlated Pair
NPV	Net Present Value
NREL	National Renewable Energy Laboratory
O&M	Operation and Maintenance
ODE	Ordinary Differential Equation

OR	Optical Ratio
ORC	Organic Rankine Cycle
PB	Power Block
PDE	Partial Differential Equation
PSA	Plataforma Solar de Almeria
PT	Parabolic Trough
RH	Reheater
SCA	Solar Collector Assembly
SF	Solar Field
SH	Superheater
TES	Thermal Energy Storage
TFX	Thermoflex
TMY	Typical Meteorological Year
UoM	Unit of Measurement
UV	Ultra Violet

Table of Contents

Acronyms	1-iv
Summary	ix
1 Introduction	1
1.1 Global energy scenario.....	1
1.2 Solar resource.....	2
1.3 Concentrating solar energy.....	4
1.3.1 General consideration	4
1.3.2 Point-focus systems	7
1.3.3 Linear focus systems.....	10
1.4 Final Considerations and Thesis Scope.....	13
1.5 Bibliography.....	14
2 Quasi-Steady State analysis	17
2.1 General description	17
2.2 Efficiency indexes	18
2.3 Example studies made with quasi-steady approach	19
2.3.1 Study 1: Comparison of available solution for Parabolic trough [11]	19
2.3.2 Study 2: Comparison between PT and linear LFR [10].....	35
2.4 Bibliography.....	46
3 Piping Model	49
3.1 Piping system	49
3.2 Solar Field preliminary sizing	50
3.3 Optimization Model	51
3.3.1 Rough Estimation of LCoE and LCoTE.....	53
3.3.2 Piping equations.....	55
3.3.3 Expansion Vessel	60
3.4 Results	61
3.4.1 Dimension Summary	62
3.4.2 Cost breakdown	63
3.5 Bibliography.....	65
4 Solar Field Model	67
4.1 Thermal Model of a single absorber tube.....	67

4.1.1	Resolution Approach	71
4.2	Preliminary Results	72
4.3	Hydraulic Network of Solar Field	74
4.3.1	Hydraulic modelling	75
4.3.2	Thermal modelling	76
4.3.3	Final problem expression	77
4.3.4	Comparison with DLR's model	78
4.4	Bibliography	85
5	Solar Field Investigation	87
5.1	Test-case selection	87
5.1.1	Shading square trajectory	89
5.2	Effect of total mass flow control	91
5.2.1	Constant mass flow (case#1)	91
5.2.2	Mass flow proportional to impinging solar energy (case#2)	94
5.3	Power block addition	98
5.3.1	Power Block modelling	98
5.3.2	Solar Field pump modelling	102
5.3.3	Simulation results	103
5.3.4	Conclusions about mass flow control	109
5.4	Morning Warm-up	110
5.4.1	Simulation results of warm-up	112
5.5	Bibliography	114
6	Cloud Movement Vector	117
6.1	Model to determine the Cloud Movement Vector	118
6.1.1	Installed measurement system	118
6.1.2	Linear Cloud Edge Model	120
6.1.3	Most Correlated Pair model	128
6.1.4	Qualitative comparison	132
6.2	Opacity Matrix	132
6.2.1	Solar field simulation with cloud opacity matrix	135
6.2.2	Idealized disturbance patterns	136
6.3	Bibliography	140
7	Energetic Comparison	143

7.1	Quasi-steady vs. Transient model	143
7.1.1	Solar field model simplification.....	144
7.1.2	Power block modelling	145
7.1.3	Clear sky daily simulation	145
7.1.4	Representative weeks.....	147
7.1.5	Annual Electricity yield	149
7.2	Bibliography.....	150
8	Conclusion and Future Developments	151
8.1	Conclusions	151
8.2	Future Developments	152
8.3	Bibliography.....	154
9	Appendix.....	155
9.1	Sun Position	155
9.2	Ratio between aperture area and real area of Parabolic Trough	156
9.3	Characteristic incidence angles for LFR	158
9.4	Heat transfer fluid properties.....	160
9.5	Available Pipe Dimension.....	161
9.6	Bibliography.....	162

Summary

The PhD thesis focuses on the linear concentrating solar power plant (CSP) (“Heat Transfer Fluid” based) technology with particular attention posed on the transient behavior of the solar field. The study is characterized by the development of modelling tools tailor-made for the analysis of different CSP aspects. The thesis work outlines can be summarized in three main parts.

In order to familiarize with linear CSP topic, the first part of the PhD thesis work focuses on quasi-steady state analysis of CSP plants. This procedure represents the state-of-the-art approach to establish the yearly performance of the whole plant. In particular, the CSP modelling can be divided in two steps; the first is the sizing of both the solar field and the power block section and the second is the prediction of part-load performance. The quasi-steady state method refers to the part-load performance estimate that considers the plant operation as a succession of steady states without the addition of any transient effects. Operatively, each time step depends on the instantaneous weather conditions without considering the previous time steps. The detailed description of this approach is offered with the help of two exemplificative studies that deal with the comparison of different technology solutions for parabolic trough and the comparison between the parabolic trough and the linear Fresnel technology respectively. To accomplish the annual energy yield calculation both an in-house code, called PATTO (PARabolic Trough Thermodynamic Optimization), and a commercial code (Thermoflex[®]) were used.

To calculate correctly the transient behavior of the solar field, a detailed model of the piping system has to be implemented. In particular, the physical dimension of each pipe segments (i.e. mass of steel, mass of HTF contained) and the expansion vessel influence the thermal inertia of the solar field that plays a fundamental role in the transient behavior of the whole system. A specific MATLAB[®] suite was developed with the purpose of sizing the piping network; in particular, the dimensioning is combined with an optimization procedure with the aim of determining the optimal configuration in terms of minimal total cost (sum of investment and operational cost). For this purpose, a cost-database of piping components is obtained from a literature review. As input, the algorithm requires the nominal HTF mass flow, the physical dimensions of the solar field and the characteristics of the available pipes. The code outputs are represented by the outer commercial diameters, the wall thickness, the thickness of the insulating material for each pipe segment and the dimension of the HTF thermal expansion system.

To study the solar field transient behavior a specific algorithm was coded in MATLAB[®]; this code implements the characteristic equations to solve the thermal behavior of the absorber tube able to capture the main transient effects. The time dependent terms are added to the steady-state formulation of thermal resistance network proposed by Forristall. Since a solar field is commonly composed by many loops connected each other by the piping system, the single absorber model represents the elemental unit of the thermal model. In order to increase the accuracy level of the model, the addition of the hydraulic network modelling is necessary to compute the mass flow distribution in the

solar field. As regards the power-block modelling, due to its lower (approximately 1:5) thermal inertia compared to the solar field one, a polynomial approach is considered with the aim of obtaining a good compromise between the accuracy and the computational efforts.

A test case simile-cloud disturbance, considered as an obscuring square that moves with a linear trajectory, is selected in order to identify the solar field response during the passage of the cloud. In particular, the solar field response is evaluated considering the mass flow distribution, the outlet temperature from both each loop and the expansion tank temperature that represents the temperature of the HTF stream entering in the power block. Following the real plant approach that in the most of cases considers the total HTF mass flow as the only control parameter of the solar field, some simple HTF total mass flow control strategies are compared in order to detect the best one from an energetic point of view. The obtained results suggest maintaining a constant HTF mass flow rate during the passage of a cloud; the most important advantages of this strategy can be summarized in the high level of simplicity, the absence of a control valve on each loops and the minimization of the defocused energy without reaching a HTF temperature level inadequate for power block operation. It is important to underline that the general results could be influenced by different boundary conditions related to the cloud disturbance. In addition, the model is used to study the solar field behavior during the morning warm-up; in particular, the solar field is operated in recirculation mode and the non-uniform reciprocal shading of parabolic trough causes a different behavior among shaded and non-shaded loops (the most eastward during the morning). The results obtained shows the absence of unsafe situations, underlying that during the morning warm-up a safe operation is possible without applying complex control strategy or defocussing a part of the solar field. In order to increase the accuracy level of the modelling, the cloud disturbance is analyzed in detail. Using solar radiation data from a ground measurement facility installed in Spain, the “Cloud Movement Vector”, representing the motion vector of the disturbance, is computed by a specific procedure proposed by Bosch and coded in MATLAB[®]. As regards the cloud opacity factor, the experimental measurement grid is used to develop a discretized opacity map. The cloud information obtained is set as input in the CSP plant model in order to evaluate the effect of a more detailed description of the disturbance. As a qualitative conclusions, the addition of the opacity distribution has a negligible effect on the solar field thermal performance; in particular the substitution of the opacity map with an uniform opacity value, equal to the spatial mean value, leads approximately to the same results diminishing at the same time the computational resources needed.

After the study of some typical transient effects of solar field, a comparison about the yearly energetic yield prediction was performed considering both a quasi-steady state methodology and a model that considers the SF thermal inertia. A simplified version of the transient model was implemented in order to allow the simulation of time period suitable to assess the energetic performance of the whole plant.

Different increasing time periods are simulated (i.e. days, weeks and year) in order to have a complete idea of the differences between the two models. The obtained results are

in agreement with independent studies found in literature that report an annual energy output overestimation of ca.10% by the quasi-steady state approach. This result confirms the necessity to consider the transient effects in annual energy yield using specific model or correcting the quasi-steady results with specific parameters. Since the suitable zone for CSP plant are located in desert or semi-desert area, the influence of cloud front passage has a lower impact than the start-up one and for that reason, a more detailed study of start-up phase (considering the power section to) will represent a future development of the study.

As regards the international collaboration established, a part of the PhD activity was carried out at Solar Research Group of the German Aerospace Center (DLR) in Stuttgart.

1 Introduction

1.1 Global energy scenario

The progressive increase of the global energy demand is a direct consequence of the world economic growth; in particular, in the last twenty year, the steep increase of new economy like China and India has produced an intensification of the energy demand that has to be faced by the whole global system. Taking into account the data of the International Energy Agency (“IEA”) [1] more than 80% of the total primary energy derives from fossil fuels. The strong use of fossil fuels with the consequent relevant emissions of CO₂ represents the most important driver of the global warming.

In Figure 1.1, the CO₂ emissions share from fossil fuels, categorized by sector, are reported (left). It is worth to notice how the energy production sector has a great impact on total amount of CO₂ emission and directly on the global warming effect.

To face this issue, which puts at risk life condition in some part of the world, the IPCC (“Intergovernmental Panel on Climate Change”) asserts that, a reduction of at least 50% in the global CO₂ emissions with respect to 2000 emissions has to be reached within 2050 in order to limit the long term global temperature rise that IPCC predicted to be between 2.0°C and 2.4°C [2].

Different technological solutions, related to energy generation and use, are available to face the global warming effect. The most promising long-term interventions can be summarized in the following list:

- Increase the use of quasi zero emissions energy production technologies. In this category, both renewable energies (i.e. solar, hydro, wind, geothermal etc.) and nuclear energy are present.
- The CO₂ deriving from combustion and industrial processes can be captured chemically or physically and sequestered.
- Increase in the use of low carbon fossil fuels; in particular the switch from coal to natural gas.
- Increase the efficiency of energy conversion processes both with technological change and switch to less energy intensive processes
- Increase of the CO₂ amount naturally absorbed by the biological system (e.g. forest growth).

It is worth to notice that no single intervention could be sufficient to face the problem of the CO₂ emissions, and only a combination of the abovementioned solutions can represent the right way of action. Figure 1.1 (right), adapted from [3], shows the impact of different strategies that are considered promising for the reduction of the carbon dioxide emissions within the limit proposed by IPCC.

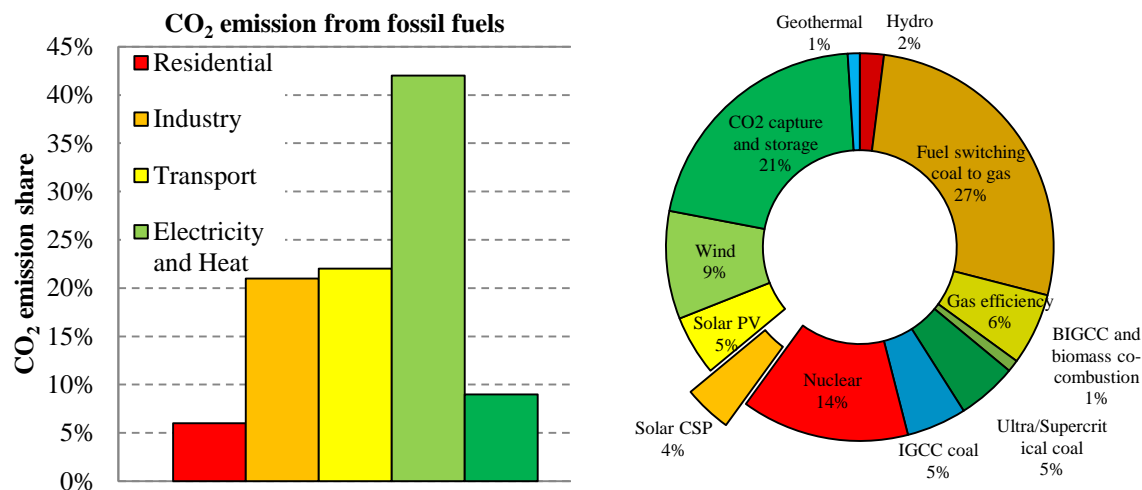


Figure 1.1 CO₂ share emissions categorized by sectors (left) and perspectives of CO₂ reduction in the power sector (right)

Focusing the attention on the solar energy, its impact on reducing the CO₂ can be quantified in approximately the 9% and considering the concentrating solar energy, in [4] it is forecasted how the CSP technology could be responsible of 9.6% of the total energy produced in 2050 if an appropriate support will be present. The concentrating solar thermal power plants are assessed to cover approximately the 40% of the energy produced exploiting solar radiation. As regards research about CSP, a growing interest can be appreciated and among the research activities widespread in the world, it is worth to cite the DOE Sun-Shot [5] initiative and the Desertec Project [6,7] that can be cited as the most promising international research projects oriented to develop the CSP technology and to increase its attractiveness from an economic point of view.

1.2 Solar resource

The sun is the energy source that grants the life on earth. The total energy that is intercepted by the Earth, outside the atmosphere, corresponds to about 500 million of TWh (outside the atmosphere) that could be sufficient to cover the world energy demand of 1000 years [8]. To identify roughly the specific solar power, it is common to refer to the solar constant value of 1366.1 W/m² [9] that represents the solar power specific to area measured outside the atmosphere at the average distance between Sun and Earth. Taking into account the presence in the atmosphere of different gases (i.e. O₂, Ozone, CO₂, H₂O etc.), aerosol and small particles, both absorption and scattering phenomena take place leading to a strong reduction of the solar energy impinging the ground thus reducing the effective available solar energy. Figure 1.2 shows the solar radiation spectrum outside the atmosphere (blue line) that can be well approximated by the radiation emission spectrum of a black body at 5776 K (black dashed). The solar spectrum after the passage through the atmosphere is presented in red, showing the strong attenuation effect and the characteristics absorption wavelengths caused by the presence of different atmosphere components (e.g. CO₂, O₃, H₂O)[10].

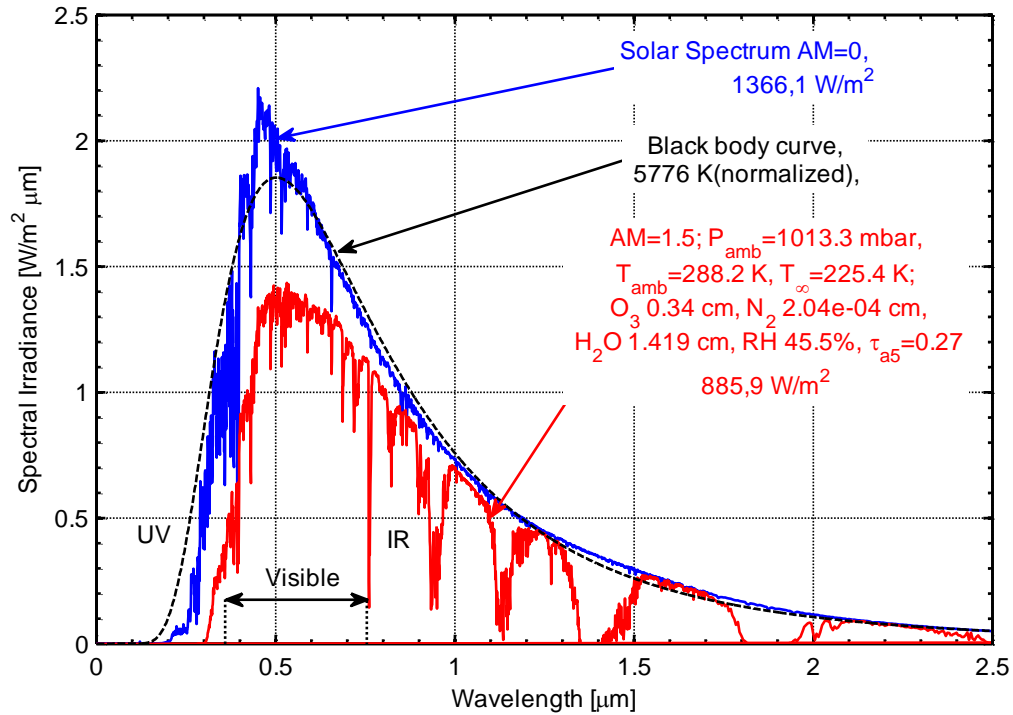


Figure 1.2 Extraterrestrial solar radiation (blue), solar spectrum after atmospheric attenuation – Air Mass =1.5 (red) and equivalent black body emission spectrum. Adapted from [11].

Due to the scattering effect, the global solar radiation can be broken down in a diffuse component and in a direct component. The latter is the part of solar radiation that can be used in concentrating solar power plants. A fundamental parameter, to have a first idea about the suitability of CSP for a location, is the Annual Direct Normal Irradiation; as a rule of thumb, the lowest acceptable value of Annual Normal Irradiation is in the range 1800-2000 kWh/m²y. The suitable location for CSP plants are contained in a zone called “sun belt” that is limited approximately by the two parallels 40° N- 40° S as shown in Figure 1.3.

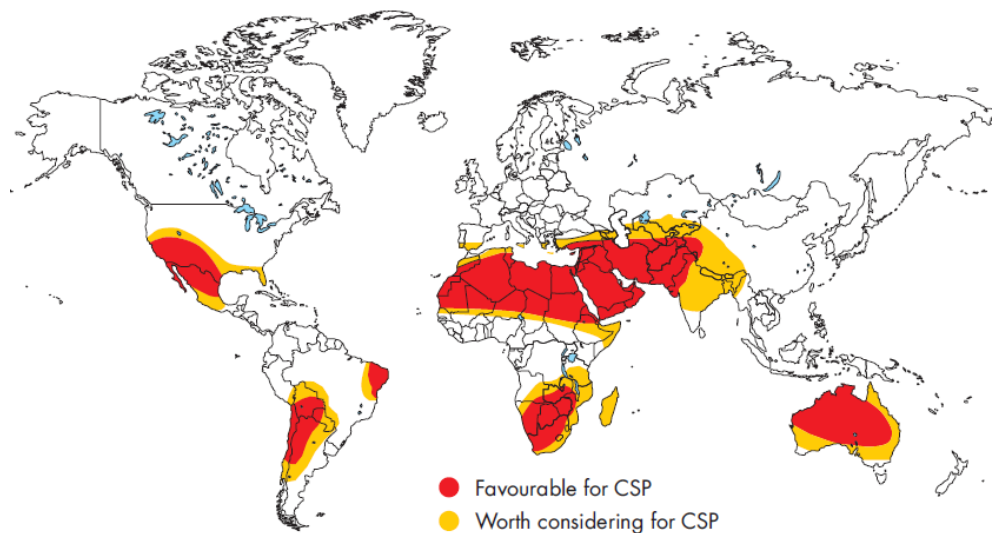


Figure 1.3 Identification of suitable location for CSP application.

1.3 Concentrating solar energy

The goal of Concentrating Solar Power resides in exploiting the solar energy through the conversion of the solar radiation in thermal energy. The thermal energy can be used as it is or as a heat source of a thermodynamic cycle to produce electric energy. The possibility of implementing a thermal energy storage can represent an advantage over other renewable energy sources (i.e. Photovoltaic, wind etc.) whereas the hybridization of the CSP plants with fossil-fuel plants represents a promising concept to increase the market penetration of concentrating solar energy technology [12].

As regards the classification of the concentrating solutions, a first approach divides the technology depending on the kind of the absorber geometry in line-focus such as parabolic troughs and linear Fresnel reflectors, and point-focus category, such as solar towers and parabolic dishes. It is important to underline that the parabolic trough technology covers more than the 90% of the total number of CSP plants as reported by [13].

Next sections, after a simple explanation of the basis of concentration, introduce briefly all the technologies that are present in the CSP market.

1.3.1 General consideration

The concentration of solar energy can be considered as a method to increase the quality level of the collected energy, in particular, it is well known that efficiency of thermodynamic cycle is proportional to the maximum temperature reachable by the concentration of solar energy. In addition to the thermodynamic advantage, the solar energy concentration leads the high temperature surface, and consequently the most expensive, to be reduced.

In this section, a simple procedure to estimate the advantages of solar energy concentration is presented and, in addition, some general considerations are introduced to assist the comprehension of CSP bases.

The coupling of the solar energy concentrating system and the thermal engine identifies a CSP plant. The global efficiency can be expressed as the product of the solar receiver efficiency and of the thermodynamic cycle efficiency as defined by the relation below:

$$\eta_{CSP} = \eta_{receiver}\eta_{cycle} \quad (1.1)$$

To simplify the treatise without losing the general meaning of this exposition, some assumptions are made:

1. The receiver is modelled as a cavity with a thermal behavior assimilated to the black body one. Therefore, the receiver thermal losses are only radiative and no convective losses are considered.
2. The thermal efficiency of the thermodynamic cycle is assumed to be equal to the Carnot cycle efficiency thus considering the maximum ideal efficiency reachable with a certain temperature level.

The solar energy concentrated by a specific device (i.e. mirrors or lenses) hits the receiver and causes its temperature to augment. In order to use the receiver thermal energy, a fluid circulates in the absorber and it is heated. The receiver temperature is higher than the ambient temperature thus implying thermal losses to the environment.

The useful thermal energy is defined by the difference between the absorbed fraction of the concentrated solar energy and the thermal losses.

Once a steady condition was reached, the energy balance equation referred to the receiver surface can be written as follows (in accordance to the first assumption):

$$\dot{Q}_{receiver} = \dot{Q}_{absorbed} - \dot{Q}_{rad} = \alpha \cdot CR \cdot DNI - \sigma \cdot \varepsilon \cdot (T_{abs}^4 - T_{sky}^4) \quad (1.2)$$

Where α is the receiver absorptivity, representing the share of impinging solar energy that is converted in thermal energy, CR is the geometrical concentration ratio, DNI is the beam normal irradiance. σ is the Stefan-Boltzmann constant [$5.67E-8 \text{ Wm}^{-2}\text{K}^{-4}$], ε is the thermal emissivity of the receiver, T_{abs} represents the absorber temperature and T_{sky} is the reference ambient temperature viewed by the receiver (both expressed in Kelvin degree).

Rearranging the energy balance, the receiver efficiency can be defined as follows:

$$\eta_{receiver} = \frac{\dot{Q}_{receiver}}{\dot{Q}_{concentrated}} = \alpha - \frac{\sigma \cdot \varepsilon \cdot (T_{abs}^4 - T_{sky}^4)}{CR \cdot DNI} \quad (1.3)$$

From the relation above, some considerations about the receiver efficiency can be made:

1. The optical properties of the absorber, in particular a high absorptivity of solar spectrum, are fundamental for a high receiver efficiency
2. The lower the thermal emissivity the higher the receiver efficiency because of the reduced thermal losses
3. A high incidence flux has a positive effect on the receiver efficiency. Once the temperature level is fixed, the thermal losses impact is mitigated by the higher impinging solar energy thus explaining the better receiver efficiency.

The second term of the global efficiency is represented by the thermodynamic cycle efficiency. Following the assumption of implementing an ideal Carnot cycle whose efficiency is defined by Eq.(1.4), the maximum efficiency conversion between the ambient temperature and the absorber temperature is considered.

$$\eta_{Carnot} = 1 - \frac{T_{amb}}{T_{abs}} \quad (1.4)$$

Plotting the relation of global efficiency, Figure 1.4 shows the effect of the properties material on the global efficiency; in addition, the Carnot efficiency, representing the highest reachable efficiency for a unity value of the absorbance and zero thermal losses is reported as a reference. From the high constant value of the receiver absorbance of 0.94, the impact of the thermal emissivity can be noted. In particular, for a medium concentrating system (CR=100) a low thermal emissivity is necessary to assure high efficiency in case of high absorber temperature (>800 K). The low emissivity and high absorbance is necessary to diminish the impact of thermal losses and to enhance the absorbed fraction of solar energy respectively; for that reason, a material that combines these two properties has to be accurately selected from both a technical and economic point of view.

In addition to the cost related to the materials properties, the solar energy concentration needs a tracking system that augments the cost of the overall system and diminishes the availability of the plant (due to the presence of moving part of the tracking device). It is worth to underline that this disadvantage is more than counterbalanced by the higher energetic efficiency that can be reached thus confirming the technical attractiveness of concentrating solar energy system.

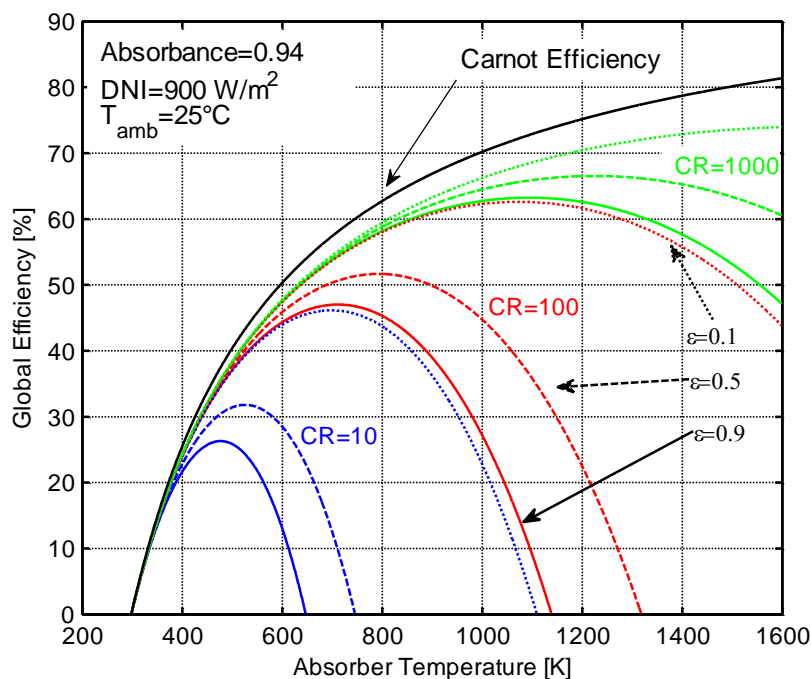


Figure 1.4 Global efficiency for different concentration ratio, emissivity and absorber temperatures. Absorbance of 0.94, DNI of 900 W/m² and ambient temperature equal to 25°C.

Once the receiver technology was fixed, the trend of global efficiency suggests that an optimum temperature, which depends on the concentration ratio, exists. In particular, the higher the concentration ratio the higher is the temperature that guarantees the best energetic performance.

After taking into account the Kirchoff's Law of thermal radiation which states that for each wavelength the absorptivity and the emissivity are equal (Eq.(1.5)), it is possible to

select the receiver material as a coating with a high absorptance of the solar spectrum and a low emissivity value at the typical wavelength of the thermal radiation:

$$\alpha_\lambda = \varepsilon_\lambda \quad (1.5)$$

In Figure 1.5 the normalized spectral power density of both the solar spectrum (AM=1.5) and of a blackbody at 300°C are shown. As it is possible to notice, the two spectrum characteristic wavelength ranges make possible to select an absorber coating with a high absorptance in the characteristic solar wavelengths and a low emissivity in the thermal radiation zone. The ideal coating reflectance is represented with a square function characterized by a cut-off wavelength enlightened in the figure below. The real behavior of real coatings approximates the ideal trend and an intensive research activity has been concentrated on finding material that, in addition to the peculiarity abovementioned, are thermally stable at high temperature.

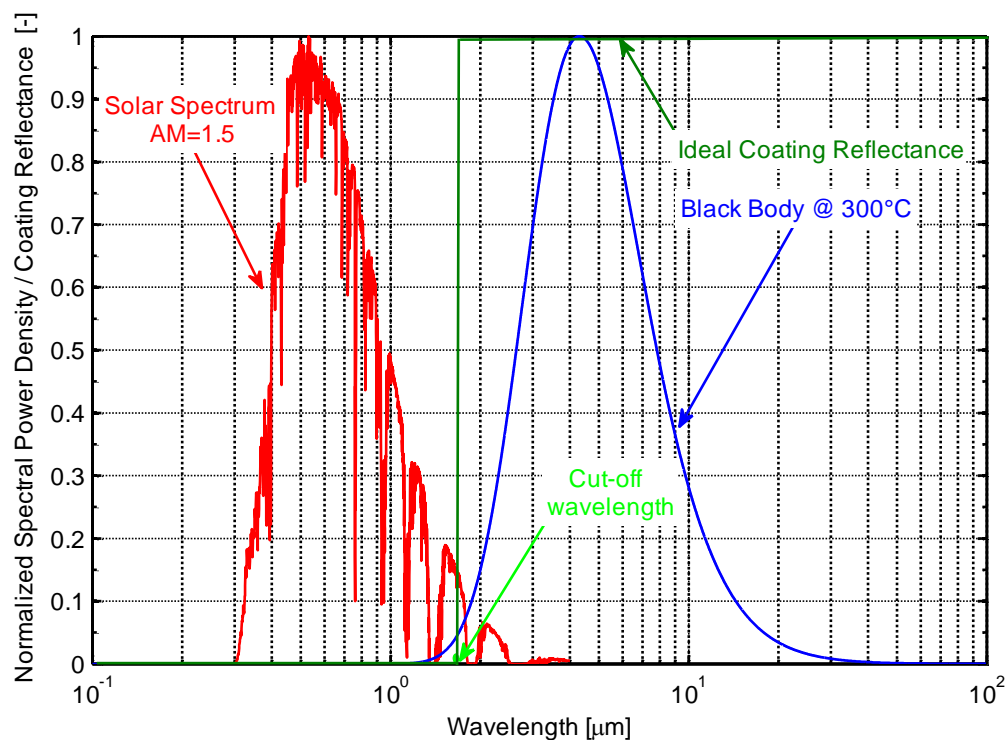


Figure 1.5 Normalized spectral power density of Solar spectrum (AM=1.5) (red) and of a black body at 300°C (blue). The ideal trend of the selective coating reflectance¹ is shown in light green.

1.3.2 Point-focus systems

The basis of this concept resides in a two axis tracking system that allows the solar energy to be concentrated on an ideal point receiver. The main advantage of the point focus systems can be identified in a higher concentration ratio (compared to linear focus systems) that leads to higher operating temperatures. The concentration ratio is of the order of thousands of suns with maximum reachable temperature that could be higher

¹ The reflectance is defined as: $\rho_\lambda = 1 - \alpha_\lambda$

than 1200 °C. As a general consideration, the abovementioned advantage has to face the high investment costs that are necessary to build a system able to concentrate high power flux on an ideal single point.

In the point-focus category, two main technologies can be recognized that span a wide range of power output. In particular, the power tower concept is suitable for power output of the order of 10 MWe or higher whereas the solar-dish solution has been studied for smaller power output up to hundred kilowatts even if some applications for big-scale plant are under study/development.

1.3.2.1 Solar dish

The solar dish design is based on the well-known optical properties of the paraboloid reflecting surface (obtained by a solid revolution of a parabola) with the receiver placed at the focal position. The two axis tracking system allows the reflector to rotate and to follow directly the “sun movement”. As regards the power production section, the most common solution is the placing of a thermal engine at the mirror focal position. Due to dimensional constraints, the name-plate of the engine has not to be higher than approximately 100 kWe and for this reason the best technological choice of the power unit is nowadays represented by the Stirling Engine [14,15]. A new research branch, that worth to be cited, is pointed towards the use of air Joule-Brayton cycle [16,17]. Besides the low power of a single unit, multi-MW plants are conceivable exploiting the modularity of the system and arranging the paraboloid in different rows [18]. An example of this solution is represented by the Maricopa Plant project in Arizona that was studied to produce 664 MWe using about 26000 dishes “Sun Catcher” (25kWe). Due to financial problem that caused the bankruptcy of the “Stirling Energy Systems” company in 2011, the power capacity of the plant was reduced to 1.5 MWe. Some early projects studied the implementation of sun-dish technology to produce superheated steam to be sent to a common steam power plant; this solution seemed to be abandoned but nowadays some interesting studies has been done in particular by the Solar Thermal Group of the Australian National University [19,20]. It is worth to underline how a solar dish Stirling collector (using hydrogen as working fluid) operated by Sandia Laboratories holds the highest value of the solar-to-electric conversion efficiency (31.25%) among concentrating solar technologies [21]. Besides the aforementioned high energetic performance, the high specific costs and some reliability issues mainly related to the high temperature Stirling power block, have been limiting the development of big-scale commercial plants and the related potential economies of scale that would have a benefic impact on the reduction of investment costs.

In Figure 1.6 both a Stirling based (left) and a steam generation sun dishes (right) are presented. In both the figures, the common row layout of sun dishes can be seen. As regards the sun dishes for the production of superheated steam, a piping system is requested in order to deliver the fluid in the solar field.

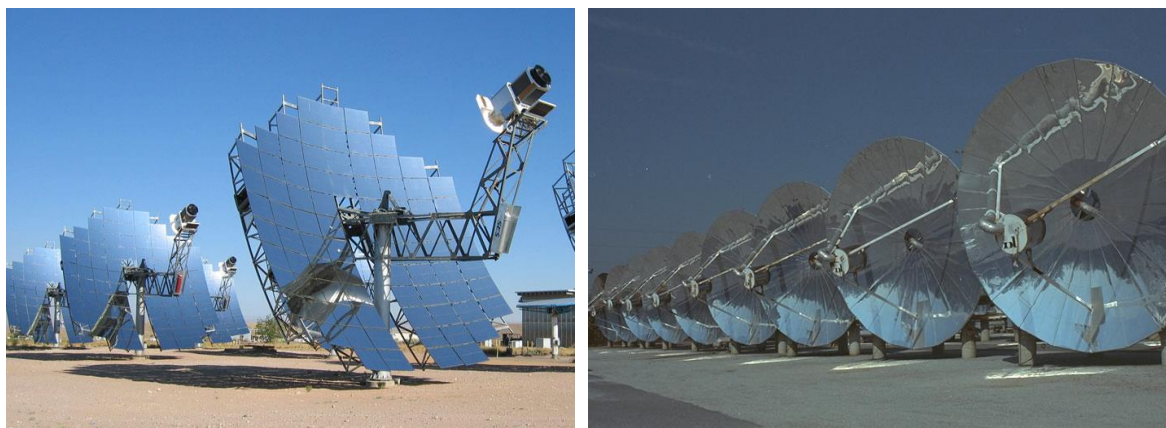


Figure 1.6 Sun-dish collectors field with a Stirling engine (left) and to produce superheated steam.

As regards small-scale solution, Infinia [22] commercializes a 3.2 kWe solar dish Stirling that are addressed to exploit the new development paradigm of “getting bigger by going smaller” as underlined by [23].

Due to the achievable high temperature, another research branch points to the use of sun dishes to be the thermal source of thermo-chemical processes as reported by [24].

1.3.2.2 Power tower

Power towers, also called Central receiver systems, uses a heliostat field, made of a large number of tracking mirrors, which reflects sun-ray to concentrate the solar energy onto a receiver placed on a fixed tower. The reflectors field is made of a big number of mirrors that are able to track continuously the sun concentrating the solar energy by typically a factor of 500-1000. As occurs in solar dish, the high concentration ratio allows reaching high temperature but due to the peculiar solar tower concept, this solution is addresses to Multi-MW scale plants only.

As regards the geometrical positioning of the mirrors and their shape, a particular care has to be taken in order to assure high optical performance. Two main categories of heliostat field layout can be identified; in particular surround fields in which the heliostats surround symmetrically the receiver, north fields (the heliostats are on the north side of the receiver) and configuration in between. In particular, the north field shape is preferred for high latitude location and for high incidence angle whereas the surround field is a better choice for location near the equator. Another driver parameter of the heliostat layout is the total occupied area (related to the goal annual energetic yield); a surround field solution is preferred in case of high capacity power plants because a north fields would have a mean distance between mirrors and the receiver too high with consequent lower optical efficiency.

Figure 1.7 shows an aerial view of the Gemasolar plant [25] (with surround field - coordinates $37^{\circ} 33' 29.11''$ N, $5^{\circ} 19' 44.6''$ W) and the PS-10 and PS-20 [26] (north field - coordinates: $37^{\circ} 26' 32''$ N, $6^{\circ} 15' 15''$ W).



Figure 1.7 Aerial view of the Gemasolar plant (right) and of the PS-10 and PS-20 power tower (left).

Regarding the receiver technology, many technological solutions can be taken into account depending on what kind of fluid has to be heated. The available commercial solution is represented by the tubular receiver concept, which is used in plants that process a heat transfer fluid (e.g. molten salt) or produce steam directly. Nevertheless the volumetric receiver together with other innovative receiver concepts (i.e. particle receiver, falling-film receivers tec.) seems to be a promising alternative to heat gaseous fluid and for thermochemical processes in which the absorber catalyze the chemical reaction [27-29].

To have an idea of the maximum reachable temperatures, the commercial solutions is represented by the use of molten salts at 565°C or by the direct production of superheated steam at the same temperature, whereas the volumetric or particle receivers are expected to allow higher temperature in the order of $1000^{\circ}\text{C} - 1200^{\circ}\text{C}$ [29].

It is important to underline how the solar tower technology has been creating a great interest in the scientific community; in particular, relevant research branches aim to find innovative solutions to increase the optical performance and to develop both new power block or thermochemical system concepts to exploit the high potential introduced by the achievable high temperatures [29].

1.3.3 Linear focus systems

The linear focus systems implement parabolic mirrors (e.g. parabolic trough) or segmented mirrors (e.g. linear Fresnel reflectors) which concentrate solar radiation on a tubular receiver in which a heat transfer fluid or directly the working fluid (i.e. water for direct steam production) circulates. Due to the different absorber geometry, the tracking system is simpler than the point-focus one; in particular, the linear focus systems implement a single axis tracking.

Focusing solar energy on a linear absorber leads to lower concentration ratio and consequently lower temperatures that are contained approximately in the range of $200^{\circ}\text{C} - 600^{\circ}\text{C}$.

As regards the impact of this technology on the CSP portfolio, the parabolic trough represents the great majority of the operating plants constituting the reference technology in CSP world.

1.3.3.1 Parabolic trough

As previously remarked upon, the parabolic trough technology covers the biggest share of the world energy production via concentrating solar energy; for that reason more detailed description is provided in the following parts.

The first parabolic trough plant experience can be traced back to the beginning of twentieth century with the demonstrative plant built by Shuman in Egypt [30]. After this first experience, different universities and research centers conducted researches about this technology but a long period without the construction of noticeable parabolic trough solar fields occurred. The long research activities culminated in mid-1980's with the construction of Multi-MW CSP Solar Energy Generating Systems (SEGS) in USA. The total installed power capacity was approximately equal to 354 MWe. Afterwards, this technological solution was forgotten until 1998 when the Eurotrough project [31] started with the aim of finding a cheaper solution for the solar collector assembly; this project can be identified as one of the most important milestone for the CSP research in Europe. The new millennium has seen a fast growing attention about CSP world, and in particular, the parabolic trough plants presence has been increased significantly reaching a total installed capacity of about 2.5 GW. As regards the location, the most of the installed capacity is located only in two nations: United States and Spain, due to the presence of both environmental (i.e. availability of zone with high solar irradiation) and economic (i.e. governmental incentives) favorable conditions. It is important to underline that interesting development projects has been inaugurated in different countries; in particular, the most active countries are India [32] and China [33]. Figure 1.8 (left) shows an aerial view of the Extresol II plant (50 MWe with an indirect thermal storage of 7.5 equivalent hours) [34] and a parabolic trough solar collector assembly is shown in Figure 1.8 (right).



Figure 1.8 Aerial view of the Extresol 2 plant (left) and picture of a parabolic trough assembly

As regards the technology, the “heart” of the parabolic trough system is the solar collector assembly (“SCA”) that is made of a parabolic through-shaped mirrors supported by a metal structure and with a tracking system. Regarding the metal structure, it has to fulfill some mechanical requirements that can be summarized in a light structure to simplify the transport and the installation, a reduced cost, a high resistance to the ambient conditions for at least 30 years.

In particular, an intensive R&D activity aims to find innovative support structures in order to reduce the investment cost without decreasing the level of robustness. To reach the desired power output, the parabolic trough solar field is arranged in parallel rows connected each other by a piping network.

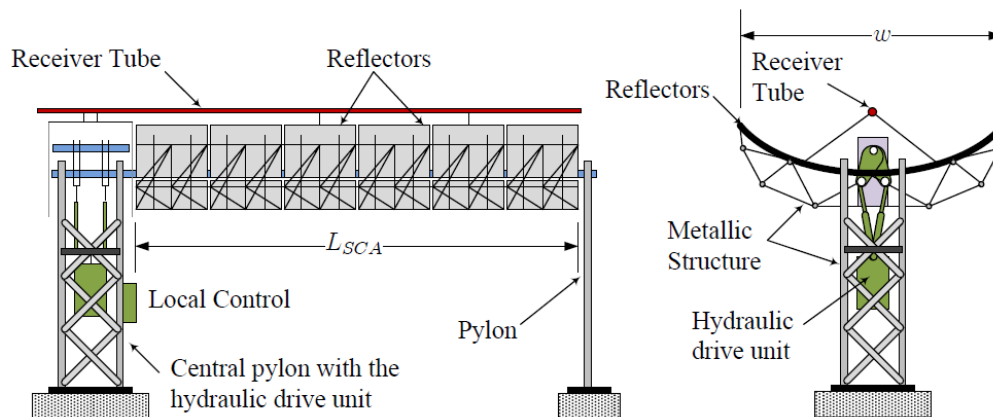


Figure 1.9 Schematic draw of solar collector assembly (“SCA”) [11].

Regarding the heat collector element (“HCE”), a selective coating is adopted in order to maximize the optical-thermal efficiency and, to further reduce the thermal losses the steel absorber tube is enveloped in a Pyrex[®] glass tube at low pressure of about 10^{-2} Pa [35]. Besides lowering the convective thermal losses, this solution implies the presence of expensive glass-to metal seals in order to prevent selective coating oxidation. In addition to the use of selective coating, the glass surface is treated with anti-reflective coating in order to enhance the transmission of the sunlight.

Due to the thermal expansion of the absorber tube, the adoption of bellows is necessary to avoid the failure of the heat collector element thus representing an important share of the HCE investment cost.

Typically, the big scale parabolic trough has a concentration ratio near to 80, the constraints that limit the increase of this value resides in the wind drag effect, which put a limit in the aperture dimension (the biggest metal structure parabolic trough has an aperture in the range 5.5 m – 6 m), and in the decrease of the intercept factor with the concentration ratio.

The total length of a solar collector assembly reaches the value of about 100 -150 m, whereas the absorber tube length is limited to a value of 4 m because of mechanical bending.

1.3.3.2 Linear Fresnel reflector

The Linear Fresnel Reflector (LFR) technology makes possible the solar energy concentration through a series of ground-based mirrors, with different curvature, that approximates the ideal parabolic shape. The mirrors can be moved independently, concentrating the solar power onto a receiver absorber placed above the ground. Comparing to the parabolic trough, the approximation of the parabola shape leads to a lower ideal optical efficiency that implies the need of a secondary reflector. In Figure

1.10 the LFR manufactured by AREVA [36] and a detail picture of the Novatech's receiver system are shown [37].

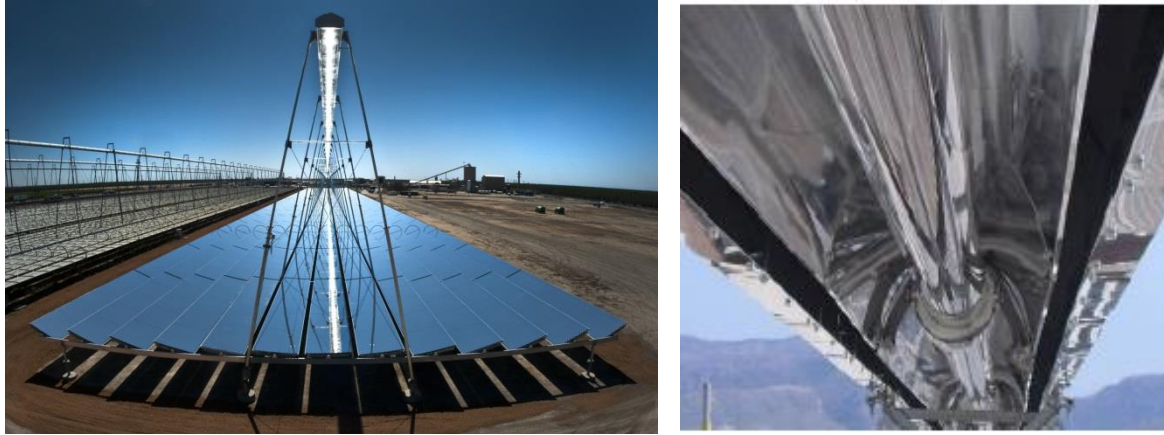


Figure 1.10 Linear Fresnel reflector developed by AREVA (left) and detailed view of the secondary reflector of Novatech Solar's absorber.

The main reason that has driven the study of LFR is the intrinsic lower investment cost that can be explained by the use of ground-based mirrors that implies lighter structure, the fixed absorber that does not need expensive rotating joints and a lower land occupation. Otherwise, the abovementioned advantages have to face the lower optical efficiency that adds a strong penalty effect that influences the cost of the energy produced.

As regards the absorber pipe, the same technological solution used for parabolic trough can be adopted.

The short life of the commercial LFR concept, the original idea is dated to 1962 by the Giovanni Francia's patent [38] and the new interest can be traced back to 2000 with Mills's study about "Compact Linear Fresnel Reflector" (CLFR) [39,40], makes reasonable to expect an additional investment cost reduction. In addition, the existing free-space for layout optimization, as underlined by [41], could make the actual techno-economic comparison with parabolic trough technology not completely fair.

1.4 Final Considerations and Thesis Scope

Concentrating Solar Power industry is a suitable response to the energy market demand of low-carbon emission solutions. The continuous increase of the installed plants around the world, even if governmental help through the incentives applied to CSP electric energy has driven it, seems to suggest that the concentrating plant power is a good energy production alternative that deserves to be further studied. To have an idea about the growing interest in CSP, at the end of 2010 the total installed capacity was 1095 MW and at the end of 2012 reached about 2500 GW [3]. As reported by [3], the CSP sector shows the highest growth rate among the renewable energies thus confirming the rising interest in developing new solutions and in strengthening the current knowledge.

The simulation of CSP plants plays a fundamental role in R&D activity because the development of modelling tools makes possible to investigate new solutions and to go deep in particular phenomena that are considered to be important in the selection of alternatives.

An intensive research activity in developing models to assess the energetic performance of CSP plants has been being carried out by the Gecos group [42] for approximately ten years; in particular, each technologies described above, was studied and the results were published on scientific journals. All the whole plant models developed does not directly consider any transient effect due to the thermal inertia of the solar field. This approximation is common in CSP simulation activity, and many works are found in literature that, with different level of accuracy, has the same main approach.

Taking into account the brief description of CSP available technologies made in the section before, the predominance in market of parabolic trough, in particular with the indirect solution, represents a good reason to examine in depth the effect of transient effects in this kind of solar field and to estimate the impact of these phenomena on predicting the annual energetic performance. In order to focus the attention on the solar field behavior, the technology without thermal energy storage and neither fossil back-up is considered.

As regards the thesis outline, chapter 2 proposes a series of efficiency indexes with the aim of providing the same parameters to compare different CSP solutions. The common CSP plants modeling approach (quasi-steady approaches) is described, and, in order to give a detailed explanation of the modelization of components, two research studies made during the PhD activity and published in two peer-reviewed scientific journals, are reported.

Chapter 3 is dedicated to the presentation of a specific model for the solar field sizing, in particular the piping network, whereas in Chapter 4, the description of the solar field thermal model, to study transient effect, is provided.

Chapter 5 is entirely devoted to the exposition of a test case results about the effect of a moving disturbance and about the warm-up of the solar field. In Chapter 6, using solar radiation data taken from an experimental facility, an implementation of an algorithm able to predict the cloud movement is presented. In addition, a real opacity matrix is used in the same model of Chapter 5 in order to identify difference in the system response.

In Chapter 7, the comparison in term of energetic performance prediction between quasi-steady approach and a model that considers the transient response of the plant is presented and in Chapter 8 the main results and possible future developments are resumed.

1.5 Bibliography

- [1] International Energy Agency. International Energy Agency ("IEA") website;2010.
- [2] Pachauri R, Reisinger A. IPCC fourth assessment report. IPCC, Geneva 2007.
- [3] Renewable Energy Policy Network. Renewables global status report 2013.

- [4] International Renewable Energy Agency. Renewable energy technologies: cost analysis series - Concentrating Solar Power 2012.
- [5] Department of Energy. SunShot Initiative website 2013;2013.
- [6] Desertec Foundation. Desertec Foundation website 2013.
- [7] Trieb F, Müller-Steinhagen H. The DESERTEC Concept-Sustainable Electricity and Water for Europe, Middle East and North Africa. Whitebook of TREC and Club of Rome-Clean Power from Deserts 2007:23-43.
- [8] Enteria N, Akbarzadeh A. Solar Energy Sciences and Engineering Applications CRC Press; 2013.
- [9] Duffie JA, Beckman WA. Solar Engineering of Thermal Processes Wiley: Hoboken, NJ; 2006.
- [10] Gueymard CA. The sun's total and spectral irradiance for solar energy applications and solar radiation models. Solar Energy 2004;76:423-453.
- [11] Vasquez Padilla R. Simplified Methodology for Designing Parabolic Trough Solar Power Plants 2011.
- [12] Peterseim JH, White S, Tadros A, Hellwig U. Concentrated solar power hybrid plants, which technologies are best suited for hybridisation?. Renewable Energy 2013;57:520-532.
- [13] CSP Today. CSP World plant locations 2011.
- [14] Stine WB, Diver RB. A compendium of solar dish/Stirling technology 1994.
- [15] Mancini T, Heller P, Butler B, Osborn B, Schiel W, Goldberg V, et al. Dish-Stirling systems: An overview of development and status. Journal of Solar Energy Engineering 2003;125:135-151.
- [16] Sigarchian SG. Modeling and Analysis of a Hybrid Solar-Dish Brayton Engine 2012.
- [17] Hybrid Solar | Brayton Energy - Research and Development in Alternative Energies - Hampton, NH - 603-601-0450;2012.
- [18] Lovegrove K, Taumoefolau T, Paitoonsurikarn S, Siangsukone P, Burgess G, Luzzi A, et al. Paraboloidal dish solar concentrators for multi-megawatt power generation 2003.
- [19] Australian National University. Australian National University - Solar Thermal Group- 2011;2011.
- [20] Cumpston J, Lovegrove K, Zapata J, Pye J. Paraboloidal Dish Arrays with Steam Energy Transport Network.
- [21] Sandia National Laboratories. Sandia, Stirling Energy Systems set new world record for solar-to-grid conversion efficiency 2008;2008.
- [22] Infinia. PowerDish 2012;2012.
- [23] Skumanich A. CSP at a crossroads: The first solar electric power plants are still proving their worth after three decades, so why aren't we seeing more CSP reach the development stage?. Renew Energy Focus 2011;12:52-55.
- [24] Dunn R, Lovegrove K, Burgess G. A review of ammonia-based thermochemical energy storage for concentrating solar power. Proc IEEE 2012;100:391-400.
- [25] Torresol Energy. Torresol Energy: Gemasolar central tower receiver 2011;2011.

- [26] Abengoa Solar. Abengoa Solar: PS10-PS20 project 2011;2011.
- [27] Romero M, Buck R, Pacheco JE. An update on solar central receiver systems, projects, and technologies. *Journal of solar energy engineering* 2002;124:98-108.
- [28] Steinfeld A. Solar thermochemical production of hydrogen—a review. *Solar Energy* 2005;78:603-615.
- [29] Ho CK, Iverson BD. Review of high-temperature central receiver designs for concentrating solar power. *Renewable Sustainable Energy Rev* 2014;29:835-846.
- [30] Ackermann A. The Utilisation of Solar Energy. *Journal of the Royal Society of Arts* 1915;63:538-565.
- [31] Geyer M, Lüpfert E, Osuna R, Esteban A, Schiel W, Schweitzer A, et al. EUROROUGH-Parabolic trough collector developed for cost efficient solar power generation 2002:04-06.
- [32] Purohit I, Purohit P. Techno-economic evaluation of concentrating solar power generation in India. *Energy Policy* 2010;38:3015-3029.
- [33] Hang Q, Jun Z, Xiao Y, Junkui C. Prospect of concentrating solar power in China—the sustainable future. *Renewable and Sustainable Energy Reviews* 2008;12:2505-2514.
- [34] European Solar Thermal Electricity Association. ESTELA Website: Extresol plant webpage 2013;2012.
- [35] SCHOTT Solar. Schott PTR-70 Receivers Designed for maximum profitability of the power plant 2013;2013.
- [36] AREVA CSP Project: <http://www.aveva.com/EN/global-offer-725/concentrated-solar-power-renewable-energies-solutions.html> 2011.
- [37] NovatecSolar. NOVATEC SOLAR's Website 2012;2012.
- [38] Silvi C. The pioneering work on linear Fresnel reflector concentrators (LFCs) in Italy 2009.
- [39] Zhu G, Wendelin T, Wagner MJ, Kutscher C. History, current state, and future of linear Fresnel concentrating solar collectors. *Solar Energy*.
- [40] Mills DR, Morrison GL. Compact Linear Fresnel Reflector solar thermal powerplants. *Solar Energy* 2000;68:263-283.
- [41] Binotti M. Linear Fresnel reflectors : study of the technology and steps toward optimization 2013.
- [42] GECOS. Politecnico di Milano: Group of Energy Conversion Systems 2013.

2 Quasi-Steady State analysis

An important research front of CSP technology is mainly oriented to develop tools in order to predict the yearly energetic performance that represents the starting point for a techno-economic analysis to select the best available solution. In this chapter, once both a general description of the most common simulation approach and a resume of the efficiency indexes are presented, the common approach, called quasi-steady state analysis, is described with the help of two example studies that deal with linear concentrator technology. The results of these two works were published in scientific journals as research articles, which are proposed integrally. In addition to the presentation of specific results, the main goal of this chapter is to familiarize the reader with fundamental concepts about linear CSP modelling that are used in the following chapters.

2.1 General description

As reported in the introductory chapter, neglecting some experience at the beginning of the last century, the research about CSP technology has been growing in quantity and quality for forty years starting from the mid of 70's with an intensity proportional to the oil price [1]. The development of simulation tools able to predict the yearly yield of a CSP plant has been playing a fundamental role in CSP research activities because these tools allow the researchers to investigate different solutions before building CSP plant or experimental facilities.

As regards the simulation tools developed to predict the energetic performances, the main differences are related to the detail level of the components modelling whereas a common procedure can be identified.

The working process that represents the common approach to developed yearly energetic analysis for CSP plant can be outlined in the following two steps:

1. *Sizing the plant*: Every components of the whole system are dimensioned taking into account some specific boundaries imposed by the considered technologies.
2. *Yearly performance*: the performance of the CSP plant is strongly influence by the part-load response. As regards the most important causes of part-load operation, it is sufficient to consider the variation of available solar energy. The “quasi-steady” approach consists of considering the plant operation as a succession of steady states without the addition of any transient effects. Operatively, each time step depends on the instantaneous weather conditions without considering the previous time steps.

Both commercial codes as Thermoflex® [2], Epsilon-Professional [3] and free-access code as System Advisor Model (SAM) [4] or Solergy [5] are available. In addition, a big number of research centers and university groups developed their own tools tailor-made for specific purposes.

2.2 Efficiency indexes

As underlined by [6] and by the SolarPACES “guiSmo” project report [7], a harmonization of technical terms and methodologies is needed in the “CSP world” in order to fairly compare different technologies and solutions. In literature, different terms are present and a precise nomenclature is necessary, in particular for the efficiency parameters.

For that reason, before describing the two selected studies, it is important to define the efficiency indexes that are used to evaluate the performance of a CSP plant. In particular, five efficiencies, introduced in previous works [8-10], cover the most important steps of the energy flow path and enlighten the impact of different plant components:

- *Optical efficiency* (η_{optical}): it compares the radiation on the absorber to the incident solar radiation on the mirror:

$$\eta_{\text{optical}} = \frac{E_{\text{receiver}}}{E_{\text{SUN}}} \quad (2.1)$$

Where $E_{\text{SUN}} = A_{\text{ap}} DNI$ represents the radiative solar power incident on the aperture area of the mirrors, while E_{receiver} represents the theoretical power available on the absorber tube surface.

- *Thermal efficiency* (η_{thermal}): takes into account the collector thermal losses as follows:

$$\eta_{\text{thermal}} = \frac{E_{\text{fluid}}}{E_{\text{receiver}}} = 1 - \frac{E_{\text{th-loss}}}{E_{\text{sun}} \eta_{\text{optical}}} \quad (2.2)$$

E_{fluid} is the net thermal power transferred to the fluid flowing in the collectors and $E_{\text{th-loss}}$ are collector thermal losses.

- *Piping efficiency* (η_{piping}) evaluates the impact of piping thermal losses (including nighttime losses) on the fluid transferred thermal power. It is expressed by :

$$\eta_{\text{piping}} = \frac{E_{\text{fluid}} - E_{\text{loss,piping}}}{E_{\text{fluid}}} = \frac{E_{\text{boiler}}}{E_{\text{fluid}}} \quad (2.3)$$

Where $E_{\text{loss,piping}}$ are piping thermal losses and E_{boiler} is the resulting thermal input to the power block.

- *Net power block efficiency* ($\eta_{\text{net_PB}}$) expresses the efficiency conversion of the thermal input into electricity:

$$\eta_{\text{net_PB}} = \frac{E_{\text{el,turb}} - E_{\text{el,pumps}}}{E_{\text{boiler}}} = \frac{E_{\text{el,net_PB}}}{E_{\text{boiler}}} \quad (2.4)$$

Considering a common Rankine water steam cycle, $E_{el,turb}$ is the steam turbine electric power output, $E_{el,pump}$ stands for condensate and feed-water pumps consumption, and E_{el,aux_cond} are condenser auxiliaries consumptions. Net power block efficiency takes into account also heat exchanger thermal losses.

- *Efficiency of solar field auxiliary* (η_{aux_SF}) expresses the impact of solar field circulating pumps, and tracking consumptions on the net power block output:

$$\eta_{aux_SF} = \frac{E_{el,net_PBturb} - E_{el,aux_SF}}{E_{el,net_PB}} \quad (2.5)$$

The product of these five efficiencies gives the overall solar-to-electric efficiency:

$$\eta_{overall} = \eta_{optical}\eta_{thermal}\eta_{piping}\eta_{net_PB}\eta_{aux_SF} = \frac{E_{el,annual}}{E_{SUN}} \quad (2.6)$$

All the efficiency indexes can be used at nominal conditions as well as for annual energy balances. At nominal conditions, all terms are powers (Watt), while in the second case, they are energies (Joule). For simplicity, plant availability is not considered because it does not provide any additional information about annual energy performances.

2.3 Example studies made with quasi-steady approach

The quasi-steady approach is described more in detail with the presentation of two studies that deal with performance analysis of linear CSP technologies.

In the following subsections, both the works are presented with the aim of describing in detail the main topics related to the quasi steady-state procedure used to assess the CSP energetic performances and to introduce fundamental concepts that are used in the next chapters. In particular, the goal of the first work is to study and to compare different solutions for parabolic trough concentrators, while the second one deals with a techno-economic comparison between linear Fresnel reflector and parabolic trough plant.

2.3.1 Study 1: Comparison of available solution for Parabolic trough [11]

The aim of this work is to compare different solar plant technologies to the state-of-the-art Nevada Solar One plant, which is chosen as the reference (designated “IND-OIL”); innovative plants studied differ in both solar field layout and HTF.

A steam cycle is used to convert thermal energy into electricity for all cases studied because, in the range of temperatures and power output considered, it is optimal from energetic and economic perspectives.

Four different plants are evaluated and compared to the reference case: the first is based on an indirect cycle with molten salts as HTF (designated “IND-SALTS”); the second is a direct steam generation plant without reheating (designated “DSG”); the last two are

“hybrid” cycles, where evaporation occurs directly in the solar field, while superheating and reheating are achieved by using an HTF that, respectively, can be synthetic oil (designated “MILAN-OIL”) or molten salts (designated “MILAN-SALTS”). Potential advantages of the hybrid solution in terms of efficiency and specific costs were already discussed in a previous paper [12]. System analysis does not consider any thermal storage, because the focus is on the conversion process of solar radiation to electricity in each typology studied, neglecting the influence of heat storage on different solutions.

Energy balances are calculated with the in-house code PATTO (PARabolic Trough Thermodynamic Optimization), able to predict the performance of solar trough-based concentrating solar power (CSP) plants in both design and off-design conditions. The code is implemented in MS Visual Basic, with Excel spreadsheets as the user interface for input and output data. Starting from the on-design sizing ([9] and [12]), the code calculates off-design performance and the annual electricity production for a specific site without thermal storage. This model was previously validated by real plant data [13], and other commercial codes [8] that have been developed specifically to investigate innovative solar plant layouts and components, both in terms of thermodynamic performance and electricity cost.

Five cases are investigated in this work and they are presented separately in the next sections. For all cases, a constant net power output of the solar plant of 50 MWe is considered; in addition, the water preheating section of the steam cycle was kept the same to emphasize the advantages and drawbacks of each solar field solution.

Concerning the power block, that is a common Rankine cycle, some assumptions are kept constant in order to have a consistent set of results that helps the comparison among the different investigated solutions. The steam turbine is divided in two sections, the high pressure (HP) section and the low pressure (LP) section whose isentropic efficiency are set to 85% and 88% respectively. The steam turbine leaving losses of the last LP turbine stage is equal to 25 kJ/kg. The feedwater pump has a hydraulic efficiency of 75% whereas the hydraulic efficiency of the condensate pump is 70%. Each pump has the same mechanical-electrical efficiency equal to 94%. The generator electrical efficiency is set to 97%. The heat exchangers train, that transfers the heat of the HTF to the cycle working fluid, is characterized by a thermal losses equal to 1.5%. The preheating line is made of seven feedwater heaters (three at high pressure, one deaerator, and three at low pressure); the bleeding pressures are chosen to maintain the same minimum temperature difference (3°C). As regards the cooling technique, an air condenser is chosen. The design ambient temperature is 30°C and the air temperature increase is 10°C. The minimum temperature difference between the air and steam (@0.096 bar) is 5°C. In order to determine the electric consumption of the fans the pressure drop is set to 9 mm_{H₂O} and the total efficiency of the air-condenser fans is 75%.

As far as the solar field assumptions concerns, the reference DNI is 800 W/m² with a zero incidence angle, solar multiple equal to one and the distance between adjacent rows is set to 15 m.

2.3.1.1 Indirect cycles: synthetic oil (IND-OIL) and molten salts (IND-SALTS)

The first technology presented is the indirect-cycle configuration that represents the state-of-the-art of the parabolic trough technology. In this solution, a HTF is used to transfer the collected energy in the solar field to the power block that is a common steam Rankine cycle. Among available HTF, synthetic oil is the choice in all the commercial parabolic trough plants (see Appendix for the thermophysical properties of synthetic oil). An innovative concept, developed by ENEA, considers the use of a mixture of salts (60%NaNO₃ + 40%KNO₃) in a parabolic trough plant [14]. The main difference between these two fluids is the working temperature limit, which is about 400°C for synthetic oil whereas molten salts allow a maximum temperature limit of 600°C. In particular the maximum temperature level considered in this study are 393°C and 550°C for synthetic oil and molten salts respectively leading to a maximum steam temperature at the turbine inlet of 370°C and 540°C in accordance to actual plant design conditions [15].

A reheater (RH), in parallel with economizer (ECO), evaporator (EVA), and superheater (SH) banks, is also used to increase steam-cycle efficiency and steam quality at the turbine outlet; steam temperature after the RH is kept equal to the SH. Both synthetic oil and molten salts are considered in this study and the layout are indicated with IND-OIL and IND-SALTS respectively. Figure 2.1 shows the layout of the indirect-cycle solutions. The solar field is modeled assuming commercially available parabolic trough collectors: in IND-OIL, formerly Siemens Concentrated Solar Power Ltd. Technology is considered for the receiver, ET-100 [16] is selected as SCA and FLABEG [17] mirrors are used, whereas Archimede Solar Energy [18] provides the absorber for IND-SALTS, because it is the only commercial receiver that has been operated above 500 °C.

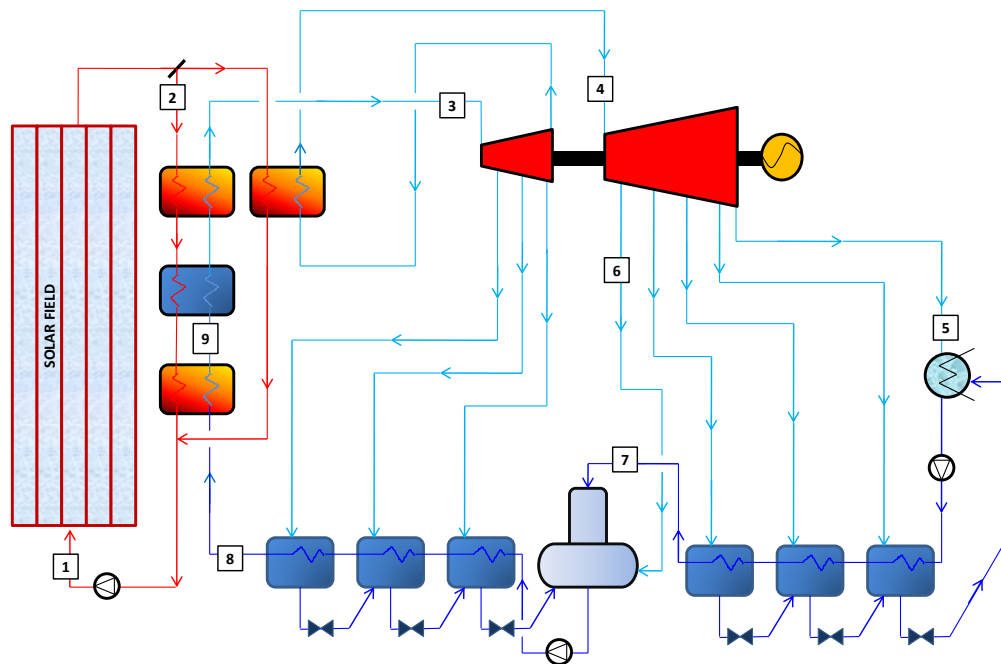


Figure 2.1 Indirect plant layout. This layout is common to both the “IND-OIL” and “IND-SALTS” configuration

Table 2.1 show the properties of the stream enlightened in the figure below.

Table 2.1 Stream properties for the two indirect layouts (IND-OIL, IND-SALTS).

Stream	Fluid type	IND –OIL			IND -SALTS		
		m [kg/s]	p [bar]	T [°C]	m [kg/s]	p [bar]	T [°C]
1	HTF	725.8	25.0 ²	308.0	355.9	15.0 ²	312.7
2	HTF	618.7	17.6	390.0 ²	296.6	3.7	550.0 ²
3	Steam	63.5	95 ²	370.0 ²	47.1	115.0 ²	540.0 ²
4	Steam	51.6	14.5 ²	370.0	37.9	14.5 ²	540.0 ²
5	Steam	49.1	0.096	45.0 ²	30.8	0.096	45.0
6	Steam	2.6	9.2	312.8	1.6	9.2 ²	471.4
7	Water	49.1	8.7 ²	143.9	36.3	8.7 ²	143.9
8	Water	63.5	117.6	260.4 ²	47.1	141.2	278.9 ²
9	Water	63.5	100	299.5	47.1	120.0	313.4

2.3.1.2 Direct cycle: direct steam generation (DSG)

In the direct cycle configuration (DSG), the steam is directly generated in the solar field, thus avoiding the adoption of a boiler in the power section. Further advantages of this solution are:

1. Solar field constant temperature in the evaporation section with benefits for solar thermal efficiency,
2. receiver maximum temperature coincident with the steam cycle one,
3. reduced solar field re-circulating pump consumptions and
4. use of demineralized water that is environment-friendly compared to synthetic oil.

Main drawbacks are strongly related to the two-phase flow in absorber tube and they can be summarized in:

1. high volumetric flow in the solar field,
2. the super-heating section composed of several short loops placed in parallel, and
3. the limited storage capacity, with negative effects during transient conditions.

The last aspect is important from operation point of view, but it cannot be outlined from energetic hourly-step simulations as in this work. In this solution, water conditions at solar field inlet are 100 bar and 279.3°C. Evaporation and superheating take place in two different parts of the solar field that are connected by a steam/water separator [19]. Steam quality at the evaporation section outlet is set equal to 0.77 as suggested by [20]: this value guarantees a good wettability of the collector preventing hot spots formation. The

² Assumptions

separated liquid fraction is sent back at the inlet of the solar field through a recirculation pump and mixed with feed-water at 260.4°C. Vapor fraction is sent to the SH section where is heated up to 540°C. Solar collector selected technology for preheating and evaporating section is the same used in IND-OIL configuration. Because of the higher pressure of steam/water compared to OIL (100 vs. 25 bar), a thicker absorber tube, probably made by the same material, should be necessary; on the other hand, ARCHIMEDE collectors are implemented for the superheating section assuming a larger thickness to withstand the higher steam delivery temperature and pressure. Differently from the previously presented layout, no reheating is adopted in order to avoid additional field sections dealing with very high volumetric steam flow, and consequent high velocity and pressure drops. A schematic of the DSG layout is presented in Figure 2.2. Characteristic stream properties of the plant are summarized in Table 2.2.

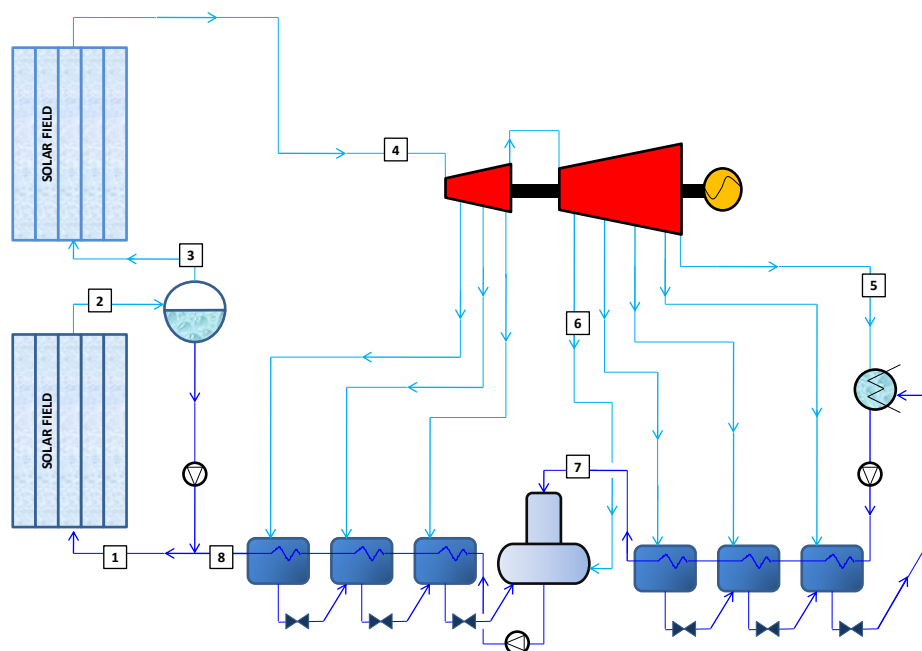


Figure 2.2 Direct Steam Generation (“DSG”) plant layout.

Table 2.2 Stream properties for the DSG layout

DSG				
Stream	Fluid type	m [kg/s]	p [bar]	T [°C]
1	Water	73.7	100 ³	279.3 ³
2	Steam	73.7	91.3	304.7
3	Steam	56.8	89.3	302.8
4	Steam	56.8	81.0	540.0 ³
5	Steam	36.7	0.096	45.0 ³
6	Steam	2.4	9.2	256.1
7	Water	44.1	8.7 ³	143.9
8	Water	56.8	100 ³	260.4 ³

³ Assumptions

2.3.1.3 Hybrid configurations: MILAN-OIL and MILAN-SALTS

The hybrid configuration, introduced in a previous paper [9], is proposed to combine advantages of direct and indirect cycles. The solar field is divided into two sections: the first performs direct steam evaporation, as in the DSG configuration; in the second section, a conventional HTF is heated. The HTF is then sent to the power block for steam superheating and reheating. This solution retains some of the DSG advantages, such as constant temperature in the evaporation section and reduced auxiliary consumption in the solar field, and it allows one to:

1. reduce volumetric flow in the solar field,
2. use a RH to improve power block efficiency,
3. maintain better control of receiver-tube temperatures in the high-temperature section, and
4. store thermal energy to increase plant availability.

In this configuration, feedwater from the steam-cycle economization line enters the solar field evaporation section and is evaporated. As in the previous case, the vapor quality at the evaporator exit is set to 0.77. The two-phase mixture is then separated and the liquid fraction is recirculated; the steam is then sent to the superheating heat exchanger where it reaches the maximum cycle temperature, which depends on the HTF used in the solar field. As for indirect cycles, two different HTFs are investigated: Therminol VP-1[®] and solar salts. In hybrid solutions, the RH heat exchanger is set in parallel to the SH heat exchanger, as shown in Figure 2.3. The solar field consists of three sections distributed around the power block in a so-called “Y” layout: two DSG sections and one SH/RH section.

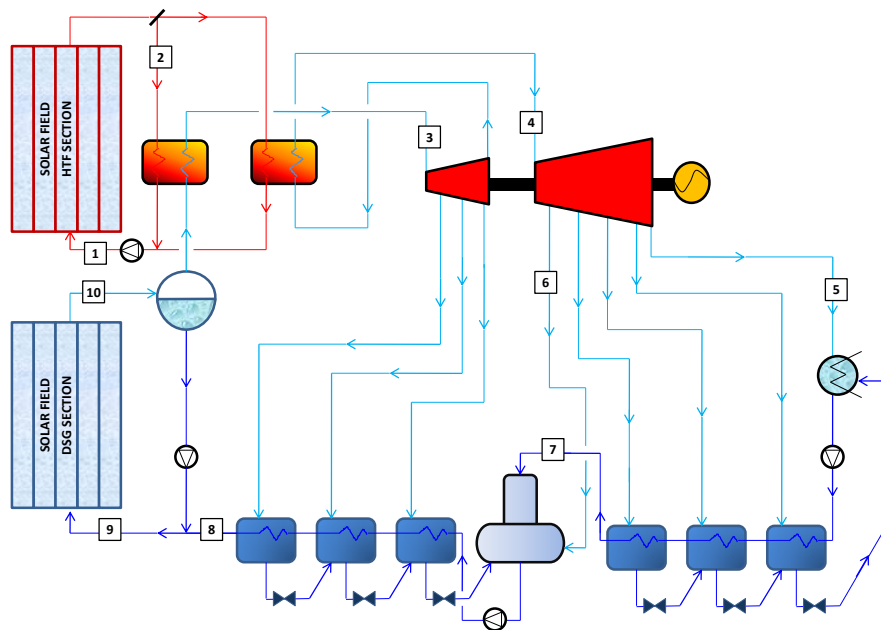


Figure 2.3 Hybrid plant layout

Table 2.3 summarizes the resulting stream properties of the plant.

Table 2.3 Stream properties for the two hybrid layouts (MILAN-OIL, MILAN-SALTS)

Stream	Fluid type	MILAN-OIL			MILAN-SALTS		
		m [kg/s]	p [bar]	T [°C]	m [kg/s]	p [bar]	T [°C]
1	HTF	192.8	25.0 ⁴	300.1	180.95	15.0	338.4
2	HTF	130.2	17.8	390.0 ⁴	112.6	8.50	550.0 ⁴
3	Steam	65.3	82.2	370.0 ⁴	48.1	81.0	540.0 ⁴
4	Steam	52.2	14.5 ⁴	370.0 ⁴	39.9	14.5 ⁴	540.0 ⁴
5	Steam	41.5	0.096 ⁴	45.0 ⁴	32.4	0.096 ⁴	45.0 ⁴
6	Steam	2.6	9.2	312.8	1.8	9.2	471.4
7	Water	49.6	8.7 ⁴	143.9	38.1	8.7 ⁴	143.9
8	Water	65.3	100 ⁴	269.4 ⁴	48.1	100 ⁴	268.4 ⁴
9	Water	84.75	100	279.7	62.52	100	278.9
10	Steam	84.75	85.2	299.4	62.52	84.0	298.4

2.3.1.4 Performance at design condition

Performance of the five studied cases is calculated with the PATTO code, which allows the use of different parabolic trough technologies; different HTFs such as synthetic oil, solar salts, or DSG; and flexible power section configurations, as well as solar field layout. The code was already discussed and validated in previous works [9,12,13] developed by the Gecos Group [21] at Energy Department of Politecnico di Milano. In Table 2.4 the results of the sizing phase are reported for all the cases.

Table 2.4 Performances in on-design conditions for different technologies.

	IND-OIL	IND-SALTS	DSG	MILAN-OIL	MILAN-SALTS
Gross Power [MW]	53.2	52.1	51.7	52.4	51.7
Steam Cycle Aux Consumption [MW]	-2.0	-1.8	-0.8	-1.1	-0.8
Total Number of Loops ⁵	64	24	53	16 + 11	22 + 17
Pump Head [bar] ⁵	8.9	13.6	19.0	14.8 + 8.6	14.7 + 7.8
Solar Field Aux Consumption [MW]	-1.2	-0.3	-0.9	-1.3	-0.9
HTF SCA Aperture Area [m ²]	278,887	254,557	-	80,304	109,267
DSG SCA Aperture Area [m ²]	-	-	247,506	187,490	138,911
Total SCA Aperture Area [m ²]	278,887	254,557	247,506	267,794	248,178
Total Required Land Area [m ²]	679,698	539,316	630,927	639,583	606,103
HTF Mass Flow [kg/s]	725.8	355.9	-	192.0	180.7
Steam Mass Flow @ turbine inlet [kg/s]	63.5	47.1	56.8	65.3	48.1

⁴ Assumptions

⁵ For DSG, MILAN-OIL, and MILAN-SALTS cases, the number of loops and pump head are split in evaporating + superheating section

η_{optical} [%]	74.4	74.7	74.5	74.4	74.5
η_{thermal} [%]	90.0	86.2	89.0	91.7	89.0
η_{piping} [%]	98.9	98.9	99.4	99.4	99.4
$\eta_{\text{net_PB}}$ [%]	34.6	38.8	38.4	34.7	38.4
$\eta_{\text{aux_SF}}$ [%]	97.8	99.4	99.9	99.2	99.6
η_{overall} [%]	22.4	24.6	25.3	23.3	25.2

Concerning the solar field, the optical efficiency depends only on the collector technology used, and no significant differences need to be highlighted, other than a slightly higher optical efficiency (+0.3) of the ARCHIMEDE solar collector due to improved optical properties. Thermal losses are mainly influenced by the collector wall average temperature and by the absorber selective coating emissivity, which is also a function of temperature [22]. SOLEL and ARCHIMEDE absorber tubes, used in the cases investigated, have very similar emissivity figures, and the difference depends only on the working temperature range; consequently, the thermal efficiency of MILAN-OIL is the highest because of its lower mean temperature, whereas IND-SALTS presents the lowest value, even if only by 6% less than the best case. MILAN-SALTS, despite its higher solar field fluid average temperature (i.e. MILAN-SALTS has RH section), reaches the same thermal efficiency as DSG; this is because the heat-transfer coefficient of steam is significantly lower than for solar salts, leading to absorber tube temperatures about 40 °C above corresponding conditions of the MILAN-SALTS superheating section, with consequent penalties.

Piping and header losses, accounted by the piping efficiency, are not very severe; PATTO software works with an imposed thermal loss per unit length, so the highest η_{piping} and consequently lowest heat losses are obtained in the DSG and hybrid plants because of the “Y” layout: the “H” solar field layout, used in IND-OIL and IND-SALTS, has longer pipes to connect all four headers. The plant that scores the best power block efficiency is IND-SALTS because of the highest steam temperature and pressure at the turbine inlet. Despite the same maximum steam temperature, DSG and MILAN-SALTS show a lower $\eta_{\text{net_PB}}$ (−0.4%) because of the lower steam pressure at the turbine inlet due to absorber tube structural limits and pressure drops in the DSG field. The small efficiency gain with RH in MILAN-SALTS (less than 0.1%) compared to DSG is justified by the:

1. low salts temperature at cold RH (about 290 °C).
2. presence of a heat exchanger with consequent heat losses that account for 1.5% efficiency loss.
3. constant isentropic efficiency used in the LP section, neglecting liquid formation penalties. Finally, the 393 °C maximum temperature of Therminol VP-1® implies the lowest PB efficiencies in both the IND-OIL and MILAN-OIL cases.

The best overall efficiencies are reached by DSG and MILAN-SALTS, which are also characterized by the lowest total mirror surface area, because of the fixed net power output. Thermodynamic advantages of these two cases vs. conventional technology (IND-

OIL) are in the range of 12%, in relative terms. It is important to notice that the DSG configuration and hybrid configurations have some intrinsic difficulties in solar field controlling strategy, due to handling a two-phase flow in the collectors as reported by [23] and [24]. Finally, DSG and MILAN-SALTS have a different total required land area even with the same SCA aperture area, because of different number of loops.

2.3.1.5 Part-load simulation

Once the whole plant was sized, the characteristics of each component are known and they have to be considered to simulate the part-load performance occurring due to the change in weather parameters (DNI, sun position, ambient temperature). In order to set the boundaries of the system, the chosen plants location is Las Vegas (see Table 2.5). The weather data in terms of DNI, ambient temperature and relative humidity are taken from [25] with a timeframe of one hour in accordance to the TMY3 standard.

Table 2.5 Geographical coordinates and weather data information of the selected location.

<i>Geographical Coordinates and Weather Data</i>	
<i>Variable</i>	<i>Value</i>
Name	Las Vegas
Latitude	36°10'30"N
Longitude	115°08'11" W
Yearly DNI	2592 kWh/m ² -y
Average Temperature	19.8°C

The whole plant can be divided in two macro-components, the solar field and the power block respectively and their off-design modelling is described in the sections below.

Solar Field:

The solar collector thermal model for off-design performance calculation is the same as the one used in on-design phase ([9], [8] based on the thermal resistance network reported by Forristall's [22]). In addition to latitude and longitude needed to calculate the sun path (see Appendix for a specific description), the tracking axis orientation is necessary to compute the angle between the sun rays and the vector normal to the aperture (incidence angle θ) which has the highest off-design impact of reducing concentrating system optical efficiency.

The Figure 2.4 shows the definition of incidence angle for PT that is identified by the angle between sunray and the normal to the aperture plane.

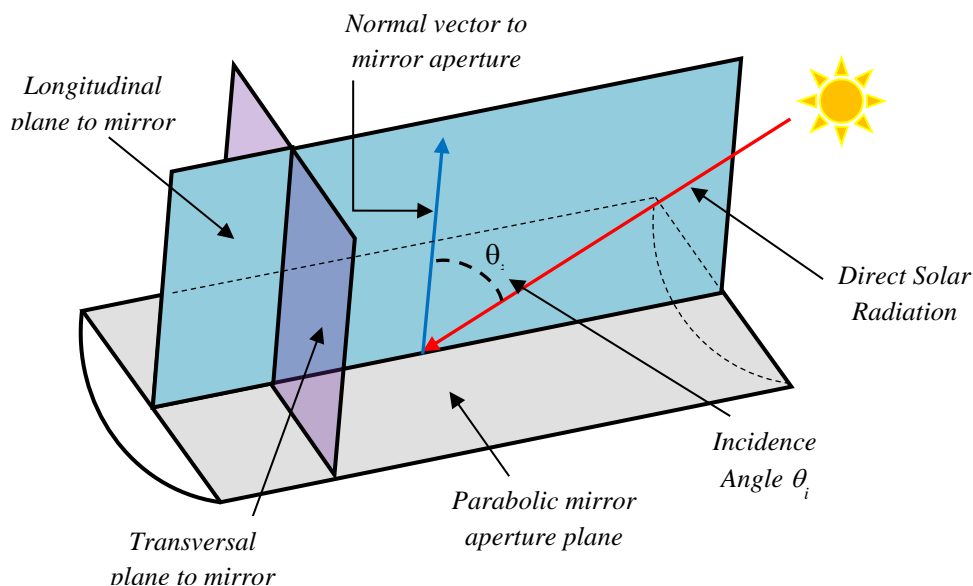


Figure 2.4 Incidence angle definition for PT concentrator (adapted from [26])

Due to the continuous tracking of PT the incidence angle belongs to the longitudinal plane. Once the sun position is defined (both the zenith and the azimuth are known), the incidence angle, in case of N-S tracking axis, can be expressed by:

$$\theta_i = a \sin(\cos(\gamma) \sin(\theta_z)) \quad (2.7)$$

Optical efficiency correction for the incidence angle is expressed by the global parameter $K(\theta)$ whose annual trend is shown in Figure 2.5.

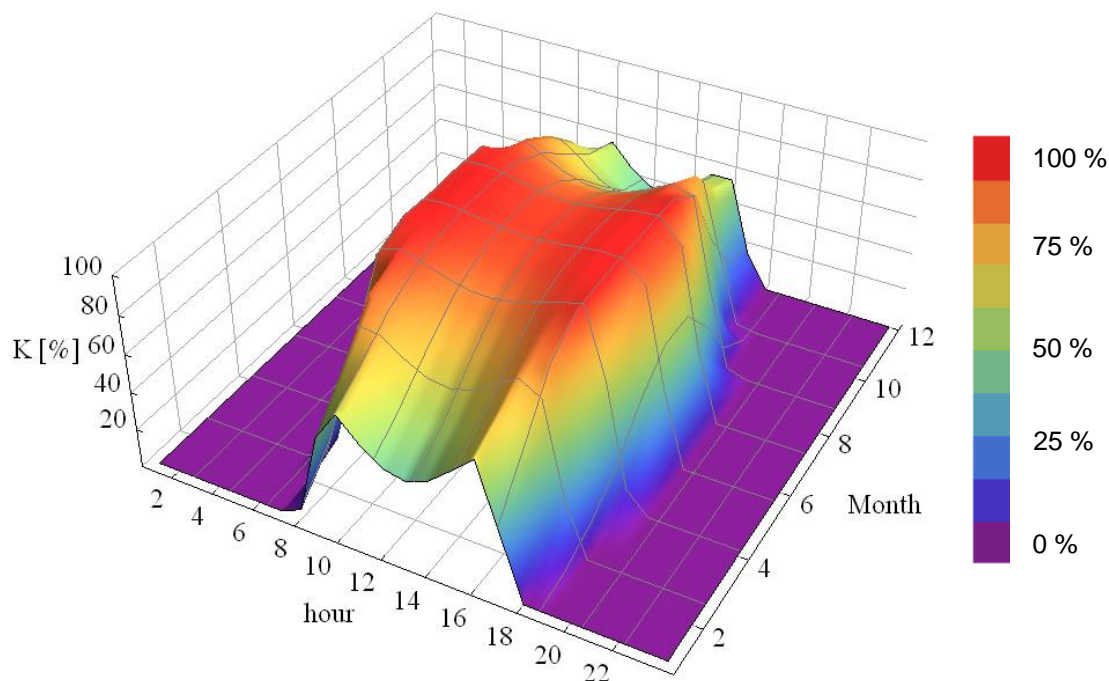


Figure 2.5 Yearly trend of $K(\theta)$ of ET-150 collector placed in Las Vegas (N-S tracking axis)

In addition to the $K(\theta)$ parameter, a row shading effect is considered to account for mutual parabolic mirror shadowing that causes a decrease in the amount of active mirror surface. The shading efficiency is influenced by the sun position, the aperture of the parabolic mirror and the spacing between adjacent rows and can be approximated by the following relation [27] (a more precise and geometrical detailed analysis is can be found in [28]).

$$\eta_{shading} = \min \left[\max \left(0; \frac{L_{spacing}}{W} \frac{\cos(\vartheta_z)}{\cos(\vartheta_i)} \right); 1 \right] \quad (2.8)$$

For simplicity, $K(\theta)$ and shading effect are directly applied to the solar radiation, as presented in Eq. (2.9), introducing the ‘‘Effective DNI’’ (‘‘EDNI’’) concept, instead of correcting the optical efficiency⁶:

$$EDNI = DNI K(\vartheta) \eta_{shading} \quad (2.9)$$

The chosen solar field control strategy at partial load is based on keeping a constant exit temperature of HTF (i.e. equal to design conditions) by varying the mass flow until 50% of the mass flow design conditions. Then, during very low solar radiation hours, HTF mass flow in the solar field is fixed, decreasing the solar field outlet temperature.

In a previous paper, we demonstrated that this strategy optimizes annual energy production [8]. The resulting temperature range for low radiation, affected by a sliding pressure turbine control, is between 250 °C and 290 °C.

In addition, for IND-SALTS and HYB-SALT configurations, minimum temperature of solar field molten salts must be kept well above the freezing temperature (220 °C), thus reducing the operating range. The minimum temperature set for solar salts is 260 °C; when conditions imply a lower temperature, a minimum mass flow of solar salts is circulated in the solar field to avoid any solidification.

Nighttime losses are included in the model, reducing the temperature of the HTF in the solar field. As regards the piping system, pressure drop and thermal losses have to be taken into account to correctly study the annual performance of the CSP plant

Once the on-design pressure drop of the piping is known, the head loss in off-design conditions is assumed proportional to the square of HTF mass flow:

$$\Delta p = k_{\Delta p} m_{HTF}^2 \quad (2.10)$$

The thermal losses are assumed to be proportional to the nominal value at rated condition and adjusted for the ambient temperature and HTF variation.

⁶ This simplification reduces computational time with limited impact on reliability of results slightly affecting envelope glass temperature.

Power Block:

The power block is the most complicated part to simulate because each component is significantly affected by off-design conditions. For the turbine, sliding pressure working conditions are assumed down to 50% of the rated load, whereas below this value, a constant pressure at the steam turbine inlet due to a partial admission stage is assumed. Turbine shut-down was assumed below 15% of the rated turbine power, as indicated by [29]. Steam turbine isentropic efficiency variation and pressure conditions at regenerative bleedings at off-design conditions are assumed, as described in [13] and [30]. In particular, an isentropic efficiency variation at part load is introduced. In off-design calculation, kinetic losses are also taken into account as a function of axial velocity at the turbine exit and are presented in Figure 2.6.

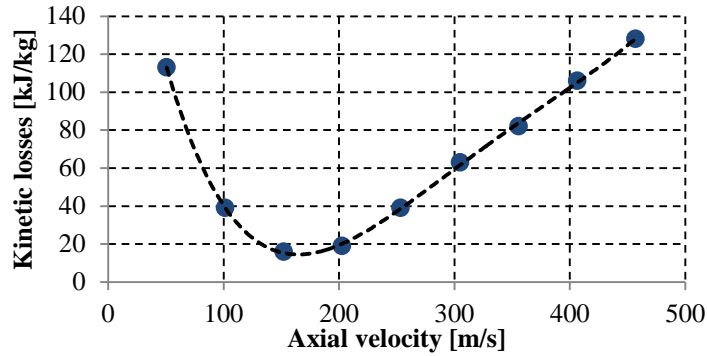


Figure 2.6 Turbine kinetic losses as a function of the axial velocity.

Boiler and feedwater preheaters performances vary at off-design conditions in terms of heat transferred and pressure drop. The following description can be applied to all heat exchangers, because of their similarity. Pressure drops are modeled as previously discussed for piping. Heat transferred is calculated by means of the Logarithmic Mean Temperature Difference *LMTD* approach [31]. The law describing coefficient *U* variation can be obtained from the definition of the coefficient itself [31]:

$$\frac{1}{UA} = \frac{1}{h_{conv,in}A_{in}} + \frac{R_{fou,in}}{A_{in}} + \frac{\ln\left(\frac{D_{out}}{D_{in}}\right)}{2\pi kL} + \frac{R_{fou,out}}{A_{out}} + \frac{1}{h_{conv,out}A_{out}} \quad (2.11)$$

All terms, but convective heat transfer coefficients h_{conv} , do not depend on mass flow, and assuming that the external to internal mass flow ratio remains constant at off-design conditions and conduction effects are negligible, the equation can be simplified as:

$$\left(\frac{U_{off}}{U_{design}}\right) = \left(\frac{m_{off}}{m_{design}}\right)^n \quad (2.12)$$

where the value of n varies between 0.6 and 0.8. Subscripts *design* and *off* indicates nominal and off-design conditions. This approach, adopted also in [13,32], is assumed

for all phases occurring in heat exchangers (steam, liquid and evaporation/condensation) allowing to calculate off-design inlet/outlet temperatures. Condenser performance is fundamental to evaluating turbine outlet pressure and, consequently, net power output and overall plant performance. Two different strategies can be used to control the condenser at off-design conditions: the first consists of maintaining constant condensing pressure by varying fan speeds, whereas in the second strategy, fans work at constant speed and condensing pressure varies. The model adopted a combination of these two strategies in the following way: condenser fans work at constant speed until the steam volumetric flow at the turbine outlet is 1.5 times that of the nominal condition (maximum condition acceptable by steam turbine). When this condition is reached, the condenser fan speed is decreased to maintain a constant volumetric flow rate. However this situation seldom occurred, because it requires high solar radiation and low ambient temperature, which is a rare combination for typical sites.

Finally, electric generator efficiency is assumed to be function of the load fraction [32] as shown in Eq.(2.13):

$$\eta_{gen} = 0.893 + 0.258LF - 0.3LF^2 + 0.12LF^3 \quad (2.13)$$

2.3.1.6 Off-design and annual simulation results

Annual simulation results, primary energy fluxes, and efficiency indexes are presented in Table 2.6, showing annual performance of the different configurations discussed above.

Table 2.6 Annual performance comparison for different plant layouts.

	IND-OIL	IND-SALTS	DSG	MILAN-OIL	MILAN-SALTS
Available Solar Energy [MWh/y]	722,875	659,812	641,536	691,006	643,277
EDNI [kWh/y-m ²]	1,961	1,955	1,959	1,961	1,958
Effective Solar Energy N-S [MWh/y]	546,986	497,732	484,929	522,870	486,096
Receiver Solar Energy [MWh/y]	406,841	372,146	361,327	388,904	362,386
Thermal energy to HTF [MWh/y]	354,098	299,661	314,513	343,231	311,958
Piping losses [MWh/y]	-9,611	-7,433	-2,562	-4,494	-2,698
Thermal energy to power block [MWh/y]	344,487	292,228	311,951	338,736	309,260
Nighttime SF aux. consumptions [MWh/y]	-20	-331	0	-3	-77
Net electric energy [MWh/y]	110,903	106,928	114,917	110,642	114,269
$\eta_{optical}$ (%)	56.3	56.4	56.3	56.3	56.3
$\eta_{thermal}$ (%)	87.0	80.5	87.0	88.3	86.1
η_{piping} (%)	97.3	97.5	99.2	98.7	99.1
η_{net_PB} (%)	33.3	37.1	36.9	33.0	37.1
η_{aux_SF} (%)	96.5	98.5	99.8	99.0	99.5
$\eta_{overall}$ (%)	15.3	16.2	17.9	16.0	17.8

Available energy represents the total amount of solar energy that could ideally be collected by the solar field. The variation among five cases depends on different solar field total aperture area calculated at on-design condition, that already was shown in Table 2.4. Effective direct normal irradiation (EDNI) takes into account the effects of $K(\theta)$ and row-shading responsible for reducing annual DNI, which is 2592 kWh/m^2 ; according to this definition, EDNI changes slightly because of the different aperture width between ET-100 and ENEA mirrors (5.77 m vs. 6 m) with a constant row pitch for all solar field configurations (15 m) and consequent different shading effect.

The amount of energy available on the absorber tube surface is named Receiver Solar Energy.

Thermal energy to HTF is significantly higher for IND-OIL and MILAN-OIL cases because of the poor power block performance. In addition, for piping losses, indirect-cycle cases are penalized because of the “H” configuration, and between HTFs, SALTS benefits of the shorter pipes. In Table 2.6, nighttime solar field auxiliaries consumptions are also shown. Differences are significant because solar fields with HTF, in particular solar salts, require nighttime recirculation to avoid solidification, whereas DSG does not. HTF recirculation will also lead to significant nighttime thermal losses (already included in Thermal energy to HTF).

For the different technologies analyzed, optical efficiency changes slightly according to the values obtained during design calculation. This is also because the same $K(\theta)$ was taken for both ARCHIMEDE and ET-100. Thermal efficiencies are significantly lower than on-design results presented in Table 2.4, and thermal losses almost doubled. The reason is that despite almost constant thermal losses, depending only on absorber tube external temperature, the average solar radiation is lower than the nominal one (see Eq. (2.9)).

The highest thermal efficiency decay compared to the nominal condition occurs for the IND-SALTS configuration; this is due to the chosen operating strategy, which switches off the power block to avoid salts crystallization at the solar field inlet for EDNI lower than about 250 W/m^2 . Even if defocusing is applied, this loss of energy is accounted as a thermal loss. This control strategy also leads to higher nighttime auxiliary consumption. DSG and hybrid configurations present the lowest thermal efficiency decay because evaporation pressure and temperature in the solar field also decrease at low radiation, reducing heat losses. This result is a consequence of the sliding pressure control strategy assumed for the turbine up to 50% of the rated load.

MILAN-OIL shows the highest thermal efficiency because it combines DSG benefits and lowest maximum temperature. The power block operates in off-design conditions for most of the year because of the absence of thermal storage.

Considering the entire solar plant, the power block is less affected by partial-load conditions because it can benefit by lower ambient temperature reduction, thus reducing condensing pressure. OIL and DSG configurations score the highest decay: low maximum temperature (OIL cases) and the absence of RH (DSG) lead to strong penalties at partial load: the power block efficiency difference between IND-SALTS and DSG was 0.4% at on-design conditions, becoming 1.2% on an annual basis. Finally, the DSG configuration significantly reduces solar field auxiliaries consumption.

Figure 2.7 shows specific monthly electric energy production (kWh/m^2) for all cases considered.

DSG and MILAN-SALTS score the highest energy production in all months, whereas IND-SALTS during the winter is the worst configuration because of the aforementioned high crystallization temperature. Comparing indirect and hybrid configurations, hybrids are always better with greater benefits at low radiation (winter period) due to the lower evaporation temperature and consequent heat losses in the solar field.

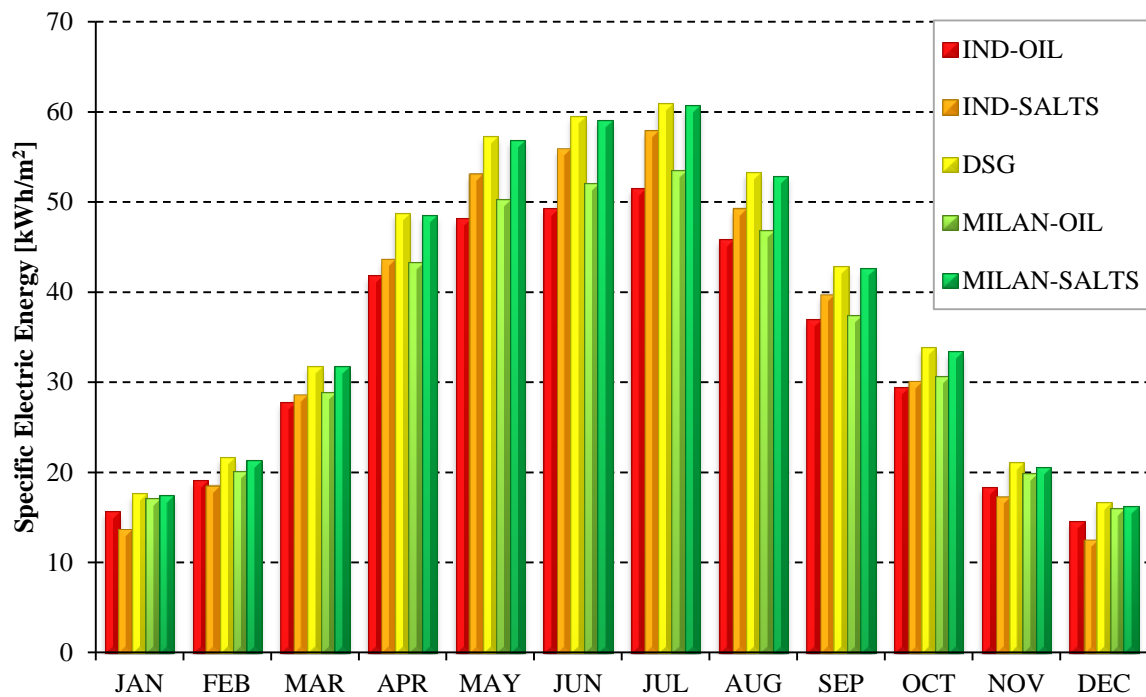


Figure 2.7 Monthly net electric energy yield per square meter of collector aperture area (kWh/m^2) for different plant layouts.

Figure 2.8 shows DNI and Specific Net power output for three days representing typical summer (21st July), spring (20th March) and winter conditions (18th December). Comparing 21st July and 18th December, characteristic effect of $K(\theta)$ and mutual shading can be noticed on net power output, in accordance with previous discussion related to Figure 2.5. Figures outline advantages of Milan configuration towards reference plant during winter period and low radiation hours thanks to the evaporation in the solar field, while radiations close to design conditions, differences reduce as also shown in Table 2.4. As far as DSG is concerned, it achieves the highest specific net power output during summer time, while in winter performances are penalized by the absence of RH. Referring to morning operation hours, a delay of about an hour from DNI can be noticed, this can be explained by the effect of mutual shading (see eq.(2.8)) which has a strong impact during the first and last hours of a day.

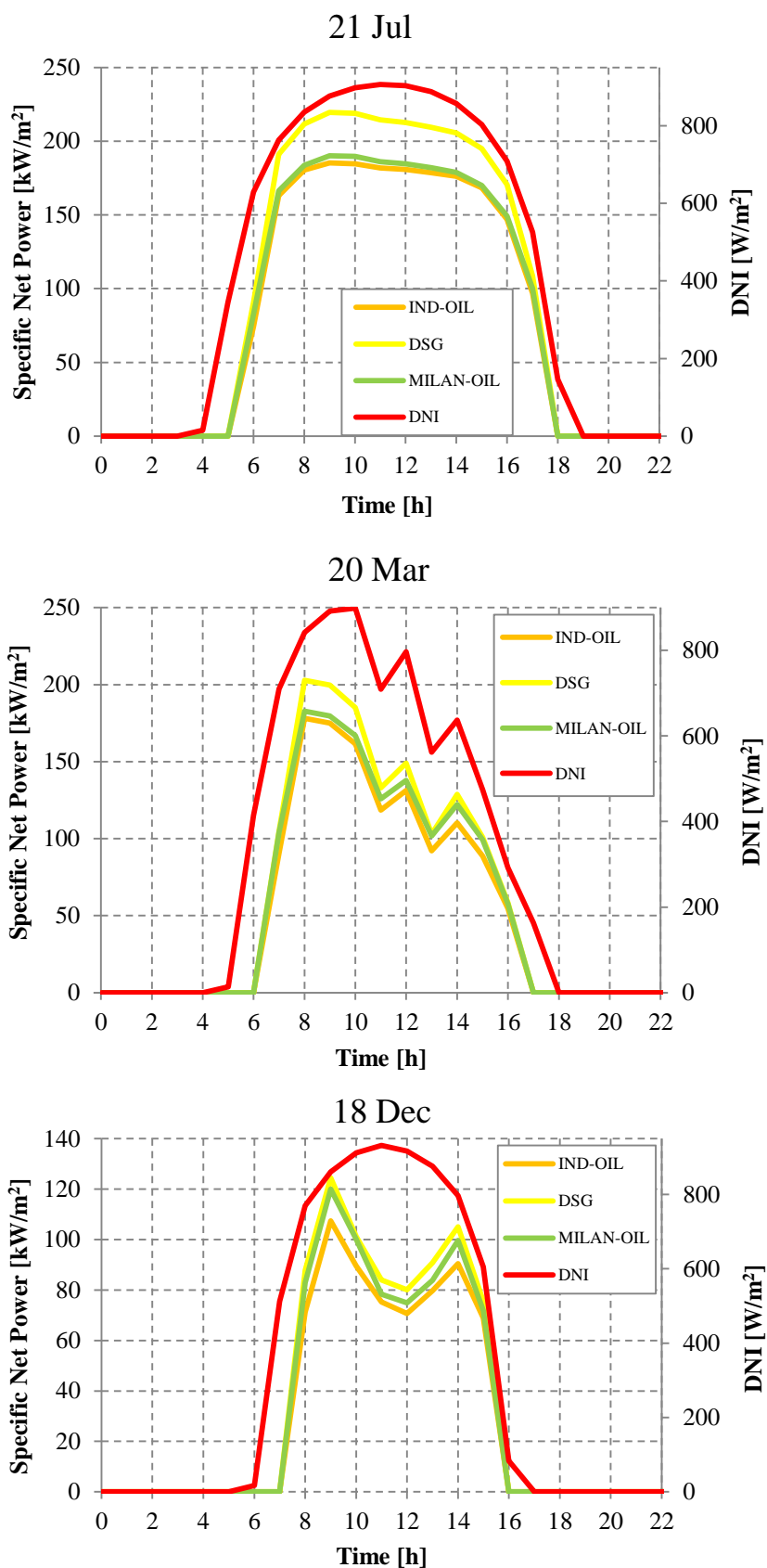


Figure 2.8 21st July (Top), 20th March (middle) and 18th December (bottom), DNI and Specific Net Power Output for IND-OIL, MILAN-OIL and DSG plant layouts

2.3.1.7 Conclusions of Study 1

This work presents a detailed comparison among five different solar plants based on parabolic trough technology: one case, IND-OIL, represents state of the art of linear CSP (i.e. Nevada Solar One or Andasol), and other four cases implemented innovative lay-out and/or heat transfer fluids. Performances, predicted by an in-house code named PATTO, are evaluated at design conditions as well as with yearly simulations.

Results indicate relevant differences among the energy performance of the considered solutions: the net yearly average solar-to-electric efficiency varies between slightly above 15% for conventional IND-OIL scheme to over 17% for DSG and MILAN-SALTS schemes, which take advantage of the higher operating temperatures of the power cycle. This superiority does not hold for the IND-SALTS scheme, which is penalized by poor performance at low DNI. In this respect, the MILAN-SALTS solution, which in addition would allow the adoption of heat storage in the salt loop, seems particularly promising. However, it should be pointed out that the presence of a heat storage of significant capacity (now not commercially feasible for DSG) could modify the plant design philosophy (for instance, suggesting the adoption of larger solar multiple) as well as the plant operating strategy, thus changing the energy balances obtained by this simplified analysis. Moreover, the plant optimization should also account for different investment costs related to the various considered options. Hence, more detailed analyses are required before drawing conclusions about the best plant configuration to be adopted in solar plants based on parabolic trough fields.

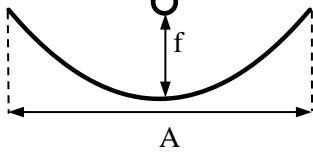
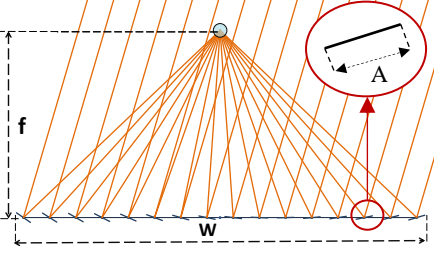
2.3.2 Study 2: Comparison between PT and linear LFR [10]

Despite of the strong presence of PT plants that represent the state of art the CSP technology, “Linear Fresnel Reflector” (LFR) have been object of an intensive research activity with the aim of studying alternative solutions to reduce the cost of electricity.

In order to clarify some aspects regarding the techno-economic performance of LFR, a comparison study with PT is developed in both energetic and economic terms. In addition to the methodology steps, previously described in section 2.3.1, a specific discussion about optical efficiency of LFR is presented in order to facilitate the understanding of the comparison.

Table 2.7 shows the main geometrical characteristics of the studied technology, in particular the PT and LFR dimensions, typical of the commercially available systems, Eurotrough-100 (“ET-100”) and Novatec for PT and LFR respectively [15,16,33].

Table 2.7 Geometrical characteristics of the two investigated technology

	Parabolic Trough (“PT”)	Linear Fresnel (“LFR”)
		
Number of primary Reflector	1	16
Aperture Width [m]	$A = 5.76$	$A = \sum A_i = 12$ $W = 16.56$
Absorber Diameter [mm]	$d = 70$	70
Concentration ratio	$A/d = 82$	171
Focal length [m]	$f = 1.716$	$f = 7.4$
Row pitch [m]	14	20.6
Secondary Reflector type	-----	CPC (<i>Compound Parabolic Concentrator</i>)
Reflective/Aperture area Ratio	$RAR^7 = 1.107$	$RAR \approx 1$

The investigated solutions differ both for the solar field concentrator technology and for the fluid circulating in the solar field, with synthetic oil as HTF for the indirect cycle (representing the linear CSP state of art) and water in case of direct steam generation (“DSG”). In this way, three cases are studied as listed below:

- Solar field based on PT and HTF (IND-PAR);
- Solar field based on LFR and HTF (IND-FRE);
- Solar field based on LFR with DSG (DSG).

In this study a commercial code specific for the simulation of power plant, Thermoflex[®], is the tool used to size and to study the part-load behavior of the whole plant.

To make a fair comparison all the plants are designed for the same DNI of 900 W/m² at zero incidence angle, with the solar multiple equal to one and without any storage system. The net power output is fixed to 50 MW_e and the cooling system considers the use of an evaporative cooling tower with a condensing pressure of 0.08 bar.

2.3.2.1 CSP plant sizing

As previously described, the plant sizing is developed with the commercial software Thermoflex[®]. In addition to the general boundaries previously described, other sizing assumptions are necessary in order to compute the on-design performance of the plant.

Starting from the indirect cycle, in both cases (IND-PAR and IND-FRE), the power block section is a steam Rankine cycle with live steam properties set at 371°C and 100 bar. In order to increase the steam cycle efficiency as well as steam quality at the turbine outlet; a

⁷ See Appendix for the calculation methodology of RAR for parabolic trough concentrator

reheater (“RH”), in parallel with an economizer (“ECO”), evaporator and superheater (“SH”), is adopted.

As regards the solar field, a simile-commercial solution is chosen for parabolic trough with a maximum temperature of synthetic oil set at 391°C. The adoption of Fresnel Novatec collectors is extended to synthetic oil although Novatec collector has been adopted only in DSG plant with an operating condition 100°C lower than typical PT working conditions. The level of generality comparison is increased considering the DSG concept. The advantages and disadvantages of DSG technology have been already resumed in the previous section in accordance with [34]. The DSG plant is representative of the commercial solution tested at the PE2 plant [35] that implements a LFR solar field. The power cycle is a saturated steam cycle with a pressure at the turbine inlet of 55 bars (@270°C). The steam quality at the outlet of solar field is set to 0.8 in order to guarantee a good wettability of the collector and minimizing the recirculation rate.

Figure 2.9 shows the plant layout of both the indirect and DSG solution, enlightening the most representative streams whose characteristics are reported in Table 2.8.

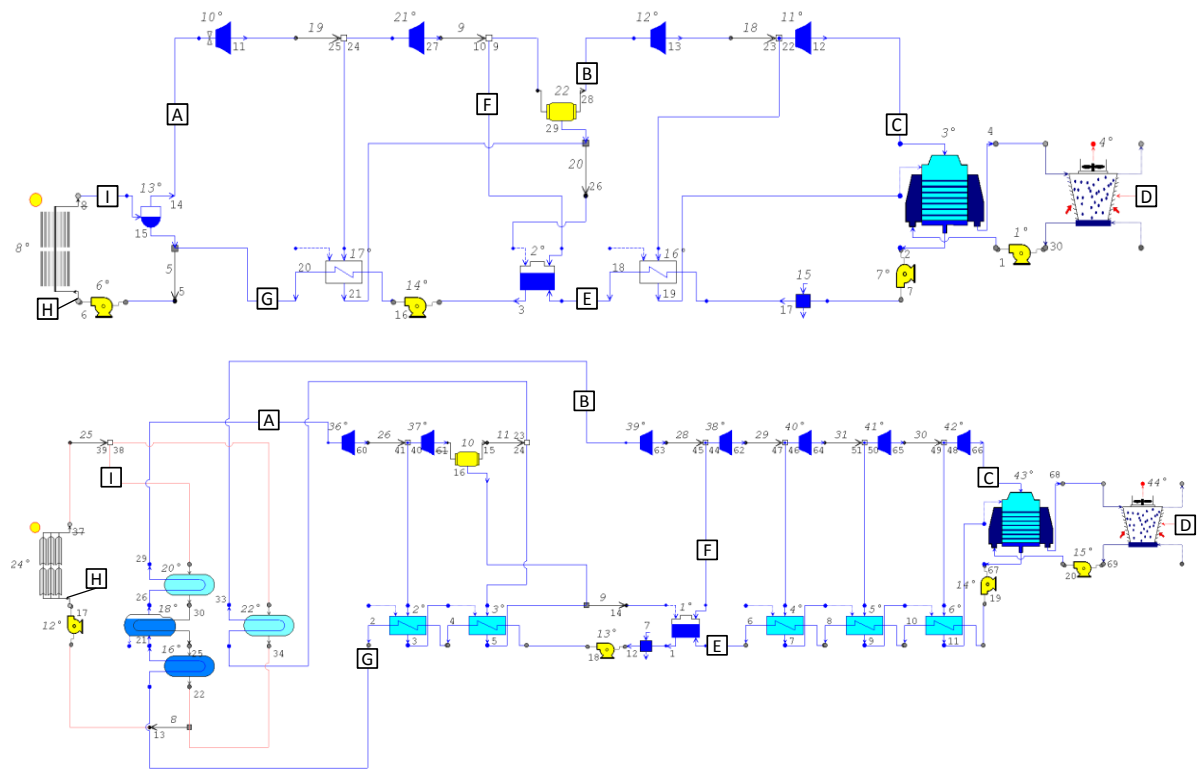


Figure 2.9 - Indirect cycle plants layout (a) and Fresnel plant layout (b). These figures are Screenshots from Thermoflex®.

Table 2.8 Stream properties for the three different studied layouts

Stream	IND - PAR				IND - FRE			DSG			
	Fluid type	m [kg/s]	p [bar]	T [°C]	m [kg/s]	p [bar]	T [°C]	Fluid type	m [kg/s]	p [bar]	T [°C]
A	Water(v)	61.1	99.9	371.0	59.9	99.9	371.0	Water(v)	77.2	55.0	270.0
B	Water(v)	49.4	18.3	371.0	48.4	18.3	371.0	Water(v)	53.5	2.7	130.0
C	Water(v)	39.8	0.1	41.5	39.0	0.08	41.5	Water(v)	49.8	0.1	41.5
D	Air	1179.1	1.0	35.0	1155.6	1.01	35.0	Air	1435.8	1.0	35.0
E	Water(l)	46.6	9.2	126.7	45.6	9.2	126.7	Water(l)	54.6	3.9	90.0
F	Water(v)	3.5	8.0	273.7	3.5	8.0	273.8	Water(v)	4.93	2.7	130.0
G	Water(l)	61.1	100.4	234.8	59.9	100.4	234.8	Water(l)	77.2	55.0	179.5
H	HTF	613.3	25.5	297.3	601.0	20.4	296.7	Water(l)	96.5	66.0	195.9
I	HTF	529.3	13.0	391.0	518.6	13.0	391.0	Water(v)*	96.5	55.0	x _v =0.8

Table 2.9 summarizes the results for design conditions, showing both some values of the most important plant parameters and the “efficiency path” of the three investigated solutions.

In literature, PT and LFR have a different definition of optical efficiency; in particular, the incident area is coincident with aperture area of PT whilst in LFR the reflective area of the primary mirrors is considered. In order to increase the level of consistency of the comparison, two additional indexes are introduced $\eta_{optical_modified}$ and $\eta_{overall_modified}$ that consider the PT reflective area to calculate the incident energy. The difference between the “standard” and “modified” definition of the optical efficiency reflect the value of RAR parameter (See the Appendix for the calculation).

The first comparison is related to the indirect solutions (IND-PAR, IND-FRE). The overall efficiency of IND-PAR, representing the state of art of parabolic trough plants, is equal to 23.53% is in accordance to existing plants performance. The IND-FRE solution achieves a lower overall efficiency mainly because of the lower optical efficiency (63.5%) than the PT (71.2%). This high difference is due to the different concentration system of PT and LFR; in particular even with sun at zenith position, the primary mirrors have to be inclined thus reducing the available mirror area. Considering the modified optical efficiency, this difference nearly disappears.

The value of solar field auxiliaries consumption reflects the advantage of LFR concerning the absence of ball-joints, that increase the HTF pressure drop, and the higher concentration ratio that leads to shorter rows.

Even if the IND-PAR and IND-FRE has the same HTF temperature-operating range, the thermal efficiency is quite different because of LFR absorber has no vacuum thus implying higher thermal losses.

The DSG solution suffers from the poor steam cycle performance that derives from the choice of a saturated cycle. The constant and lower temperature of water in the absorber tube implies a higher thermal efficiency compared to the HTF cases.

Although LFR has a lower overall efficiency, the required land area is considerably lower because of the lack of a minimum distance between modules as occurs in PT solar field to avoid reciprocal shading. A minimum clearance between parallel LFR rows is necessary to allow the maintenance of the system.

Table 2.9 Performance at on-design conditions for technologies investigated

<i>Sizing Results</i>			
<i>Parameter</i>	<i>IND-PAR</i>	<i>IND-FRE</i>	<i>IND-DSG</i>
Gross power [MW]	54.87	53.45	52.52
Steam cycle aux cons. [MW]	1.72	1.68	1.40
Cooling tower aux cons. [MW]	0.65	0.63	0.85
Number of operating flow paths	72	75	43
Pump head [bar]	23.34	10.86	11.01
Solar field aux cons. [MW]	2.51	1.14	0.19
Net power output [MW]	50.0	50.0	50.0
Total SCA aperture area [m ²]	235,899	268,596	289,101
Total required land area [m ²]	683,902	594,465	593,205
η_{optical}^8 [%]	71.24	63.65	63.64
$\eta_{\text{optical_modified}}$ [%]	64.35	63.65	63.64
η_{thermal} [%]	95.22	91.99	95.43
η_{piping} [%]	99.17	98.44	99.78
$\eta_{\text{net_PB}}$ [%]	36.74	36.71	31.88
$\eta_{\text{aux_SF}}$ [%]	95.23	97.78	99.62
η_{overall} [%]	23.53	20.69	19.25
$\eta_{\text{overall_modified}}$ [%]	21.25	20.69	19.25

2.3.2.2 Optical efficiency definition of LFR

Before describing the part-load simulation of the investigated plants, an additional discussion about LFR optical efficiency is presented.

As it is possible to expect from the different shape of the concentrator, the optical behavior of PT and LFR will show some differences that strongly influence the yearly yield of these two technologies.

In the previous section, the importance of predicting the performance during part-load condition of PT plants is underlined; in particular the presence of the incidence angle implies a penalty in the optical efficiency and for that reason, the forecast of the optical differences between the LFR and PT technologies plays a fundamental role to understand the comparison results. The first evidence about the different behavior of LFR and PT technology can be extrapolated from the comparison between Figure 2.4 and Figure 2.10

⁸ Optical efficiency is calculated starting from nominal data, then adding a cleanliness factor of 0.95 for both LFR and PT. This coefficient can be higher for LFR because it is easier to clear.

that show the incidence angle definition for PT and LFR respectively. In particular, LFR have a more complicated situation, due to the different concentration method, and for that reason, two sunray projections are necessary to define exhaustively the incidence angle [36]. In order to simplify the description of the problem, the selected planes are chosen to be orthogonal and coincident with the longitudinal and the transversal plane. The relation between sun's position (zenith and azimuth angle) and the incidence angles are reported in Table 2.10; the relations in the table below provide the three projections of sunrays as function of sun position most commonly found in literature. The geometrical proof is offered in a specific section of the Appendix.

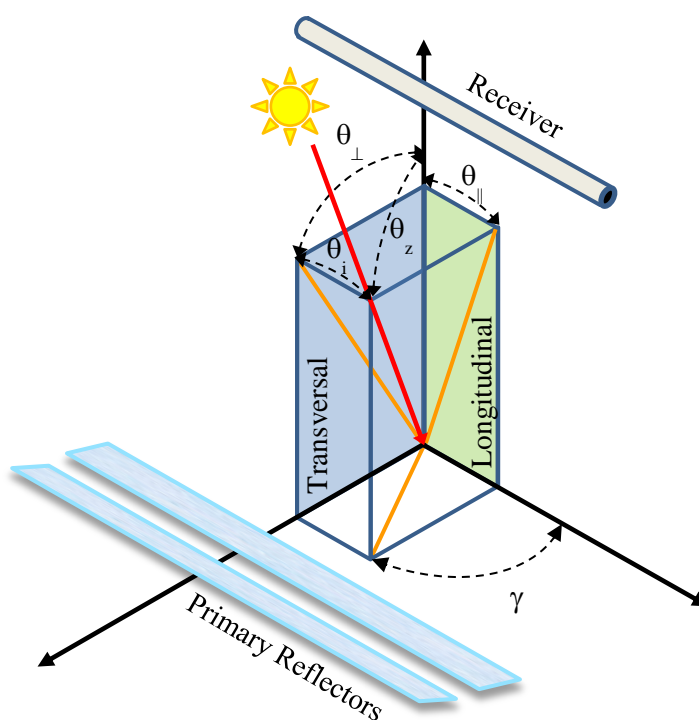


Figure 2.10 Characteristic angles for horizontal LFR with N-S orientation (adapted from [37]).

Table 2.10 LFR characteristic angles (tracking axis orientated in N-S direction).

<i>Characteristic LFR angles</i>		
<i>Description</i>	<i>Relation with sun angles</i>	
Angle between the vertical axis and the sunray vector projection on the longitudinal plane	$\theta_{\parallel} = \text{atan}(\cos(\gamma)\tan(\theta_z))$	(2.14)
Angle between sunray vector and its projection on the transversal plane	$\theta_{\perp} = \text{asin}(\cos(\gamma)\sin(\theta_z))$	(2.15)
Angle between the vertical axis and the sunray vector projection on the transversal plane	$\theta_z = \text{atan}(\sin(\gamma) \tan(\theta_z))$	(2.16)

From the comparison between equations (2.7) and (2.15), it is possible to notice that the relation to compute θ_i is the same as in case of PT.

Concerning Linear Fresnel concentrator, correction of optical efficiency is more complex, due to different characteristic angles as aforementioned.

In agreement with the $K(\theta)$ factor used in PT, Linear Fresnel IAM (“Incidence Angle Modifier”) considers cosine effect, primary mirrors mutual blocking and shading, secondary reflector and support shading, optical properties variation and intercept factor modification.

Due to the presence of two incidence angles, the IAM has to be expressed as a function of two angles (graphically represented as a surface). In order to simplify the use of IAM, the common approach is to express the incidence angle effect on LFR optical performance as a product of two separated IAM for two different projection planes as commonly adopted in the study of CPC concentrators [38]. This process of factorization adds an approximation to the original surface as found by [36,37] and in both these studies the factorization pair made of θ_i and θ_{\perp} is detected to be the most accurate:

$$IAM(\gamma, \theta_z) = IAM(\theta_i; \theta_{\perp}) \cong IAM(\theta_i)IAM(\theta_{\perp}) \quad (2.17)$$

In particular, in [36] is stated that, although a big error is obtained for big incidence angle, the chosen factorization implies a yearly efficiency (weighted on solar energy) error lower than 1%. Figure 2.11 shows the effect of incidence angles on the two IAM functions of the Novatec solar system [33] present in Thermoflex[®]'s database [2]; in particular the characteristic oscillating shape of $IAM(\theta_{\perp})$ till approximately 45° is due to the movement of the secondary reflector shade that reduces the effective mirror aperture area.

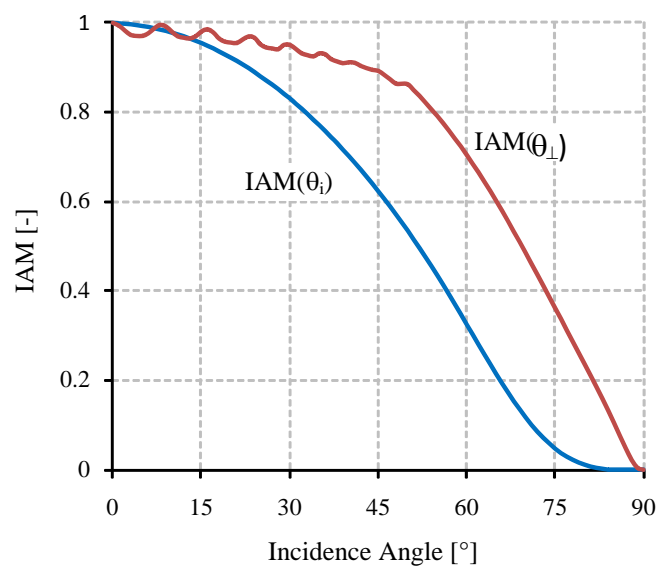


Figure 2.11 IAM factorization in longitudinal (θ_i) and perpendicular direction (θ_{\perp}) of Novatec’s technology in Thermoflex[®] database.

The end-losses effect is not taken in to account in the LFR IAM and thus it has to be considered with the following relation (equal to the PT one):

$$\eta_{end-losses} = 1 - \tan(\theta_i) \frac{D_{pm}}{L_{abs}} \quad (2.18)$$

Where D_{pm} is the mean distance among primary mirrors and the absorber and L_{abs} is the length of the absorber tube.

The optical efficiency for linear Fresnel reflector is expressed as:

$$\eta_{optical_LFR} = \eta_{optical_LFR}|_{0^\circ} IAM(\theta_i) IAM(\theta_\perp) \eta_{end_loss} \quad (2.19)$$

Where $\eta_{optical_LFR}|_{0^\circ}$ is the nominal optical efficiency and $IAM(\theta_\perp)$ and $IAM(\theta_i)$ are the two Incidence Angle Modifiers, that take into account the reduction of nominal optical efficiency with the two corresponding incidence angles typical of a Fresnel Collector. The end losses of the collector are taken into account through η_{end_loss} that is equal to one in case of sun at the zenith.

2.3.2.3 Energetic Yearly performance

This section presents the yearly performance results of the investigated cases assessing a comparison both from an energetic and economic point of view.

Exploiting the capabilities of Thermoflex[®], a detailed part-load modelling is conducted in order to compare the technologies in terms of yearly performance.

Concerning the solar field optical behavior, the data needed to calculate the optical efficiency are set as input in TFX[®].

As far as solar field thermal behavior is concerned, a specific thermal model available in TFX[®] (based on [39]) and different tracking system consumptions are considered for PT and LFR technology (0.5 W/m² and 0.16 W/m² respectively).

As regards the power block modelling, TFX[®] handles all the components part-load description.

In particular: steam turbine isentropic efficiency variation and realistic pressure conditions at regenerative bleedings at off-design conditions are taken into account, as well as boiler and feedwater preheater performances [2]. Input defined by the user is the steam turbine control modality at part load. TFX[®] allows grouping all the different sections of steam turbine in the so-called ‘‘Steam Turbine Assembly’’, guarantying better accuracy in the prediction of off-design performances.

In order to prevent steam turbine damages during high radiation hours, gross power output increase with respect to nominal power output is limited to a maximum value of 8%, eventually defocusing a portion of the solar field. Turbine shut down is assumed below 15% of design conditions as indicated by [29].

Turbine start up is also taken into account: 30 minutes ramp is considered when power block has been shut down for less than 24 hours (hot start up), while 1 hour ramp is

assumed for longer shut down periods (cold start up). Condenser off-design operation is considered varying condensing pressure as a function of ambient temperature and heat rejected. A minimum value of 0.04 bar which is half of design conditions, is assumed, by varying the number of condenser active cells. Pumps are assumed electric driven with electronic control which guarantees high efficiency also in off-design conditions; night oil circulation pump consumption for the two HTF plants is considered too.

The plant is located at Las Vegas and the weather data are taken from [25].

First, to understand better the energetic comparison among the different cases, it is important to show the results of comparison in the optical annual performance of PT and LFR. In Figure 2.12 the annual Optical Ratios (“OR”) of PT (top) and LFR (bottom), defined as the ratio between off-design optical efficiency and zero incidence angle optical efficiency, are shown.

Regarding the trend of this function, IAM (θ_i) of PT presents a maximum during the day at 10 and 16hr, while the presence of IAM (θ_{\perp}) in LFR leads to a smoother shape, with lower efficiency, in particular for high incidence angles. In general, the PT’s optical performance are characterized by a higher value during the year representing one of the most important advantage over the LFR technology [10].

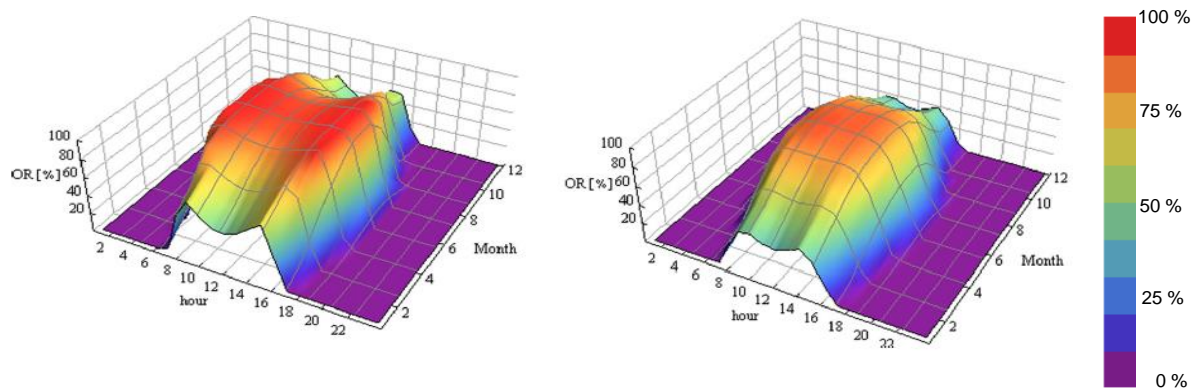


Figure 2.12 Example of annual OR map for PT (left) and LFR (right) for plants located in Las Vegas.

Table 2.11 resumes the annual energetic results obtained with the procedure previously described.

The available solar energy represents the maximum theoretical solar energy value that can be exploited by the CSP plant. This value is the DNI multiplied by the primary mirrors area and thus, it is linked to the sizing of the plant and thus the technologies with the lower overall efficiency are characterized by the larger reflective area because of the net power output is the same.

Receiver solar energy is the energy that is concentrated on the absorber and thus it takes into account the optical efficiency of the concentrator. The higher gap among the receiver solar energy suggests that the optical efficiency gap between PT and LFR increases in part-load condition.

The last row of the table shows the values of the overall efficiency that indicates the PT solution as the best energetic performance solution.

Table 2.11 Annual results for the investigated cases

	IND-PAR	IND-FRE	DSG
Available solar energy [MWh/y]	609464	696185	749336
Receiver solar energy [MWh/y]	321473	265271	290412
Net electric energy [MWh/y]	97818	75189	76226
η_{optical} (%)	52.75	38.10	38.76
η_{thermal} (%)	92.73	85.84	92.08
η_{piping} (%)	98.64	98.25	99.75
$\eta_{\text{net_PB}}$ (%)	34.45	34.19	28.73
$\eta_{\text{aux_SF}}$ (%)	96.57	98.29	99.47
η_{overall} (%)	16.05	10.80	10.17

The monthly electricity production is shown in Figure 2.13. The PT energy output is the highest one in every month of the year. Comparing the two LFR solutions, DSG has a higher output during the winter months, due to its higher thermal efficiency that has a stronger effect in low DNI conditions (during summer this effect is negligible).

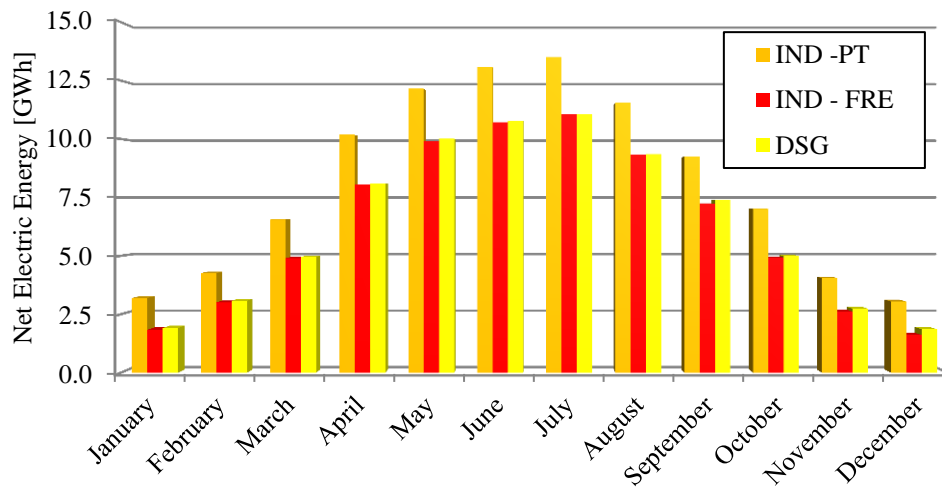


Figure 2.13 Monthly net electricity production for the three investigated technologies

2.3.2.4 Preliminary Economic Assessment

As previously said, the main advantage of LFR technology lies in the lower investment cost mainly derived by the cheaper primary mirror, lighter structure and absence rotating joint and/or flexible connecting pipes [36]. In order to quantify how this advantage could overcome the lower energetic performance, a simplified economic analysis is performed to estimate the maximum cost of LFR that matches the PT costs. Following the procedure to compute the Cost of Energy “COE” taken from IEA [40], the COE is calculated by setting the net present value (NPV) of the power plant to zero. This can be achieved by

varying the kWh price until the revenues balance the cost over the whole lifetime of the power plant with a 25 yr lifetime of the plant and 8% of discount rate.

The main results of the economic analysis is presented in Table 2.12; in order to enlighten the effect of the assumptions values on the conclusion the assumptions taken from a similar study [41] are considered.

Table 2.12 Economic assessment for the three investigated cases

		IND-PAR		IND-FRE		DSG	
Nominal Net Power	MW	50		50		50	
Total mirror surface	m ²	235899		268596		289101	
Total Land surface	m ²	683902		594465		593205	
Equivalent hours	kWh/kW _{nom}	1956		1504		1522	
Assumptions	-	Politecnico	Morin[33,41]	Politecnico	Morin	Politecnico	Morin
Land specific cost	€/m ²	0	7	0	7	0	7
Power block specific cost	€/kW	667.5	882.64	667.5	882.64	605	800
Indirect cost and contingencies	%plant cost	31	20	31	20	31	20
O&M	M€	2.5	3.6	2.1	3.1	2.1	3.1
Solar Field	€/m ²	220	275	17.3	137.1	125.73	150.1
Reduction	%	-	-	46.68	50.15	42.85	45.42
COE	€/kWh	156.3	176.1	156.3	176.1	156.3	176.1

In order to have the same COE of PT technology, the LFR equivalent cost should be about 45%-50% lower than PT. The main reasons, responsible of a so strong cost reduction, might be the lighter structures, easier tracking system, cheaper mirrors and higher concentration ratio reducing absorber specific costs.

In addition to this general consideration, it is worth to notice that the DSG case shows a small advantage. This means that the lower power block cost, mainly due to the absence of heat exchangers and lower temperature level, counterbalances the lower yearly energetic yield.

Finally, even if the assumptions and the methodologies are different from other works, the obtained results are very similar giving confidence in achieved results.

2.3.2.5 Conclusions of the second work

This work discussed the application of two different commercial solar linear collectors in concentrated solar power plants. The first technology, which can be considered the state of the art, is parabolic trough, while the second one, Fresnel technology, can be considered as a promising way to reduce electricity cost. In order to make a detailed comparison, both an indirect and direct cycle are considered for Fresnel technology. Plant design conditions are defined assuming a net power output of 50 MWe. Calculations are carried out with a commercial code named Thermoflex[®], able to describe power plants either at rated and off-design conditions.

Results at nominal conditions evidenced a slightly superiority of parabolic trough over Fresnel with indirect cycle, mainly because of the higher optical efficiency with the conventional definition. Adopting a modified index which is more consistent, this

difference almost disappears. Fresnel with DSG showed a significantly lower efficiency of about 6% points, because of the saturated steam cycle adopted.

Parabolic trough predominance is even larger comparing net electricity production over one year: calculated overall efficiency is 16% (15%, if referred to reflective area) compared to 10% of Fresnel plants.

Fresnel suffers of a significant optical efficiency decay that is about 40% on an average basis. In particular, optical efficiency decreases for high incidence angles even if no shadowing issues between modules are present like in Parabolic Trough plants. This decay is significant also because of the concentration ratio assumed for LFR which is twice than PT.

However, Fresnel is seen as a promising technology because of investment cost savings (e.g. lighter structure is required, fewer civil works, easier glass cleaning), thus only a detailed economic analysis will determine if cost reduction related to the considered Fresnel technology compensates the lower performances. Moreover, different Fresnel collectors technologies, with other receiver shapes, could lead to optical and thermal performance improvement. These activities are on-going and will be discussed in future works.

A simplified economic assessment shows that Fresnel should halve specific investment cost of parabolic trough in order to be competitive. This target seems reasonable since Fresnel has lighter structure, could lead to improve optical and thermal performance.

2.4 Bibliography

- [1] Geyer M, Mancini T. From Research to CSP Market Introduction Progress and Advances of Concentrating Solar Power Technologies 2006:16-19.
- [2] Thermoflow Inc. Thermoflex v.23 User Guide 2013.
- [3] STEAG Energy Services GmbH - System Technologies. EBSILON(R) Professional for engineering and designing energy and power plant systems 2013.
- [4] National Renewable Energy Laboratory ("NREL"). System Advisor Model (SAM) website.
- [5] Sandia National Laboratories. CSP Software & Tools: Solergy 2013.
- [6] Hirsch T, Bachelier C, Dersch J, Eck M, Feldhoff JF, García-Barberena Labiano J, et al. Guidelines for CSP Yield Analysis: Definition of Elementary Terms 2013.
- [7] SolarPACES. Guidelines CSP Performance Modeling "guiSmo" 2013;2013.
- [8] Manzolini G, Giotri A, Saccilotto C, Silva P, MacChi E. A numerical model for off-design performance prediction of parabolic trough based solar power plants. J Sol Energy Eng Trans ASME 2012;134.
- [9] Manzolini G, Giotri A, Saccilotto C, Silva P, Macchi E. Development of an innovative code for the design of thermodynamic solar power plants part A: Code description and test case. Renew Energy 2011;36:1993-2003.
- [10] Giotri A, Binotti M, Silva P, MacChi E, Manzolini G. Comparison of two linear collectors in solar thermal plants: Parabolic trough versus Fresnel. J Sol Energy Eng Trans ASME 2013;135.

- [11] Giotri A, Binotti M, Astolfi M, Silva P, Macchi E, Manzolini G. Comparison of different solar plants based on parabolic trough technology. *Sol Energy* 2012;86:1208-1221.
- [12] Manzolini G, Giotri A, Saccilotto C, Silva P, Macchi E. Development of an innovative code for the design of thermodynamic solar power plants part B: Performance assessment of commercial and innovative technologies. *Renew Energy* 2011;36:2465-2473.
- [13] Giotri A, Saccilotto C, Silva P, Macchi E, Manzolini G. A numerical model for off-design performance calculation of parabolic trough based solar power plants. *ASME Int Conf Energy Sustainability, ES 2010*;2:617-626.
- [14] ENEA. Progetto "Archimede": Realizzazione di un impianto integrativo presso la centrale ENEL di Priolo Gargallo(SR) 2007.
- [15] Fernández-García A, Zarza E, Valenzuela L, Pérez M. Parabolic-trough solar collectors and their applications. *Renewable and Sustainable Energy Reviews* 2010;14:1695-1721.
- [16] Geyer M, Lüpfert E, Osuna R, Esteban A, Schiel W, Schweitzer A, et al. EUROROUGH-Parabolic trough collector developed for cost efficient solar power generation 2002:04-06.
- [17] FLABEG. FLABEG: Solar product information - Parabolic Mirrors for Concentrating Solar Power 2011.
- [18] Archimede Solar Energy. Archimede Power Plant -ENEL-Priolo Gargallo 2013;2013.
- [19] Eck M, Schmidt H, Eickhoff M, Hirsch T. Field test of water-steam separators for direct steam generation in parabolic troughs. *J Sol Energy Eng Trans ASME* 2008;130:0110021-0110026.
- [20] Zarza E, Rojas ME, González L, Caballero JM, Rueda F. INDITEP: The first pre-commercial DSG solar power plant. *Sol Energy* 2006;80:1270-1276.
- [21] GECOS. Politecnico di Milano: Group of Energy Conversion Systems 2013.
- [22] Forristall RE. Heat Transfer Analysis and Modeling of a Parabolic Trough Solar Receiver Implemented in Engineering Equation Solver National Renewable Energy Laboratory; 2003.
- [23] Taitel Y, Minzer U, Barnea D. A control procedure for the elimination of mal flow rate distribution in evaporating flow in parallel pipes. *Solar Energy* 2008;82:329-335.
- [24] Birnbaum J, Feldhoff JF, Fichtner M, Hirsch T, Jocker M, Pitz-Paal R, et al. Steam temperature stability in a direct steam generation solar power plant. *Solar Energy* 2011;85:660-668.
- [25] National Renewable Energy Laboratory. National Solar Radiation Data Base: 1991-2005 Update: Typical Meteorological Year 3 2008;2013.
- [26] Montes Pita MJ. Análisis y propuestas de sistemas solares de alta exergía que emplean agua como fluido calorífero 2008.
- [27] Stuetzle T, Blair N, Mitchell JW, Beckman WA. Automatic control of a 30 MWe SEGS VI parabolic trough plant. *Sol Energy* 2004;76:187-193.

- [28] Vasquez Padilla R. Simplified Methodology for Designing Parabolic Trough Solar Power Plants 2011.
- [29] Bellintani E. Project Engineer Franco Tosi Meccanica, personal communication 2009.
- [30] Macchi E, Perdichizzi A. Theoretical Prediction of the Off-design Performance of Axial-flow Single Stage Turbines 1977;2:1867-1896.
- [31] Bergman TL, Incropera FP, Lavine AS, DeWitt DP. Fundamentals of Heat and Mass Transfer Wiley; 2011.
- [32] Patnode AM. Simulation and performance evaluation of parabolic trough solar power plants 2006.
- [33] NovatecSolar. NOVATEC SOLAR's Website 2012;2012.
- [34] Hirsch T, Feldhoff JF, Hennecke K, Pitz-Paal R. Advancements in the field of direct steam generation in linear solar concentrators-a review. Heat Transfer Eng 2014;35:258-271.
- [35] National Renewable Energy Laboratory. Concentrating Solar Power Projects 2013;2013.
- [36] Binotti M. Linear Fresnel reflectors : study of the technology and steps toward optimization 2013.
- [37] Mertins M. Technische und wirtschaftliche Analyse von horizontalen Fresnel-Kollektoren 2009.
- [38] McIntire WR. Factored approximations for biaxial incident angle modifiers. Sol Energy 1982;29:315-322.
- [39] Stine WB, Harrigan RW. Solar Energy Systems Design John Wiley and Sons Inc.; 1985.
- [40] International Energy Agency. International Energy Agency ("IEA") website;2010.
- [41] Morin G, Dersch J, Platzer W, Eck M, Häberle A. Comparison of Linear Fresnel and Parabolic Trough Collector power plants. Solar Energy 2012;86:1-12.

3 Piping Model

The approximated piping modelling, which is the most common choice in quasi-steady approach as described in the previous chapter, is not sufficient to provide information that can be used for a detailed transient analysis that needs an accurate sizing of the hydraulic network. The sizing of the distribution piping represents the first step needed to perform the transient analysis of the solar field. In particular, the physical dimensions of the piping define the thermal inertia of the system that plays a fundamental role in the transient behavior of the solar field.

In this chapter, a specific methodology to size the solar field piping with single phase circulating fluid is analyzed. In particular, the driving idea is the search of an optimum configuration that minimizes the total cost of the network system.

First, a general description of the piping is provided and successively, a description of the relations used to dimension the hydraulic network and the implementation of the sizing procedure in a specific algorithm is presented. Particular attention is posed to the requested inputs and to the main assumptions that are needed by the implemented model.

At the end of the chapter, in order to show the potentiality of the developed model, a representative solar field is considered and the results of the test case, both technical and economical, are presented and discussed.

3.1 Piping system

The goal of the piping system is to distribute the HTF in the different parts of the solar field. In particular, the cold fluid, leaving the power block, is pumped to the solar field and distributed to all the loops with a pipe system identified by the name “cold header”. The HTF is heated up in the solar collector loops and harvested in the “hot header” that sent it to the power block. The fluid circulation is handled by a pump that provides the energy to win the pressure drops in the hydraulic network. In order to face the thermal expansion of the circulating fluid, the use of an expansion tanks system is mandatory.

As regards the pipe network scheme, the most common layout adopted in big scale electricity production CSP plant is the so-called “central feed”. This solution is characterized by a central position of the cold and the hot header. Andasol [1] and SEGS [2] piping systems can be considered as examples of this configuration. Another difference in the layout is between the “H” and “I” configurations that differ in the number of subsections the solar field is divided in.

A schematic of the solar field “central feed” configuration is shown in Figure 3.1 underlining the difference between the “H” and “I” layout solutions. Additionally, the nomenclature of the most important components of the solar field, which is used in the following sections of this chapter, is presented.

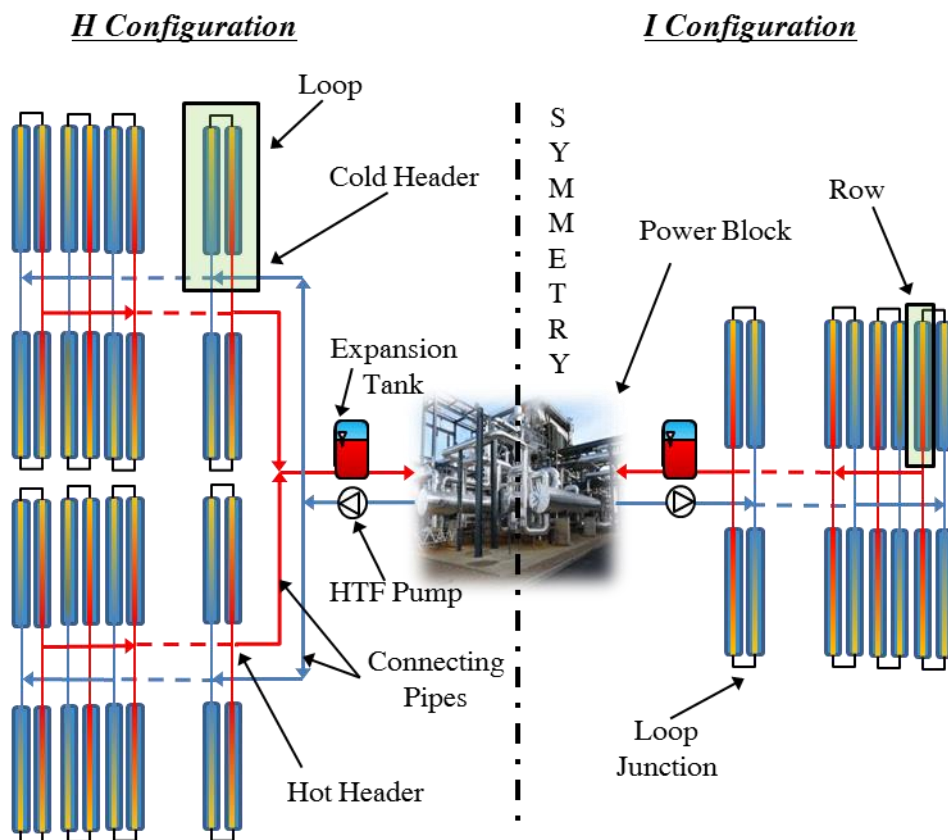


Figure 3.1 Schematic of “central feed” solar field layout (the symmetry axes defines the “H” and “I” configuration).

Regarding alternative piping system layouts, as underlined in [3], two additional categories, named “direct return configuration” and “reverse-return configuration” can be identified. Both of these solutions have the cold header and hot header placed in the opposite sides of the collector row. It is important to underline that the main advantage of the “reverse return” is represented by a more balanced loop working conditions even if the presence of longer connecting pipes and the limited accessibility to the loop make this solution not attractive and not used in any CSP plant. The “direct return” configuration is used, as reported by [4], in the PE2 [5] plant based on the Linear Fresnel Reflector (“LFR”) because of the bigger row length that mitigates the effect of the higher value of absorber height in comparison to the parabolic trough (“PT”).

In the following sections of this chapter, the model implemented to size the piping system is presented, showing in detail the main steps considered to model the piping network.

3.2 Solar Field preliminary sizing

Before starting with the detailed dimensioning of the piping network, a preliminary sizing of the solar field is necessary in order to obtain the main characteristics requested by the pipe network sizing procedure.

The preliminary inputs requested for solar field sizing can be summarized in:

- *Heat Transfer Fluid*: the HTF thermophysical properties are needed in order to compute the thermal/hydraulic performance of the solar field. In Appendix the properties of the most used HTF are reported.
- *Temperature level of the SF*: depending on the HTF chosen in the previous step, the temperature of cold and hot part of the piping have to be fixed. For example, the use of high temperatures synthetic oils leads to temperatures ca. 290°C and ca. 390°C for cold and hot level respectively (in case of use as heat source of a big scale Rankine cycle). The temperature influences the fluid properties and the main characteristics of the pipe segments.
- *Technology of solar concentrator*: both PT and LFR can be considered. The main properties that have to be set are, the aperture width, the optical efficiency of the concentration system and the thermal loss behavior of the absorber tube. These two efficiencies can be put together in an optical-thermal efficiency (η_{opt_th}) that takes in to account the energetic loss starting from the DNI to the useful thermal energy transferred to the HTF.
- *Length of each loop (L_{loop})*: due to the discrete available length of SCA, an integer number of SCA is present in a loop.
- *Total aperture Area (W_{total})*: this value is approximated because of the discrete SCA aperture area. It is calculated as the product of the parabolic mirror aperture (W) and the loop length.

Once a sizing DNI and a Solar multiple (SM), representative of the on-design condition, are chosen, it is possible to compute the number of loop and the mass flow circulating in each loop, which represents the starting point for the dimensioning of the hydraulic network, with the following relations:

$$n_{loop} = \frac{W_{total}}{L_{loop}W} \quad (3.1)$$

$$m_{loop_HTF} = \frac{DNI\eta_{opt_th}WL_{loop}SM}{h_{hot} - h_{cold}} \quad (3.2)$$

Where h_{hot} and h_{cold} are the enthalpies of the hot temperature level and the cold temperature respectively.

3.3 Optimization Model

Once the main characteristics of the solar field are set and computed, it is possible to develop a specific tool for the sizing of the piping system; the chosen programming language is Matlab[®] that allows a fast coding and makes available a huge database of mathematical functions that reduces the coding time.

The main scope of this suite is to find the physical dimensions of the pipe system, in terms of mass of steel and HTF, that is used in the transient model presented in the next chapter.

The core of the sizing method is represented by an optimization procedure in order to find the optimal configuration of the pipe system, in terms of tube dimensions, that minimizes the total cost expressed as the sum of investment cost and operational cost. The objective function that is handled by the optimization algorithm can be expressed by:

$$\min(C_{total}) = \min(C_{investment} + C_{operational}) \quad (3.3)$$

Figure 3.2, showing the qualitative behavior of the goal function and its main components, justifies the need of an optimization approach because of the existing trade-off between the investment cost (proportional to the size of piping components) and the operational cost pump electric consumption that shows an increase with the increase of mean velocity (decrease of pipe internal diameter) due to the augmentation of pressure drop. In order to simplify the visualization of the trend the total cost is plotted vs the mean fluid velocity in the pipes that contains information related to the dimension of pipe.

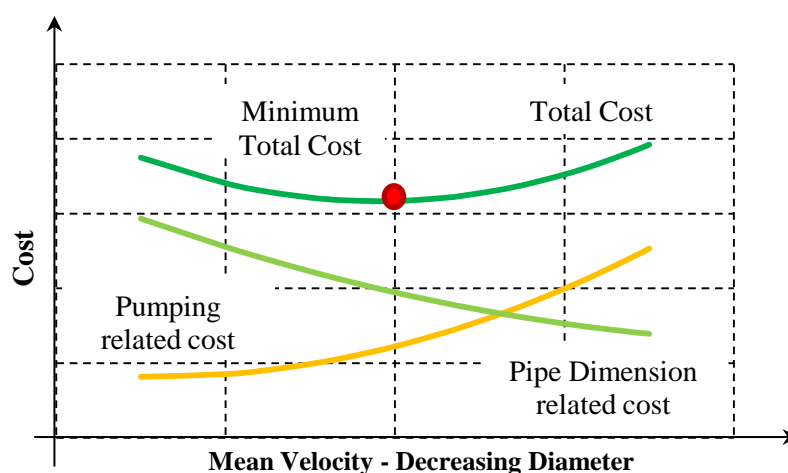


Figure 3.2 Qualitative trend of the total cost share of piping system

The thermal losses have to be taken into account and for that reason, in addition to the inner diameter; the insulation thickness of each pipe segments has to be added to the problem as unknowns. As regards the pipe segments dimension, it is important to underline that a limited number of pipe diameters are commercially available; for that reason the problem is solved treating the unknowns as continuous variables and approximating the solution with the “closest” commercial available configuration.

A separate analysis of the goal function can be useful to identify the main elements that have to be considered.

The total investment cost is the sum of the cost of all components considered in the piping and the labor cost necessary for the construction. The main components considered for the cost estimation in this model are listed below:

- *Pipe material* cost considers the mass of steel and insulation needed for the construction of the tubes
- All the *fittings* needed to adjust the HTF flow belong to this category (i.e. valves, elbows, contractions, expansions, rotating-joints). The supports of each pipe segment belong to this category too.
- *HTF pump* that provides power to the fluid to circulate in the hydraulic circuit.
- *Mass of HTF* contained in the solar field network (headers, loops, expansion tank)
- *Labor* to erect the system (i.e. mounting, welding etc.)

The mathematical relation to compute the investment cost summarized in the list above can be written as follows:

$$C_{investment} = \sum_{i=1}^{N \text{ of materials}} (c_{MAT_i} \times m_{MAT_i}) + C_{fittings} + C_{labour} + C_{HTF} \quad (3.4)$$

As regards the operational cost, the electricity consumption of the HTF pump and the thermal losses toward the ambient have to be taken in to account as expressed in the next equation:

$$C_{operational} = C_{pumping} + C_{thermal_loss} \quad (3.5)$$

The requested inputs and the various assumptions, needed to define completely the optimization problem, are discussed in detail in the next section. In addition, the main relations used by the optimization model are presented next.

3.3.1 Rough Estimation of LCoE and LCoTE

Before running the optimization suite, it is necessary to have a rough estimation of both the levelized cost of the electricity (“LCoE”) and the levelised cost of thermal energy (“LCoTE”) that are required to calculate the operational cost of the piping system. These two parameters are used to express the electric energy consumption/thermal losses as an equivalent capital cost with a process analogous to that reported in [6].

It is important to underline that the LCoE and the LCoTE calculated represent a first approximation that is adopted only to evaluate the impact of operational costs.

The relations below allow calculating the LCoTE and LCoE:

$$LCoTE = \frac{c''_{SF} \times FCR}{\eta_{optical} \eta_{thermal} DNI_{yearly}} \quad (3.6)$$

$$LCoE = \frac{\left[c''_{SF} + \left(\frac{C_{PB}}{A_{tot}} \right) f \right] FCR + O\&M}{\eta_{optical} \eta_{thermal} \eta_{PB} DNI_{yearly}} \quad (3.7)$$

As presented in the previous equations, the values of these techno-economic parameters are influenced by the energetic performance of the investigated CSP plant; thus an approximate evaluation of the annual energy fluxes (both thermal and electrical) is requested and it is described in the following parts of this section.

Once the localization of the plant is decided, the yearly DNI profile is known (DNI_{yearly}) and considering the geographical coordinates, in addition to the concentrator technology, the yearly optical efficiency ($\eta_{optical}$) can be calculated. Consequently, the yearly effective DNI (EDNI) impinging the solar field can be computed with the same procedure described in the Chapter 2.

With the aim of decreasing the computational effort of the optimization procedure a set of efficiencies for the whole CSP plant (solar field + power block η_{PB}) can be taken from previous studies about parabolic trough CSP plant as the one presented in the Chapter 2. It is important to underline the dependency of the adopted efficiencies on the user input; in particular, the optical efficiency depends on the location of the plant and the collector technology. As regards the thermal efficiency $\eta_{thermal}$, a thermal model presented in [7] (derived from the published research of Forristall [8]) is used in order to have the characteristic thermal performance of an absorber tube.

Regarding the main requested economic assumptions, it is worth to remind the FCR (“Fixed Charge Rate”)⁹ [10] and the specific costs of both the solar field c''_{SF} [€/m²] and the power block C_{PB} [€/kW]). In addition to these informations, in order to take in to account the yearly cost of operating and maintenance of the CSP plant, an O&M cost is considered.

The main assumptions essential to calculate the energetic performance of the plant are resumed in Table 3.1 showing typical range of the values.

Table 3.1 Assumptions for the calculation of LCoE and LCoTE (the presented ranges are indicative).

<i>Assumptions for LCoE and LCoTE</i>		
Name Variable	Range	UoM
Location	Sun Belt	-
Hourly DNI series	e.g. TMY3	-
Solar Field Technology	PT/LFR	-
$\eta_{optical_SF}$	60-85	%
$\eta_{thermal_SF}$	85-95	%
η_{Net_PB}	25-40	%
FCR	0.09-0.15	-
Specific Cost Solar Field	120-250	€ m ⁻²
Specific Cost of PB	700-1200	€ kW ⁻¹

⁹ FCR is the percentage of capital cost that must be repaid during each year of operation [9].

As can be deduced from the wide range of energetic parameter, the developed model can handle CSP solutions that use both different concentrator technologies (LFR or PT) and different power block solution (i.e. commercial steam Rankine cycle with different temperature levels, Organic Rankine Cycle etc.) giving to the written tool a wide applicability range that can span all the linear CSP plants with HTF.

3.3.2 Piping equations

In this section the sizing of the piping system is presented, in particular the equations to size each segment and to calculate the pressure drop are explained. In a dedicated subsection, the cost estimate assumptions are described.

As regards the input to complete the definition of the optimization procedure, the user has to fix some input parameters, listed below, that define the main characteristics of the solar field network:

- *Field configuration* which defines the number of subsections. The most common values are 2 (“I” configuration) or 4 (“H” configuration) depending on both the available land area and the total aperture area.
- *Spacing between collector rows* with the aim of diminishing the effect of reciprocal shading. In CSP plant the value of the spacing between adjacent mirrors is in the range of 2 – 3 times the aperture area.
- *Fittings type* is determined by the user (i.e. type of valves, ball-joint) or, in some cases, it is implicitly fixed by the configuration of the pipe network (i.e. number of elbows).
- *Minimum pressure (@solar field outlet)* which limits the lowest value of pressure in SF, with a security margin, to avoid phase transition of HTF.
- *Physical Properties of pipe steel and insulation material.*

Once the total mass flow, the mass flow in the loop and the number of sections are known from section 3.2, the first step is the calculation of the mass flow rate in each pipe segments of the header.

For a generic cold (hot) header pipe segment the corresponding mass flow is:

$$\dot{m}_{C+1} = \dot{m}_C - 2\dot{m}_{row} \quad (3.8)$$

$$\dot{m}_{H+1} = \dot{m}_H + 2\dot{m}_{row} \quad (3.9)$$

The mass flow in the pipe segments between headers and absorber tubes would be for all the rows equal to \dot{m}_{row} , while the mass flow in the connecting pipe would be equal to the mass flow delivered in each section of the solar field $\dot{m}_{HTF_sections} = \frac{\dot{m}_{HTF_TOT}}{N_{sections}}$.

In Figure 3.3 qualitative diameter profile of a representative hot header in a central feed configuration is presented.

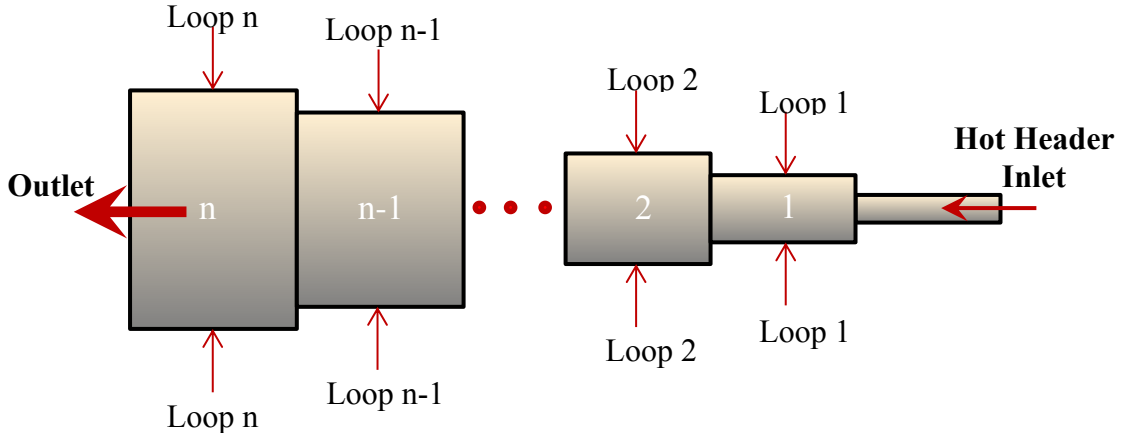


Figure 3.3 Example of hot header diameter profile in a central feed configuration.

Pressure drops are directly responsible of the electric energy consumption in the solar field. All the pipes are considered to be placed at ground level, neglecting the effect of the change in the elevation.

The total pressure drop is expressed by the sum of distributed and localized pressure drop. The next relations have to be considered for each pipe segment of the hydraulic network:

$$[\Delta p] = [\Delta p_{dist}] + [\Delta p_{conc}] \quad (3.10)$$

Regarding the distributed head loss, the Darcy Weisbach equation is used [11]:

$$[\Delta p_{dist}] = [f] \frac{[L]}{[D_{IN}]} \left(\frac{4[\dot{m}_{HTF}]}{\pi[D_{IN}]^2} \right)^2 \frac{1}{2[\rho_{HTF}]} \quad (3.11)$$

The inner friction factor is computed with Churchill's correlation[12] reported below:

$$[f] = 8 \left(\left(\frac{8}{[Re]} \right)^{12} + ([A] + [B])^{-3/2} \right)^{1/12} \quad (3.12)$$

$$[A] = \left[2.457 \log \left(\frac{1}{\left(\frac{7}{[Re]} \right)^{0.9} + 0.27 \frac{\varepsilon}{[D_{IN}]}} \right) \right]^{16}; \quad [B] = \left(\frac{37530}{Re} \right)^{16} \quad (3.13)- (3.14)$$

Where Re is the Reynolds number and ε is the absolute roughness of the pipe (a common value in CSP modellization is 0.0457mm).

The length of each pipe segments is related to the row spacing that is set by the user. In addition, the presence of “U-shape” (see Figure 3.4-left-) additional lengths is necessary to compensate thermal expansion during working condition and thus they have to be taken into account. The length of these “compensation U bends” depends on the operative temperature and the pipe diameter as reported in [13].



Figure 3.4 Extra lengths needed for thermal expansion (left). Posing of pipe insulation (right) (Kuraymat-Egypt) [14]

The fittings (i.e. valves, elbows, ball joints etc.) are responsible of localized pressure drop that has to be taken into account in order to determine the total pressure drop in the solar field. In [6] and [15] a K-factors list of the more common fittings is presented. The thermal compensating “U-bends” is considered with the addition of four elbows to the piping segment.

Once the mass flow and pressure profile are known, the next step is the physical sizing of the pipe segments.

After selecting the pipe material and the operating temperature that have an impact on the maximum allowable stress, it is possible to obtain the tube thickness and the outer diameter with the following relations [16]:

$$[t] = \frac{([p] - 1.01325)[D_{IN}]}{2[\sigma_{steel}] - 1.6([p] - 1.01325)} \quad (3.15)$$

$$D_{ext} = D_{in} + 2t \quad (3.16)$$

Where p is the operating pressure, D_{IN} is the inner diameter, σ_{steel} is the pipe material allowable stress, and t is the tube thickness.

The pressure of each segment is calculated starting from the pressure of the segment before (considering the flow motion sense) and the estimated pressure drop. The minimum pressure in the system is located at the hot header outlet and it is important to guarantee that its value is higher than the minimum allowable pressure in order to avoid the phase transition of the HTF. Synthetic oil like Therminol VP1[®] or DowTherm-A[®]

have a saturation pressure at 390°C equal to 9.59 bar and 9.37 bar respectively. High temperature molten salts ($T_{max}=560^{\circ}\text{C}$), due to the very low saturation pressure (few Pascals) [17] request the minimum pressure to be set above the atmospheric pressure in order to avoid ambient air entering in the pipe [13].

In Table 3.2, the density and the allowable stress of the most common pipe materials are shown. In particular AISI 316H is used in PT plants that handle molten salt with a “hot” temperature around 550°C whereas, in case of synthetic oil plants the common material is ASTM A106 (both for “cold” and “hot” header).

Table 3.2 Piping materials properties used in CSP plant

<i>Piping Materials Properties</i>			
Name	Density [kg m ⁻³]	Allowable Stress [MPa]	
		@T=390°C	@T=550°C
AISI 316H	8000	109.5	100
ASTM A106	7850	103.4	-

To complete the dimensioning of the piping system, the thermal losses have to be considered. During each optimization step, the insulation thickness is known (it is an optimization variable) and the thermal losses of each pipe segment can be computed with the following relation [18] (the steel tube conductive resistance, the convective inner surface resistance and outer surface resistance are negligible and thus not considered):

$$[q'_{loss}] = \left[\frac{(2\pi[k_{INS}]([T_{HTF}] - T_{amb}))L_{PIPE}}{\ln\left(\frac{[D_{OUT_PIPE} + 2t_{INS}]}{[D_{OUT_PIPE}]}\right)} \right] \quad (3.17)$$

Where k_{INS} is the thermal conductivity of insulation material, T_{amb} is the ambient temperature and t_{INS} represents the insulation thickness.

In Table 3.3 the thermophysical properties of the insulation material commonly used in solar field application are presented [18].

Table 3.3 Thermophysical properties insulation

INSULTATING MATERIALS PROPERTIES				
Header	Name	Density [kg m ⁻³]	Thermal conductivity [W m ⁻¹ °C ⁻¹]	
			@T _{mean} ¹⁰ =207.5°C	@T _{mean} =287.5°C
COLD	MinWool-1260 [®]	96.0	0.079	0.089
HOT	THERMO-12 [®] Gold	232.0	0.072	0.084

¹⁰ Mean temperature assuming ambient temperature equal to 25°C

3.3.2.1 Cost of Piping

Starting from the physical dimension it is possible to estimate the weight of the pipe that, together with the external diameter and to the type of material, is the variables useful to express the cost function in the following common form:

$$C_{material_pipe} = f(D_{est}; Material) Weight_{pipe} \quad (3.18)$$

In Figure 3.5, an example of the specific cost of pipe, function of the inner diameter, is presented. In addition, the specific cost trend line is shown. The same procedure is adopted for the insulation cost that is expressed by a constant specific cost (€/kg).

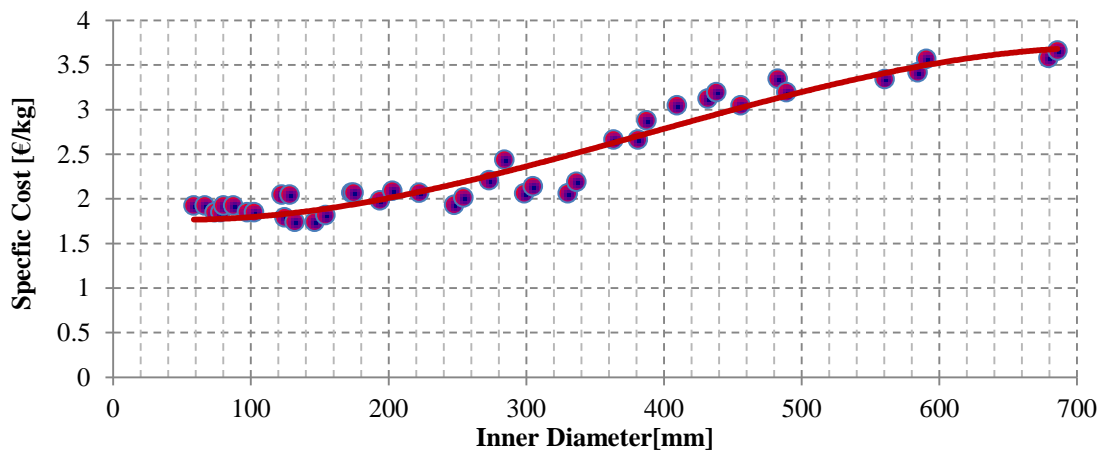


Figure 3.5 Weight-specific cost of pipe segment function of the inner diameter. The trend line is in red.

As regarding the fittings investment cost, once the number and the type are known, the cost is expressed taking into account data obtained from suppliers present in the market [6].

The impact on the investment cost of HTF pump is considered through its specific power cost (expressed in [€/kW]) derived from Thermoflex[®] database. The nameplate electric power of the pump is derived from the total mass flow rate and the total pressure drop of the solar field with the following relation:

$$P_{pump} = m_{HTF} \frac{\Delta P}{\eta_y \eta_{org-el} \rho_{HTF}} \quad (3.19)$$

Where m_{HTF} is the total mass flow rate, ΔP is total pressure drop of the hydraulic network¹¹, η_y is the hydraulic efficiency, η_{org-el} is the mechanical and electric efficiency and ρ_{HTF} is the density of the HTF processed by the pump.

In order to sum the operational cost to the investment cost it is necessary to calculate an equivalent capital cost of both the electric consumption and the thermal losses.

To take in account the yearly pumping energy of the HTF pump it is possible to estimate a mean power that considers the part-load operation of pump during the year as suggested in [6]. To estimate the equivalent capital cost the following equation is used:

$$C_{pumping} = \frac{E_{yearly-pumping} LCOE}{FCR} \quad (3.20)$$

The same procedure is used to estimate the equivalent cost of the yearly thermal losses; the only difference is that in this case the LCOTE is considered.

3.3.3 Expansion Vessel

The expansion vessel is a fundamental component for the safe operation of a close loop circuit. The scope of the expansion vessel is to compensate the expansion of the HTF fluid due to the change of the density with temperature [19].

As a first approximation, a simple sizing approach is adopted, in order to estimate the volume of the expansion tank and in particular, the volume of HTF contained.

As regards the positioning of the expansion tank, it can be placed on the cold side or the hot side of the piping. In plant without a thermal energy storage (“TES”) the expansion tank is placed in the hot side in order to exploit the thermal capacitance of this component to face changes in impinging solar energy [20-23]. Plants with indirect thermal energy storage place the expansion tank, which in this case has the only function of allowing HTF expansion, in the cold side in order to use low cost material and secondary to diminish its total dimension [1].

Adopting a direct thermal storage system, like the Archimede plant [24], the expansion tank is substituted directly by TES tanks.

First, to size the expansion tank is necessary to calculate the total volume of HTF both in the collector loop and the pipe segments with the following relation:

$$V_{tot} = n_{loop} V_{int_loop} + \sum_{i=1}^{n_{cold}} V_i + \sum_{j=1}^{n_{hot}} V_j \quad (3.21)$$

As reported in [19,25] the expansion tank level is 25% at ambient condition¹² while during operation condition the tank is full for 75% in order to assure a security margin.

¹¹ Since the central feed configuration is chosen, the ΔP is the sum of pressure drop in cold header, loop and hot header.

¹² An ambient reference condition temperature of 25°C is chosen

Once these specifications are known, the increment of HTF volume can be calculated with:

$$\Delta V_{HTF} = \left(\frac{\rho_{ref}}{\rho_{cold}} - 1 \right) (V_{cold}) + \left(\frac{\rho_{ref}}{\rho_{hot}} - 1 \right) \left(V_{hot} + V_{collectors} + \frac{1}{4} V_{tank} N_{tank} \right) \quad (3.22)$$

The common technical solution to arrange the requested volume is to use a multi tanks system; considering the common dimension of a single tank of 283 m³ [26] the necessary number of tanks (first integer number) can be determined. In this work, an expansion system configuration as the one described in [20] is adopted; in particular the expansion system has no overflow-tank and it is modelled as a single vessel in which all the mass flow goes through.

Regarding the investment cost of the expansion system, it is approximated equal to the cost of the HTF inside the expansion vessel.

3.4 Results

The developed suite exploits the capability of Matlab[®] optimization algorithm in order to obtain an optimum configuration that minimizes the total cost. At the end of the optimization process handled by the “Optimization ToolBox” [27] the results concern both the physical dimensions and the costs of the hydraulic network.

In the next subsections, the most significant outputs are presented for a solar field identified by the following characteristics Table 3.4.

Table 3.4 Resume of the most representative characteristics of the solar field considered for the optimization process of the piping system.

<i>INPUT SOLAR FIELD</i>		
Name Variable	Value	UoM
N°Subsection	2	-
HTF name	Therminol VP-1	-
Solar Multiple (SM)	1	-
Sizing DNI	1000	W m ⁻²
Total Aperture Effective Area	ca.235000	m ²
N°SCA per loop	4	-
SCA length	150	m
Tube Absorber Tech.	SCHOTT PTR70[28,29]	-
SCA tech.	EUROTROUGH-150	-
Total HTF Mass Flow	716.9	kg s ⁻¹
N°Loops	72	-
mass flow in each loop	9.96	kg s ⁻¹
Row Spacing	17.4	m
Minimum Pressure	15	bar
T hot	390	°C
T cold	290	°C
Location	Daggett (USA)	-

3.4.1 Dimension Summary

At the end of the optimization process, the model gives back the inner diameter and the thickness of each pipe segments that will be of crucial importance in determining the transient behavior of the solar field. In particular, the total mass of steel and the total HTF mass will be used to model the thermo-fluid performance of the whole solar field. Considering in detail the dimension of each pipe segments, the inner diameter and the thickness profiles of each segments are reported in Figure 3.6 (each solar field subsection has 36 header segments (hot and cold)+2 connecting pipe to the power block (hot and cold))+ 1 hot U-junction between two row of each loop. The pipe segments are identified by a number; the segment "1" is the cold header pipe that connects the power block to the solar field whereas the pipe "20" is the hot header pipe that delivers the heated HTF to the power block. The last pipe segment of the red series represents the U pipe that is present in each loop.

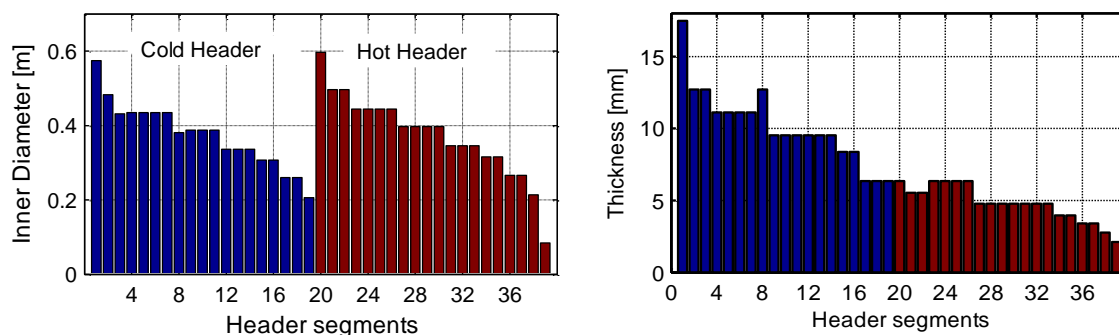


Figure 3.6 Example of output of inner diameter (left) and thickness of each pipe segment.

In Figure 3.6 it is possible to notice that the inner diameter does not show a relevant difference between the hot and cold header due to the small difference in fluid density. The inner diameter of the hot header is slightly bigger than the cold header one; this result implies that the velocity is nearly the same in each pipe segments that is a common approach used to size the headers as reported in [4]. The smaller operating pressure of the hot section derived from the pressure drop of both the cold header and the loop can explain the smaller pipe thickness of hot header; in particular, this effect has a greater impact in comparison to the decrease of the allowable stress due to the higher operating temperature.

From the trend presented in figure above, it is possible to notice how the availability of discrete pipe diameters is reflected by the obtained results that show some value that does not follow the main trend (e.g. the pipe thickness of the 9th segment).

The value of total pressure drop is computed equal to 18.0 bar with the cold header and hot header having approximately the same impact (ca. 2.5 bar) thus leading to an electric consumption by the circulation pump of 2.6 MW_e. The hydraulic network characteristic of central feed configuration implies that additional pressure drops are needed to assure a constant mass flow rate in each loop. The placing of a valve at the entrance of each loop solves this issue, and the value of the desired head loss derives from the solution of the hydraulic network. In Figure 3.7 the additional pressure drops, necessary to balance the hydraulic network, are shown.

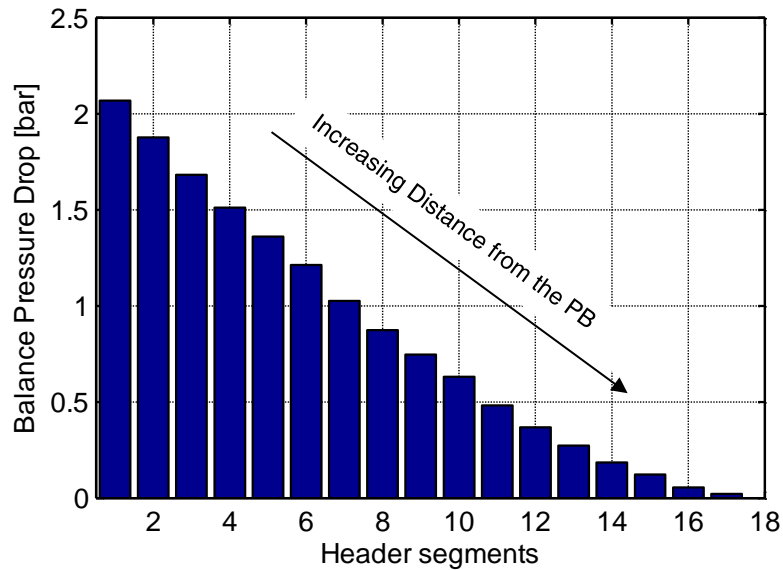


Figure 3.7 Additional pressure drops to balance the loop in design condition. The results are presented for eighteen loops because they represent the loops of half subsection.

As regards the insulation thickness, the optimization solution gives a mean specific heat loss of 100 W/m for the cold header and 150 W/m for the hot header in accordance to [30].

As far the expansion system concerns, it consist of 3 vessels of 283 m³ each.

The total mass of HTF contained in the solar field is approximately 891 ton whereas the steel weight is 247 ton.

It is important to remember that, in the following chapters, the transient analysis is performed referencing to the solar field defined by the characteristics presented above.

3.4.2 Cost breakdown

In addition to the physical dimension of the pipe segments, the optimization model can provide some useful information about the cost share of different components.

Starting from this info, the impact, from an economic point of view, of possible enhancements is evaluated.

In Figure 3.8 the goal function of the optimized piping solution is presented with each components impact underlined. The objective function contains the cost of each components described in the previous sections. Both investment cost and operational cost are considered and a rough estimate of the specific economic weight can be made.

In particular the operational cost (bordered black), constituted by pump electric consumption and thermal energy losses, accounts approximately the 37% of the goal function.

Total Costs Breakdown

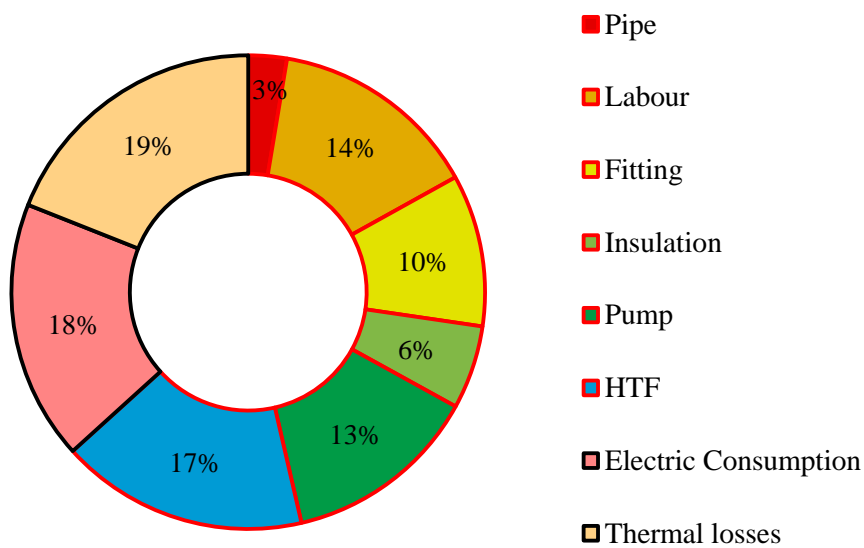


Figure 3.8 Total cost (goal function of the optimizer) breakdown for the solution described in the previous section. The operational cost are bordered black while the investment costs are bordered red.

In addition to the total cost shares, the investment costs breakdown is presented in Figure 3.9 showing the impact of the different main components of the piping system. In particular, it is worth to see that the material cost covers only a small fraction of the investment cost (ca. 4%) while the sum of labor, fittings and insulation covers nearly the 48%.

In Figure 3.9 the contribution to operational cost is presented showing that the electric consumption imputable to the solar field pump and the equivalent cost of the thermal loss have the same economic weight in an optimized configuration as underlined in [31].

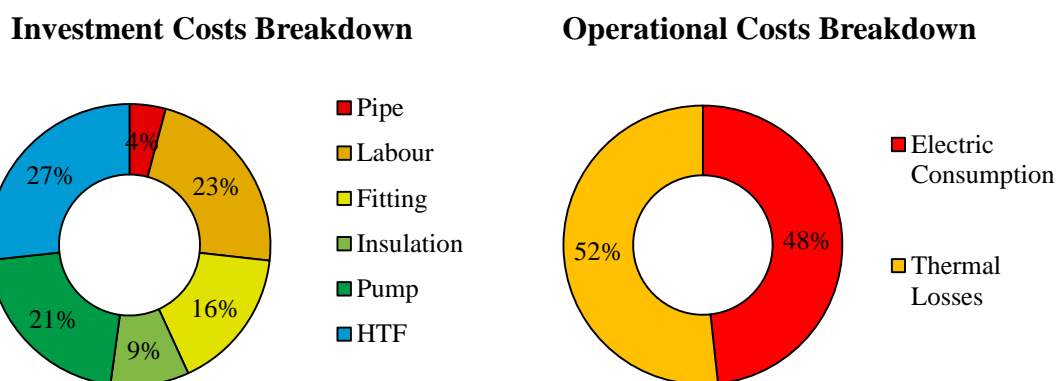


Figure 3.9 Investment cost (left) and Operational cost (right) of the optimized configuration

In literature, it is common to find value of aperture area specific investment cost that does not contain the pump and the HTF in the solar field. In this work, these two values are

considered part of the objective function of the optimization suite because of their strong relation with pipe segments dimension.

To evaluate the obtained results the “literature” specific cost of the piping is calculated obtaining a value of ca. 17 €/m² in agreement to the results shown in other studies about the piping network of parabolic trough concentrators [6,32].

3.5 Bibliography

- [1] Solar Millennium. Solar Millennium AG - The Construction of the Andasol Power Plants. - Archives - Technology - References and Projects - Andasol (Spain) 2012;2012.
- [2] National Renewable Energy Laboratory. NREL: TroughNet - U.S. Parabolic Trough Power Plant Data 2012;2012.
- [3] Goswami DY, Kreith F. Handbook of Energy Efficiency and Renewable Energy Taylor & Francis; 2007.
- [4] Binotti M. Linear Fresnel reflectors : study of the technology and steps toward optimization 2013.
- [5] NovatecSolar. NovatecSolar Website;2013.
- [6] Kelly B, Kearney D. Parabolic trough solar system piping model. Final Report, National Renewable Energy laboratory 2006.
- [7] Manzolini G, Giotri A, Saccilotto C, Silva P, Macchi E. Development of an innovative code for the design of thermodynamic solar power plants part A: Code description and test case. Renew Energy 2011;36:1993-2003.
- [8] Forristall RE. Heat Transfer Analysis and Modeling of a Parabolic Trough Solar Receiver Implemented in Engineering Equation Solver National Renewable Energy Laboratory; 2003.
- [9] Flueckiger SM, Iverson BD, Garimella SV. Economic optimization of a concentrating solar power plant with molten-salt thermocline storage. J Sol Energy Eng Trans ASME 2014;136.
- [10] Lovegrove K, Stein W. Concentrating Solar Power Technology: Principles, Developments and Applications Elsevier Science; 2012.
- [11] Citrini D, Nosedà G. Idraulica CEA; 1987.
- [12] Churchill S. Friction factor equations spans all fluid-flow ranges. Chemical Engineering Journal 1977;7:91-92.
- [13] ENEA. Progetto "Archimede": Realizzazione di un impianto integrativo presso la centrale ENEL di Priolo Gargallo(SR) 2007.
- [14] Flagsol GmbH. Flagsol GmbH Webpage 2012.
- [15] Crane Co. Flow of Fluids through Valves, Fittings, and Pipe Crane Australia Pty. Limited; 1995.
- [16] American Society of ME, American National SI. Power Piping: ASME Code for Pressure Piping, B31 American Society of Mechanical Engineers; 2012.

- [17] Bradshaw RW, Siegel NP. Molten nitrate salt development for thermal energy storage in parabolic trough solar power systems. Proceedings of ES2008, Energy Sustainability 2008:10-14.
- [18] Theodore L. Bergman, Lavine A, Incropera FP, Dewitt DB. Fundamentals of Heat and Mass Transfer Wiley.
- [19] Solutia. Therminol information bulletin no 4: "Heat transfer system expansion tank design" 1999.
- [20] GRÄTER F, LA PORTA F, BICKMEYER W, MÖBIUS C. Expansion system in the Heat-Transfer-Medium circuit of a solar thermal power plant 2011.
- [21] Jones S, Pitz-Paal R, Schwarzboezl P, Blair N, Cable R. TRNSYS modeling of the SEGS VI parabolic trough solar electric generating system. Solar Engineering 2001:405-412.
- [22] Acciona. Palma del Rio Power Plant 2011.
- [23] Glatzmaier GC. Measurement of Hydrogen Purge Rates in Parabolic Trough Receiver Tubes SolarPACES; 2010.
- [24] Archimede Solar Energy. Archimede Power Plant -ENEL-Priolo Gargallo 2013;2013.
- [25] Vasquez Padilla R. Simplified Methodology for Designing Parabolic Trough Solar Power Plants 2011.
- [26] Lippke F. Simulation of the part-load behavior of a 30 MWe SEGS plant 1995.
- [27] MathWorks. Optimization Toolbox: Solve standard and large-scale optimization problems 2013;2013.
- [28] Burkholder F, Kutscher CF. Heat Loss Testing of Schott's 2008 PTR70 Parabolic Trough Receiver National Renewable Energy Laboratory; 2009.
- [29] SCHOTT Solar. Schott PTR-70 Receivers Designed for maximum profitability of the power plant 2013;2013.
- [30] Giostri A, Saccilotto C, Silva P, Macchi E, Manzolini G. A numerical model for off-design performance calculation of parabolic trough based solar power plants. ASME Int Conf Energy Sustainability, ES 2010;2:617-626.
- [31] Kearney D, Herrmann U, Nava P, Kelly B, Mahoney R, Pacheco J, et al. Assessment of a molten salt heat transfer fluid in a parabolic trough solar field. TRANSACTIONS-AMERICAN SOCIETY OF MECHANICAL ENGINEERS JOURNAL OF SOLAR ENERGY ENGINEERING 2003;125:170-176.
- [32] CSP Today. CSP Today Research & Reports: Parabolic Trough Report 2013.

4 Solar Field Model

Once a detailed sizing of the piping network is made, the second step to study the thermal behavior of the solar field is the development of a model able to simulate different operating conditions. Referencing to the solar field layout obtained with the running of the model described in Chapter “Piping Model”, a thermo-hydraulic model is developed in order to be able to capture the main transient effects induced by the passage of cloud or characteristic of the morning start up.

The model of a single absorber tube is presented with a detailed description of the adopted approach. Since the solar field comprises all the absorber tube and the piping headers, the modelling boundaries have to be extended to cover the whole system. Starting from the single receiver model the complete solar field model is described.

Once the description of the implemented modeling approach is concluded, some test-cases are considered and a validation phase compares the outputs of the developed model with a model used at DLR.

Regarding the output of the model, some results about the solar field behavior are presented with the aim of describing some critical situations that are not possible to be captured by a quasi-stationary approach of solar field modelling.

4.1 Thermal Model of a single absorber tube

Concerning the linear focusing technology (in particular the parabolic trough), the thermal models found in literature can be placed in three main categories that differ in the level of the modelling accuracy and in the goal of their application. In particular, it is possible to identify the following subcategories:

- “*Zero or 1-D steady state models*” are used in steady state model and in yearly performance studies. The simplest model that belongs to this category implements a heat loss correlation in order to solve a single equation only. The next step is the addition of a spatial discretization of the absorber tube and the solution of the thermal network for each discretized element obtaining a set of algebraic non-linear equations [1,2]. The receiver model used in Chapter 2 belongs to this category.
- “*Zero or 1-D transient models*” are built to catch the transient effect due to the thermal inertia effect of the absorber tube. These models aim to study the dynamic effects that are not considered by the steady state models; in particular, this category comprises the methods used to develop new control designs or to analyze the dynamic behavior impact on the energetic performance of the solar field. Additionally, this group of modeling approach can be divided in lumped or distributed models depending on the requested level of accuracy [3-5]. The model that is considered in this chapter and described in this section belongs to this category.

- “2D/3D models (transient or stationary)” are suitable to study heat transfer and fluiddynamic problem in detail [6,7] . These detailed models can be useful to go deep into the physics of the absorber tube behavior (i.e. thermal elongation of the absorber pipe, flow pattern in DSG etc.) nevertheless, because of very high level of modelling accuracy and consequently huge computational resources needed, this approach cannot be used for simulation of an entire solar field.

The developed model is based on the set of partial differential equations (“PDE”) that represents the energy balance laws of the “Heat Collector Element” (HCE) considered as the combination of HTF phase, the metal wall of the absorber tube and the glass envelope. As regards the impinging energy flux, a non-uniform shape that depends on the reflector technology characterizes the solar energy concentrated on the absorber. In Figure 4.1 the real flux distribution of energy impinging on the absorber tube of a LS-2 assembly is shown; the energy profile is obtained with the NREL’s optical ray-tracing software SOLTRACE [8,9] freely available from the NREL’s website. The shade of the absorber tube on the mirror leads to the characteristic behavior in the range 120°-240°. Besides these considerations about energy flux distribution, a common modelling approach consists on assuming a uniform circumferential distribution of concentrated solar irradiation and a uniform radial temperature distribution for the fluid, absorber tube and glass envelope.

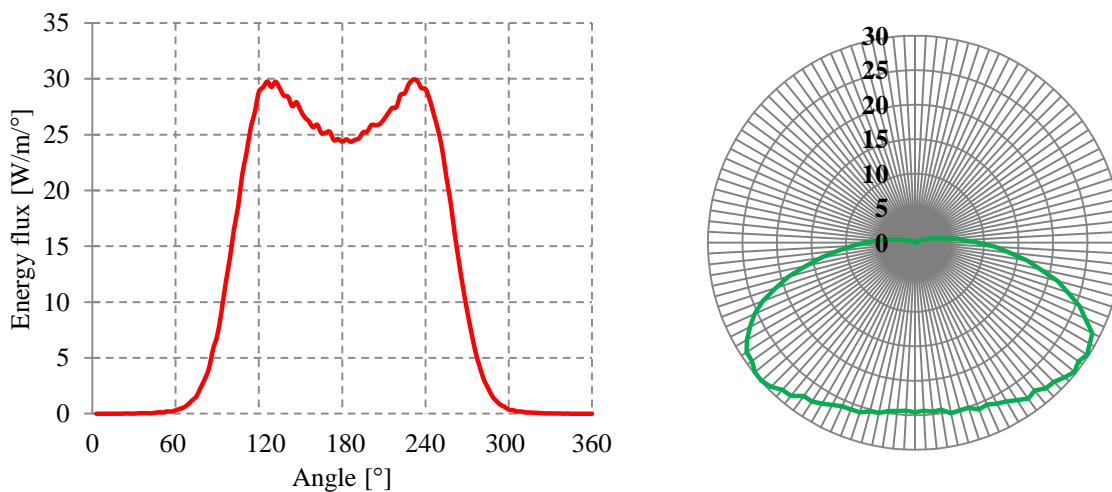


Figure 4.1 Thermal energy flux on the absorber tube of a parabolic trough concentrator obtained with the raytracing software (SOLTRACE). (LS-2 Concentrator, Aperture=5 m, External absorber diameter=70 mm, Concentration Ratio”CR”= 22.74 as defined by Rabl [10])

As regards the HTF, it is modelled as an incompressible fluid therefore the thermophysical properties are functions of temperature only as reported in Appendix.

In the following, the mathematical formulation of the transient problem is presented for each part of the absorber tube (HTF, absorber tube and glass envelope). The first step is the identification of the energy fluxes that have to be taken into account by the model. Focusing the attention on a generic radial section of the HCE (see Figure 4.2), it is possible to identify three nodes which represent the three main surfaces (HTF, pipe

absorber and the glass envelope). Concerning the thermal model of the radial section, the main energy fluxes can be summarized, as suggested by [11] and shown in Figure 4.2, in:

1. *Concentrated Solar Energy*: the parabolic mirror concentrates solar energy on the absorber. To calculate this flux the DNI has to be known together with the optical efficiency of the concentration system and aperture area of the mirror.
2. *Absorbed energy by the glass (q_{sol_glass})*: the glass (Pyrex[®] glass-borosilicate glass) absorbs a small fraction of the concentrated solar energy. A common value of solar absorptivity of Pyrex[®] glass is 2% [12].
3. *Impinging solar energy on the pipe absorber*: the glass envelope transmits only a part (e.g. 94%) of the solar radiation that impinges the metal pipe.
4. *Absorbed Solar Energy by the absorber pipe (q_{sol_steel})*: the selective coating of the absorber captures a high fraction (e.g. 95%) of the impinging solar flux.
5. *Thermal energy transmitted to the HTF (q_{in_HTF})*: the hot absorber pipe transfers the thermal energy to the HTF [13].
6. *Thermal Energy exchanged between the metal tube and the glass envelope ($q_{internal}$)*: the temperature difference between the metal pipe and the glass envelope leads heat to be transferred from the steel wall to the glass wall. As presented in [12,14], convection [15] and radiation heat transfer [16] take place.
7. *Thermal energy loss toward the ambient ($q_{external}$)*: the total heat loss is produced by the heat exchange (radiation and convection [17,18]) between glass envelope and ambient.

With the same methodology used in [12], a thermal resistance network that considers all the aforementioned contributes can describe the problem in the radial section. Solving the thermal balance means to find the temperatures of the nodes that represent the unknowns of the thermal problem.

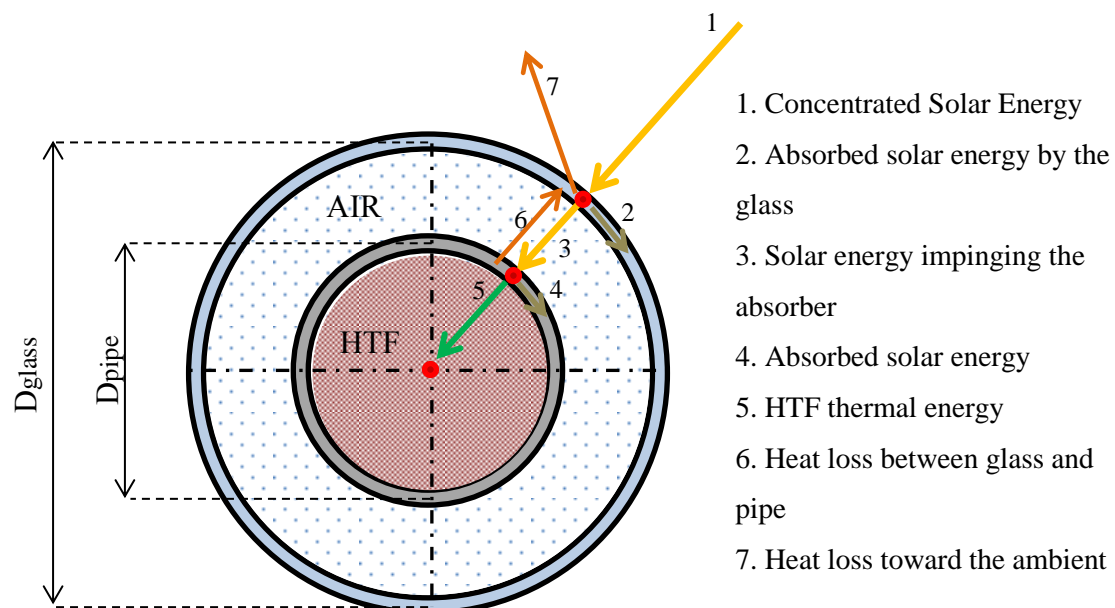


Figure 4.2 Absorber scheme with main energy fluxes. The red dots represent the discretization node the radial section.

In order to describe exhaustively the absorber tube, the temperatures of the nodes along the longitudinal direction are necessary. For that reason, the following set of differential equation (t is the time), describing the balance relations, can be written (x representing the longitudinal direction):

In particular, the fluid energy balance is proposed in equation (4.2):

$$\frac{\partial(\rho u)_{HTF}}{\partial t} + \frac{\partial(\rho v h)_{HTF}}{\partial x} = q_{in_HTF} \quad (4.1)$$

Where ρ identifies the density, u is the internal energy, h is the enthalpy.

The balance equation of the solid wall, considered as steel pipe:

$$\begin{aligned} \rho_{steel} c_{p_{steel}} A_{steel} \frac{\partial T_{steel}}{\partial t} \\ = k_{steel} A_{steel} \frac{\partial^2 T_{steel}}{\partial x^2} - q_{in_HTF} - q_{internal} + q_{sol_steel} \end{aligned} \quad (4.2)$$

Where $c_{p_{steel}}$ is the heat capacity of the absorber material, A_{steel} is the absorber sectional area, T_{steel} is the absorber temperature and k_{steel} is the thermal conductivity of the absorber material.

In analogy to the absorber tube balance equation, the glass envelope balance can be expressed with the following relation:

$$\begin{aligned} \rho_{glass} c_{p_{glass}} A_{glass} \frac{\partial T_{glass}}{\partial t} \\ = k_{glass} A_{glass} \frac{\partial^2 T_{glass}}{\partial x^2} + q_{internal} - q_{external} + q_{sol_glass} \end{aligned} \quad (4.3)$$

As regards the continuity equation for the heat transfer fluid, it is written as:

$$\frac{\partial \rho_{HTF}}{\partial t} + \frac{\partial(\rho v)_{HTF}}{\partial x} = 0 \quad (4.4)$$

Where v is fluid velocity.

It is important to underline that the involved energy fluxes depend on the x coordinate because of the existing dependence on the temperature of the nodes.

The momentum balances is expressed with a steady-state formulation that states that the pressure difference is represented by the pressure drop due to friction.

In order to close the differential problem, initial and boundary conditions are necessary.

As initial condition, the temperature profile along x -coordinate of the three radial nodes (fluid, steel and glass) is imposed. Referring to the boundary condition of the solid surface, the extremities of the steel pipe and the glass envelope are assumed adiabatic while, regarding the HTF, the inlet temperature is imposed.

$$T_{HTF,j}(t = 0) = T_{HTF_initial} \quad (4.5)$$

$$T_{steel,j}(t = 0) = T_{steel_initial} \quad (4.6)$$

$$T_{glass,j}(t = 0) = T_{glass_initial} \quad (4.7)$$

4.1.1 Resolution Approach

After the set of equations that represents the problem is identified, the next step is to develop a resolution approach that is able to solve the system of PDEs.

The solution is based on the approximation of a PDEs system with a system of ordinary differential non-linear equations (“ODE”). To reach this purpose a spatial discretization is applied (see Figure 4.3) in order to express the space derivative with a finite difference scheme. A system of temporal ODEs is obtained and solved by the Matlab[®] ODE solvers that treat the temporal discretization autonomously with time adaptive algorithms.

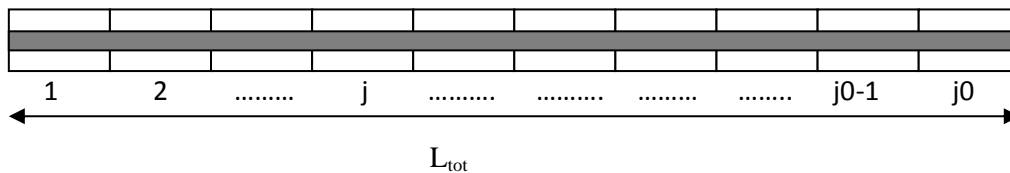


Figure 4.3 Spatial discretization of the absorber tube

Referencing to the spatial discretization shown above, the approximation of the partial derivative can be expressed as:

$$\Delta x = \frac{L_{tot}}{j_0} \quad (4.8)$$

$$\frac{\partial T_j(z, t)}{\partial x} = \lim_{\Delta z \rightarrow 0} \left(\frac{T_j(t) - T_{j-1}(t)}{\Delta x} \right) \quad j = 1, 2, \dots, j_0 \quad (4.9)$$

$$\frac{\partial^2 T_j(z, t)}{\partial x^2} = \lim_{\Delta z \rightarrow 0} \left(\frac{T_{j-1}(t) - 2T_j(t) + T_{j+1}(t)}{\Delta x^2} \right) \quad j = 1, 2, \dots, j_0 \quad (4.10)$$

As regards the number of discretized elements, a tradeoff between the accuracy of results and the computational effort arises. As stated by the study reported [19], that deals with a thermal model for LFR, the longitudinal spatial resolution marginally affects the steady-state solution. In particular, the parameter that affects the simulation results is the temperature rise in each discretized element that was fixed to 20°C corresponding to 5 discretized elements (for a global temperature rise of 100°C).

On the contrary, the research presented in [20] underlines that for transient study the dynamic response is influenced more strongly by the longitudinal spatial resolution and

the trade-off between accuracy and computational time is more important because of the higher computational intensive solving procedure.

For that reason 100 discretized segments for each loop is considered to be sufficient to simulate correctly the described problem (for a loop of 600 m each element is 6 m long).

The pressure loss calculation is accomplished by a semi-empirical correlation able to estimate the pressure drop. It is important to consider that this model is the basis element of the model of the whole solar field; for that reason to reduce the computational efforts an explicit formulation of friction factor is used [21]:

$$[f] = 8 \left(\left(\frac{8}{[Re]} \right)^{12} + ([A] + [B])^{-3/2} \right)^{1/12} \quad (4.11)$$

$$[A] = \left[2.457 \log \left(\frac{1}{\left(\frac{7}{[Re]} \right)^{0.9} + 0.27 \frac{\varepsilon}{[D_{IN}]}} \right) \right]^{16}; [B] = \left(\frac{37530}{Re} \right)^{16} \quad (4.12)-(4.13)$$

4.2 Preliminary Results

In this section, some preliminary results of the thermal model of an absorber tube are presented. Two different situations are shown, in order to introduce some of the model peculiarity that will be used in the next chapters.

In accordance to the choice made in Chapter 3, the considered technologies are PTR-70 and Eurotrough ET-150 for receiver and SCA respectively; this choice represents the state-of-art of parabolic trough CSP plants.

The main receiver characteristics of the solar receiver are summarized in Table 4.1.

Table 4.1 Absorber tube characteristics considered in this chapter

<i>ABSORBER TUBE</i>		
Name Variable	Value	UoM
Optical Efficiency	78.0	%
Glass absorptivity	0.02	-
Coating Emissivity	0.09 @T=390°C ¹³	-
Aperture Width	5.75	m
Effective Aperture Width	5.45	m
SCA length	150	m

In Figure 4.4, the temperature behavior of a single loop, during warm-up, is shown in a 2-D map that shows the temperature values of each discretized segments during the simulation time. The initial temperature for each discretized segments (fluid, pipe steel

¹³ The thermal emissivity is a function of temperature as reported in [22]

and glass) is 90°C while the inlet HTF flow is 7.5 kg/s . The ramp of EDNI is idealized by a linear interpolation between the starting value ($t=0$) of 54 W/m^2 and the final value ($t=400$) of 120 W/m^2 . The inlet temperature is constant during time and equal to 94°C .

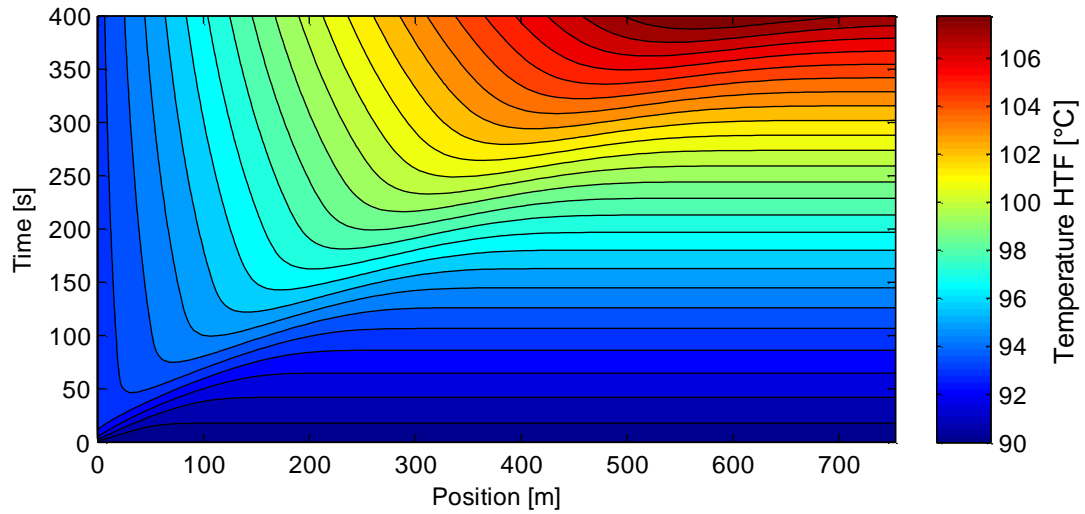


Figure 4.4 Temperature-time map of the absorber tube considered in the first example.

In the second example, the effect of a step EDNI variation on a 600 m length loop (with the same SCA and absorber technologies) is considered through the analysis of three different case-studies that consider the same effective power loss induced by a step disturbance.

As regards the HTF stream, the inlet temperature is constant and equal to 290°C and the mass flow is set to 7.7 kg/s .

The first two conditions concern the same shading function ($\text{EDNI}_{t=0\text{s}}=800\text{ W/m}^2$ - $\text{EDNI}_{t=700\text{s}}=0\text{ W/m}^2$ - $\text{EDNI}_{t=2700\text{s}}=800\text{ W/m}^2$) but applied to different sections of the loop (first half and second half of the loop). The third condition has a shading function with step amplitude half of the previous one but in this case, it is applied to the entire loop length.

Figure 4.5 shows the shading function (top) and the trend of loop outlet temperature (bottom).

The initial shape of the signal (approximately in the time range $0\text{-}300\text{ s}$) represents the stabilization of the outlet temperature to the stationary value of 393°C ; this fact is due to the value of the initial condition that are not exactly the steady one. The blue line, representing the case with the shading applied to the last 300 m , shows an outlet temperature decrease immediately when the shading occurs ($@700\text{ s}$). Due to the change of impinging solar energy a new steady-state condition is reached approximately to 340°C . When the solar energy disturbance disappears ($t=2700\text{ s}$) the temperature starts to increase until the design temperature of 393°C is reached.

The opposite situation is represented by the application of shading function on the first half of the loop (red line). As it is possible to notice, the same characteristic temperature

levels can be recognized. The typical effect of throughput-time¹⁴ leads to a time delay compared to response of the blue line signal; when the EDNI disturb is cancelled (or added) the impact on outlet temperature can be appreciated after approximately 800 s (half the throughput time – ca. 100 seconds) as enlightened by the dashed circle in the figure below.

As regards the green-dotted series, an intermediate behavior can be observed with a weaker temperature gradient that is a direct consequence of the lower EDNI change.

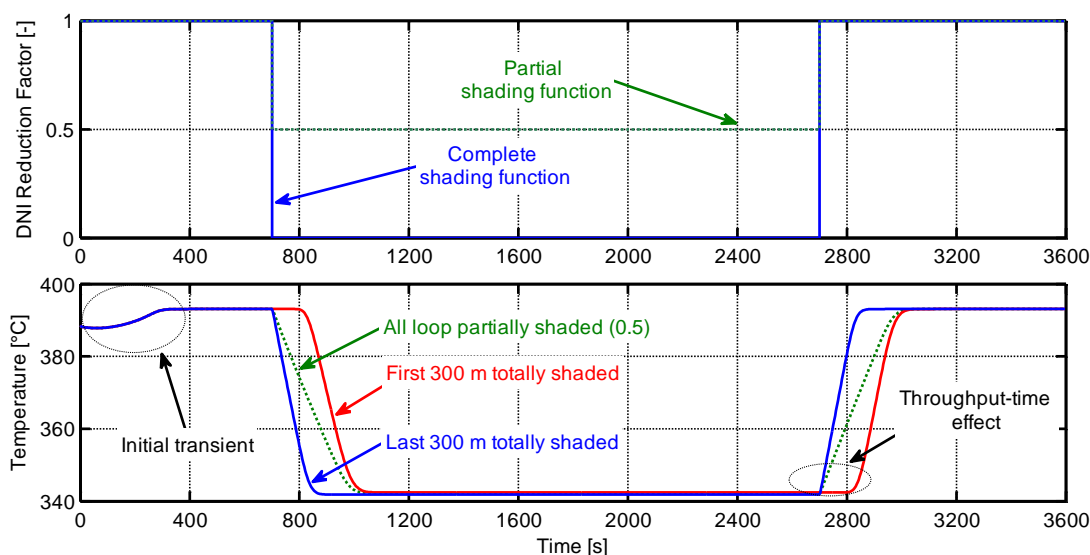


Figure 4.5 Reduction of EDNI signals (referred to the sizing condition of 800 W/m²). Outlet temperature profile of a solar absorber tube due to different steep decreases in effective direct normal insolation (bottom).

It is important to underline that the model of a single absorber does not allow capturing the real transient effect of a solar field (e.g. partial cloud shading) and can be limiting for the study of the complete solar field response. For that reason, the single absorber model will be integrated in the complete solar field modelling.

4.3 Hydraulic Network of Solar Field

As previously described, the solar field is made of many loops connected each other through the piping system shown in the specific Chapter 3 “Piping Model”.

The model of one representative absorber is not sufficient to capture the most important transient effects caused by, for example, the passage of a cloud that covers partially the solar field. The addition of the whole piping system, considered from both the hydraulic and thermal behavior, is necessary to increase the level of the model reliability although increasing at the same time the complexity of the model.

In the next sub-sections, an explanation of the modelling of the header system is presented.

¹⁴ The throughput-time is the time a fluid particle needs to travel from the loop entrance to the exit.

4.3.1 Hydraulic modelling

The addition of the HTF distribution system leads to consider the problem of finding the mass flow in each loop that balance the network instead of fixing it as in the single absorber model. This solution approach is fundamental because of the temperature impact on fluid properties that links the thermal model and the hydraulic model together.

In Figure 4.6 a schematic drawing of solar field is presented in order to facilitate the explanation of the balancing problem. Before starting with the description of the problem, a nomenclature resume is provided in order to identify correctly the different components of the hydraulic network; in particular, we have (taking into account a single section):

- The loops are indexed by a number that identifies the distance from the solar field inlet and by the relative position in the section (LEFT (*l*) and RIGHT (*r*)).
- The inlet in the solar field is called “*In_cold*” while the hot stream output is called “*Out_hot*”.
- The header pipe segments are identified by the collector loops number at the extremities.

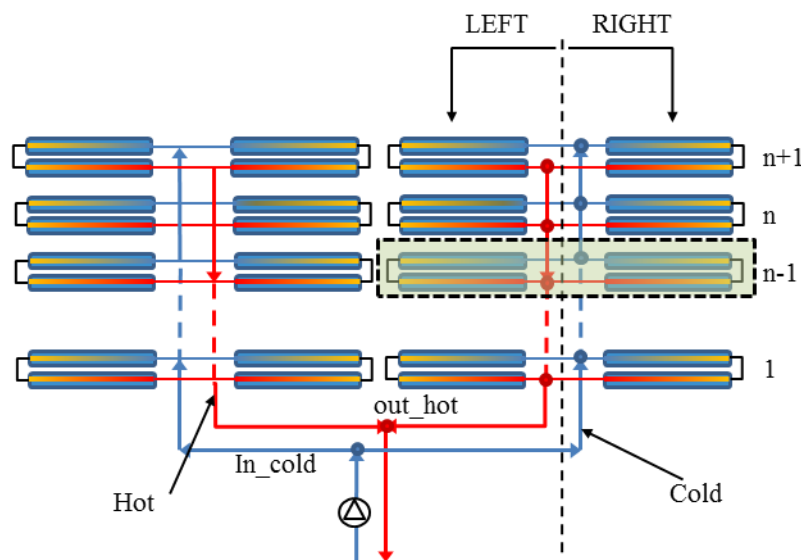


Figure 4.6 Drawing of the solar field section useful to explain the balancing problem

The first relation that is necessary to solve the hydraulic network problem is the continuity equation that applied to each node takes the following form as expressed below for the hot header:

$$m_{n/R} + m_{n/L} + m_{n/n+1} = m_{n-1/n} \quad (4.14)$$

In the second step a generic grid *n* (enlightened in Figure 4.6) is considered, the mass flow rate in the left loop and the right loop must verify the equivalence of the pressure drop in the two loops as presented in the following relation:

$$\Delta P_{n/R} = \Delta P_{n/L} = \Delta P_n \quad (4.15)$$

It is possible to add this relation for each node:

$$P_{n/cold} - \Delta P_n = P_{n/hot} - \Delta P_{n/n-1} \quad (4.16)$$

Remembering that pressure drop in each segment is function of mass flow, HTF properties (i.e. density and dynamic viscosity) and piping dimensional characteristics (i.e. inner diameter and fittings):

$$\Delta P_{n/x} = f(m, \rho, \mu, D_{int}, fittings) \quad (4.17)$$

As it is possible to appreciate from the head loss correlation, the pressure drop value is influenced by the thermophysical properties. From a qualitative point of view, a partial shading of the solar field induces an uneven temperature distribution among the loops thus leading to different HTF thermophysical properties (the properties are temperature dependent as reported in the Appendix). Considering the characteristic hydraulic network relations, the mass flows in each loop are arranged spontaneously in order to verify equations (4.14) - (4.16).

As far as the hydraulic network solving algorithm concerns, the pressure drop function presents a high level of nonlinearity thus requesting a suitable solving algorithm (See Eq.(4.17)). The KINSOL solver, part of SUNDIALS suite [23] and adapted for the MATLAB environment [24], developed by the Lawrence Livermore National Laboratory, is chosen because of its reliability and higher computational speed if compared with the Matlab “*fsolve*” function.

4.3.2 Thermal modelling

To complete the hydraulic system modelling, the thermal behavior of each pipe segments has to be simulated. In agreement to [25] a lumped capacitance approach is implemented. Once the physical dimension of the pipe is known, it is possible to estimate the total thermal capacitance and to concentrate it in each node. The same approach is used for the expansion tank considered, in each time, perfectly mixed.

The ODE that represents the lumped capacitance approximation is formulated as follows:

$$C_i \frac{dT_i(t)}{dt} = m_{HTF}(h_{HTF_in} - h_{HTF_out}) - q_{loss} \quad (4.18)$$

Where C_i is the thermal capacitance of the i-segment and q_{loss} is the thermal losses of the header segment.

The lumped capacitance approximation is chosen in order to not increase the computational efforts maintaining an adequate level of accuracy.

4.3.3 Final problem expression

The final problem, which comprises all the additional terms previously described, is made of both the thermal and the hydraulic problem.

It is important to underline that mass flow distribution is solved in each time step chosen by the ODE solver that transmits the temperature of each discretized segment and the inlet mass flow rate in the solar field.

Putting together the relations described above, the differential problem can be expressed by:

Energy balance of Heat Transfer Fluid node (j-th discretized segment):

$$\rho_{HTF} c_{p_HTF} A_{HTF} \Delta x \frac{dT_{j,HTF}}{dt} + m_{j,HTF} h_{j,HTF} + m_{j-1,HTF} h_{j-1,HTF} = q_{conv,j,HTF} \Delta x \quad (4.19)$$

Energy balance of Absorber Tube node(j-th discretized segment):

$$\begin{aligned} \rho_t c_{p_t} A_t \Delta x \frac{dT_{j,t}}{dt} \\ = \frac{k_t A_t}{\Delta x} [T_{j-1,t} - 2T_{j,t} + T_{j+1,t}] \\ - (q_{j,conv} + q_{j,envelope} - q_{j,abs_sol}) \Delta x \end{aligned} \quad (4.20)$$

Energy balance of Glass Envelope node(j-th discretized segment):

$$\begin{aligned} \rho_g c_{p_g} A_g \Delta x \frac{dT_{j,g}}{dt} \\ = \frac{k_g A_g}{\Delta x} [T_{j-1,g} - 2T_{j,g} + T_{j+1,g}] \\ - (q_{j,amb} - q_{j,envelope} - q_{j,abs_sol}) \Delta x \end{aligned} \quad (4.21)$$

Energy balance of Piping segments (i-th piping segment):

$$C_i \frac{dT_i}{dt} = m_{HTF} (h_{HTF_in} - h_{HTF_out}) - q_{loss} \quad (4.22)$$

Mass Balance (j-th discretized segment --- i-th piping segment):

$$\frac{V_j d\rho_j}{dt} = m_{j-1} - m_j \quad (4.23)$$

Where V_j is the volume of j-th segment.

Network Pressure problem: the system of algebraic non-linear equation that represents the hydraulic problem has to be solved for each time step.

4.3.4 Comparison with DLR's model

In order to validate the solar field modelling described in the previous sections a comparison with the DLR's model [5] (implemented in Modelica[®] [26]) is presented in this section. In particular, three base test cases are analyzed in order to obtain a preliminary validation of the developed code results. A characteristic of these test cases is that they present symmetrical boundary conditions among the loops in terms of effective DNI. In this way the comparison is made simpler avoiding the memory bottleneck of the DLR's model that is a direct consequence of its higher level of flexibility (it was originally developed to handle phase transition).

4.3.4.1 Steep increase of DNI

The first test-case is chosen to test the response of the system to a steep increase in the EDNI impinging on the solar field. The inlet mass flow is kept constant to the sizing value. The profile of EDNI and total HTF mass flow rate are shown in Figure 4.7.

As regards the initial condition, the HTF temperature at time zero is set to 340°C while the initial temperature of the piping system is set to 290°C and to 390°C for the cold section and the hot section respectively.

The HTF inlet temperature is fixed to 290°C (constant during time).

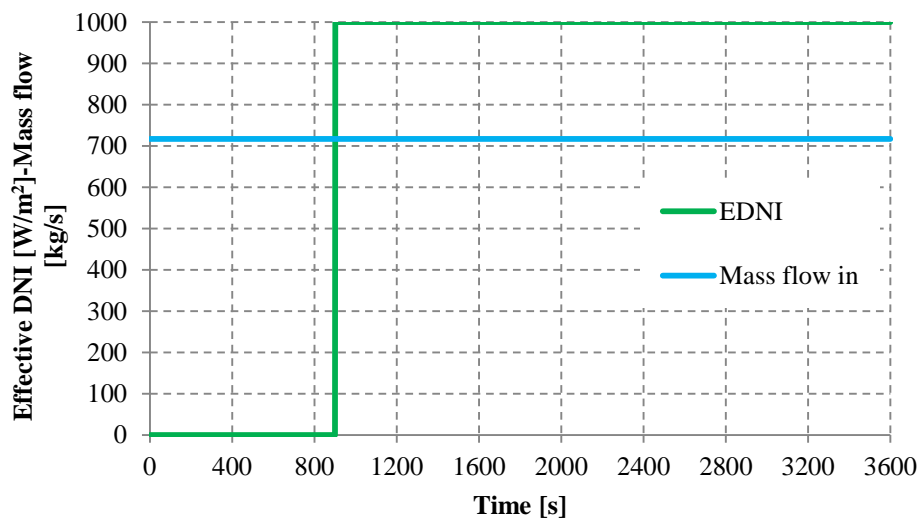


Figure 4.7 Steep increase of DNI with constant inlet mass flow (Test case #1)

In the next two figures a comparison between the DLR's model (blue) and the developed model (red), taking into account both the outlet temperature and the mass flow rate of the loop #1, is proposed.

The outlet temperature of the first loop of both the models is presented in Figure 4.8 and four main zones can be noticed. The first can be identified by a low gradient of outlet HTF temperature caused by the heat loss toward the ambient.

Once the fluid at 290°C, which entered the absorber, reaches the outlet it is possible to identify the second zone characterized by a steep decrease in temperature.

When the temperature gradient reaches a null value, the steady state conditions (@DNI=0 W/m² and T_{inlet}=290°C) are reached and the temperature profile shows a flat behavior.

When the solar energy step brings the EDNI to 1000 W/m², the temperature begins to rise until reaching the new steady state value. As can be noticed from the temperature trend of the figure below, the two models show a good agreement; the small difference in the initial can be ascribed to a different initialization of mass flows distribution.

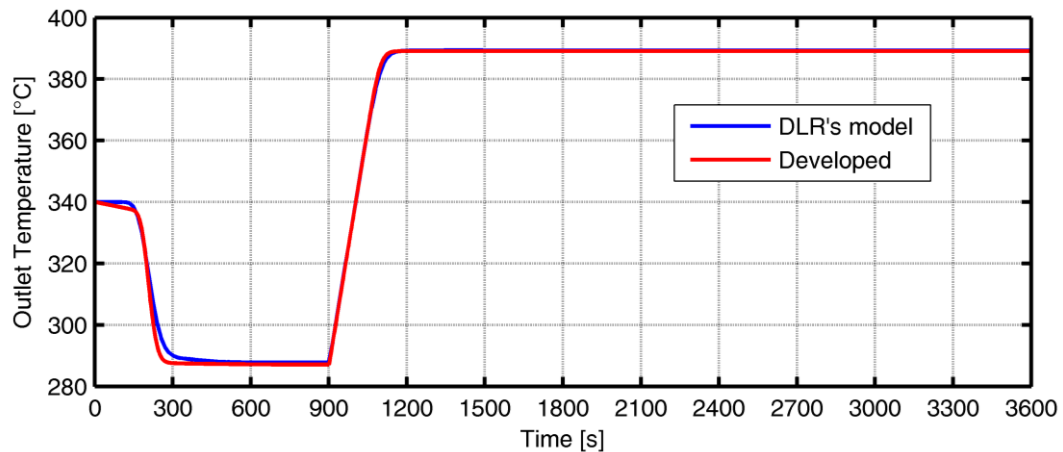


Figure 4.8 Outlet temperature of loop#1 (test case 1). Blue line → DLR's model Red line → Developed model.

The outlet mass flow of the loop #1 is presented in Figure 4.9, showing the comparison between the DLR's model (blue line) and the developed model (red line).

Looking at the plot, at the very beginning of the simulation, the outlet mass flow of DLR's model shows a steep increase that is due to the initialization of the problem. After this few seconds, the mass flow rate of the two models is the same and this point can be considered as the real starting time of the comparison. The first flat zone is reached when the system has a temperature equal to the steady state one. The little difference in the outlet mass flow is due to the different condition with respect to the sizing condition; in particular, the solution of the hydraulic problem leads to a mass flow rate that shows differences among the loops of the solar field that will be slightly unbalanced. The increase in temperature due to the EDNI step causes an increase of HTF temperature and consequently a negative gradient of density. Taking into account the relation expressed in section 4.3.3, the mass flow at the outlet is higher than the mass flow at the inlet. Once the new steady state condition is reached, the gradient of whole system density becomes zero and the mass flow will reach exactly the value of the sizing condition.

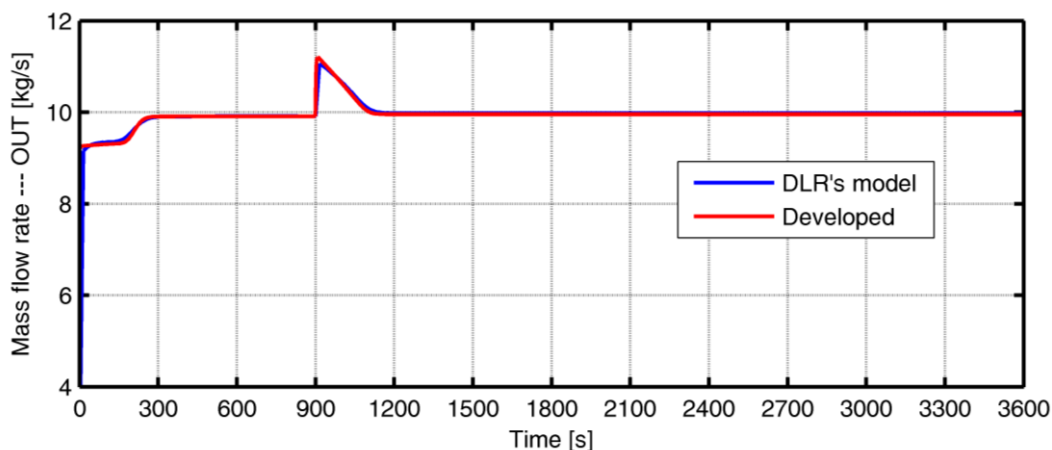


Figure 4.9 Outlet mass flow of the loop#1 (test case 1). Blue line→ DLR’s model Red line→Developed model.

4.3.4.2 Steps profile of both EDNI and mass flow rate

The second test case aims to study the response of the whole solar field to a more complex time profile of both the EDNI and mass flow rate. In particular, the inlet mass flow profile follows the profile of DNI with the aim of maintaining a constant outlet temperature. Operatively, for each EDNI, the mass flow circulating in each the loop is calculated by a steady-state thermal model; as it is possible to notice from the figure below, the relation between the HTF mass flow and EDNI is quasi-linear proportional.

Figure 4.10 shows the DNI and the mass flow profile that are characteristic of the current test case.

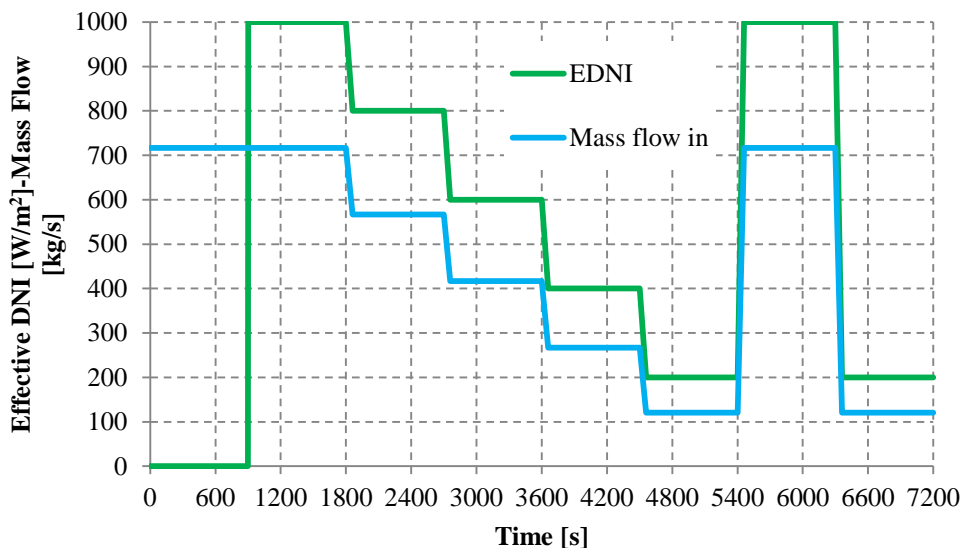


Figure 4.10 EDNI profile combined with total mass flow rate profile (test case #2)

The comparison in Figure 4.11 shows a good agreement in the outlet temperature prediction. In particular, the aim to maintain the same outlet temperature is completely reached, showing that a proportional variation of mass flow rate can be a simple regulation strategy that, for this test case, gives good control results of the outlet HTF temperature.

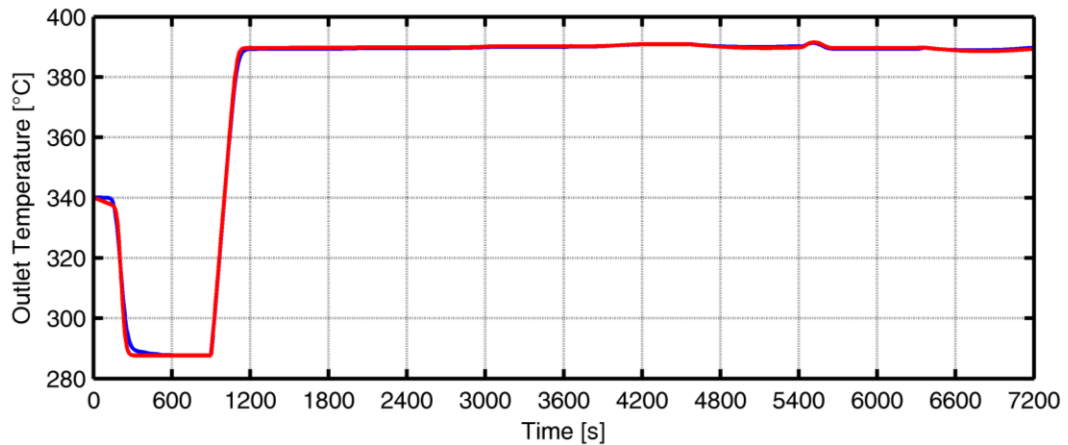


Figure 4.11 Outlet temperature profile of the loop#1 (test case #2)

4.3.4.3 Perpendicular disturbance front

The third test case considers the movement of a shading front that covers symmetrically all the solar field. A view of the shading profile is shown in Figure 4.12 (left) while the graphical view of the front movement over the solar field is at the right side of the picture. The modelling of the shading profile is obtained with the use of a series of rectangles that obscure completely the sun, moving with a speed of 1 m/s as shown in the figure below. The initial distance of shading front from the solar field is set to 1800 m and the distance between successive rectangles is 100 m.

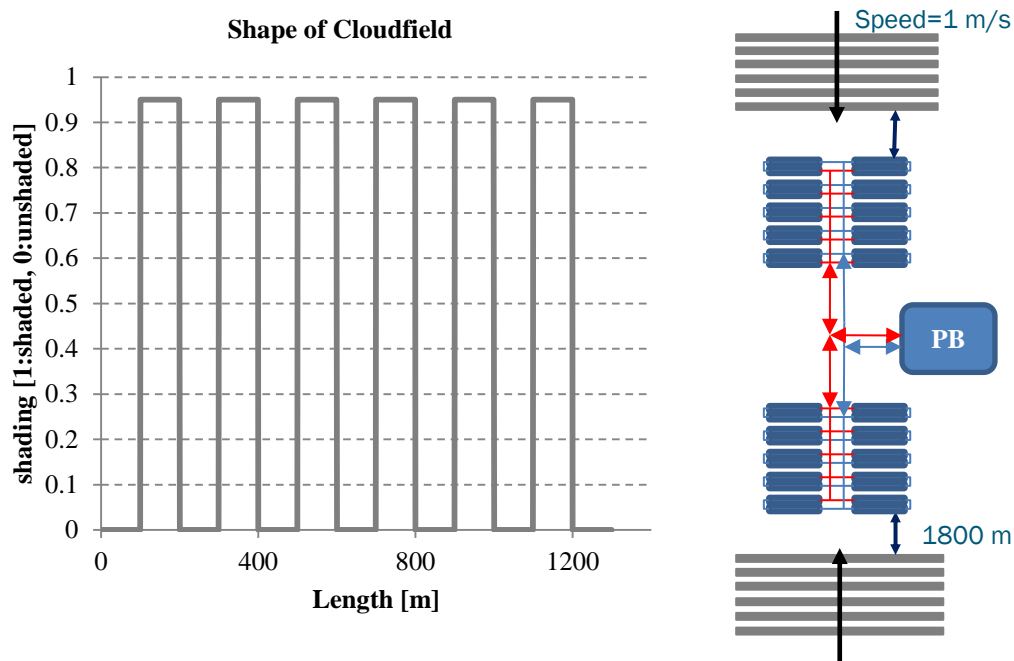


Figure 4.12 Shading profile of test case #3 (left). Drawing of the front movement (right). The tracking axis of the SCA is oriented in N-S direction.

To increase the level of flexibility, the user can set the specific dimension (length and width) and the movement vector (speed and direction) of the disturbance. For simplicity, the movement of each rectangle is modelled as a uniform linear motion.

In order to simplify the calculation of intersection with the discretized segments (that are represented as rectangle see Figure 4.13), the rectangular shape to represent the shading disturbance is chosen. Since the shade movement is continuous, the rectangle can shade totally or partially the collector absorber segments causing a decrease in the concentrated solar energy.

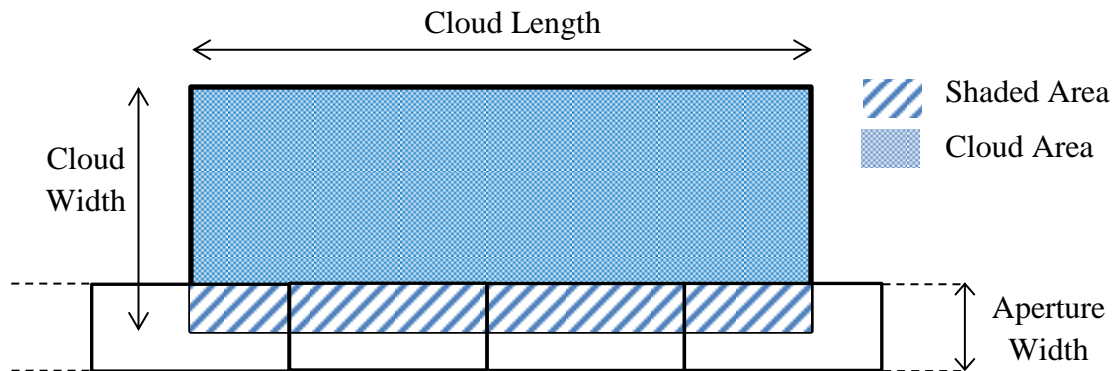


Figure 4.13 Drawing of a shading rectangle with aperture segments of a loop

The outlet temperature of each loop is presented in Figure 4.14; the DLR's model prediction is at the top whereas the results of the developed model is at the bottom of the figure. Because of the symmetrical movement of the disturbance, the loop behavior reflects this kind of condition therefore 18 temperature series are identifiable (opposite loops see the same conditions).

The movement of disturbance in E-W direction caused the temperature profile to be translated in time as underlined in the figure below.

After the initial flat temperature zone, the partial shading of the loops produces a characteristic shape of the signal temperature. In particular, considering each loop, it is possible to identify the first linear decrease due to the initial covering and the trend change when the rectangle moves away.

The increase of temperature is due to the solar energy impinging the loop during the unshaded situation; the temperature increase is stopped by the next shading rectangle that covers the loop. This behavior is repeated for each shading rectangle giving a pseudo sinusoidal signal shape. It is important to underline that, during this test case, no stationary condition is reached when the shading front is acting.

The small temperature increase, enlightened in a red box, is caused by the mass flow unbalance produced by the difference in temperature of each loop. Taking into account the effect of the first rectangle, the density of the last loop increases (the HTF temperature decreases) with a consequent rise of the mass flow rate circulating in this loop. The remaining loops will have a mass flow lower than the on-design one and for that reason, the outlet temperature of them rises. From a qualitative point of view, the two models present the same behavior of the outlet loop temperatures.

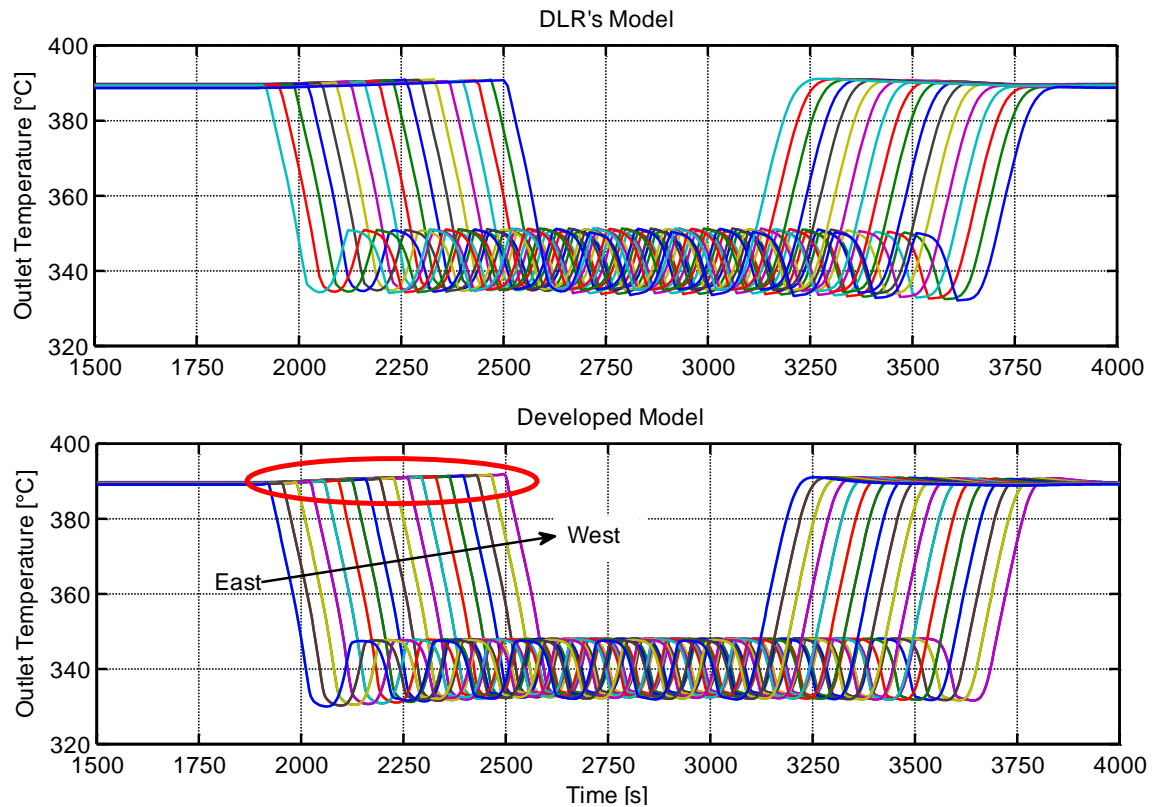


Figure 4.14 Temperature outlet of each loops of the solar field (time range 1500 s – 4000 s). The DLR's model (top) and the developed model (bottom).

To show the difference between the two models, a zoom of the temperature oscillations of the nearest loop to the power block (see. Figure 4.12) predicted by the DLR's model and the developed transient model is presented in Figure 4.15. The small discrepancy in outlet temperature, before the cloud front reaches this loops, is probably induced by small difference in hydraulic network assumption (i.e. different pressure drop correlations). The small differences of outlet temperature can be explained by different shape of the shading functions between the two models. In particular, DLR's model is discrete (0-1) while in the developed model the value of segments shading is continuous.

Focusing the attention on the temperature oscillations zone, it is possible to notice how the two models show a good agreement in predicting both the temperature oscillation amplitude and the frequency thus leading to conclude that the implemented model can be a reliable tool to describe transient effect of linear CSP solar field.

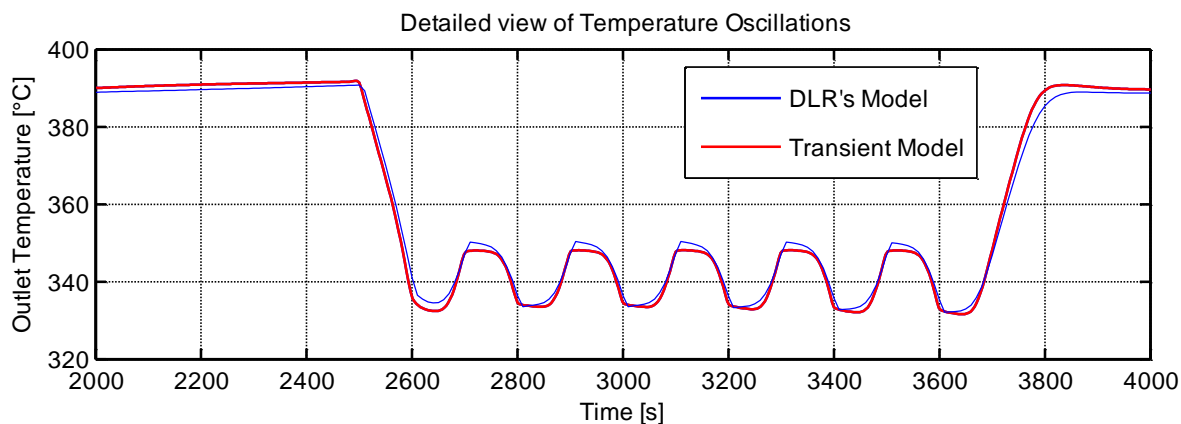


Figure 4.15 Particular view of the temperature oscillations predicted by the DLR's (blue line) model and the model developed in this thesis (red line).

In addition to the outlet loop temperature, the expansion tank temperature calculated by the developed model, is presented in Figure 4.16. The expansion tank temperature, starting from a value of 290°C, shows a first increase before the passing of the cloud front mainly caused by the HTF contained in the hot header (at an initial temperature of 390°C). The passage of the cloud disturbance produces a cooling of the tank without temperature oscillation; this fact is due to the thermal inertia of the hot header and especially of the expansion tank system that implies a strong dumping effect on the temperature.

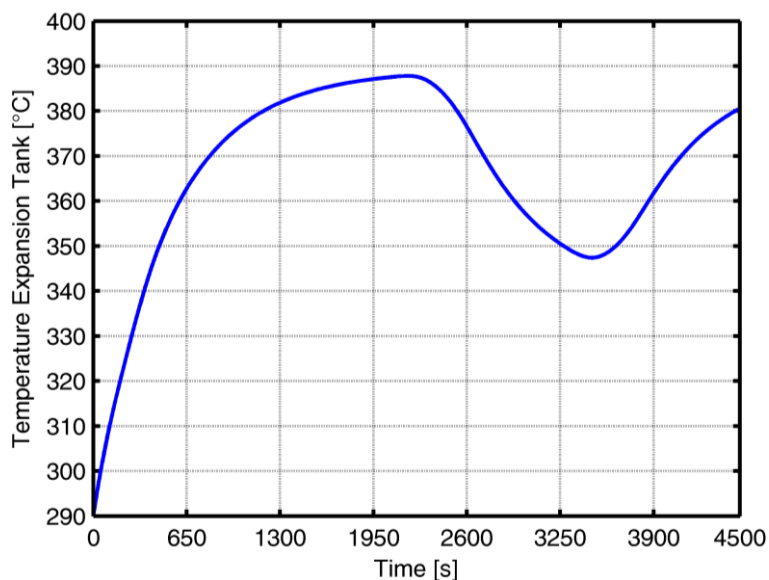


Figure 4.16 Outlet temperature of the expansion tank (test case #3).

4.4 Bibliography

- [1] Odeh SD, Morrison GL, Behnia M. Modelling of parabolic trough direct steam generation solar collectors. *Sol Energy* 1998;62:395-406.
- [2] Lippke F. Simulation of the part-load behavior of a 30 MWe SEGS plant 1995.
- [3] Camacho EF, Rubio FR, Berenguel M, Valenzuela L. A survey on control schemes for distributed solar collector fields. Part I: Modeling and basic control approaches. *Sol Energy* 2007;81:1240-1251.
- [4] Eck M, Hirsch T. Dynamics and control of parabolic trough collector loops with direct steam generation. *Solar Energy* 2007;81:268-279.
- [5] Hirsch T, Eck M, Steinmann W. Simulation of transient two-phase flow in parabolic trough collectors using Modelica 2005;7.
- [6] Ho CK. Computational fluid dynamics for concentrating solar power systems. *Wiley Interdisciplinary Reviews: Energy and Environment* 2013:n/a-n/a.
- [7] Lobón DH, Valenzuela L, Baglietto E. Modeling the dynamics of the multiphase fluid in the parabolic-trough solar steam generating systems. *Energy Conversion and Management* 2014;78:393-404.
- [8] Wendelin T. Soltrace: A new optical modeling tool for concentrating solar optics. *Int Sol Energ Conf* 2003:253-260.
- [9] National Renewable Energy Laboratory. Soltrace Optical Modelling Software 2013.
- [10] Rabl A. Active Solar Collectors and their Applications Oxford University Press, USA; 1985.
- [11] Stuetzle T, Blair N, Mitchell JW, Beckman WA. Automatic control of a 30 MWe SEGS VI parabolic trough plant. *Sol Energy* 2004;76:187-193.
- [12] Forristall RE. Heat Transfer Analysis and Modeling of a Parabolic Trough Solar Receiver Implemented in Engineering Equation Solver National Renewable Energy Laboratory; 2003.
- [13] Gnielinski V. New equations for heat and mass transfer in the turbulent flow in pipes and channels. *NASA STI/Recon Technical Report A* 1975;75:22028.
- [14] Manzolini G, Giotri A, Saccilotto C, Silva P, MacChi E. A numerical model for off-design performance prediction of parabolic trough based solar power plants. *J Sol Energy Eng Trans ASME* 2012;134.
- [15] Ratzel AC, Hickox CE, Gartling DK. Techniques for Reducing Thermal Conduction and Natural Convection Heat Losses in Annular Receiver Geometries. *Journal of Heat Transfer* 1979;101:108-113.
- [16] Bejan A, Kraus AD. *Heat Transfer Handbook J*. Wiley: New York; 2003.
- [17] Churchill SW, Chu HH. Correlating equations for laminar and turbulent free convection from a horizontal cylinder. *Int J Heat Mass Transfer* 1975;18:1049-1053.
- [18] Zukauskas A, Ziugzda J. Heat transfer of a cylinder in crossflow 1985.
- [19] Binotti M. Linear Fresnel reflectors : study of the technology and steps toward optimization 2013.

- [20] Zaversky F, Medina R, García-Barberena J, Sánchez M, Astrain D. Object-oriented modeling for the transient performance simulation of parabolic trough collectors using molten salt as heat transfer fluid. *Solar Energy* 2013;95:192-215.
- [21] Winning HK, Coole T. Explicit Friction Factor Accuracy and Computational Efficiency for Turbulent Flow in Pipes. *Flow, Turbulence and Combustion* 2013;90:1-27.
- [22] Burkholder F, Kutscher CF. Heat Loss Testing of Schott's 2008 PTR70 Parabolic Trough Receiver National Renewable Energy Laboratory; 2009.
- [23] Hindmarsh AC, Brown PN, Grant KE, Lee SL, Serban R, Shumaker DE, et al. SUNDIALS: Suite of nonlinear and differential/algebraic equation solvers. *ACM Transactions on Mathematical Software (TOMS)* 2005;31:363-396.
- [24] Serban R. SundialsTB v. 2.4.0, a Matlab interface to SUNDIALS 2012.
- [25] Vasquez Padilla R. Simplified Methodology for Designing Parabolic Trough Solar Power Plants 2011.
- [26] Modelica and the Modelica Association. Modelica website 2013.

5 Solar Field Investigation

Once the simulation model was implemented and discussed, a test case is selected in order to infer some considerations about the behavior of a parabolic trough solar field during the passage of a cloud front.

In order to develop a transient analysis that has, as main goal, the understanding of solar field behavior during the passage of a cloud front, some assumptions have to be made.

To fulfill the investigation of transient effects the following steps have to be followed:

1. A selection of the cloud front characteristics that are requested to simulate the interaction between the cloud and the solar field.
2. A detailed solar field sizing is necessary and to reach this purpose the model described in Chapter 3 can be adopted.
3. Using the solar field thermal model introduced in Chapter 4, it is possible to obtain information related to time variation of temperatures and mass flows in the solar field network.

In the next sections, the input data and the results related to the steps above are presented. As regards the results analysis, the attention is focused on underlining the peculiar behavior that can be captured adding the modelling of transient effects that are neglected in the quasi-steady state approach. In addition, the developed model is intended to be useful to understand the effect of the accuracy level used and to compare some simple control strategy.

In agreement with the choice made in the previous chapter, the solar field has the same characteristics reported in Chapter 3.

5.1 Test-case selection

As underlined by [1], the characterization of a cloud front can be defined by the velocity, cloud movement direction, opacity, frequency and shape. These parameters influence how the solar field is covered and, therefore, how the solar field reacts in terms of mass flow distribution and temperatures. A qualitative forecast of the effect of this parameter on the behavior is presented below.

In particular, cloud velocity is associated with the level of transient implying that the faster the cloud front the stronger the thermal response of solar field. The cloud direction affects the way the system responds, for example, a cloud front that covers symmetrically the field will lead to a situation characterized by a flow distribution reflecting the symmetry of the disturbance. On the contrary, the absence of any symmetry pattern in the disturbance increases the level of complexity. As regards the cloud front frequency, this parameter affects, in analogy to the cloud direction, the shape of response. The cloud opacity can range theoretically from zero to one. For instance in [2], different cloud categories are identified depending on the attenuation level of solar radiation (i.e. a cirrus can have an attenuation level of 80 % whereas a cumulus can transmit more than the 60

% of the sunlight). The cloud identification is completed with the shape and the sharpness of the edges. From a qualitative point of view, the effect of the shape can be assimilated to the direction one, whereas the sharpness of the edge impacts the velocity of the transient response (i.e. strong change in opacity due to sharp edge implies a fast transient). Complete cloud data are difficult to find in literature thus requesting a dedicated experimental setup to achieve the data necessary to characterize the location. Starting from the data presented in [3] related to Tucson (AZ), a statistical analysis was performed by [1] taking into account the size, speed and frequency that characterized the cloud front. Figure 5.1 shows the results of this data processing that identify the mean cloud that can be considered for the following study. In particular, a mean size of 3.51 km and a mean speed of 4.64 m/s are inferred. As regards the direction of the disturbance movement, no information are reported in [1] thus requesting a further analysis in order to identify the cloud direction.

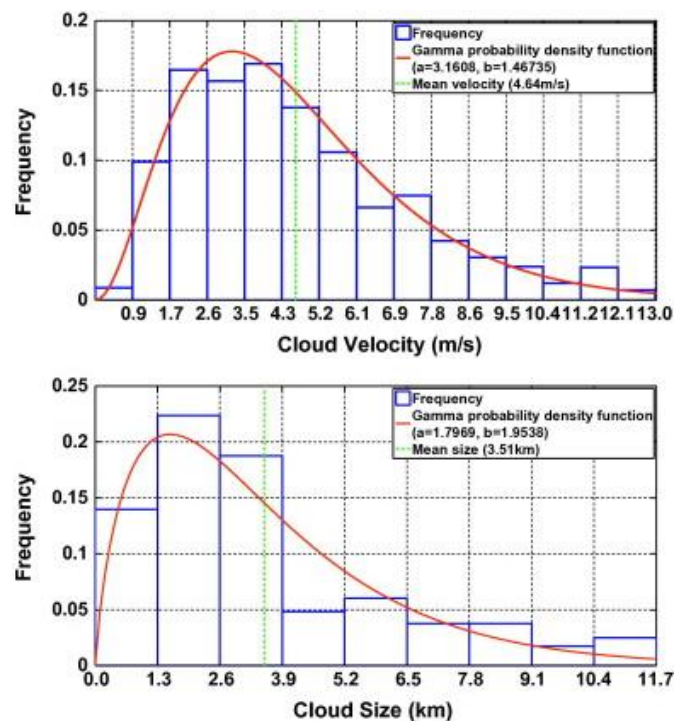


Figure 5.1 Frequency analysis of direction and speed of clouds [1]

Considering TMY-3 data for Tucson (AZ) [4], the more probable cloud direction is assumed to be equivalent to the mean wind direction calculated during sun time ($DNI > 0$) equal to 219° (S-W). In accordance to the approach presented in Chapter 4, the cloud is idealized by a square, which obscures completely the mirrors; besides simplifying the simulation this choice represents one of the worst cases that can be investigated because of the sharp edges and the high opacity value. As regards the speed and the direction, the values coming from the study previously presented are considered. In order to diminish the computational time the square length is equal to 2 km; this approximation is believed not to influence the main considerations about simulation results. The effective direct

normal radiation in clear sky conditions is set to the design value of 1000 W/m^2 . The cloud front characteristics that are taken as test-case are summarized in Table 5.1.

Table 5.1 Cloud characteristics considered in the study of solar field transient response

<i>Cloud Characteristics</i>		
Parameter	Value	UDM
Cloud mean size	2.0	km
Shape	Square	-
Opacity	1	-
Speed cloud	4.64	m s^{-1}
Direction	219	$^\circ$
Clear Sky EDNI	1000	W m^{-2}

The solar field physical dimensions are fundamental to predict correctly the shading disturbance movement. The solar field dimensioned by the optimization algorithm presented in Chapter 3 is considered for this study (see Table 3.4). In Figure 5.2 the main dimensions are graphically reported. In particular, both the power block and the balance of plant (e.g. electrical substation etc.) occupancy are estimated roughly from the satellite views of CSP plant around the world, available in Google Earth[®] [5].

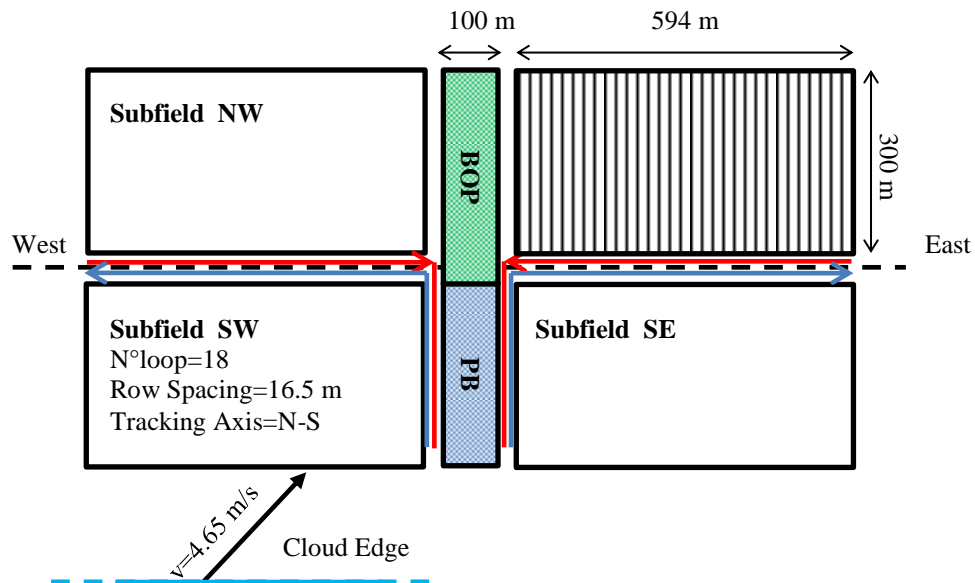


Figure 5.2 Layout of the CSP plant studied (tracking axis of PT is oriented in N-S direction)

To avoid excessive computational time, the simulation time is set, where not specified differently, to 3600 s.

5.1.1 Shading square trajectory

The results presented in the next sections refer to the situation and the assumptions described above. Before showing the outputs, to understand better the simulation results,

a graphical view of the shading trajectory is presented in Figure 5.3 with some characteristics situations underlined. In particular, it is possible to identify six different phases of the shading process that differs in the reciprocal interaction between the square cloud and the CSP plant:

0. The cloud, due to its initial distance to the solar field edge, has not reached the parabolic trough field yet. Considering the most Southward edge of the solar field as the origin of an imaginary Cartesian system reference, the initial position of the nearest cloud edge can be expressed by $[-300;-500]$. The disturbance reaches the solar field approximately after 170 s.
1. The square shades partially the solar field; in particular, the shading effect is non-symmetrical as regards both the macro-sections (e.g. North, South) and the loops of the same section.
2. The shading disturbance covers the whole West section and a part of the East section. The loops of East section are covered symmetrically during time.
3. The square, due to its physical dimensions, that are bigger than the solar field one, completely covers the parabolic mirrors field.
4. The square movement exposes both the West and East section
5. The cloud leaves the solar field (approx. 615 s after the starting time) that is completely irradiated by the sun

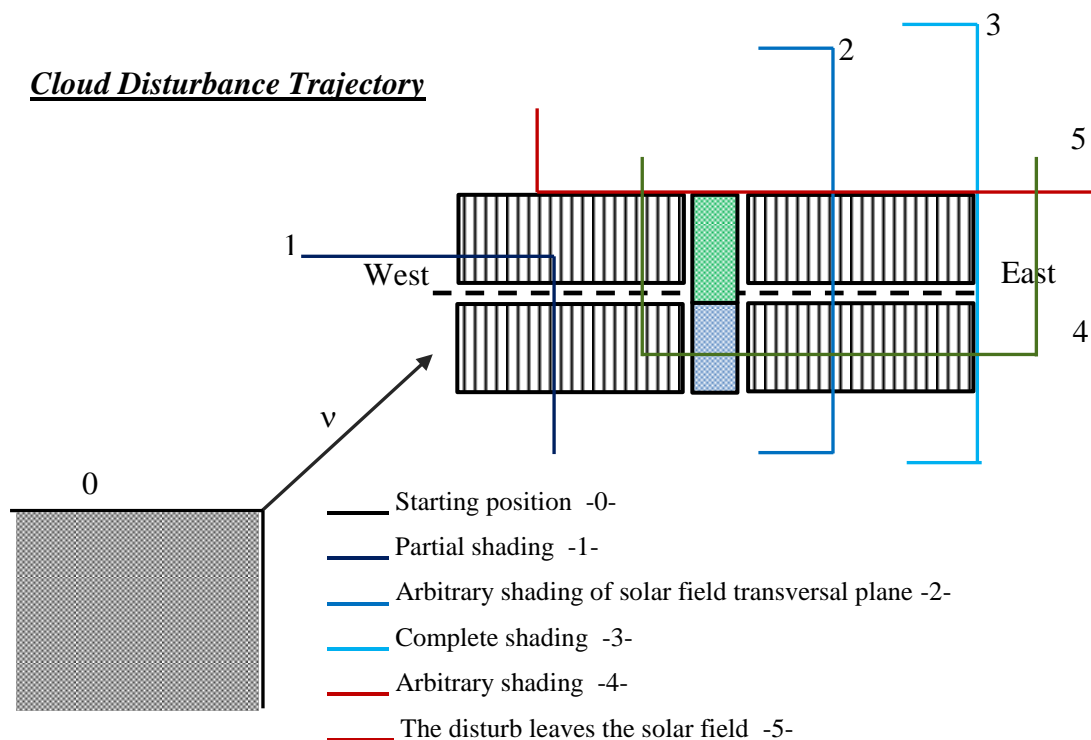


Figure 5.3 Shading trajectory. Note that for simplicity purpose the figure is not drawn to scale.

In the next section that deals with the simulation results about thermo-hydraulic behavior of solar field, the different phases described above can be approximately identified considering the shape of the thermal response.

5.2 Effect of total mass flow control

The operating parameter that can be set is the total HTF mass flow processed by the pump. Referring to the test case selected, two simple mass flow control strategies are considered in order to identify possible response differences. This first study considers the solar field behavior only, in particular the inlet solar field temperature is kept constant to 290°C; this choice aims at giving a preliminary idea about the main characteristics of the thermo-hydraulic response of the parabolic trough field. In the following subsections, the two cases are described and with the help of graphical representation of results, the response of solar field is analyzed.

5.2.1 Constant mass flow (case#1)

The first case (case#1) considers the simplest situation. The HTF total mass flow is kept constant during the disturbance passage; in this case, the plant operator does not care of the cloud and does not modify the operating parameters of the solar field. Figure 5.4 shows the temperature behavior during time of the expansion tank and at the outlet of the last hot header pipe segment, which connects the solar field to the expansion vessel. From the comparison between the two trends, it is possible to notice the strong influence of the expansion vessel in dumping the temperature oscillation; this effect derives from the initial choice of positioning the expansion system at the hot side of solar field. As previously said, CSP plant with thermal storage implements the expansion vessels in the cold side leading to higher temperature oscillations that can be faced by the TES operating strategy. The temperature of the last hot header pipe can represent with good approximation the behavior of a solar field with the expansion tank placed on the cold side.

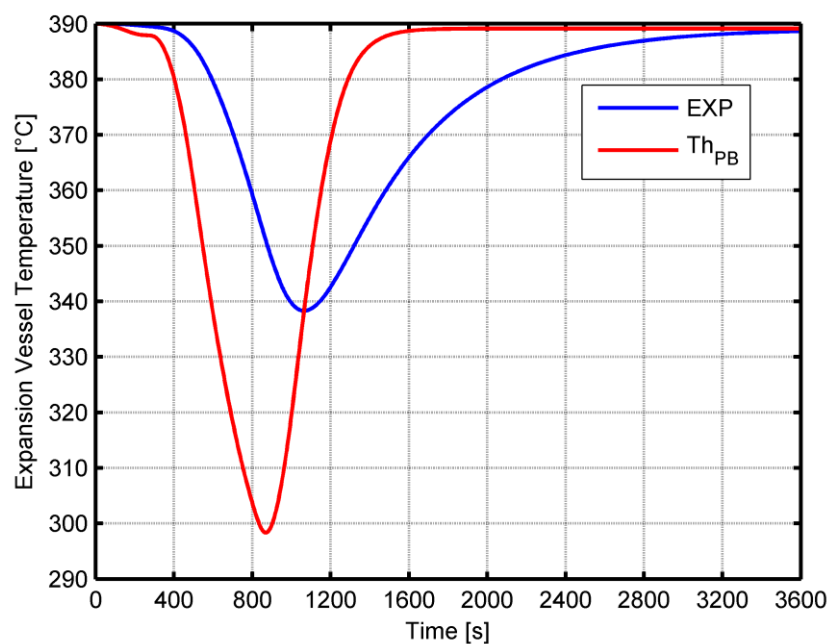


Figure 5.4 Temperature of expansion tank (blue) and of the last SF pipe segment that delivers the HTF to the expansion tank (red) (case#1).

Because of the piping network layout, the solution of the thermal-hydraulic problem leads to mass flow unbalance respect to the on-design condition. Due to the decrease of impinging solar energy, the temperature of shaded area decreases and consequently the change of HTF properties, mainly the density, causes the mass flow split fraction between West-section and East-section to change. In particular, the colder is the section the higher is the mass flow that is delivered to this zone as well described by Figure 5.5 (referred to West section). From the mass flow profile, shown in the figure below, it is possible to notice how the asymmetrical covering involves an oscillating mass flow in West section. As shown in Figure 5.3, the cloud covers the West section first thus leading to an increase in the mass flow circulating. Following the cloud movement, the mass flow distribution between the solar field sections is a good representation of the shading movement presented in Figure 5.3; the plant operator can use the shape of mass flow signals to recognize a misdistribution of the impinging energy (e.g. partial cloud cover, broken mirrors etc.).

Because of the mass conservation law applied to the whole system the West section mass flow is complementary to the East section one.

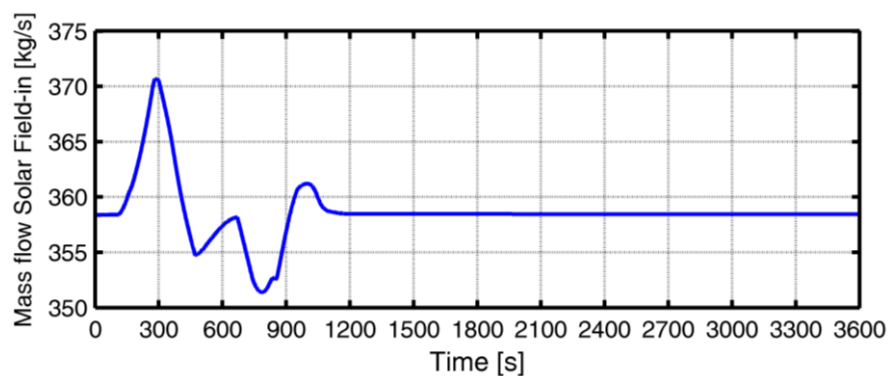


Figure 5.5 Mass flow rate in the West section of the solar field.

The same explanation given above for the mass flow distribution in solar field section can be extended and proposed again to describe the mass flow distribution among the loops. The thermo-hydraulic behavior of the loops produces the outlet temperature trend shown in Figure 5.6.

Taking into account Figure 5.3, some characteristic situations that occur during the simulation time can be identified. The cloud does not influence the first ca. 170 s and the outlet temperature is equal in each loops; the small oscillation is due to the initial conditions that are not exactly equal to the steady state. This zone is presented in both the West and East section and, in particular, it is delimited by the effect of the incoming cloud that causes the progressive reduction in outlet temperature. The longer uniform period, present in the East section, is due to the time needed for the cloud to reach this section and the slight temperature increase derives from the lower mass flow split to the east section (as reported in Figure 5.5).

Taking into account that the lower is the temperature the lower are the receiver heat losses, the temperature decrease zone reaches a flat zone because the inlet temperature is

constant to 290°C. Once the impinging solar energy begins to increase, the loop temperature rises until reaching the second flat zone coincident with the steady state condition. The different trends of the temperature loop presented in figure below are justified by the non-symmetrical shading effect.

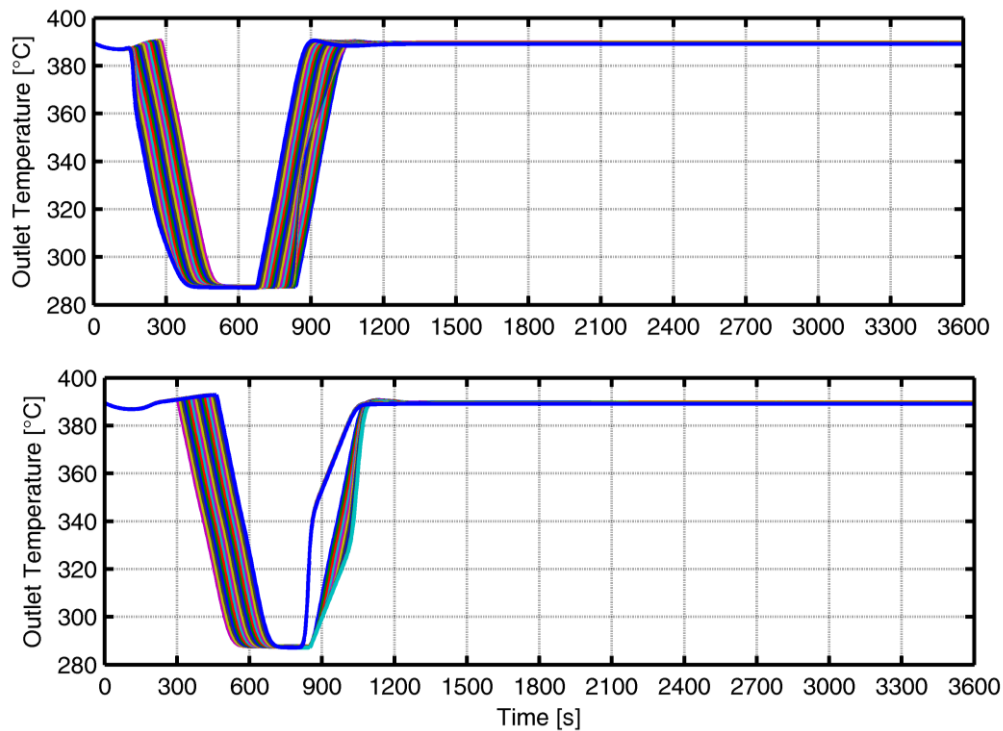


Figure 5.6 Loop outlet temperature of selected loops. Both West (top) and East (bottom) sections are reported.

With the aim of describing better the shading effect on the loop outlet temperature, a zoom of the figure above, showing the time range 100 s – 1200 s, is presented in Figure 5.7. The temperature computed at the loop outlet is shown both for the West section (top) and for the East section (bottom). Focusing on the East section of the solar field, the cool-down phase shows a characteristic trend that is a direct consequence of the disturbance movement reported in section 5.1.1; in particular the outlet temperature shows the same gradient for each loop because the “shading square” covers the East section in a progressive and symmetrical way in the North-South direction. Due to the shade symmetry only eighteen trends (representing a subsection half) can be identified. As regards the heat-up phase, a different situation occurs and, as labeled in the plot space, the un-shading process is characterized by non-uniformity between the South and North subsection that implies a remarkable difference in the outlet temperatures behavior. In particular, the loops of South subsection are uncover in the same way (along the S-N direction) thus leading to the same temperature behavior as enlightened in the Figure 5.7. As regards the North subsection, the uncover phase occurs both in W-E and S-N direction thus implying more complex situation in which the W-E disturbance movement is reflected by the different detachment time of single series form the lower temperature series. Focusing the attention on the West section, a more complex response occurs due to the asymmetry in the solar field covered area during both the cool-down and heat-up

phase; in particular, the temperature trend of loops with the same irradiation conditions tend to be very similar (the difference is due to the non-linearity of hydraulic network).

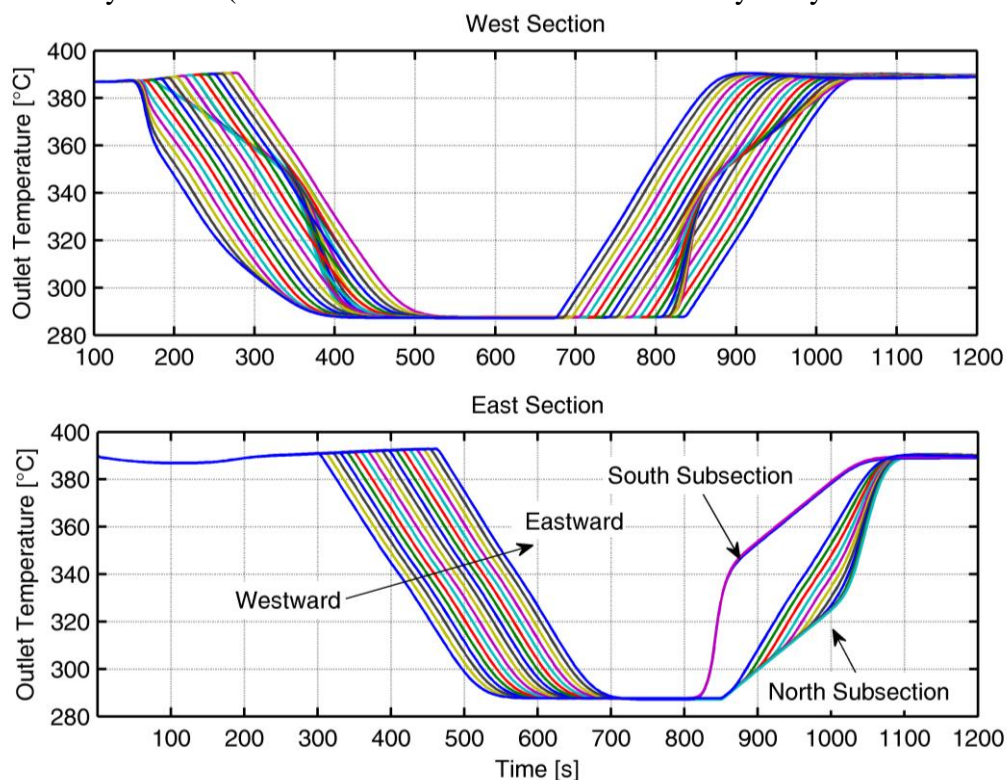


Figure 5.7 Detail of the time interval 100 s – 1200 s. Both West (top) and East (bottom) sections are reported.

5.2.2 Mass flow proportional to impinging solar energy (case#2)

In the second case (case #2), the influence of total mass flow change is taken into account with the aim of extrapolating some peculiar behavior that can be captured with the developed model. The total HTF mass flow is varied following the total solar energy available for concentration. To simplify the modelling, the total mass flow follows linearly the impinging solar energy until a minimum value set to 25% of the on-design value as suggested by [6]. In Figure 5.8 the total mass flow delivered by the HTF pump is shown. The initial flat zone denotes that the shading disturbance has not reached the solar field yet. The HTF mass flow ramp down, due to the progressive cover, reaches the minimum value of 25% design value. After a zone of constant mass flow, the following phase is an evidence of the gradual uncovering until the clear sky condition (on-design).

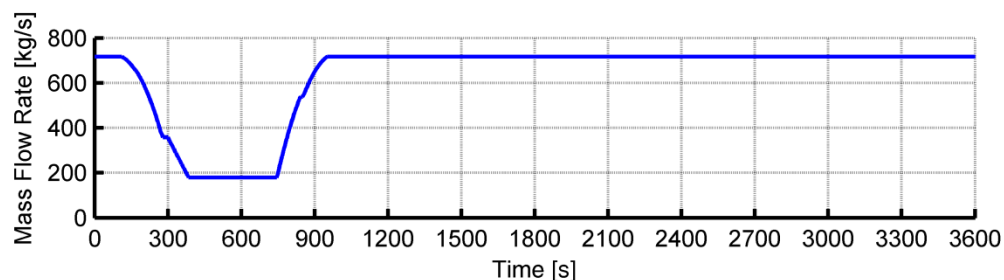


Figure 5.8 Total HTF mass flow during time.

It is worth to notice that this approach is commonly used, with some variations, in quasi-steady approach in order to simulate an idealized control of HTF temperature.

Thanks to this case study, the main difference between the quasi-steady approach and an approach that considers the transient effects can be identified.

In particular, the common approach, besides not considering the transient effect, does not take into account the spatial extension of the solar field neglecting the effect of non-uniform weather boundary conditions. The physical extension of both the solar field and the “square cloud” play a fundamental role in the shape of thermal behavior.

Considering the control strategy of HTF total mass flow, the decrease of impinging solar energy implies a reduction in HTF mass flow delivered by the main pump that influences the hydraulic performance of each loop (from a qualitative point of view the loop mass flow is lower). The finite cloud dimension and its motion leads to the simultaneous presence of both shaded and irradiated loops; focusing the attention on an irradiated loop it is straightforward to understand that the lower loop mass flow together with a high radiation causes a temperature level higher than the on-design one. The change of HTF thermophysical properties, mainly density dependence on temperature, enhances this effect as previously described in section 5.2.1.

Figure 5.9 shows the outlet temperature of each loop during time indicating both the high level of asymmetry of the loop thermohydraulic reaction and temperature peaks.

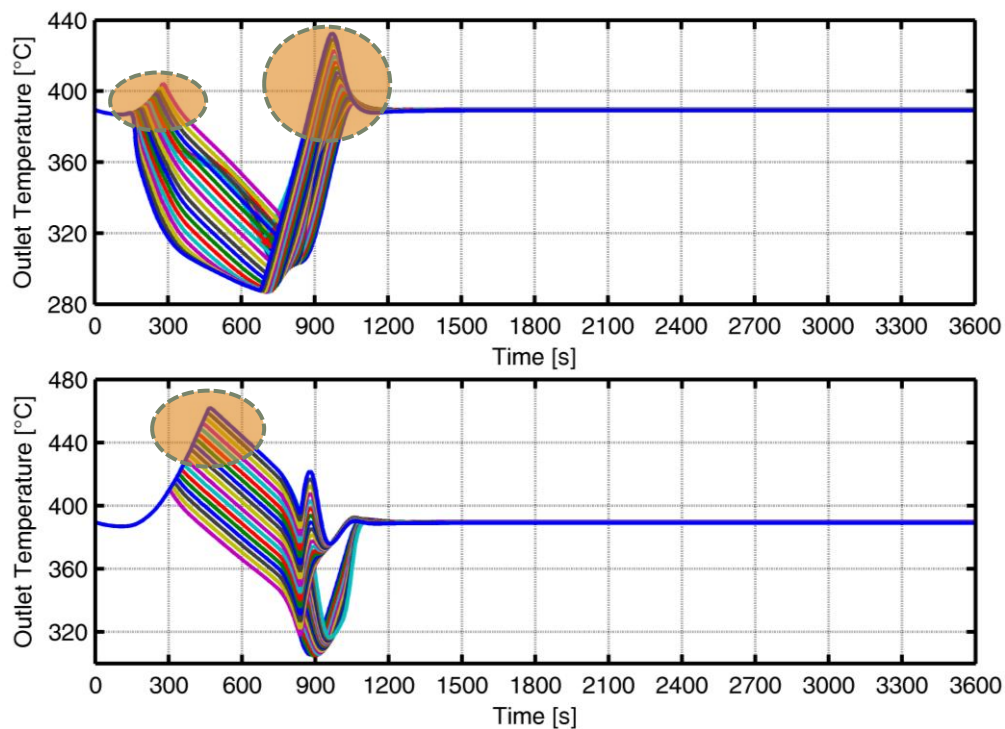


Figure 5.9 Temperature at the loop outlet of both the West section (top) and East section (bottom).

The overheating of irradiated loops, enlightened in Figure 5.9, can jeopardize both the HTF thermal stability and the absorber coating integrity. To comply security constrains, the defocusing of parabolic mirrors is implemented in the code. From an operative point

of view, the defocussing of parabolic trough mirror consists in the generation of an incidence angle in the transversal plane in order to reduce the intercept factor. A ray-tracing simulation, using the Soltrace tool [7] with the assumptions resumed in Table 5.2, is performed in order to assess the influence on intercept factor of transversal incidence angle that is the main parameter to defocus the parabolic mirror. The obtained trend (see Figure 5.10.), showing an intercept factor of about zero for a defocussing angle of 1.5°, validates the assumption of idealized (instantaneous) defocusing action.

Table 5.2 Ray tracing assumption to study the effect of defocussing angle on intercept factor.

<i>Ray Tracing Assumptions</i>		
Parameter	Value	UoM
Concentrator Technology	ET-150	-
Aperture width	5.76	m
Absorber diameter	70	mm
Function Error Distribution	Gaussian	-
σ_{sun}	2.8	mrad
$\sigma_{\text{specularity}}$	0.5	mrad
σ_{slope}	3.00	mrad

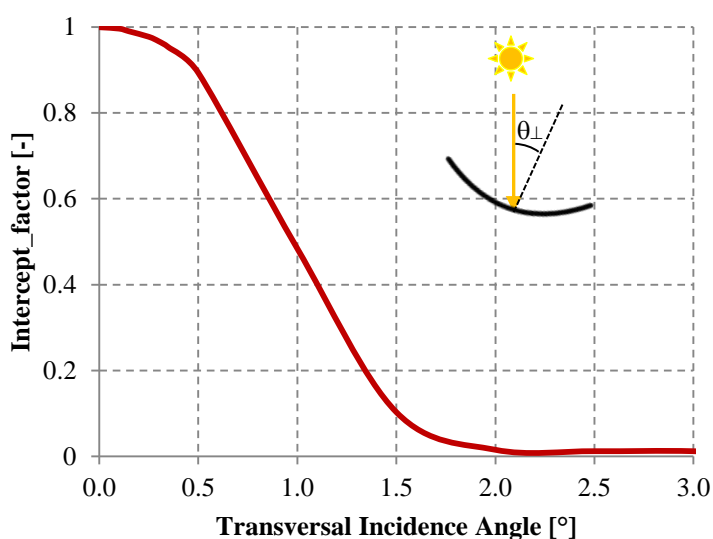


Figure 5.10 Intercept factor of a PT function of the transversal incidence angle (Eurotrough-150 “ET-150”) concentrator with absorber tube diameter equal to 70 mm).

Regarding the maximum temperature threshold, an arbitrary value inferior to 400°C can be chosen. The simulation results presented in the next sections, following a conservative approach, refer to a maximum temperature limit of 393°C; beyond this value the defocusing operation starts.

Figure 5.11 enlightens the defocussing system behavior that guarantees a safe operation of the solar field. In particular, the comparison between Figure 5.9 and Figure 5.11 identifies well the effect on the outlet loop temperature (that represents presumably highest temperature zone) of the activation of the defocusing control.

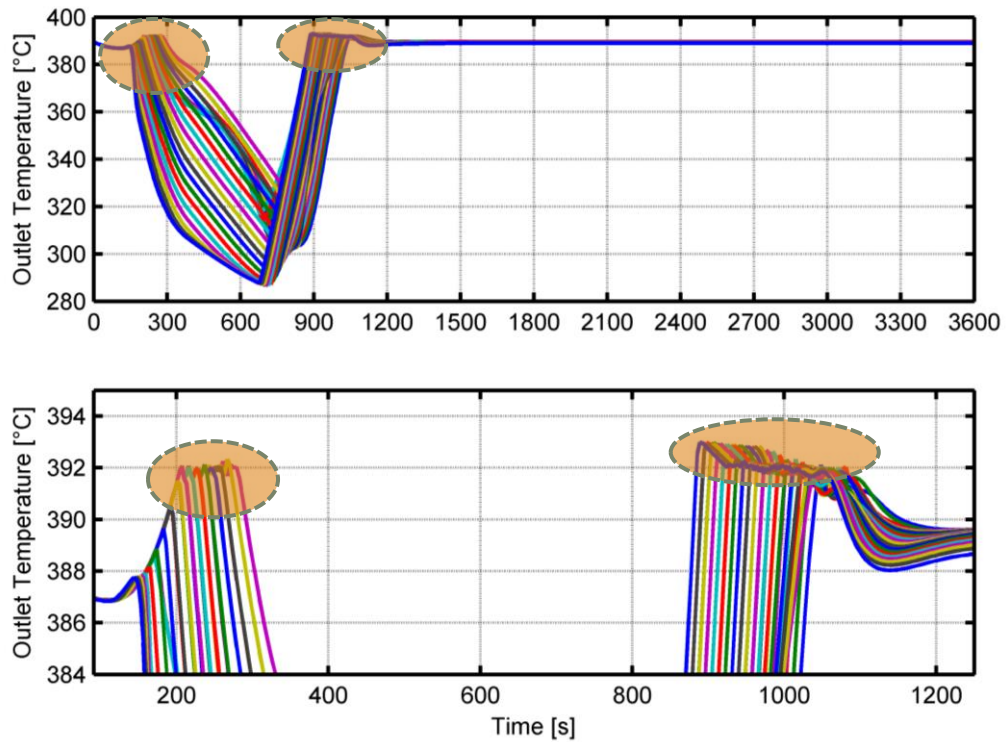


Figure 5.11 Effect on loop outlet temperature of defocusing operation.

In Figure 5.12 the temperature behavior of the expansion tank and at the outlet of the last hot header pipe segment are shown.

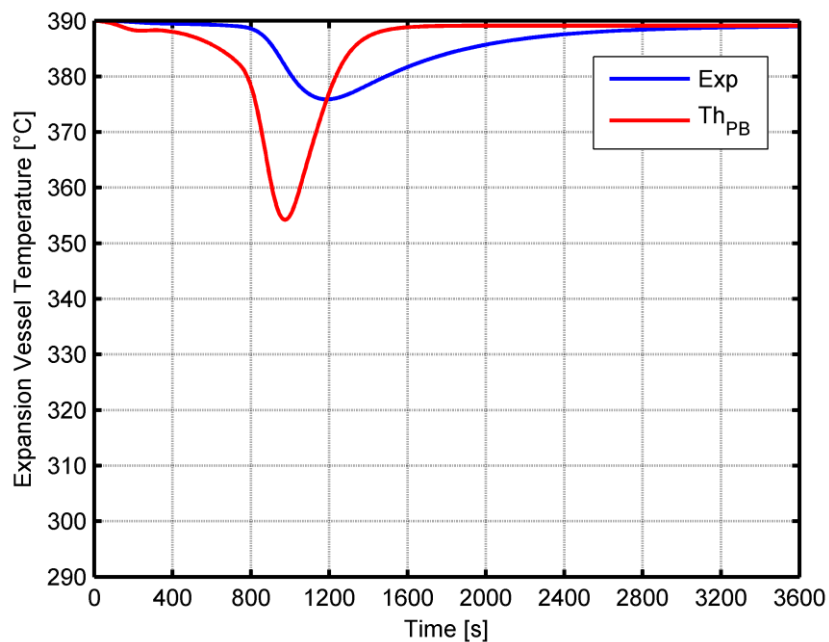


Figure 5.12 Temperature of expansion tank (blue) and of the last SF pipe segment that delivers the HTF to the expansion tank (red) (case#2).

Comparing Figure 5.4 (case #1) and Figure 5.12 (case #2) the main difference that can be noted resides in the amplitude of the temperature oscillation that is smaller for the current

case because of the lower mass flow during dark period. In addition, a delay in the temperature trend can be appreciated because of the higher HTF travel time that is a consequence of the reduced mass flow rate. It is important to underline that the requested defocussing action represents an energetic penalty decreasing the attractiveness of this solution.

5.3 Power block addition

The two cases described above concentrate their attention on the solar field only, considering the absence of the power block and assuming a constant HTF temperature at the inlet of solar field (290°C). In this test case (case#3) the power block section is considered through a simple model in order to evaluate the change in simulation results. Initially, the next subsections deal with the definition of the power block and successively with both the component modelling in the transient suite and simulation results obtained with the addition of the power block section.

5.3.1 Power Block modelling

As described in Chapter 2, the power block receives the HTF mass flow from the solar field and converts the thermal energy in electric energy. Regarding the scale of CSP plant, with particular attention to plants that implement the linear focusing technology, two categories can be easily identified that imply different solutions for the power block section:

1. *Small scale*: this category contains CSP plants with a nameplate electric power output in the range of starting approximately from 10 kW till 5000 kW. The most suitable technology for this size of plants is the Organic Rankine Cycle (“ORC”) as described in detail in [8]. It is important to underline that small scale CSP plants represents a very little share of the energy produced with concentrated solar energy but, as reported in [9], a growing interest in this technology can be noticed (in particular for applications in rural zones).
2. *Big Scale*: the plants belonging to this category have a Multi-MW power capacity typically ranging from 30 MWe to 150 MWe [10]. This category is responsible of more than the 99% of the total electric energy produced with linear CSP plants. As regards the power block technology, a conventional steam Rankine cycle is adopted in the totality of the big scale plants.

In this section, the modelling approach of the power block is presented focusing the attention on both the sizing phase and the part-load performance prediction. The commercial software Thermoflex[®] (“TFX”) is used for that phase exploiting its capabilities to design the plants and to predict in detail the part-load performance of all the components.

In the next parts of this work, the considered power block solution belongs to the second category, even if the same procedure would be used for ORC plant too in case of smaller solar field.

5.3.1.1 Sizing

The first step of the power block study is the sizing of the plant in order to have an idea of the main characteristics of all the components. In Figure 5.13 a reference power block layout is presented. As shown in the figure below, the power block is a common RH steam cycle with a HP turbine inlet steam temperature and pressure of 370°C and 100 bar respectively. As regards the condensing system, a wet cooling tower adopted with a condensing pressure of 0.08 bar. The wet condensing system is the more common choice in CSP plants, even if the growing interest in the minimization of the water consume is leading to consider air condenser as an alternative cooling technique [11]. It is important to underline that power block solution for big scale plant with synthetic oil as HTF presents a high level of standardization and the number of high-pressure feedwater heaters mainly represents the main difference in components layout.

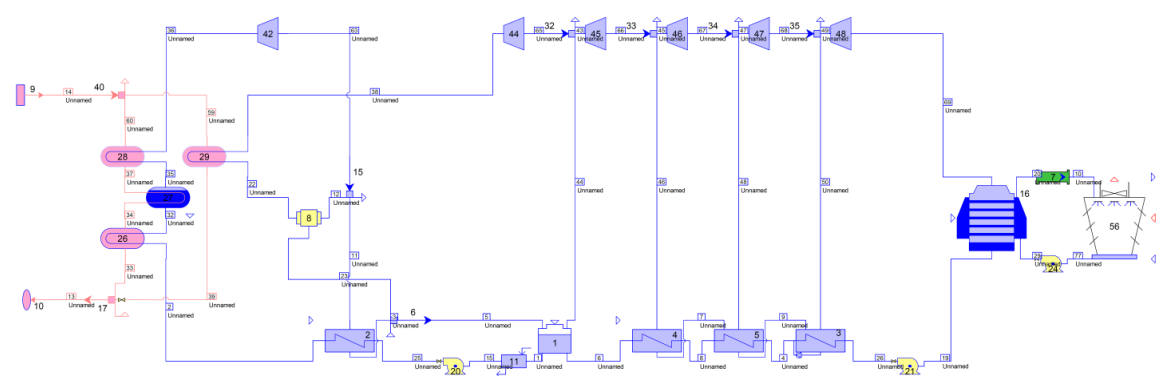


Figure 5.13 Layout of a typical power block section of a CSP plant without thermal energy storage.

The main assumptions related to the power block section and related to the cooling system are summarized in Table 5.3. The values of reported parameters refer to the power block section similar to Andasol I-II [12,13]; in particular the choice of the power block technology is driven by the presence of numerous information sources related to this plant and by the high standardization level that represents [14].

Table 5.3 Main assumptions for the sizing of the power block and the wet cooling system.

<i>Power Block Assumptions</i>		
Parameter	Value	UoM
HP Turbine inlet pressure	100	bar
SH/RH outlet temperature	370	°C
Condensing pressure	0.08	bar
Isentropic Efficiency HP Turbine	85	%
Isentropic Efficiency LP Turbine	87	%
Alternator Electric-Organic Efficiency	98.1	%
<i>Condensing system Assumptions</i>		
Type	Wet Cooling	-

Transient effects in linear concentrating solar thermal power plant

Outlet Temperature cooling water	34.81	°C
DT pinch water condenser	2.78	°C
DT approach cooling water-wet bulb	4.98	°C
Fun Hydraulic Efficiency	72.7	%
Cooling Water Pump Hydraulic Efficiency	75	%
Cooling Water Pump Electric-Organic Efficiency	96.5	%
Inlet Air Wet Bulb Temperature	23.8	°C

Thermoflex23[®] provides all the sizing results that define completely the power block characteristics. A brief summary of the most important results are reported in Table 5.4.

Table 5.4 Main characteristics of the power block taken as reference case.

<i>Power Block</i>		
Parameter	Value	UoM
HTF Mass flow to Power Block	510	kg s ⁻¹
HTF Temperature to Power block	390	°C
HTF Temperature out to Power Block	290	°C
HP steam mass flow	52.65	kg s ⁻¹
HP inlet steam pressure	100	bar
T out SH	370	°C
LP inlet steam pressure	17.74	bar
RH outlet temperature	370	°C
Condensing pressure	0.08	bar
Cooling water mass flow	3211	kg s ⁻¹
T in cooling water	28.81	°C
T out cooling water	34.81	°C
Dry Air Mass flow	2584	kg s ⁻¹
Wet Cooling Tower Air Dry bulb inlet temperature	30	°C
Wet Cooling Tower Air Dry bulb outlet temperature	30.88	°C
Net power block efficiency	36.4	%

As described extensively in Chapter 2 "Quasi-Steady State analysis", once the sizing of power block components are complete, the part-load modelling can be studied in order to achieve the performance behavior at different ambient conditions.

5.3.1.2 Off-design simulation

The behavior of the power block during part load situations plays a fundamental role in the performance prevision of the plant. In particular, the absence of a TES implies a stronger effect of weather data on the power cycle that does not benefit the energy dumping properties of the storage. TFX handles all the characteristic equations of each component with a particular attention in the steam turbine performance in part-load conditions. The "Steam Turbine Assembly" plug-in allows a highly detailed simulation of the behavior of the steam turbine considering specific correlations derived from both experimental and theoretical studies [15]. The addition of the TFX model in the developed

solar field Matlab[®] suite would lead to unacceptable computational time. For that reason, in order to moderate the computing efforts needed, a parametric study about the power block behavior in part-load operation is conducted with the aim of finding polynomial expressions of the most important parameters useful to simulate the whole CSP plant. In a previous published study a similar polynomial approach was presented [16] and in analogy, the power block performance are evaluated varying both the HTF stream properties (mass flow rate and temperature) and the wet bulb temperature. Regarding the turbine inlet pressure a “sliding pressure” control is selected [17]. The two parameters that embody the interaction between the power section and the external environment (i.e. solar field and electric network) are the electric power output and the temperature at the outlet temperature of heat exchangers train. The power output and the outlet temperature can be expressed with the following function:

$$P_{el} = f(T_{HTF,in}; T_{wb}; m_{HTF}) \quad (5.1)$$

$$T_{HTF,out} = g(T_{HTF,in}; T_{wb}; m_{HTF}) \quad (5.2)$$

The power ratio map, function of the mass flow rate and the HTF inlet temperature, is shown in Figure 5.14; in order to allow the visualization of the power map the wet bulb temperature is fixed to the design value. The choice of use fractional parameters can be useful to express characteristics of power blocks that belongs to the same category avoiding different simulations for each considered plants.

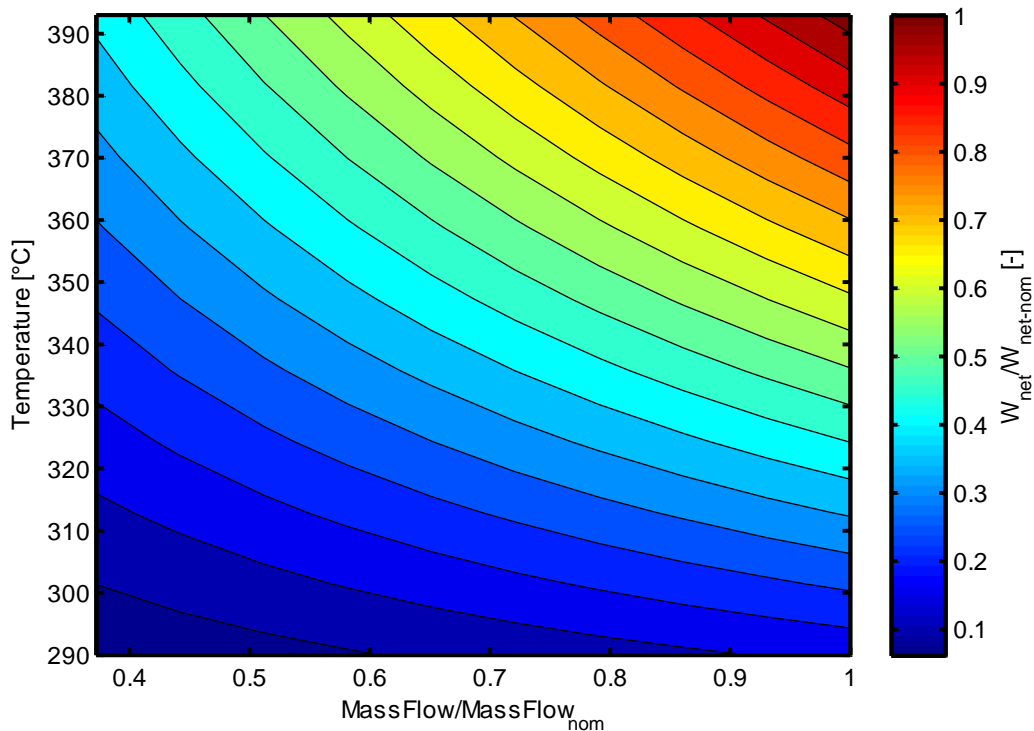


Figure 5.14 Power output ratio of the reference power block function of HTF mass flow and HTF temperature.

In addition to the power output, the HTF return temperature is necessary to couple the PB model with the SF model. Figure 5.15 shows the dependence of HTF exiting from the power block on the mass flow and the inlet temperature of the HTF.

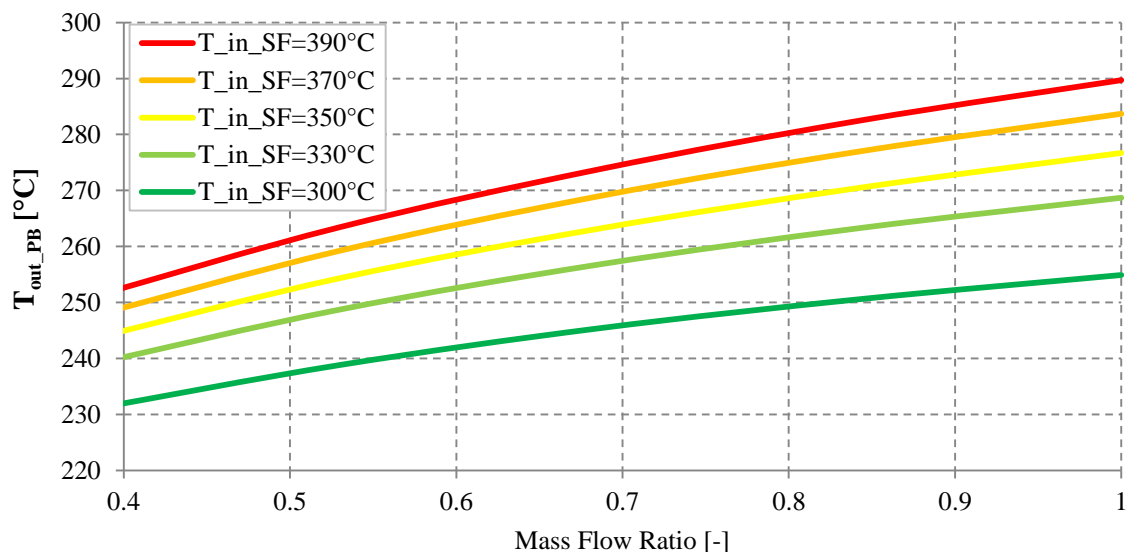


Figure 5.15 HTF temperature at solar field inlet function of the mass flow rate and the temperature of the HTF.

Once the polynomial representing the power block were obtained, it is necessary to have a first idea about the thermal inertia associated with the power block components. For that reason, the total mass of the heat exchangers is evaluated in order to decide if the dynamic model of power block components can be avoided. The results provided by TFX, in terms of mass of both steel and fluids, have been verified with “Aspen Exchanger Design & Rating (EDR)” [18], a commercial software specifically developed to size heat exchangers. A simplified model to estimate the thermal energy inertia, during start-up phase, of both the solar field and the PB is taken from [19] and it confirms that the PB start-up energy results in relation less than 1:5 of solar field. Because of the bigger thermal inertia of the solar field, the power block is approximated with a steady state approach, leading to a combined dynamic and steady-state modelling approach of the whole system.

5.3.2 Solar Field pump modelling

The pump that allows the HTF to circulate in the solar field is modelled as described in the Chapter 3 and in particular, the ratio between the current efficiency and the name-plate efficiency is represented by the curves shown in Figure 5.16.

In the figure below, assuming an ideal hydraulic power proportional to the third power of mass flow rate, the effect of pump efficiency variation in part-load is the reason why the ratio of consumed electric power is higher that the ratio of hydraulic power. As a first approximation, the pump is modelled with a polynomial without considering any transient effects.

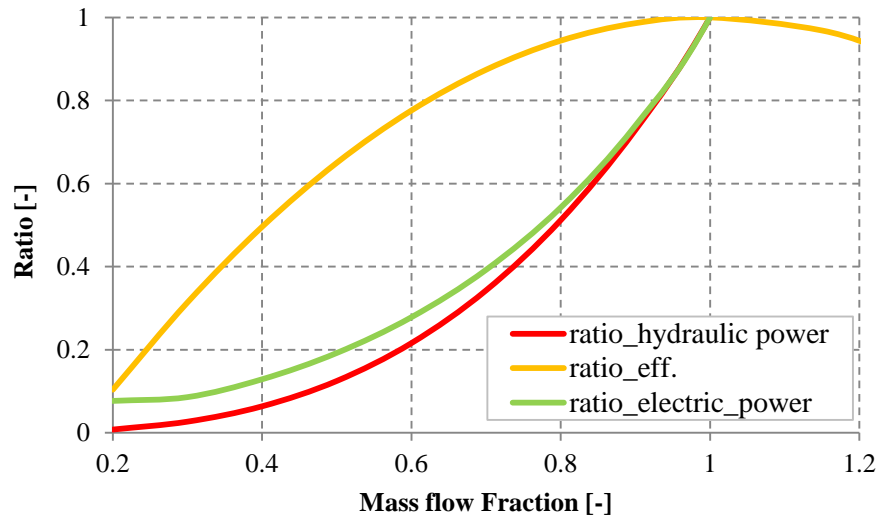


Figure 5.16 Part-load characterization of solar field main pump.

5.3.3 Simulation results

With the addition of the PB section, it is possible to run a new set of cases with the aim of extending the study described in section 5.2. In the first analysis, maintaining the same linear relation between HTF total mass flow and impinging solar energy, four cases are considered that differ in the minimum mass flow (with the same SF inlet temperature). The second study takes into account the effect of PB on the temperature at the solar field inlet. The third part of the analysis focuses the attention on the addition of a time delay in the control of total mass flow. The comparison among the different cases is based on the energetic output expresses by the power ratio of the whole CSP plant.

5.3.3.1 Constant SF inlet temperature

Two cases are added to the constant temperature cases that differ in the minimum mass flow rate limit. The power block polynomial, presented in section 5.3.1.2, is used to evaluate the power output ratio, defined as the ratio between the actual power output and the power output in on-design condition. This parameter is used as figure of merit between different solutions. These cases are ideal because they consider only the power output of a hypothetic power block, without considering the effect of power block on the return temperature. In Figure 5.17, the total mass flow, the temperature at solar field outlet and the power block output ratio are shown.

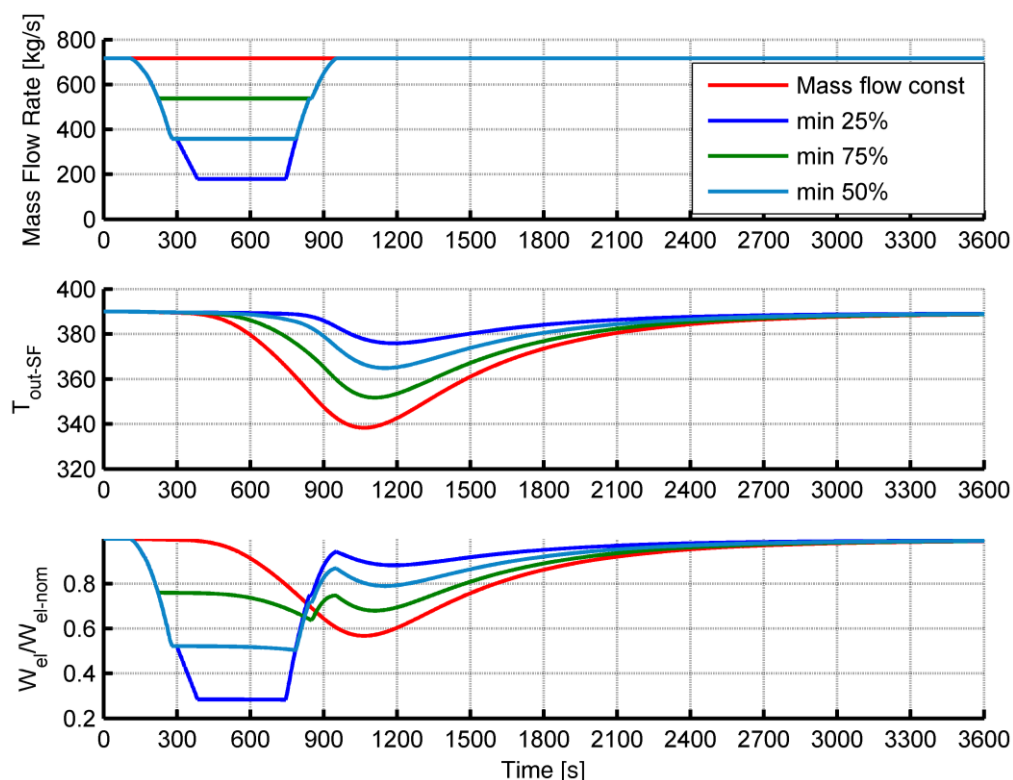


Figure 5.17 Total HTF mass flow (top), SF outlet temperature (middle) and power ratio (bottom) of the four investigated case (considering a constant HTF inlet temperature of 290°C).

To identify the best solution among the case presented in Figure 5.17, the integral energetic output is computed showing that the case with constant mass flow is the best solution in terms of energetic output. In particular; the case#1 has an integral power ratio value 3 percentage points higher than the HTF proportional regulation (min 25%). As underlined in section 5.2, the defocused system operates in order to assure safe conditions. In Figure 5.18, the solar field defocused fraction is reported. The main reason behind worse energetic performance obtained by modulating the mass flow can be identified in the dumped energy. The effect of part-load performance has a minor effect in affecting the different control strategies. In accordance to the integral power output ratio, the lower is the mass flow limit the higher is the fraction of wasted energy, which represents the main penalty of the system. Even if the mass flow is kept constant, the defocusing system acts in case#1 (red line) because of the change in thermophysical properties of fluid that leads to a mal flow rate distribution in solar field loops, nevertheless this effect has a small impact on the loop temperature thus leading to small fraction of defocused energy.

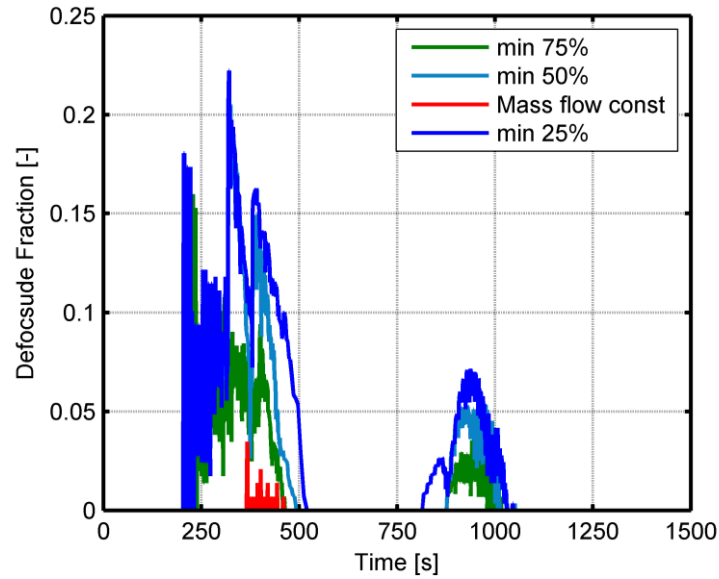


Figure 5.18 Defocused fraction of the solar field for the investigated case.

5.3.3.2 Inlet SF temperature influenced by power block

The same mass flow control strategies of the study above are considered but, in these cases, the effect of power block on solar field inlet temperature is taken into account. Instead of a constant value of 290°C, the power block polynomial introduced in 5.3.1.2 is used increasing the accuracy level of the modelling. In Figure 5.19, the total mass flow, the temperature at solar field outlet and the power block output ratio are shown.

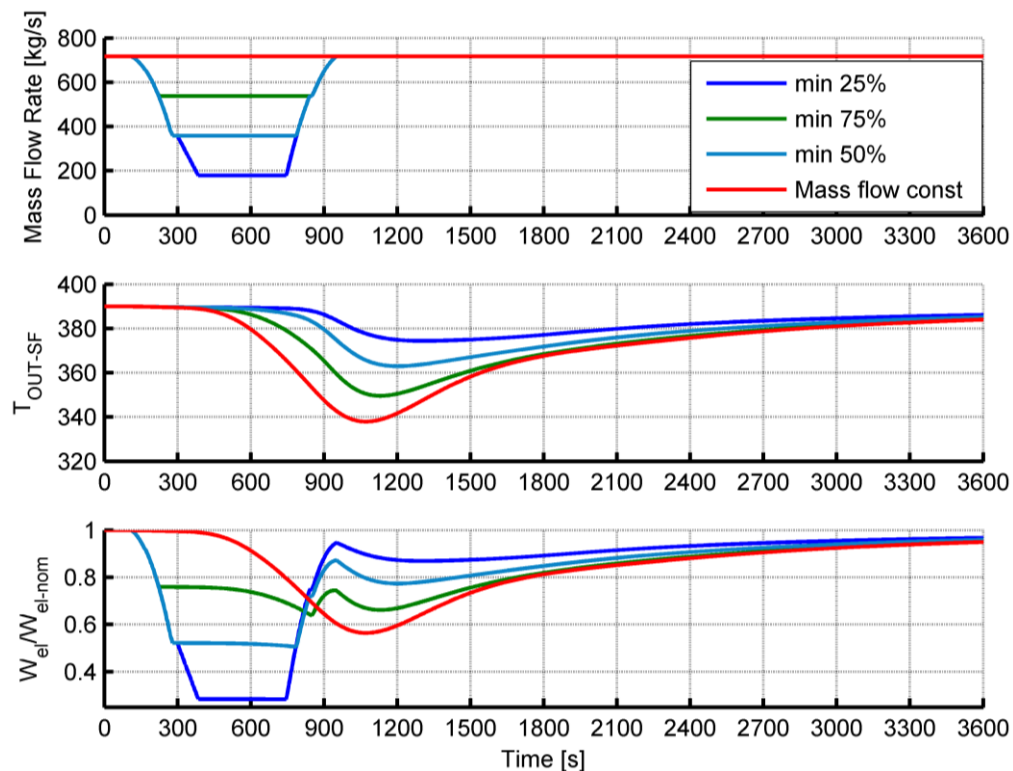


Figure 5.19 Total HTF mass flow (top), SF outlet temperature (middle) and power ratio (bottom) of the four investigated case (considering the power block effect on the HTF inlet temperature).

Some differences arise from the comparison between Figure 5.17 and Figure 5.19 even if the main conclusions about the energetic performance are the same. In particular, the power block effect on outlet temperature can be seen in the trend of outlet solar field temperature that shows a slower heat up phase. To clarify the influence of power block modelling on thermal behavior, Figure 5.20 shows the temperature behavior during time of the expansion tank and at the outlet of the last hot header pipe. The two extreme cases are considered characterized by a constant mass flow during time and an impinging energy proportional mass flow with a minimum value of 25% respectively. It is evident how the addition of power block effect on return temperature has a relevant influence on thermal performance of the solar field implying both a lower mean temperature and a longer time requested to reach the steady state conditions.

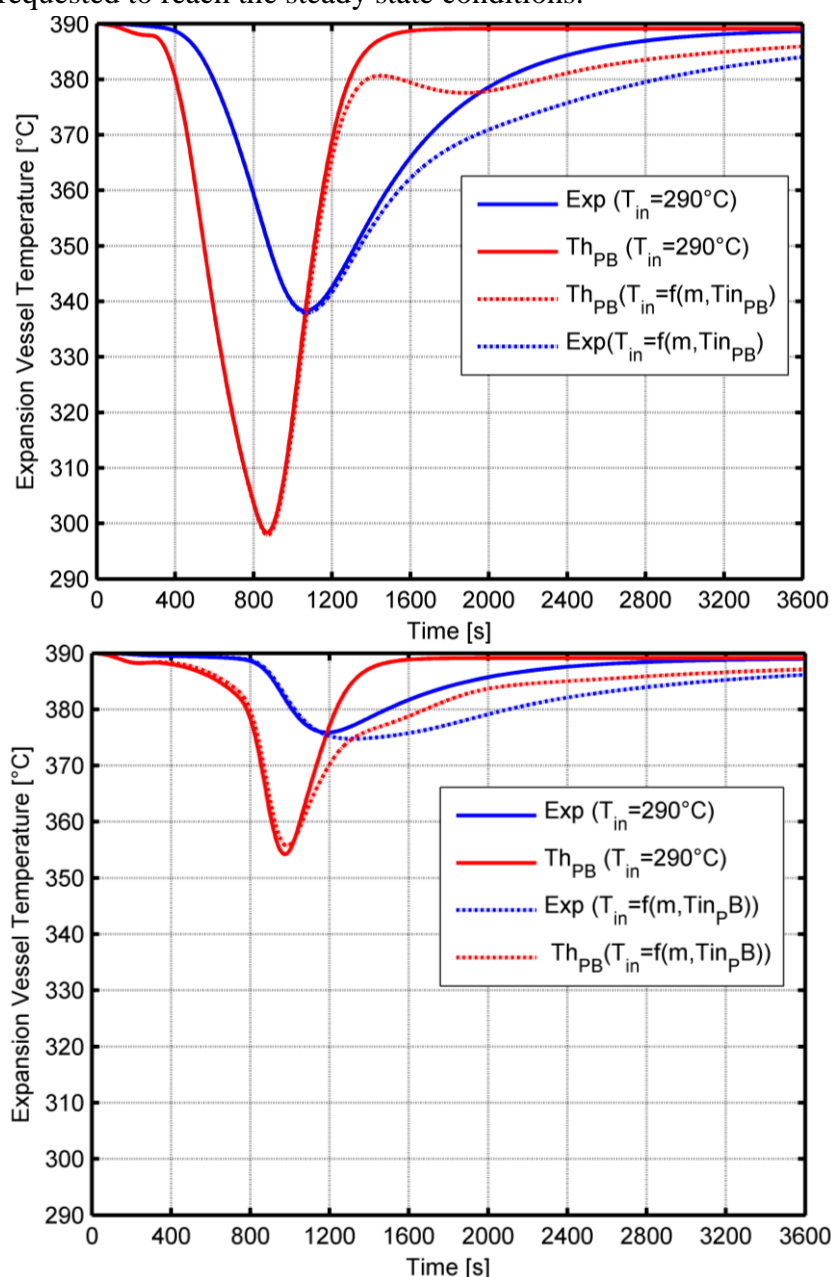


Figure 5.20 Temperature of expansion tank (blue) and of the last SF pipe segment that delivers the HTF to the expansion tank (red). Trends considering PB are dashed. Case with constant mass flow rate (top) and case with proportional mass flow rate with a minimum set to 25% (bottom).

5.3.3.3 Action delay

Following the main idea of checking simple solar field control strategies, the procedure that links the total HTF mass flow to the solar field impinging solar energy is extended with the addition of a delay in changing the mass flow rate. From the defocussing trend shown in Figure 5.18, it is evident how the decrease of mass flow ,during the initial shading period, is too fast and leads the irradiated loops to be defocused. This effect suggests that the addition of a time delay in modifying the mass flow could have a positive influence on the energetic performance of the whole system.

A delay of 250 s is considered but, as reported in Figure 5.21 (red-dotted line), it involves a worse situation because the advantage of the defocused energy strong reduction during the shading phase is overtaken by the defocused energy during the un-shading phase (red-dotted series). This consideration suggests that an acceptable compromise can be represented by a control action that is characterized by a delay during the shading period and an instantaneous action during the un-shading phase (shown by the dotted-purple series). From the figure below (purple-dotted line), the addition of delay strongly reduces the defocusing energy, obtaining a situation similar to the constant mass flow case.

The last consideration leads to conclude that instead of adding a delay in the mass flow rate regulation, maintaining the same mass flow could be a good solution to face the cloud disturbance.

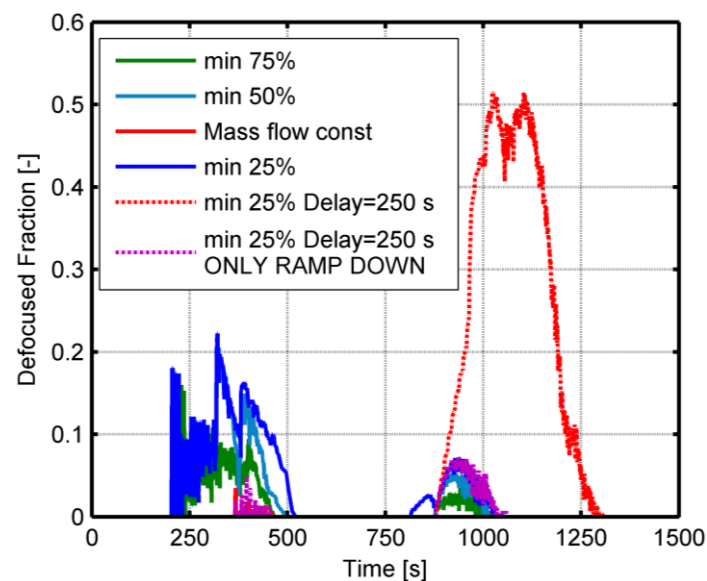


Figure 5.21 Defocused fraction of the solar field for the investigated cases. The solutions that consider a delay strategies are identified by a dotted.

In Figure 5.22 the effect of a delay in changing the mass flow control is reported, in terms of tank temperature and power output ratio. The figure shows how the addition of delay only for the ramp down phase does not add any remarkable improvements thus confirming the goodness of maintain a constant HTF mass flow rate. In particular, the temperature at the expansion tank outlet shows an intermediate behavior between the curves of proportional change of mass flow with a minimum value of 50% and 25% respectively.

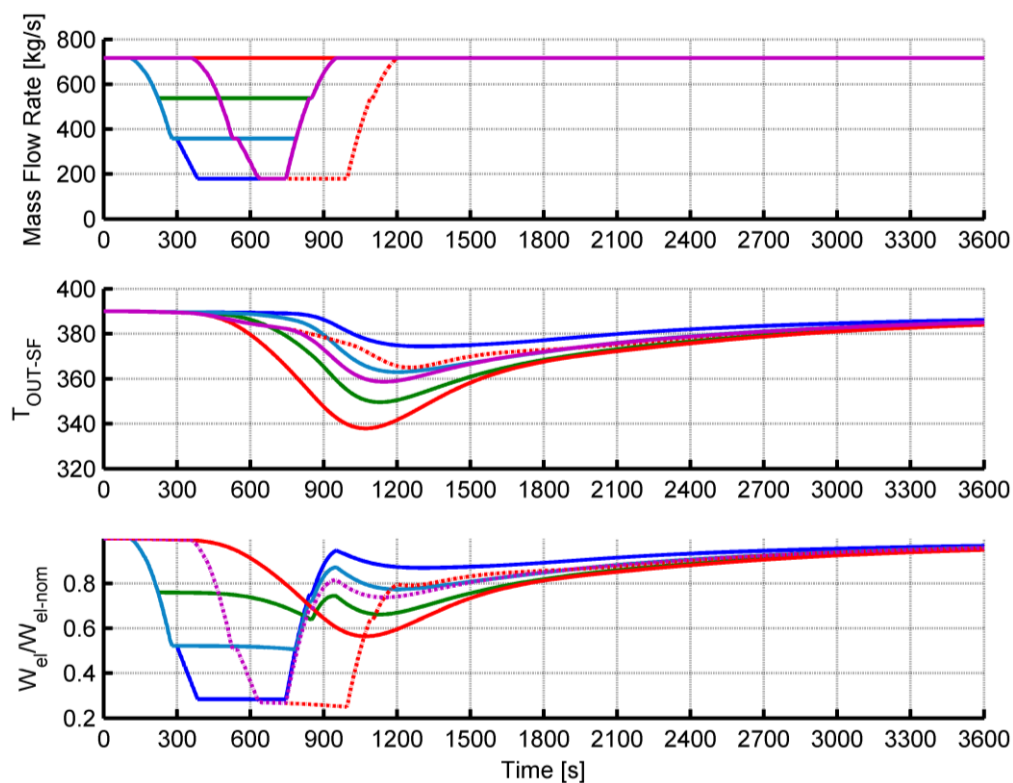


Figure 5.22 Effect of delay actions on energetic performance.

5.3.3.4 Live Steam considerations

Focusing the attention on the steam turbine, a parameter, that can indicate the presence of possible issues, is the live steam temperature gradient. As reported by [20] a gradient steam temperature at turbine inlet of $5^{\circ}\text{C}/\text{min}$ can be identified as a limit to guarantee the secure operation of the turbine and to not affect the lifetime of the component. This value has to be considered as a rule of thumb due to the high variability in turbine construction that depends on the manufacturer's choices. Considering the case#1, which is chosen, as previously said, as a good control strategy it is possible to evaluate the live steam gradient. In Figure 5.23 the live steam and HTF temperature at the power block inlet are shown (bottom); the steam gradient (top) is in the range from $-6^{\circ}\text{C}/\text{min}$ to $4^{\circ}\text{C}/\text{min}$ and as a first approximation, it can be considered a safe situation.

From Figure 5.23 (bottom), the reduction of temperature difference between the live steam and HTF is explained by the sliding pressure control of the steam turbine; in particular the HTF mass flow is maintained constant whereas the mass flow of steam generated is reduced thus leading to reduced temperature difference between the two streams

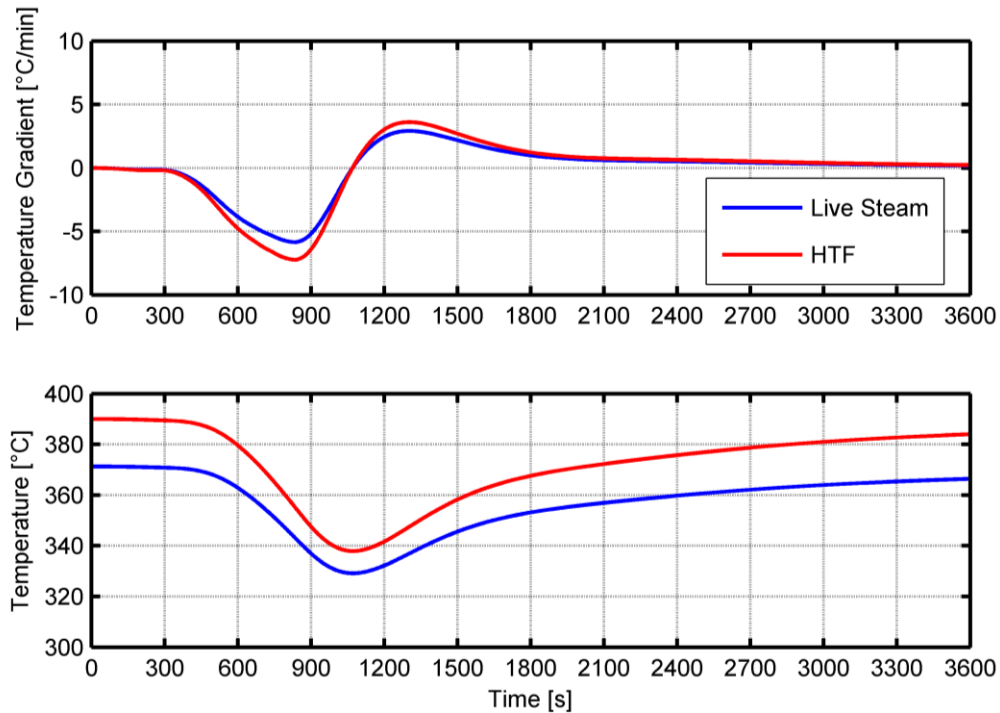


Figure 5.23 Temperature gradient of both HTF and live steam (top) and absolute value of HTF and live steam temperature (bottom) – Referred to constant mass flow case.

5.3.4 Conclusions about mass flow control

From the analysis presented in this section some conclusions, regarding the mass flow control, can be drawn. Limiting the consideration to the disturbance presented in this section, even if it represents a situation that strongly affects the solar field performance, the best way to face the passage of the cloud front seems to keep the mass flow at the on-design value. The advantage of this kind of control can be resumed in:

1. *The simplicity:* the system does not encounter any unsafe condition and there are no active strategies to be implemented. The operator does not act on any control parameter and leaves the solar field free to adapt to the new conditions.
2. *No need of control valves on each loops:* this characteristic simplifies the scheme layout and reduces the investment cost of the solar field. To maintain exactly the same mass flow, an action on solar field pump is necessary (i.e. varying the rotational speed) to face the change of hydraulic behavior due to temperature change. Nevertheless, this regulation does not imply particular issues because of the small influence of density change on total pressure drop.
3. *The defocused energy is minimized:* A constant mass flow minimized the energy loss related to defocussing, thus representing an energetic advantage.
4. The other total mass flow control strategies assume indirectly that the total impinging solar energy is known at every time. This condition finds a difficult application in real condition because the measures of DNI can be spatially discrete.

It is important to underline that these conclusions can show a certain level of dependence on the kind of disturbance considered and that they are strongly affected by the chosen indirect solar field technology. The addition of more sophisticated control strategies could have a positive effect on plant performance but it is reasonable to think that the constant mass flow strategy could be a good solution for the reasons listed above.

It is worth to notice that, in case of DSG plant, the more complex thermo-hydraulic behavior, as underlined by [21], needs to the development of specific tool capable to handle the phase transition [22]. Different studies are present in literature, [20,23] are reported as examples, that deal with transient simulation of DSG plant but, due to the high computational efforts to solve the problem, the analysis is limited to few loops in a solar field. These studies show a system response to the cloud passage that is completely different from the case of an indirect CSP plant and, therefore, the optimum control strategy can be very different and complex (i.e. control valves on each loops are mandatory). The analysis of transient characteristics of DSG plant is beyond the scope of this work and it would be object of future works.

5.4 Morning Warm-up

During normal operation, every morning the solar field needs to be warmed up to reach the starting temperature of the power block. As reported in [24], the allowable minimum temperature of the synthetic oil can be 50°C while during normal operation the HTF is cooled down until approximately 180°C [25]. The warm up of the solar field is commonly not considered in steady state simulation and in this section a more detailed transient analysis is presented in order to go in to this topic. During the morning, because of the sun position, big difference between DNI and EDNI is present. As described in the Chapter 2, the most important effect of the high incidence angle can be summarized in the end-loss effect, cosine effect, IAM and reciprocal shading. As an example, the effects that reduce usable DNI are summarized in Figure 5.25 for 9 July 2013 at the Plataforma Solar de Almeria (37° 5' 30.12" N, 2° 21' 29.88" W). As presented in the figure below, the reciprocal shading is the most important reduction DNI effect during the morning for a summer day as the chosen one.

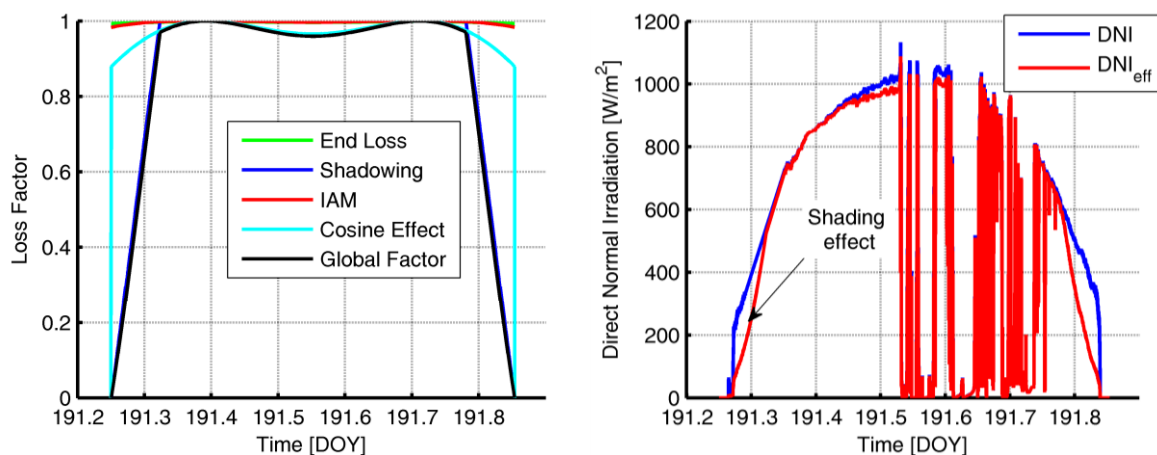


Figure 5.25 Optical effects reducing the usable DNI (10/07/2013 at Almeria) (left). DNI and EDNI (right).

A peculiarity of the reciprocal shading effect lies in its spatial effect on the collectors of the solar field. For example, as shown in Figure 5.26, the most eastward SCA are not shaded by other mirrors and, for that reason, this loop is characterized by a different spatial solar energy distribution (the same effect can be noticed for the most westward SCA during the last hours of the day). This unbalance in the spatial energy radiation among the loops will cause a non-uniform thermo-hydraulic behaviors that are possible to analyze with the developed thermal model.

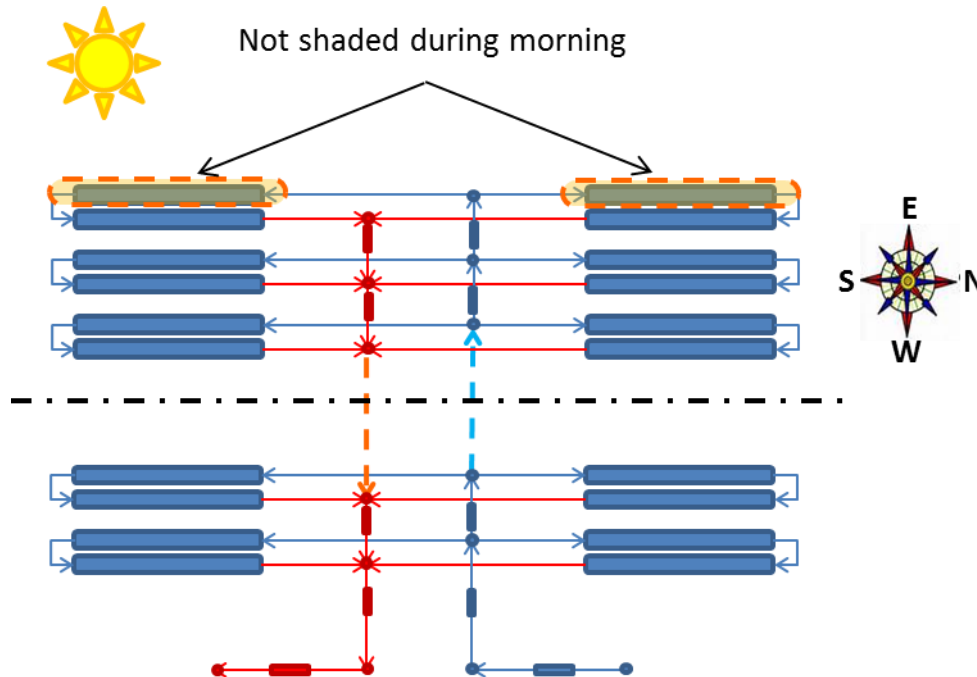


Figure 5.26 Subsection drawing with the part of loops that are not shaded by other mirrors enlightened.

To simulate the spatial distribution of EDNI, the enlightened part of the last loops collects the EDNI calculated considering all the reducing DNI effects except the reciprocal shading whereas, the solar energy impinging the other loops is obtained taking into account the reciprocal shading too. The recirculation mode, in which the HTF of the expansion tank is pumped directly to the inlet of the solar field (the heat exchangers train of power block is by-passed), is selected. This operation mode is commonly used in real plant during the start-up in order to reduce the time needed to reach the starting temperature of the power block.

As regards the value of total mass flow that circulates in the solar field a simple relation is used: the HTF mass flow is set to be proportional to the total usable solar energy on the solar field as presented in Figure 5.27.

Three different phases in mass flow can be identified (as shown in the plot below):

1. EDNI lower than the 25% of the on-design EDNI thus mass flow rate has a constant value equal to the 25 % of the sizing value.
2. The increment of mass flow rate follows the EDNI trend that is characterized by the reciprocal shading.

3. The reciprocal shading effect disappears and the gradient on mass flow rate is related to the increment of EDNI.

As regards the initial conditions, the temperature of the solar field is set to 50°C in order to consider the worst case.

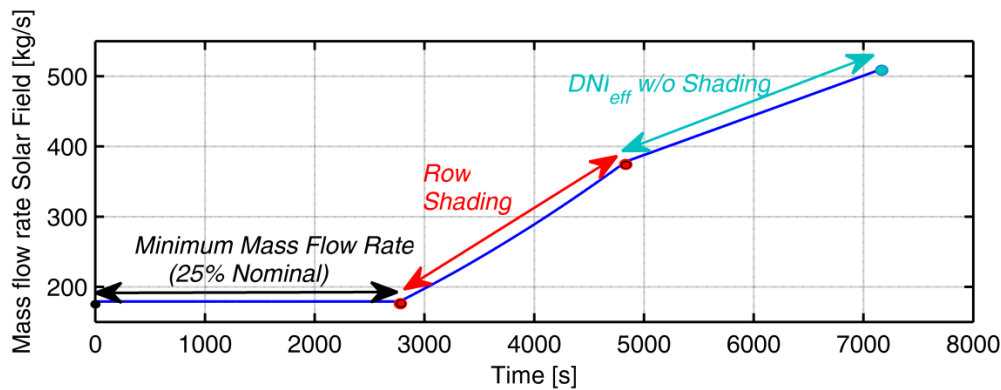


Figure 5.27 Total mass flow rate at the inlet of the solar field.

5.4.1 Simulation results of warm-up

Considering the solution of the differential problem described in the Chapter 4, the most east-ward loop is heated up more quickly than the others thus implying a lower mass flow that enhances a fast warming of the irradiated loops.

The outlet temperature of loop belonging to the east solar field subsection is shown in Figure 5.28. The faster warm up of the last loop can be noticed even if it does not represent a danger for the integrity of the absorber tube. In the warm up period (time range starting from 0 s to approx. 3000 s), the two loops that are not shaded gain much energy with a higher absolute value of temperature that, compared with the remaining loops, can reach a maximum difference of 50°C.

After the period when the reciprocal shading is active, the solar input is equal for every plot resulting in a different behavior of the solar field. The hydraulic network tends to balance itself and this effect can be seen in the gradient change of outlet temperature of the last two loops. After this period, the difference between the outlet temperatures of loops is mainly ascribed to the travel time of HTF in the piping system which implies that west-ward loops have a higher temperature because of their closeness to the inlet of the solar field.

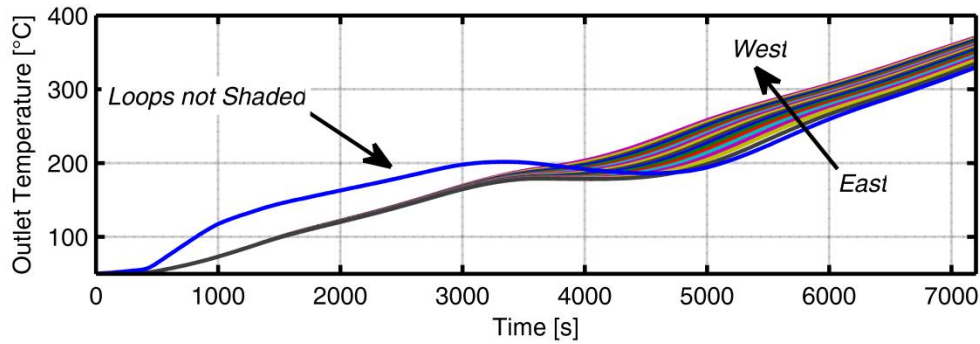


Figure 5.28 Temperature the outlet of loops of the east subsection of solar field (simulation time: 2h).

In Figure 5.29 the temperature maps plotted in a space length/time of the eastward loop (#1) and the westward loop (#18) are shown. It is possible to notice the different behavior of these two loops that have opposite boundary conditions.

In particular, from that kind of plot it is possible to consider all the time history of the loop, noticing that the outlet temperature is representative of the behavior of all the segments of the loop.

Temperature Map Loop 1 (Most West) and 18 (Most East)

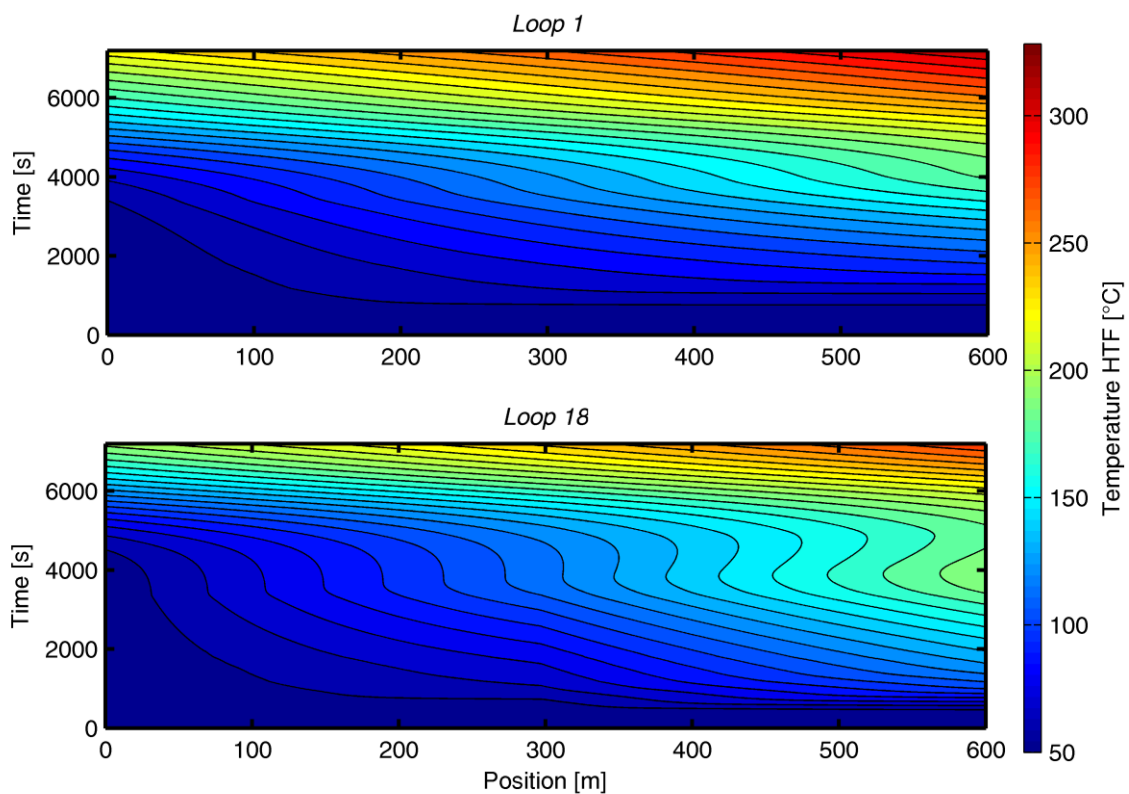


Figure 5.29 Temperature map of the eastward (loop #18) and westward loop (#1)

The temperature of the expansion tank is presented in Figure 5.30, it is important to underline that the recirculation mode implies that the temperature of the expansion vessel is equal to the temperature of the mass flow entering in the solar field. The temperature trend of the expansion tank shows an initial period with no perturbation and after

approximately 1500 s the temperature increase starts. As regards the shape of the response, it is possible to notice that the temperature gradient follows quasi-linear trend thus leading to possible operation advantages in the prevision of the system behavior. The warm-up period is characterized by a ramp period until the reaching of a temperature of 300°C that represents a feasible starting point of the power block. From this time, it is possible to assume that recirculation mode is interrupted and the HTF is sent to the heat exchangers train of the power block.

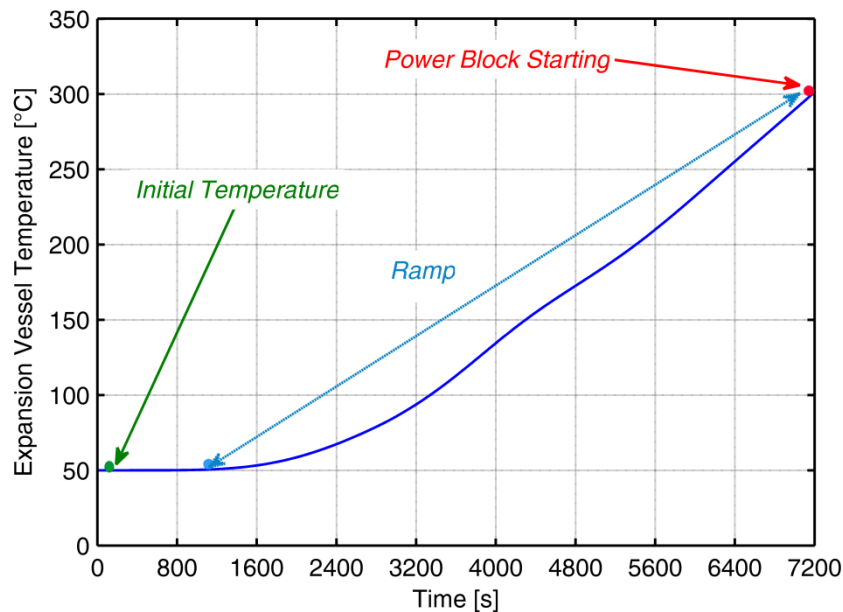


Figure 5.30 Expansion tank temperature during the warm up period

5.5 Bibliography

- [1] Augsburger G, Favrat D. Modelling of the receiver transient flux distribution due to cloud passages on a solar tower thermal power plant. *Solar Energy* 2013;87:42-52.
- [2] Martínez-Chico M, Batlles FJ, Bosch JL. Cloud classification in a mediterranean location using radiation data and sky images. *Energy* 2011;36:4055-4062.
- [3] Aerospace Corp.,. Preliminary Definition of Barstow Standard Cloud Model. Technical Report. 1978;SAN-1101/PA2-23.
- [4] National Renewable Energy Laboratory. National Solar Radiation Data Base: 1991-2005 Update: Typical Meteorological Year 3 2008;2013.
- [5] Google Inc. Google Earth 2013.
- [6] Lippke F. Simulation of the part-load behavior of a 30 MWe SEGS plant 1995.
- [7] Wendelin T. Soltrace: A new optical modeling tool for concentrating solar optics. *Int Sol Energ Conf* 2003:253-260.

- [8] Quoilin S, Broek MVD, Declaye S, Dewallef P, Lemort V. Techno-economic survey of Organic Rankine Cycle (ORC) systems. *Renewable and Sustainable Energy Reviews* 2013;22:168-186.
- [9] Quoilin S, Orosz M, Hemond H, Lemort V. Performance and design optimization of a low-cost solar organic Rankine cycle for remote power generation. *Sol Energy* 2011;85:955-966.
- [10] National Renewable Energy Laboratory. NREL: TroughNet - U.S. Parabolic Trough Power Plant Data 2012;2012.
- [11] Turchi C, Wagner M, Kutscher C. Water Use in Parabolic Trough Power Plants: Summary Results from WorleyParsons' Analyses. *Contract* 2010;303:275-3000.
- [12] Relloso S, Delgado E. Experience with molten salt thermal storage in a commercial parabolic trough plant; Andasol 1 commissioning and operation 2009:14-18.
- [13] Solar Millennium. Solar Millennium AG - The Construction of the Andasol Power Plants. - Archives - Technology - References and Projects - Andasol (Spain) 2012;2012.
- [14] Macchi E, Silva P, Giotri A, Saccilotto C, Astolfi M, Binotti M. Attività di modellazione di un impianto solare termodinamico a concentrazione parabolico lineare tipo Andasol 2010.
- [15] Thermoflow Inc. Thermoflex v.23 User Guide 2013.
- [16] Manzoloni G, Giotri A, Saccilotto C, Silva P, MacChi E. A numerical model for off-design performance prediction of parabolic trough based solar power plants. *J Sol Energy Eng Trans ASME* 2012;134.
- [17] Binotti M, Giotri A, Astolfi M, Colombo L, Macchi E, Manzoloni G. Partial admission vs sliding pressure applied to DSG solar plant based on linear Fresnel reflector. *SolarPACES* 2011 2011.
- [18] AspenTech. Aspen Exchanger Design & Rating ("EDR") 2013.
- [19] Hirsch T, Fabian Feldhoff J, Schenk H. Start-up modeling for annual CSP yield calculations. *J Sol Energy Eng Trans ASME* 2012;134.
- [20] Birnbaum J, Feldhoff JF, Fichtner M, Hirsch T, Jocker M, Pitz-Paal R, et al. Steam temperature stability in a direct steam generation solar power plant. *Solar Energy* 2011;85:660-668.
- [21] Hirsch T, Feldhoff JF, Hennecke K, Pitz-Paal R. Advancements in the field of direct steam generation in linear solar concentrators-a review. *Heat Transfer Eng* 2014;35:258-271.
- [22] Eck M, Hirsch T. Dynamics and control of parabolic trough collector loops with direct steam generation. *Sol Energy* 2007;81:268-279.
- [23] Valenzuela L, Zarza E, Berenguel M, Camacho EF. Control scheme for direct steam generation in parabolic troughs under recirculation operation mode. *Solar Energy* 2006;80:1-17.
- [24] Patnode AM. Simulation and performance evaluation of parabolic trough solar power plants 2006.
- [25] Binotti M. Linear Fresnel reflectors : study of the technology and steps toward optimization 2013.

6 Cloud Movement Vector

As underlined in the previous chapter, the cloud movement over the solar field can be a parameter of fundamental importance in studying the working conditions of a solar field. In particular, the presence of clouds represents the first source of uncertainty in forecasting the solar field power output thus short time range weather forecast (< 1 min) [1] can help the operation of CSP plant. The fundamental parameter that identifies the cloud front movement is the so called “Cloud Motion Vector” (“CMV”), defined as a motion vector with info related to the direction and the speed of the cloud. This cloud info can be useful to predict the interaction between the solar field and the cloud thus helping to predict the solar field behavior.

It is worth to consider that real CSP plants could be operated more safely if cloud direction were available before the cloud front reaches the solar field.

For this reason, a new method, found in literature, is presented and adopted to treat experimental data with the aim of obtaining information about a cloud that can be used in the thermo-fluiddynamic model described in the previous chapter. Besides the CMV, the second important cloud parameter is its transmittance (or opacity). The knowledge of this info helps to increase the level of cloud modelling accuracy. For that, an estimation of the real radiation transmittance of the cloud front, based on available experimental data, is presented at the end of this chapter.

In Figure 6.1, the solar field of the Andasol group power plants (Andasol I-II-III) partially covered by a cloud is shown [2]. The clouds captured by the photo are representative of a possible operating condition in CSP plant when an high solar radiation is available but the presence of isolated clouds can make more difficult the prediction of the solar field performance.



Figure 6.1 Picture of the Andasol solar field partially covered by a cloud (Guadix (ES) $37^{\circ} 18' 0''$ N, $3^{\circ} 8' 0''$ W).

The chapter organization can be resumed in a first part where the CMV identification problem is described and the obtained results are discussed. The second part, using the CMV results, deals with the solar field behavior prediction and evaluates the effect of a more real modelling approach.

6.1 Model to determine the Cloud Movement Vector

The calculation of the CMV is the main object of this section and a specific procedure is implemented as a MATLAB[®] suite. It is important to underline that the goal of these procedures is to have an estimate of a cloud vector to be used in the solar field model described in the previous chapter

As regards the methods available to calculate the CMV, two main categories depending on the source of the data are found in literature:

- *Image processing*: this was the traditionally used method. Cloud images taken by a camera or satellite are used to estimate the CMV with an image processing algorithm as the one presented in [3].
- *Ground based*: direct measurements of solar irradiation with different sensors are used to calculate the CMV with algorithms able to process the solar irradiation signals.

Regarding a qualitative comparison between "Ground based" and "Image processing" methods, the first shows a certain complexity to acquire the data and an infrequent time of update (e.g. 15-30 min). The local ground measurements is the best solution in the case of short-term CMV forecast as underlined in [4] and for this reason the GHI measurements data, coming from an installed experimental facility, are elaborated with the algorithms described by Bosch et al. [5].

In the next sections, a treatment procedure that used experimental data is presented with the aim of estimating the cloud vector starting from a series of measured data. As regards the experimental facility, a short description is offered in the next subsection. It is important to underline that the algorithms presented give CMV results that are characterized by a certain margin of error, which will be discussed in detail in a dedicated section.

6.1.1 Installed measurement system

The experimental setup is located at the Plataforma Solar de Almeria ("PSA") [6] and it is owned by CIEMAT and German Aerospace Research Center ("DLR") [7,8]. The main purpose of this experimental facility is the study of the effect of solar irradiation patterns on the simulation of thermo-hydraulic behavior of a representative collector loop. For that reason, a GHI measurement grid made of 20 sensors was built and inaugurated in July 2013. The main grid is divided in 4 subgrids called "diamond" identified by their position (NW, NE, SW,SE). In accordance, each sensor in the subgrid is identified by its cardinal position (North, South, East, West, Central) (e.g. NEN, NEW, NES, NEE, NEC).

An aerial picture of the experimental setup at the PSA is presented in Figure 6.2 (left); in addition to the GHI measurement grid, two solar towers facilities (made of receiver and heliostat field) and a parabolic trough loop are visible. The distance between the central sensor and the other sensors in a "diamond" is equal to 50 m as shown in Figure 6.2 (right).



Figure 6.2 Installed GHI measurement grid at Plataforma de Almeria [6] (snapshot taken from Google Earth [9]) (coordinates: 37° 5' 30.12" N, 2° 21' 29.88" W) (left). Sketch of a diamond with the main length reported (right).

The experimental facility is able to measure the Global Horizontal Irradiance (“GHI”) with a sample frequency of 1 Hz. In addition to the GHI measure grid, a single weather station able to measure the DNI and the Diffuse Horizontal Irradiance (“DHI”) was installed.

Once the GHI is measured by each sensors of the grid and the DHI is known by the single weather station, an approximate value of DNI is calculated with the following relation [10] (the zenith angle θ_z is calculated knowing the location and the local time [11] -see Appendix-):

$$DNI = \frac{GHI - DHI}{\cos\theta_z} \tag{6.1}$$

It is important to underline that the value of DNI calculated for each sensors represents an approximation because the DHI derives from an instrument placed at single location and thus there is a discrepancy in time that, as a first approximation, can be considered negligible.

A daily profile (10th of July 2013) of solar irradiation is presented in Figure 6.3 showing the different contribution of solar radiation at the ground level (the data are relative to the NW subgrid); in particular a cloudy day is selected. The characteristic shape profile of GHI and DNI for a summer day, can be identified; due to the cosine of zenith angle the DNI series has more gradual trend and a lower maximum value compared to GHI one. During a typical winter day the opposite situation occurs. As regards the DHI, the power peaks are coincident to the decrease of GHI caused by a passage cloud.

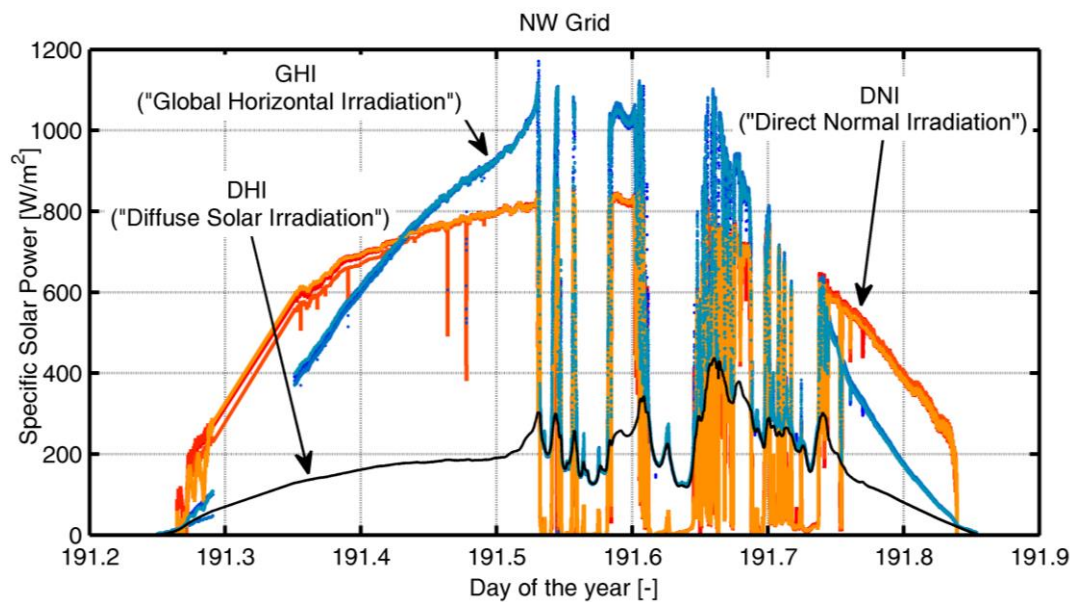


Figure 6.3 Available data obtained from the NW grid and from the weather station (10th of July 2013).

In the figure above, a range of time without measure data can be noticed (the data are linearly interpolated in the time range approximately defined by 191.30 to 191.35 DOY); this fact is representative of the short life of the experimental setup that needed some adjustments to the grid sensors.

Once the measurement facility is briefly described, in the next subsection the models used to determine the cloud vector are presented. The parameter that is taken into account by the models is the GHI derived from the experimental grid described above.

6.1.2 Linear Cloud Edge Model

The first model considered to determine the CMV is the so-called “Linear Cloud Edge Model” (“LCE”).

This model was first developed by the “Centre for Renewable Resources and Integration of the University of California” [5]. This method is based on the concept of “Cloud Events” that identifies both the passage of edge cloud and the passage of cloud front bands with a different opacity. Once the measured GHI profiles are known, it possible to identify the effect of a cloud event as the offset between the measured data and a “clear-sky” bell shape approximation.

Figure 6.4 (left) presents a GHI profile typical of cloudy day measured at the Plataforma Solar de Almeria (10th of July 2013) and, a possible visual explanation of the concept of “cloud events” is sketched in Figure 6.4 (right) taking in to account a sky-image taken from [12] (given for explicative purposes only). The cloud edge is sketched as a red line whereas a cloud zone with an opacity variation is contained in a dashed circle.

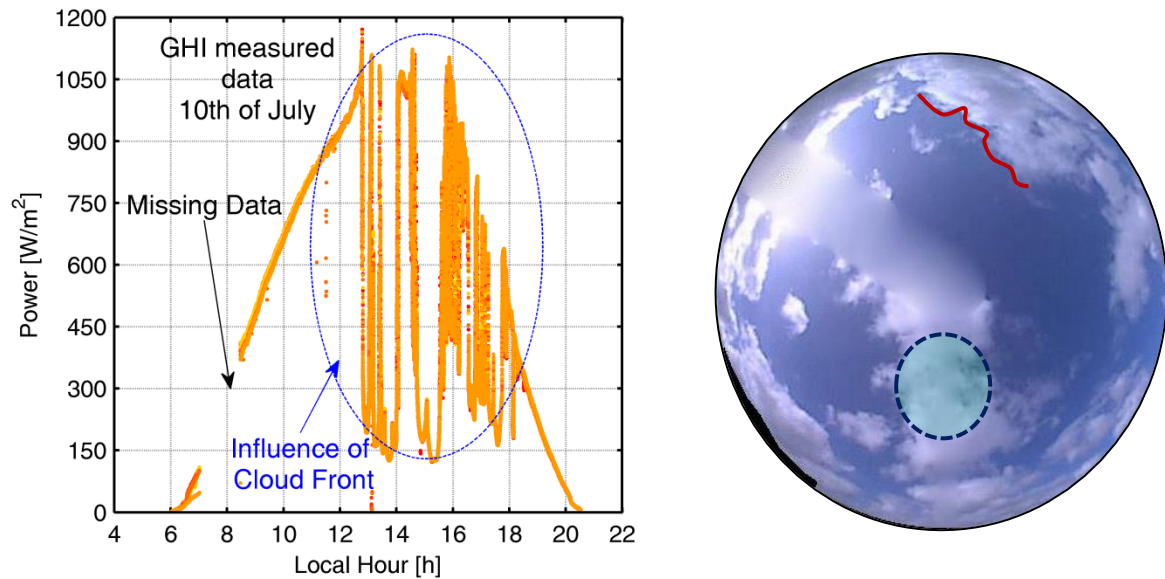


Figure 6.4 Profile of GHI measured data at Plataforma de Almeria at 10-July-2013 (left). Example of sky camera image with possible cloud events enlightened (right).

6.1.2.1 Model description

In this section, a brief description, taken from [4], is presented in order to explain the bases of LCE method.

The experimental setup needed by the LCE method is made of a triplet of sensors (the experimental grid makes available different triplets), which measure GHI and records the data as a time series. In addition, some assumptions to simplify the problem are necessary:

1. The shape of the cloud edge across the sensors is considered linear
2. The CMV is assumed to be constant during the passage of the cloud above the sensors.
3. The cloud dimension is sufficient to cover all the three sensors

An explanatory drawing, which helps to understand the geometrical basis of the LCE method, is reported in Figure 6.5; for simplicity, the sketch is based on the passing of a cloud edge. Starting from Figure 6.5, it possible to identify the main geometric elements used to calculate the CMV. Table 6.1 summarizes the nomenclature of the geometric elements considered to describe the problem.

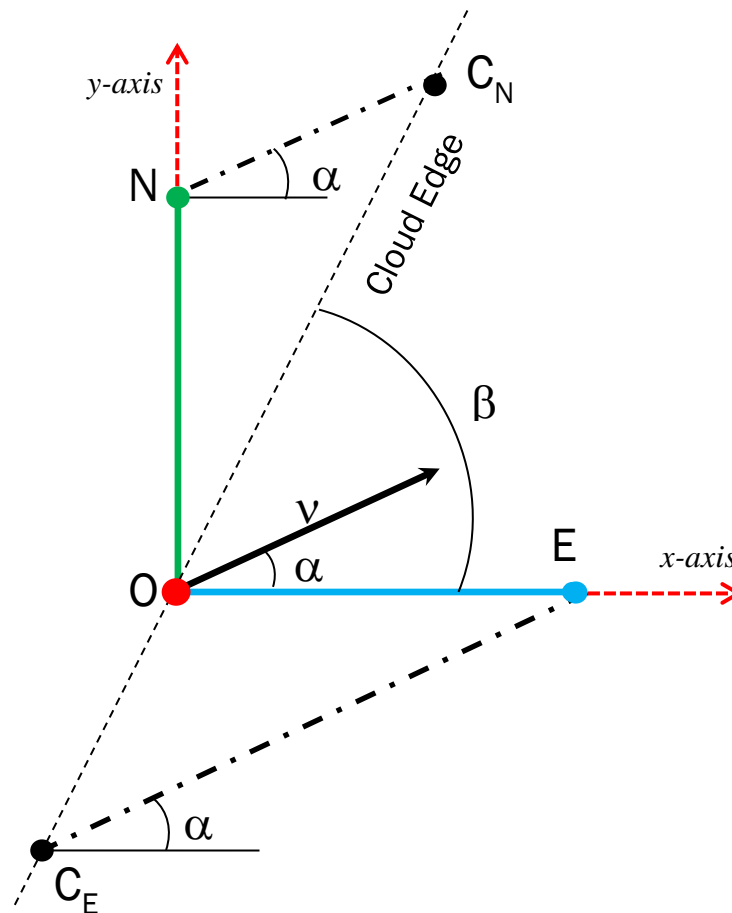


Figure 6.5 Sketch of the “Linear Cloud Edge Model” (Adapted from [4]).

Table 6.1 List of useful geometrical entities used to develop the LCE model.

<i>Geometrical entities for LCE</i>		
Name	UoM	Description
O	-	Sensor position
E	-	Sensor position
N	-	Sensor position
$\overline{C_E E}$	m	Distance covered by the cloud to reach the E sensor
$\overline{NC_N}$	m	Distance covered by the cloud to reach the N sensor
$\overline{C_E C_N}$	m	Cloud edge moving through the triplet of sensors
t_{ON}	s	Time that the cloud needs to move from C_N to N
t_{OE}	s	Time that the cloud needs to move from C_E to E
β	°	Angle of the considered cloud edge (measured from the OE direction)
v	$m s^{-1}$	Cloud speed that represents the magnitude of the CMV
α	°	Angle that defines the direction of CMV (measured from the OE Direction)

Considering an orthogonal triple (this choice is made to simplify the geometrical treatment) characterized by a distance D , it is possible to outline the procedure to calculate the CMV.

The kinematic equations of uniform linear motion, considering the drawing in Figure 6.5, can be expressed with the following vectors relations:

$$\overrightarrow{OE} - \overrightarrow{OC_E} = t_{OE} \vec{v} \quad (6.2)$$

$$\overrightarrow{OC_N} - \overrightarrow{OC'_N} = t_{ON} \vec{v} \quad (6.3)$$

Applying the Law of Sines [13] to the triangles $\triangle ONC_N$ and $\triangle OEC_E$ a formulation of β , function of t_{OE} and t_{ON} can be obtained:

$$t_{ON} \sin \alpha + t_{OE} \cos \alpha = \frac{D}{v} \quad (6.4)$$

In the equation above, the time t_{ON} and t_{OE} derive from the analysis of measured GHI profile while, once the distance between the sensors is known, the two remaining unknowns are the direction and the magnitude of the CMV. To close the problem of CMV identification, the number of unknowns has to be equal to the number of equations. Considering two successive cloud passages above the sensors (identified by the subscripts 1 and 2) with different cloud edge orientation β , the following set of two equations can be written:

$$t_{ON_1} \sin \alpha + t_{OE_1} \cos \alpha = \frac{D}{v} \quad (6.5)$$

$$t_{ON_2} \sin \alpha + t_{OE_2} \cos \alpha = \frac{D}{v} \quad (6.6)$$

Solving the system above, the direction α can be determined and substituting the obtained value in one of the equations above gives back the speed of the cloud.

$$\alpha = \tan^{-1} \left[-\frac{t_{OE_2} - t_{OE_1}}{t_{ON_2} - t_{ON_1}} \right] \quad (6.7)$$

6.1.2.2 Procedure

Starting from the real measured data, a description of the procedure used to treat the GHI signals is presented.

First, a day that presents a GHI profile strongly affected by clouds is needed to test the algorithm; the selected day is the 10th of July 2013.

To test the method it is important to select a period of time characterized by the presence of many ‘‘cloud events’’ intended as both the passage of cloud edges and maxima/minima of cloud opacity factor that imply a high variability of GHI.

As shown in Figure 6.6 (top) a time range of a hour going from 16:30 p.m. to 17:30 p.m. is chosen because it is strongly affected by the cloud front with a high frequency of change in GHI value. Figure 6.6 (bottom) shows a zoom of the selected hour with the signals of each NE grid sensors presented.

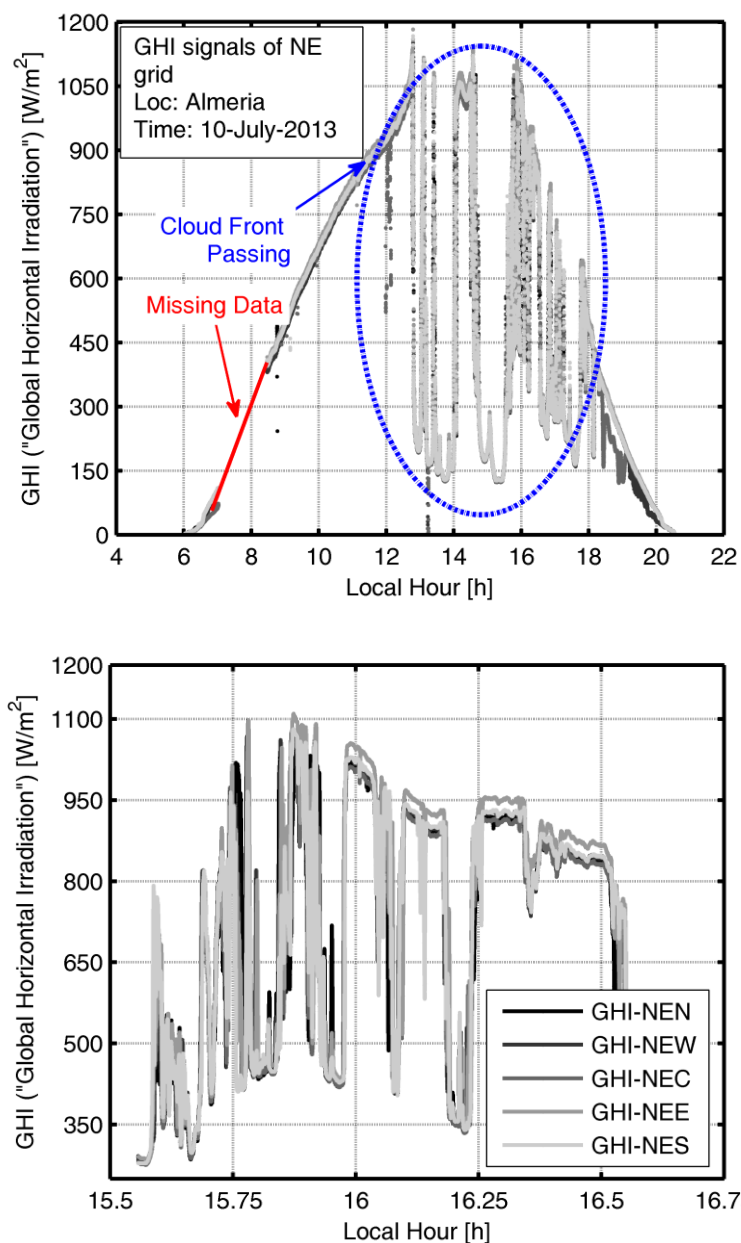


Figure 6.6 GHI profile measured 10th of July 2013 in the NE subgrid (top) and the selected range 15:30 to 16:30 (Local Time) (bottom).

As underlined in [5,14] a procedure to preprocess data is necessary with the aim of diminishing the level of noise that could be detected by the model as local maxima/minima thus leading to results with a high level of uncertainty. The preprocess procedure can be summarized in five separated steps:

1. A moving average to erase the highest level of noise
2. Global maxima are selected in a moving window of time. In this way the “events” with the highest GHI variability are identified.

The effect of the first two step of preprocessing is shown in Figure 6.7; in particular all the maxima/minima selected after the step-1 is represented by a circle (•) while the

maxima/minima resulting from the treatment of step 2 are enlightened by cross (x). It is noticeable how the preprocessing activity reduces gradually the number of “cloud events” accepted.

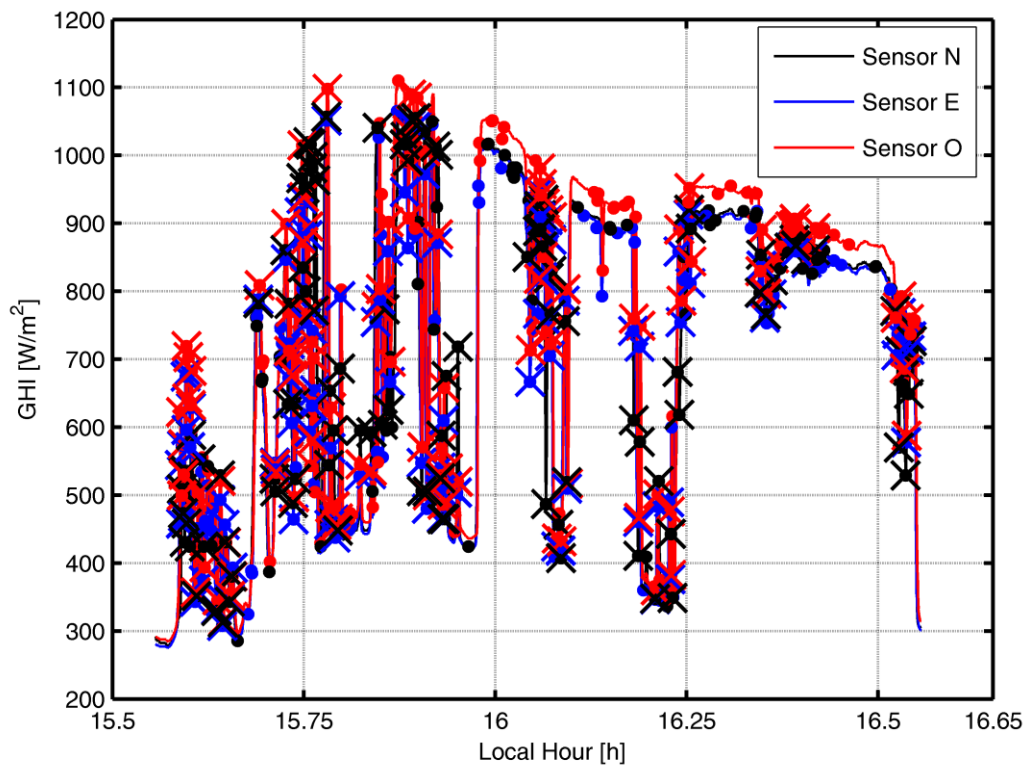


Figure 6.7 Selected maxima and minima after the first two (1-2) preprocess steps of GHI data

The next steps of the preprocessing procedure are:

3. Only maxima with 5 monotonous ascending/descending values are selected in order to have a high probability to capture relevant maxima/minima
4. Only simultaneous peaks are useful to identify the CMV. For that reason, the three maxima for each sensors are considered simultaneous if they are in a time range smaller than 10 sec.
5. As previously underlined, two cloud events are needed to use the LCE method. For that reason, two cloud events are required to occur within 2 min.

Figure 6.8 (top) shows the accepted maxima/minima, identified by a cross (x), in a selected time range of 15 min, while the plot in Figure 6.8 (bottom) shows nine cloud events that can be used by the LCE method. In particular, the three signals show a good agreement regarding the shape and each cloud events of each sensors can be easily identified and matched with the other two. In addition the time delay of the cloud event are easily identified.

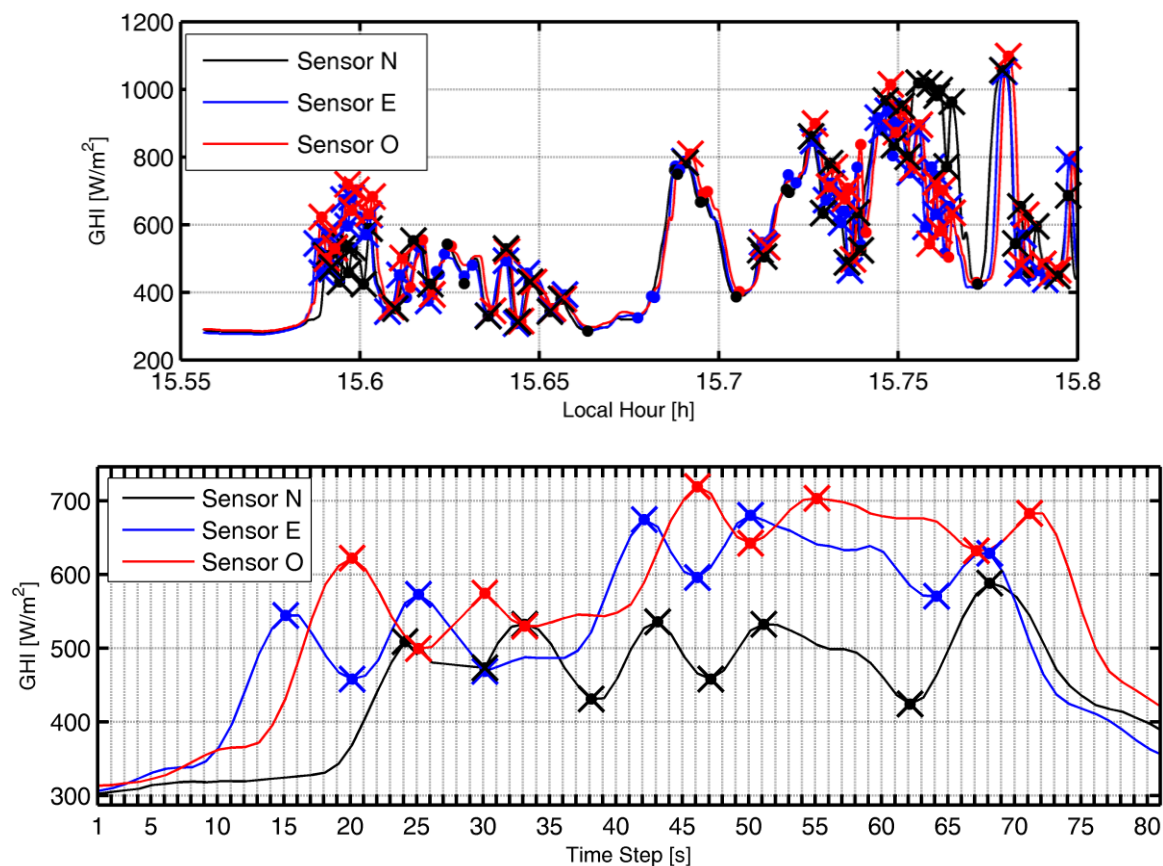


Figure 6.8 Effect on of steps 3-4-5 of the preprocessing. The dot series represent the “cloud events” obtain after the application of steps 1-2. Cross series are the selected cloud events that can be used by the LCE method (top). A zoom of the GHI series that shows nine cloud events in the first 80 seconds of the selected time range (bottom).

6.1.2.3 Results

Following all the steps outlined before and applying the geometric considerations written in 6.1.2.1, the LCE method gives back a series of different CMVs that need to be analyzed in order to figure out the most probable CMV in the selected time range.

In Figure 6.9, the computed CMVs are shown, the elements of the series are colored by density function that indicates the reciprocal vicinity of the points in order to understand the CVM that represents better the real movement of the cloud.

In Figure 6.10, an alternative visualization of results in form of histograms is proposed that helps to conclude that the CMV in the time range (16:30 pm – 17:30 pm) is characterized approximately by a direction E→W and a speed in the range 10 m/s-15 m/s.

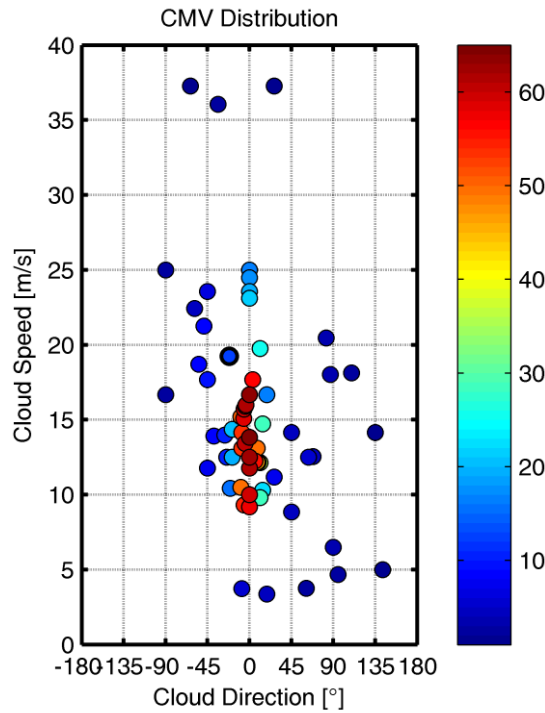
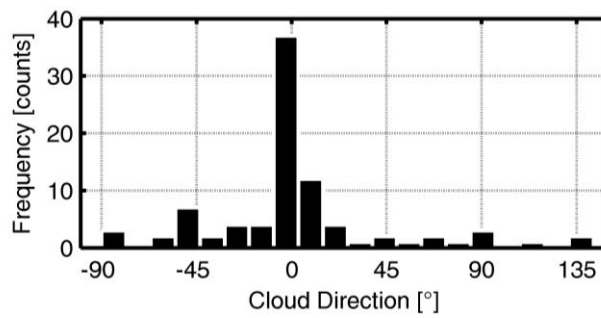


Figure 6.9 Distribution of CMV (speed and direction) colored by the density function.



Cloud Direction at Almeria Solar Facility:

- N-->90°
- S-->270°
- W-->180°
- E-->0°

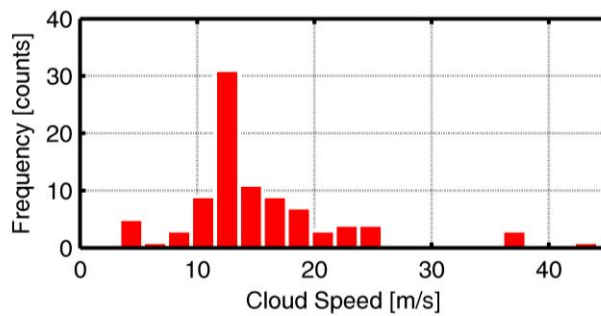
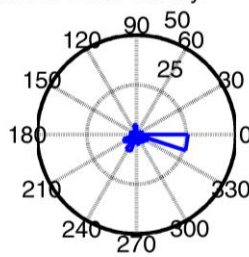


Figure 6.10 Cloud speed and direction distribution of the obtained results.

It is worth to notice that this approach gives a sort of probability information thus implying a certain level of uncertainty. The increment in the frequency of sampling could help to obtain results that are more reliable but increasing at the same times the cost of the equipment and the noise effect. For that reason, a trade-off between reliability and investment cost occurs thus requesting an analysis to identify the best equipment components.

6.1.3 Most Correlated Pair model

The second method that can be used to determine the CMV, using a set of ground measured data, is a model based on the cross correlation analysis of the signals. In particular, in [4] is stated that “for a pair of sensors aligned with the cloud movement, the signals of irradiance I_A and I_B are highly correlated and it is possible to obtain the highest correlation if the upwind sensor time series is lagged by the travel time of the cloud between sensors”.

After reminding the definition of cross correlation of two signals expressed by (6.8) (e.g. A and B as shown in Figure 6.11), it is possible, in principle, to analyze different pairs of signals in order to find the best cross correlated pair [15]:

$$r_k = \frac{\sum_{i=1}^n (I_{A_i} - \bar{I}_A) (I_{B_i} - \bar{I}_B)}{\sqrt{\sum_{i=1}^n (I_{A_i} - \bar{I}_A)^2} \sqrt{\sum_{i=1}^n (I_{B_i} - \bar{I}_B)^2}} \quad (6.8)$$

The most cross-correlated pair indicates the direction of the cloud vector while, once the time lag is determined and the distance between the two sensors is known, it is possible to calculate the velocity of cloud:

$$v = \frac{D}{t_{AB}} \quad (6.9)$$

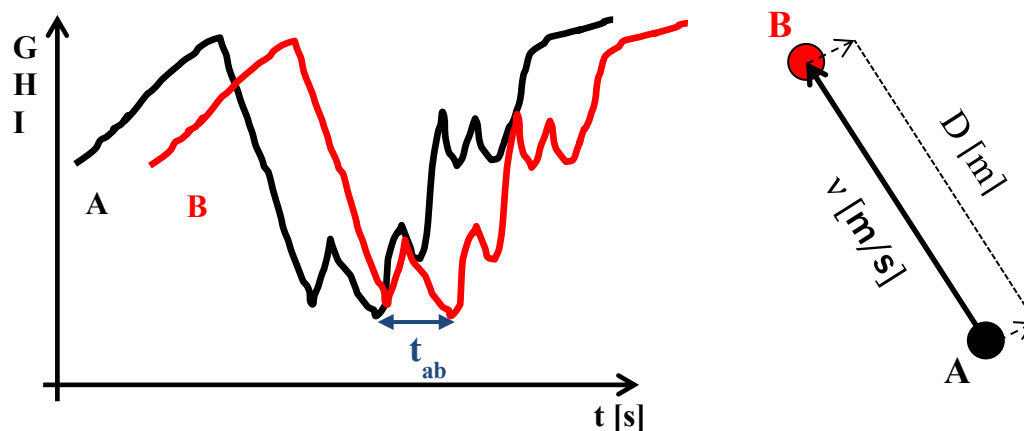


Figure 6.1 Draw that shows two signals (A and B) perfectly translated in time with enlightened their time lapse (left) and the clod vector perfectly aligned with the two sensors of the considered pair (A, B).

In this work, the MCP method is used to have a “rough” validation of the results obtained with the LCE; in particular, for the available ”diamond” layout only few directions can be investigated and this limitation leads to results that are useful only to have an estimation with a high level of uncertainty. In particular, once the direction of CMV calculated with the LCE is $E \rightarrow W$ the most correlated pair should be the NEE and NCE.

Regarding the NE “diamond” data, the time range processed with LCE method is split in time steps of 250 s in order to evaluate if the obtained results are reasonable. The CMVs for each time range are listed in Table 6.2; it is worth to notice that the most of calculated CMVs are in accordance to those derived from the LCE model partially confirming the previous results.

Table 6.2 Most correlated pairs obtained with the MCP method in different time range. The value that present some discrepancy are enlightened.

MCP Results		
Time Range [s]	Direction [-]	Speed [m/s]
1-251	W \rightarrow E	12,5
251-501	N \rightarrow S	∞
501-751	W \rightarrow E	12,5
751-1001	W \rightarrow E	12,5
1001-1251	W \rightarrow E	16,7
1251-1501	W \rightarrow E	12,5
1501-1751	N \rightarrow S	∞
1751-2001	W \rightarrow E	12,5
2001-2251	W \rightarrow E	12,5
2251-2501	W \rightarrow E	16,7
2501-2751	W \rightarrow E	12,5
2751-3001	NW \rightarrow SE	23,6
3001-3251	NW \rightarrow SE	23,6
3251-3501	NW \rightarrow SE	23,6

In Figure 6.12, the GHI profile relative to the first time range (1-250 s) (up) and the cross correlation value of the most cross correlated pair are presented showing the existing time lags among the five signals (bottom).

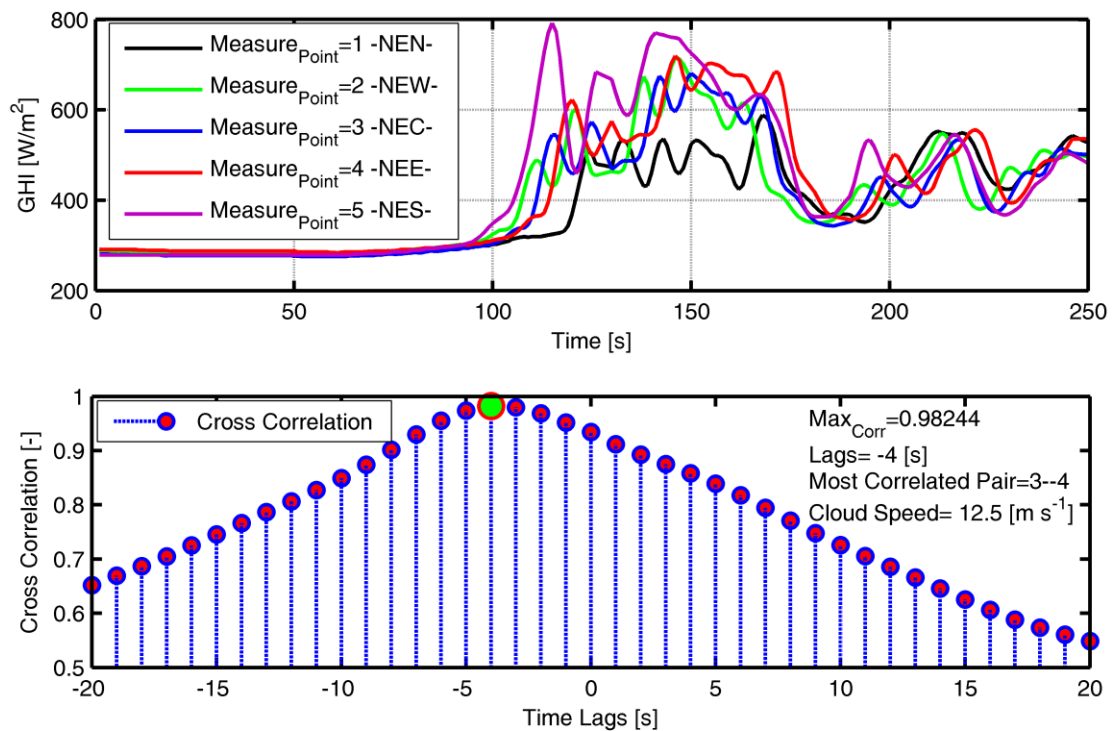


Figure 6.12 Example of the GHI profiles measured by the NE “diamond” of the grid (up) and cross correlation value for the most correlated pair (the time lag is enlightened) (bottom).

From the table above two different categories of CMV results that disagree with the LCE’s output can be enlightened (red and green). The red data categorize results that completely disagree with the LCE; in particular, the time periods of this data are characterized by a GHI profile which is more or less flat as occurs in Figure 6.13, for this period the calculation of cross-correlation gives meaningless output due to the absence of a cloud front.

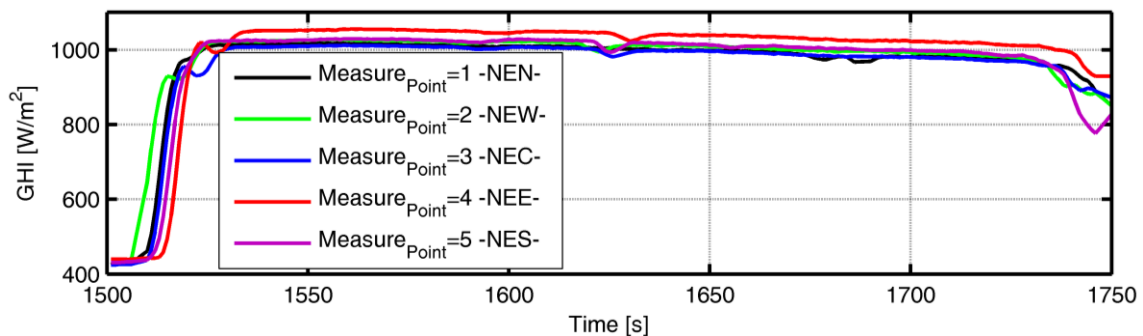


Figure 6.13 GHI profile measured by the NE “diamond” for the time range 1501-1750 s.

As regards the green values, their presence at the end of the selected hour could be an evidence of a change of CMV that rotates from $W \rightarrow E$ to $NW \rightarrow SE$.

6.1.3.1 Possible alternative layout

As far a qualitative comparison between the LCE method and the MCP concerns, it is worth to underline that MCP method is more reliable than the LCE method because of its strong math basis. On the contrary, it has some critical points that make this procedure not convenient for the available experimental facility. In particular, many sensors are needed in order to span a lot of possible directions (pair of sensors) and the signals have to be well calibrated in order to not add noise that can jeopardize the cross correlation analysis.

Regarding the available experimental setup, it is possible to identify a certain number of directions as shown in Figure 6.14 but in this case, the problem of different distance among pairs arises adding another uncertainty that makes the comparison between the two methods more difficult.

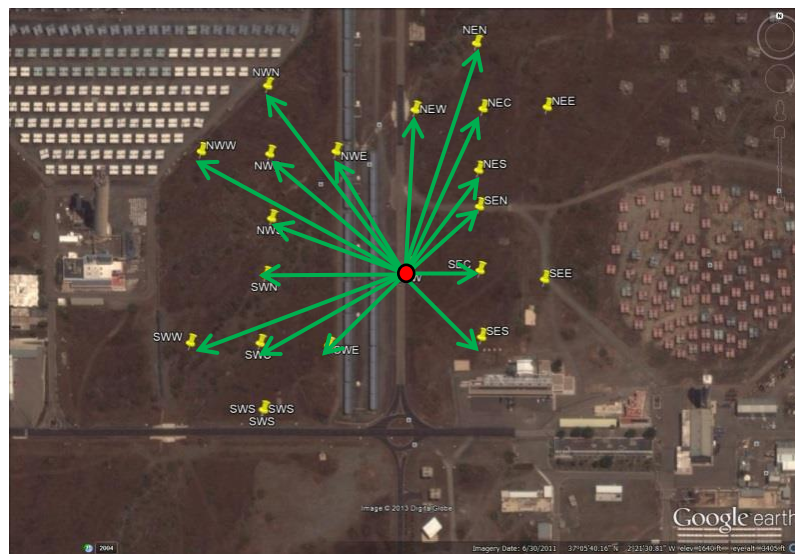


Figure 6.14 Available directions for the grid layout at Plataforma de Almeria

As stated in [4] a good disposition of sensors can be the one drawn in Figure 6.15 that enables to study different directions. The semicircular lay-out implies an equal distance between sensors.

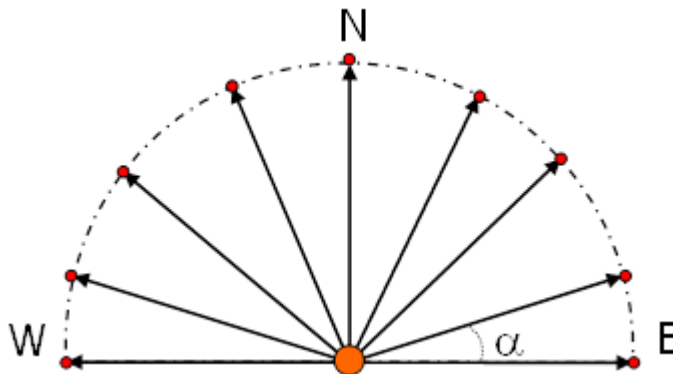


Figure 6.15 Semi-circle configuration of measurement point with 10 sensors (n=10).

Obviously, the accuracy of direction and speed prediction depends on the number of adopted sensors. A simple relation, extrapolated with straightforward geometrical considerations, can be used to calculate the accuracy (ε) of the semicircle configuration reported in Figure 6.15:

$$\varepsilon_{dir} = \frac{180^\circ}{2(n-1)} \quad (6.10)$$

$$\varepsilon_{speed} = 1 - \cos \frac{\alpha}{2} \quad (6.11)$$

6.1.4 Qualitative comparison

Once the LCE and MCP method are described and the results obtained are found to be in accordance, some conclusions about a qualitative comparison can be drawn in order to outline the advantage/disadvantage of both models in relation to their range of applicability in CSP sector.

As regards the MCP method, it is worth to underline that it is the ground base method and allows having the most reliable results. On the contrary, it needs a big number of sensors in order to span many directions leading to an increment of both investment and O&M cost. Another requirement is that the sensors have to be well calibrated in order to give back, as output, signals well-suited for the cross correlation analysis.

Regarding the LCE method, a triplet of sensors is sufficient thus implying a cheaper system than for the MCP method. The characteristic of LCE of treating the shape of the signals in form of maxima/minima allows working with sensors that do not need an accurate calibration. These considerations can lead to the conclusion that LCE method could be an interesting solution to forecast the effect of a cloud front before it reaches the solar field. In particular, this possibility could be exploited in direct steam generation (“DSG”) plants that are known to be more subject to solar radiation change than CSP plants that use a single phase HTF. As an example, it is possible to imagine some sensors triplets placed along the perimeter of the solar field that can identify both the direction and the speed of the cloud front before it reaches the solar field. In this way, the plant operator has a certain time to adjust some control parameter thus simplifying the solar field operation and avoiding unsafe operating conditions.

6.2 Opacity Matrix

In addition to the CMV, the experimental facility can be exploited to obtain the cloud opacity spatial pattern. This info can be added to the thermo-fluid model in order to increase the level of accuracy of the simulations and to evaluate if some relevant effects on solar field performance could occur.

To evaluate a reliable cloud opacity pattern, a column of sensors (N-S) is selected and the measured DNI profile is compared to a clear sky approximation in order to calculate the parameter named “cloud opacity” and defined as follow:

$$OP[-] = \left(1 - \frac{DNI_{cloud}}{DNI_{clear-sky}} \right) \tag{6.12}$$

As regards the values of the defined cloud opacity 0 represents a total transmittance while 1 stands for a total cover condition.

The real GHI profile measured by the NE and the clear sky approximation, which is used to estimate the DNI with relation (1.1) , are presented in Figure 6.16.

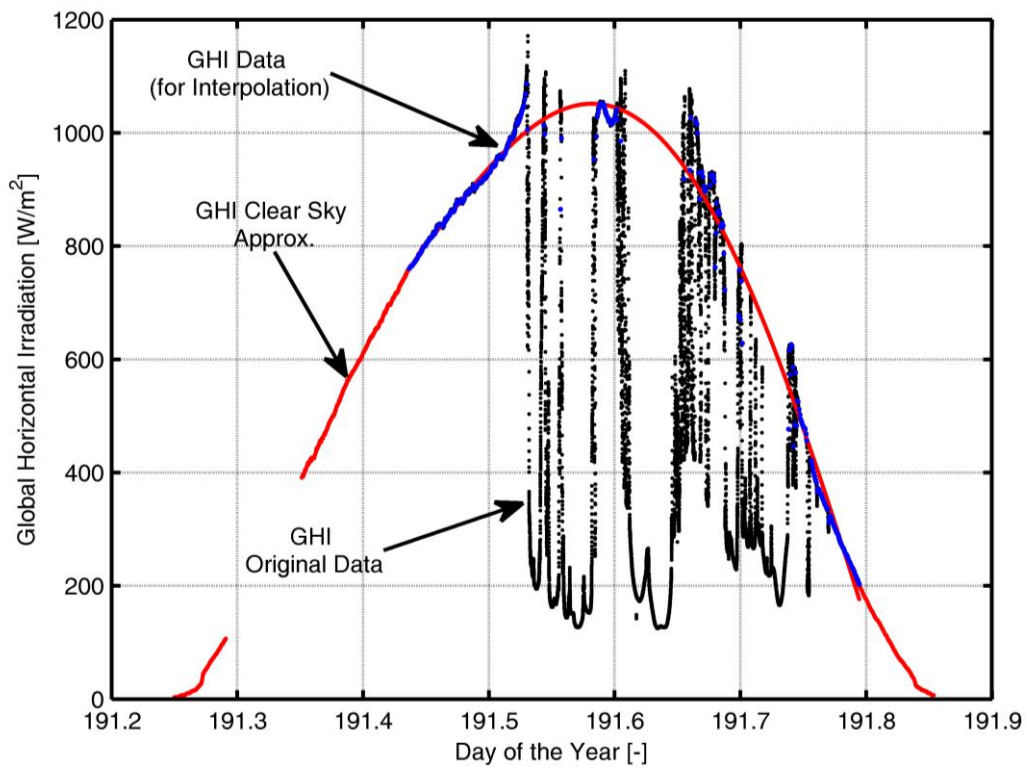


Figure 6.16 Real GHI profile measured by NEC (black) and its approximation of a clear-sky condition (red).

In Figure 6.17 a graphic explanation of procedure to attain the cloud opacity is shown in relation to the position of a pseudo solar field with N-S tracking axes and to the CMV computed before. Every n-seconds the solar radiation is recorded in each sensors of the column, in this way it is possible to build a 2-D map of cloud opacity.

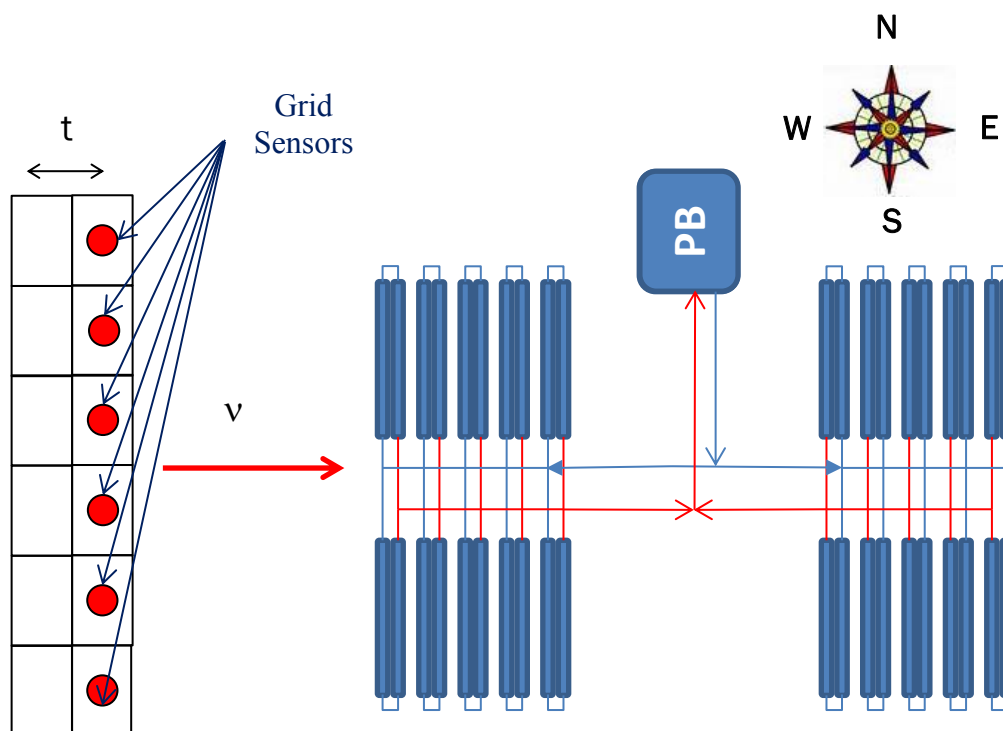


Figure 6.17 PT field compared to a hypothetical column of sensors to capture the opacity pattern.

With the aim of decreasing the dimension of the matrix and consequently to avoid high computational efforts for the thermo-hydraulic model, a 5 min time range is chosen with a sampling time range of 4 s that gives a space resolution of 50 m (the cloud speed is 12.5 m/s). The corresponding cloud opacity pattern is reported in Figure 6.18 (idealized as a rectangular matrix). Due to the available measurement points the rectangle height is 300 m but in the next parts the cloud is mirrored along axis (W-E) in order to cover the solar field symmetrically.

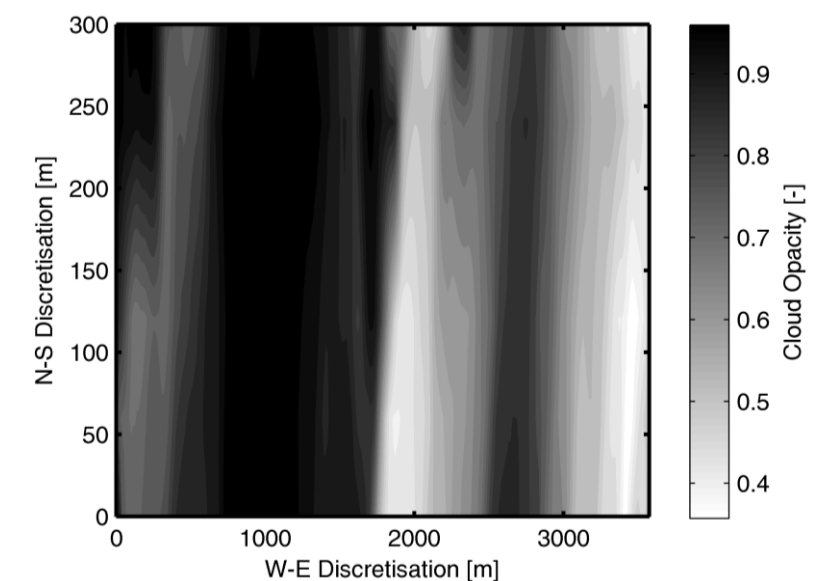


Figure 6.18 Cloud Opacity measured by the sensors grid 10th of July 2013 during the time range 16:30 pm– 16:35 pm (CMV: direction= W→E speed=12.5 m/s)

6.2.1 Solar field simulation with cloud opacity matrix

This section presents the study of the transient analysis with the cloud information obtained with the analysis described above (e.g. CMV and opacity pattern). In particular three cases with different opacity patterns are shown; the first case considers the real opacity matrix of Figure 6.18, the second case has the same geometrical dimension but an uniform opacity value equal to the mean value of the first case (opacity=0.65) and the last case considers an uniform opacity value of 1. As it is possible to notice from Figure 6.19, that shows the loop outlet temperature of each case, the introduction of the opacity matrix does not seem to lead significant differences if compared to the case that considers a mean value of opacity. The main effect is represented by the temperature oscillations that are caused by the cloud opacity bands well identifiable from the graphical representation of the opacity matrix. The biggest difference obviously arises comparing the “real” cloud with the case with a uniform value because of the different “shaded energy”.

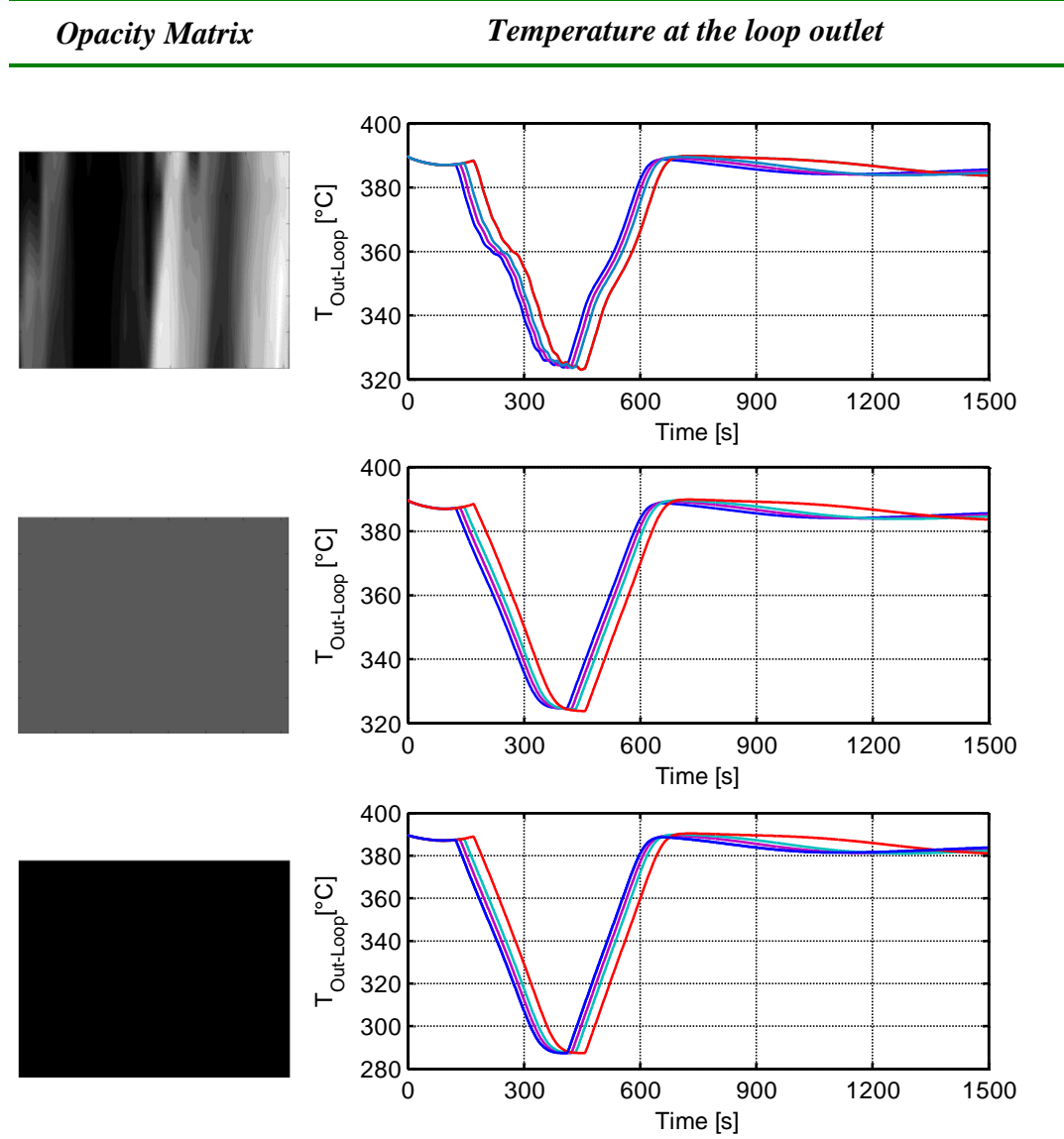


Figure 6.19 Outlet temperature profile for different opacity modelling of the moving disturbance.

The obtained results help to conclude that the addition of an accurate cloud opacity pattern representation does not produce additional info that could modify the considerations made before related to a uniform opacity map. It is important to underline that, even if an exact pattern matrix is not necessary, the modelling approach considering an unit value of opacity is too limiting and can lead to results very different from the real condition.

6.2.2 Idealized disturbance patterns

In order to go deeper in the understanding of the solar field transient behavior, three idealized cloud disturbance patterns are considered. Some bounds to the characteristics of the disturbance are fixed in order to establish a fair comparison about the effects on the solar field performance of the different disturbance characteristics.

The three disturbances are all characterized by different values of opacity and they are chosen to have the same integral value of opacity during time (see. Equation (6.13)):

$$I_{OP} = \int_{t_{in}}^{t_{fin}} OP dt \quad (6.13)$$

Because of the same geometrical dimension of the “square cloud”, the last condition is achieved varying the speed of the disturbance.

To concentrate the attention on the disturbance effect, the HTF total mass flow rate is maintained constant to the design value and the weather EDNI value is considered uniform in space and constant during simulation time (1000 W/m²).

Considering boundary conditions of the chosen idealized disturbances, the case #1 is represented by a “square cloud” with an opacity value of one moving at 12.5 m/s in direction W-E, the case #2 has an uniform opacity equal to 0.5 and velocity half than the case #1.

The last case considered (case #3), has an opacity distribution with three bands of total covering and three clear bands; to maintain the same opacity integral the velocity is equal to case #2.

The three disturbance profiles are graphically presented in Figure 6.20 both in a Cloud opacity-Time Cartesian space and through a sketch of the cloud, showing the main parameters necessary to identify completely the boundary conditions.

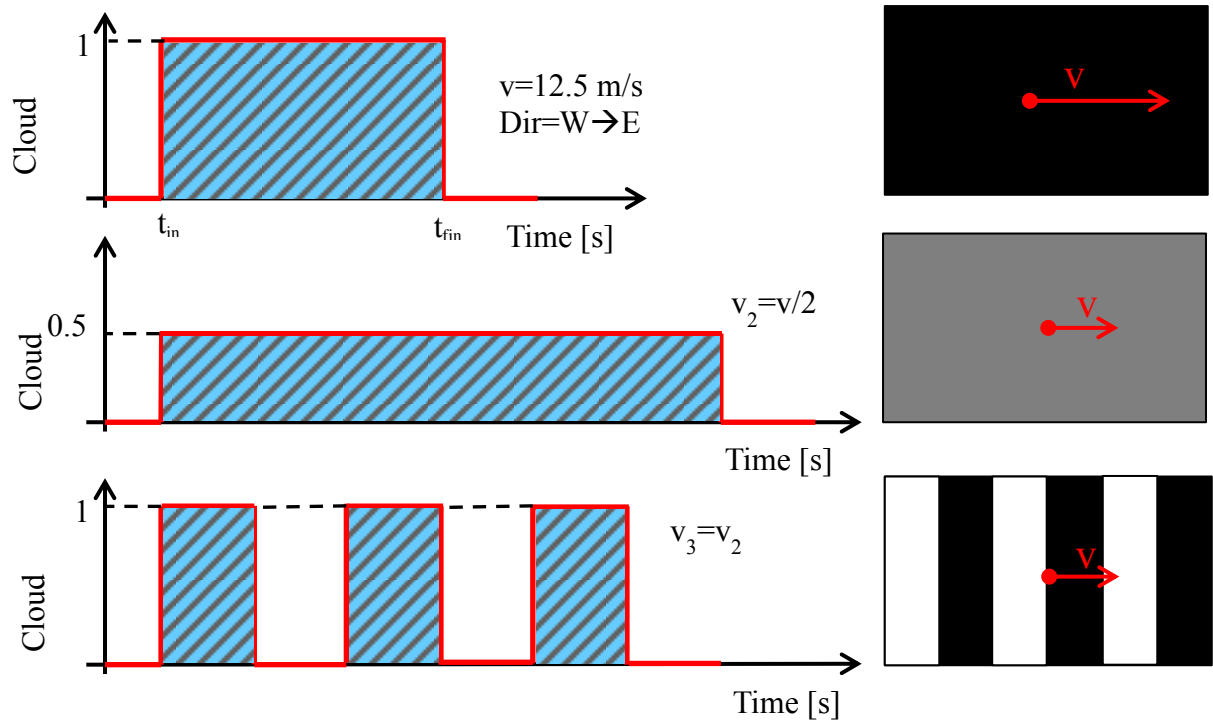


Figure 6.20 Idealized Cloud disturbance signals that are taken into account.

6.2.2.1 Simulation results

The response of the solar field to the three disturbances is studied with the transient model described in Chapter 4. The first parameter that is considered is the outlet temperature of each loops shown in Figure 6.21 for each cases. In order to facilitate the explanation of the results five zones of the temperature outlet profile can be identified:

1. *Initial approaching*: it terminates when the cloud front approaches the solar field.
2. *Cool down zone*: the shading effect shows its effect reducing the outlet temperature of the loop.
3. *Intermediate zone*: After the cool down, the outlet temperature shows a more or less stable area where the temperature oscillations are very small.
4. *Heat up zone*: the disturbance progressively moves over and the energy impinging on the solar field increase heating up the absorbers.
5. *Reaching stationary*: After the strong gradient of the “Heat up zone”, the temperature tends to the design value.

From the comparison among the plots of Figure 6.21, the difference in time duration of the first zone can be noted because of the different cloud speed that influences the instant when the shading square starts to cover the solar field. In particular, the disturb-1- has a shorter “initial approaching” phase due to its higher speed.

The shape of the “Cool down” zone is strongly influenced by the value of opacity that determines the temperature gradient; in particular, both case#1 and case#3 show the same cooling gradient because of the unit value of opacity.

As regards the “Intermediate zone”, the time extension reflects the movement speed of the disturbance, whereas the temperature value depends on the opacity value. In every case, the outlet temperature reaches a value near to the steady condition relative to the effective impinging solar energy. In case#3, temperature oscillations arise because of the disturbance profile (see Figure 6.20) that does not allow a complete temperature stabilization.

The “Heat up” zone has the same characteristics of the “Cool down” zone previously described.

Regarding the last zone, it is possible to notice the same trend for each case that tends to reach the steady state condition.

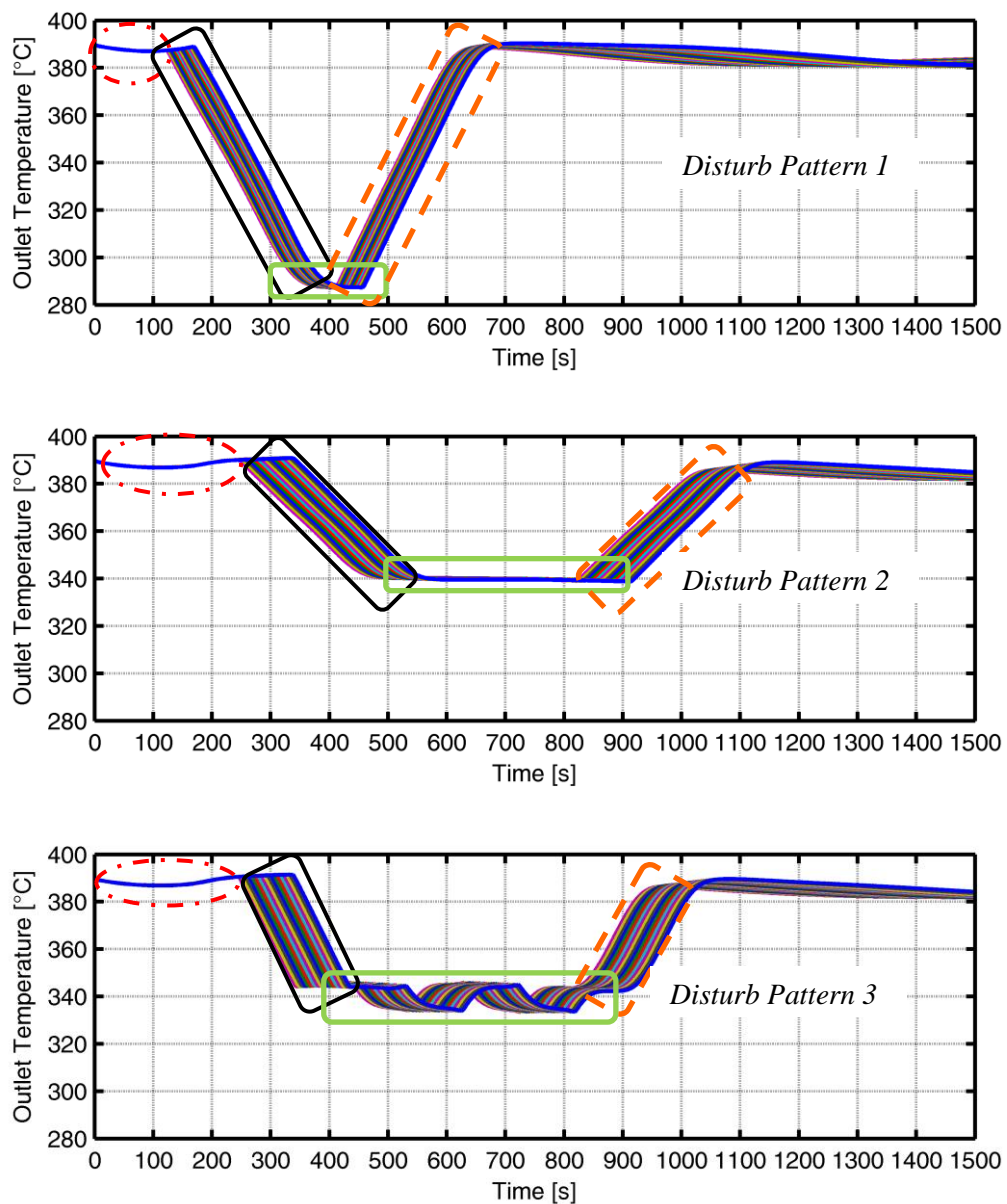


Figure 6.21 Loop outlet temperature of the investigated cases

The temperature maps of the westward loop of the investigated cases are shown in Figure 6.22. The same zones outlined about the outlet temperature can be recognized for each loop longitudinal positions.

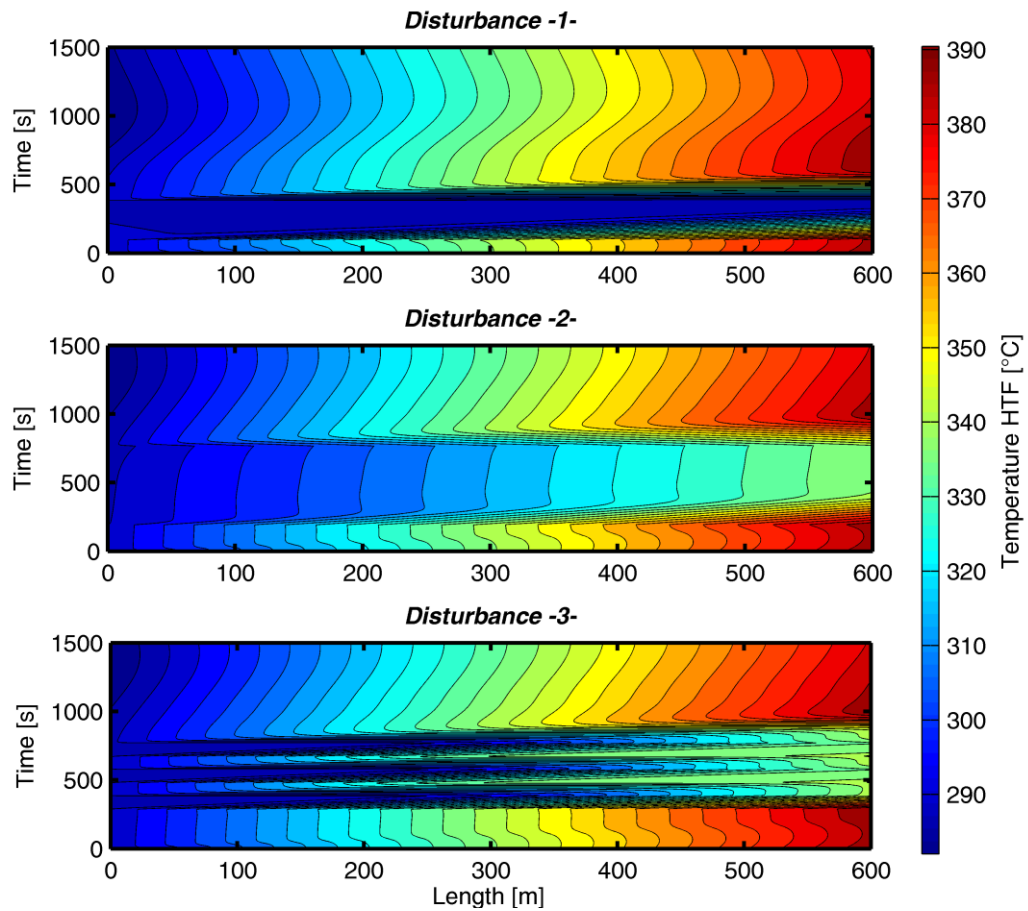


Figure 6.22 Temperature map of the last loop for the three investigated cases

In Figure 6.23, the temperature at the expansion tank outlet is shown for the three investigated cases. The disturbance#1 has the steepest decrease of temperature due to the total opacity of the square disturbance. Comparing the disturbance#2 and disturbance#3 the same temperature profile shape can be observed with a time delay caused by the different temperature gradient as observed in Figure 6.21. In particular, the use of a uniform opacity allows obtaining a HTF temperature of the stream sent to the power block that shows small differences from the case with three opacity bands; this can justify the adoption of this simplified modelling approach.

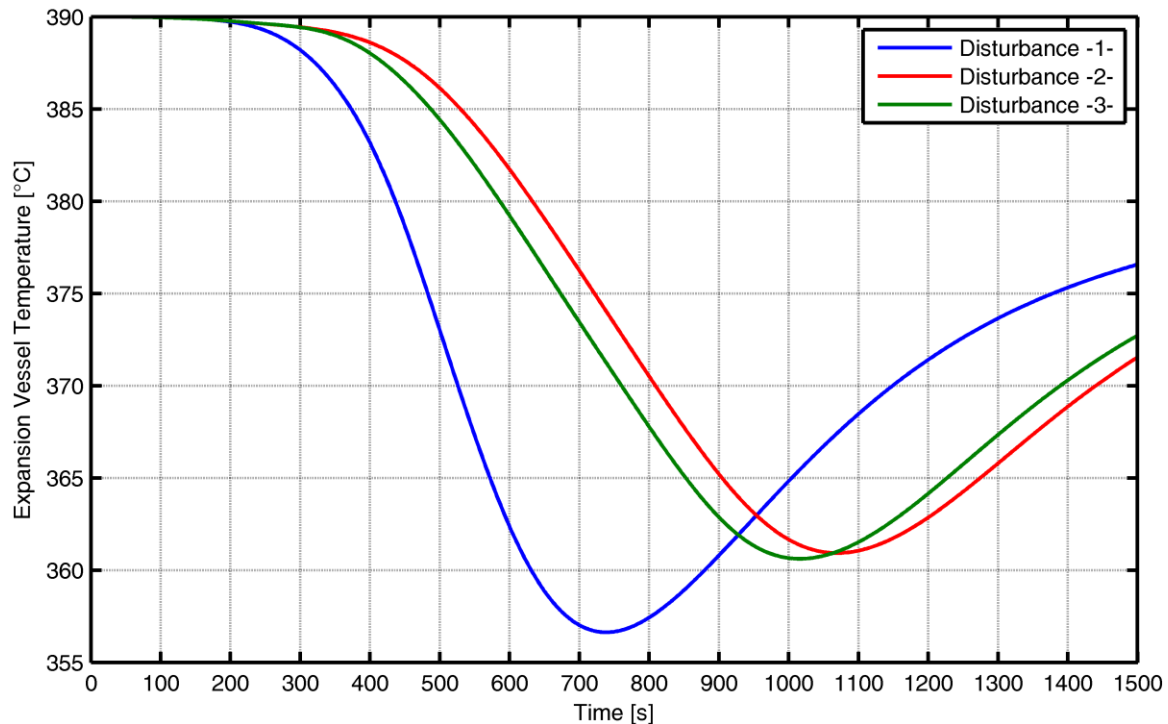


Figure 6.23 Temperature at the outlet of the expansion tank for the three investigated cases

6.3 Bibliography

- [1] Modica GD, d'Entremont R, Mlawer E, Gustafson G. Short-range Solar Radiation Forecasts in Support of Smart-grid Technology.
- [2] Solar Millennium. Solar Millennium AG - The Construction of the Andasol Power Plants. - Archives - Technology - References and Projects - Andasol (Spain) 2012;2012.
- [3] Wood-Bradley P, Zapata J, Pye J. Cloud tracking with optical flow for short-term solar forecasting.
- [4] Bosch JL, Zheng Y, Kleissl J. Deriving cloud velocity from an array of solar radiation measurements. *Solar Energy* 2013;87:196-203.
- [5] Bosch JL, Kleissl J. Cloud motion vectors from a network of ground sensors in a solar power plant. *Solar Energy* 2013;95:13-20.
- [6] Ciemat. Plataforma Solar di ALmeria "PSA" 2013.
- [7] DLR ("Deutsches Zentrum für Luft- und Raumfahrt"). DLR - Institute of Solar Research 2013.
- [8] DLR - Institute of Solar Research. Plataforma Solar de Almeria: " Research under Practical Conditions in Europe"biggest Test Center for Concentrating Solar Power (CSP) 2011.
- [9] Google Inc. Google Earth 2013.
- [10] Duffie JA, Beckman WA. *Solar Engineering of Thermal Processes* Wiley: Hoboken, NJ; 2006.
- [11] Reda I, Andreas A. Solar position algorithm for solar radiation applications. *Solar Energy* 2004;76:577-589.

- [12] Kleissl J, Coimbra CFM, Washom B. Solar Variability, Forecasting, and Modeling Tools.
- [13] Regiomontanus J, Petrejus J, Schöner J. De Triangulis Omnimodis Libri Quinque In aedibus Io. Petrei; 1533.
- [14] Bosch JL, Zheng Y, Kleissl J. Cloud velocity estimation from an array of solar radiation measurements. World Renew Energy Forum, WREF, Incl World Renew Energy Congr , Colorado Renew Energy Soc (CRES) Annu Conf 2012;3:1968-1973.
- [15] Zheng Y, Zhang X, Peng G. Cloud Motion Derivation with a Pyranometer Array Measurements.

7 Energetic Comparison

The last part of the PhD work deals with an approximate analysis of the difference in the annual energy yield simulation between a quasi-steady state approach and the model that is presented in the previous chapters. The goal of this part of the study is to evaluate the difference in the energetic production in order to understand how neglecting main transient effects in quasi-steady simulation penalizes the results accuracy. It is important to underline that this study is only addressed to estimate the difference in energy yield results and for that reason some simplificative assumptions has been made.

As regards the quasi-steady state modelling approach, Thermoflex-23[®] is used in agreement with the method considered to extrapolate the polynomial description.

As far the solar field is concerned, the same technology and physical dimensions are used in agreement with the studies of previous chapters.

7.1 Quasi-steady vs. Transient model

The comparison between the two models can be made considering different time periods and DNI conditions; in this section the simulation results of representative days and weeks are reported in order to compare the performance predictions of the two considered approaches and to quantify how the modelling of transients could be beneficial in making the simulation results more accurate. As regards the state-of-the-art modelling tools that are based on the quasi-steady approach, three simple ways to account for transient effects without a direct modelling can be identified as stated by [1]. In the most simple, an hourly basis simulation is performed and correction factor is applied to the annual electricity yield. The second solution can be the selection of a DNI or EDNI threshold that acts as a limit to power production that can be corrected with a single factor. The last way-out can be represented by the addition of a time delay to the power-block start time. Different combinations of the three methods described can be implemented; in particular, the simulations models developed by the Gecos group, as described in Chapter 3 , implement a DNI threshold and an empirical time-delay parameter.

In the following subsections, the main assumptions of both the solar field and power block modelling are presented and the results of the energetic performance are provided.

The selected location for the CSP plant is Eldorado Valley (35° 52' 12.66" N, 114° 55' 58.5" W) and the available DNI data are sampled with a time step of 1 min. The choice of a quite short-time data resolution aims to allow the short-term fluctuations of solar irradiance to be captured. As underlined by [2], a broken clouds condition can be hidden by an hourly time resolution. For example, an intermediate value of 500 W/m² at 12:00 in an hourly weather data series can be caused, with a high level of probability, by a cloud front that can be identified only with measured data sampled more frequently than every hour. To clarify the impact of the data resolution, we can focus the attention on the qualitative results of a quasi-steady model, which will predict a constant output correspondent to 500 W/m² whereas, for a high resolution DNI data that hour, whose

mean value is 500 W/m^2 , could be affected by a certain number of start-up and shut-down produced by the cloud front passage.

7.1.1 Solar field model simplification

The CSP plant model that considers the solar field transient behavior can be used to simulate the energetic output for time periods that are suitable for this kind of purpose (e.g. days). Obviously, a trade-off between the requested accuracy and the computational efforts is to be taken into account.

In particular, as reported in Chapter 2 “Quasi-steady states model”, the annual electricity yield is commonly performed with time steps of one hour because of the format file of the weather data sources [3,4]. This fact, in addition to the time-step adaptive peculiarity of the ODE solvers, leads to a huge set of output points that cannot be handle by the developed transient model.

It is important to remember how the developed model is characterized by a level of accuracy that allows studying in detail some particular operating situations of the system but due to the intrinsic complexity related to the modelling of every loop, it implies strong computational energies. In addition, a big amount of computational resources is requested by the hydraulic network calculation too. This characteristic makes the model usable for short time period analysis but not applicable to long time periods.

For that reason, some simplifications, in addition to the assumption described in the Chapter 4, can be made in order to have a shorter running time of the model with the aim of decreasing the associated computational requests without an unacceptable decrease of the accuracy level.

With the purpose of maintaining a suitable level of accuracy and increase the simulation efficiency to perform an energetic analysis, the following simplifications are used:

1. An empirical heat loss model can be used instead of solving the detailed thermal resistance network described in Chapter 4. The empirical heat loss formulation of different absorber technologies can be found in literature [5,6] or can be derived from a parametric study made with specific models (in-house developed or found in literature) [7,8]. The behavior of a specific absorber tube can be approximated with a polynomial function of the absorber wall temperature and, in order to identify the parameters that mainly affect the heat losses, a parametric study was made with the model described in [9]. The obtained results are in agreement to previous works [10,11] and underline that, as a first approximation, once the technology was set, the HCE heat loss can be modeled as a function of the temperature difference between the receiver tube temperature and the ambient temperature as reported below:

$$q_{loss} = f(T_{abs} - T_{amb}) \quad (7.1)$$

2. All the loops that constitute the solar field can be substituted with a representative loop. In this way the number of equations is reduced losing information related both to the spatial distribution of the solar radiation and to the mass flow unbalance. Therefore, the total mass flow is considered to be equally distributed in each loop.
3. The DNI disturbance is not modeled with the square cloud approach and a uniform impinging solar energy is assumed. In this way the calculation of the shading area, that represents one of the highest computational bottleneck, does not affect the computational time.

Regarding the last point of the list above, some additional considerations have to be made when deciding how to use the DNI data; in particular, the literature available DNI data are measured in a single point thus not considering the spatial distribution of a cloud front. This constraint limits the applicability of the complete transient model only in study that has a grid base measured data sampled for a long time period (e.g. one year). Consequently, the solar field spatial modelling cannot be exploited completely and for that can be reasonably neglected.

As reported before, the available weather data does not contain any info about ambient temperature and for that reason, the effect of ambient temperature on the power block performance is neglected. This restriction does not limit the correctness of the comparison offered below.

7.1.2 Power block modelling

In agreement with the approach outlined in Chapter 5, the power block is modeled through a polynomial approach derived by parametric studies run with Thermoflex23[®]. The power block layout, representative of the state-of-art of large scale CSP power plant, has the same characteristics shown in Chapter 5.

In the transient model, the power block is supposed to start/stop when the HTF temperature (outlet of expansion tank) is equal to 300°C. As regards the power output, a lower bound is set to the 10% of the design value in accordance with [9].

7.1.3 Clear sky daily simulation

As a first stage, in order to not superpose the effect of steep DNI variations caused by cloud passage, two clear sky days are selected and in this way, only the influence of the incidence angle is taken into account by the selection of two days in different seasons (21st June – Summer Solstice-) and (24th of December).

In addition to the previously described assumptions, the total HTF mass flow value is proportional to EDNI with a minimum limit set to 25% of the design value as advised by [12].

In Figure 7.1 the power ratio, the DNI and the EDNI of the chosen days are reported.

Considering the results of 21st of July, some typical differences between the two methodologies can be noticed. Considering the transient mode (light blue) the power ratio trend shows an initial time delay in starting time because of the solar field thermal inertia

that identifies the thermal energy needed to heat up both the steel and HTF masses till the operating threshold temperature (300°C). The difference between the two modelling approaches diminishes progressively reaching an equivalent prediction for both the two models occurring approximately at 10:00 LST. Because of the low gradient of EDNI due to the incidence angle effect, typical of a summer day (particularly in the summer solstice), the two models keep on predicting the same power output ratio. This power performance correspondence is maintained until the solar energy captured by the solar field is insufficient for the quasi-steady model to produce electric energy. On the opposite side, the transient model captures the presence of the thermal inertia of the solar field, showing how the power plant exploits the residual thermal energy mainly contained in the expansion vessel system and in the hot header. This situation can be appreciated in qualitative terms by visiting a real operating plant that carry on producing electricity even if the EDNI is zero (i.e. due to the reciprocal mirrors shading during the morning).

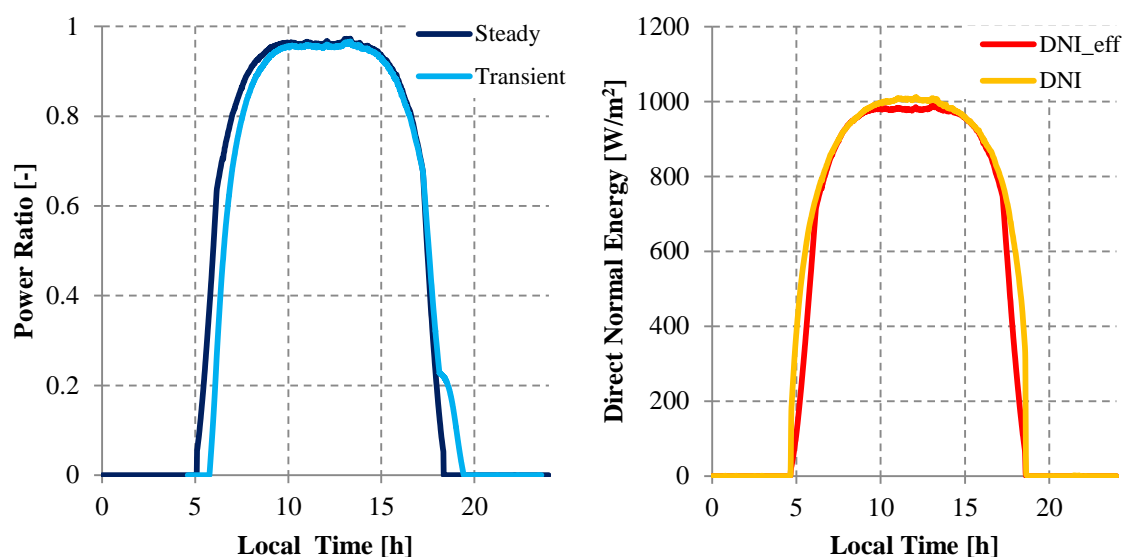


Figure 7.1 Power ratio prediction of the two investigated models (left) and DNI and EDNI trend (right) for 21st of June.

In Figure 7.2 the results of the comparison of the winter day are presented. The power ratio profiles related to the clear-sky winter day indicate the strong part-load operation of the plant that is caused by the relevant penalty effects of the incidence angle described in Chapter 2 (see. Figure 7.2 (left)). The winter EDNI is not sufficient to heat up the system as fast as during the summer day and thus leading to a longer heat-up period. Once the power ratio of transient model reaches the similar value of the quasi-steady model, the same behavior described for the summer day can be appreciated; in particular at the end of the day, with a zero DNI, the power block continue to produce electric power.

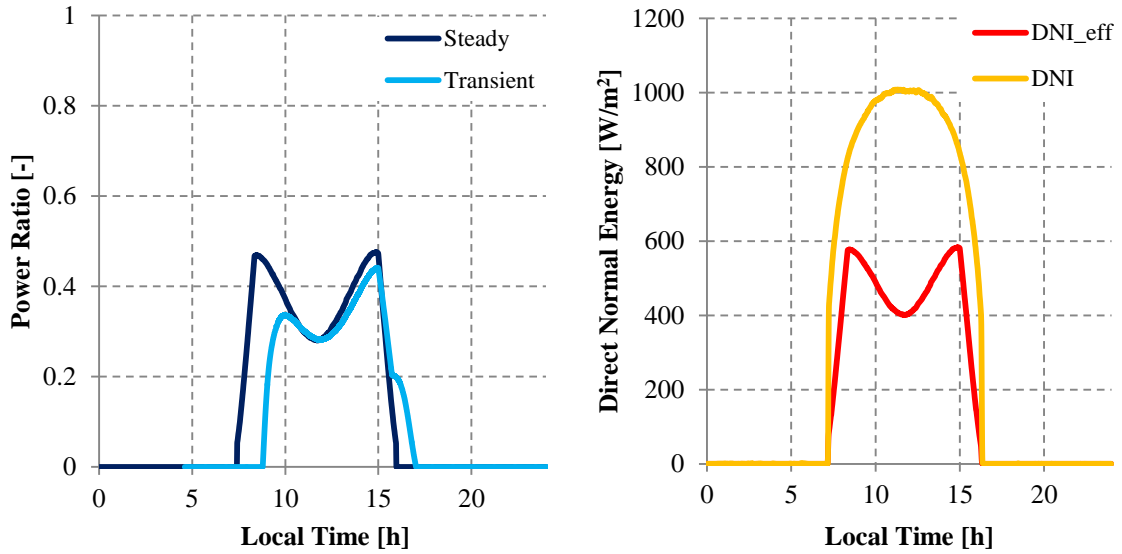


Figure 7.2 Power ratio prediction of the two investigated models (left) and DNI and EDNI trend (right) for 31st of December.

The energetic comparison between the two models is performed considering the integral value of the “power ratio”. As expected from the previous discussion and in agreement with other studies found in literature [1,2,13] the quasi-steady model overestimates the electricity production; in particular the selected summer day results show an overestimation of about 5% while in the winter day the overestimation increases to a value of 19.8 %.

Although only two clear-sky days are selected, it is possible to conclude that the start-up energy demand, mainly necessary to heat the mass of steel and HTF, strongly influences the energetic yield prediction of the CSP plant and some precautions have to be taken into account to correct the quasi-steady results. In addition, it is important to underline that the developed transient model ignores the specific start-up sequence of the power block section that can be briefly summarized by: heating-up of the heat exchanges train, synchronization of turbine, load ramp-up. These processes are strongly dependent on the specifications of components manufacturers that are commonly not, or difficultly, available. As suggested by [1], a correction factor can be used to link the ideal start-up energy to the real life one.

7.1.4 Representative weeks

To analyze more cases that cover more operating states, three weeks with both clear and cloudy conditions are considered. The selected three time periods related to seasons (i.e. Summer, Spring, Winter) are for winter, the week starting from 24th till 30st of December, for spring, the week starting from 17th till 23th of March and for summer the week starting from 20th till 26th of June.

As regards the HTF mass flow regulation, the adoption of a control scheme that link the mass flow to the EDNI with a linear proportion would lead to some issues during cloudy days. Indeed, the cloud passage can produce a high DNI frequency change that would be

followed by a proportional HTF mass flow rate change thus leading to unrealistic power output gradient. In order to solve this issue, a simple and conservative HTF mass flow control can be considered as follows: the same mass flow time schedule of a clear sky day is maintained for every days of the week. Therefore, this approach prevents from both exceeding turbine gradient power constrain and defocussing of solar field.

In Figure 7.3, Figure 7.4 and Figure 7.5 the power ratio and EDNI are considered respectively for summer week, spring week and winter week respectively.

As far as clear day is concerned, the same remarks presented for the single day can be made. It is possible to appreciate how the two models treat cloudy days differently; in particular considering the 173th day of the year it is worth to notice how the first steep DNI variation influenced instantaneously the steady-model results whereas the solar field thermal inertia, considered by the transient model, dumps this change maintaining a more or less constant power output. This fact can be observed in the second cloudy period of the day of summer week that presents a shutdown period for the steady approach while the transient method allows the power block to run without interruptions.

In spring week, the clear-sky days share the same qualitative behavior of clear-sky days in summer week. The main difference is due to the effect of incidence angle penalties that have a stronger effect on EDNI value of spring week. If the 78th day of the year (DOY) is taken into account, both the models predict the same shutdown period because of the low EDNI caused by a strong presence of clouds. During this time, the transient model goes in recirculation mode in which a constant mass flow rate (25% of the design value) is circulated in solar field.

As regards the winter week, the same situations described for the two other weeks can be noticed.

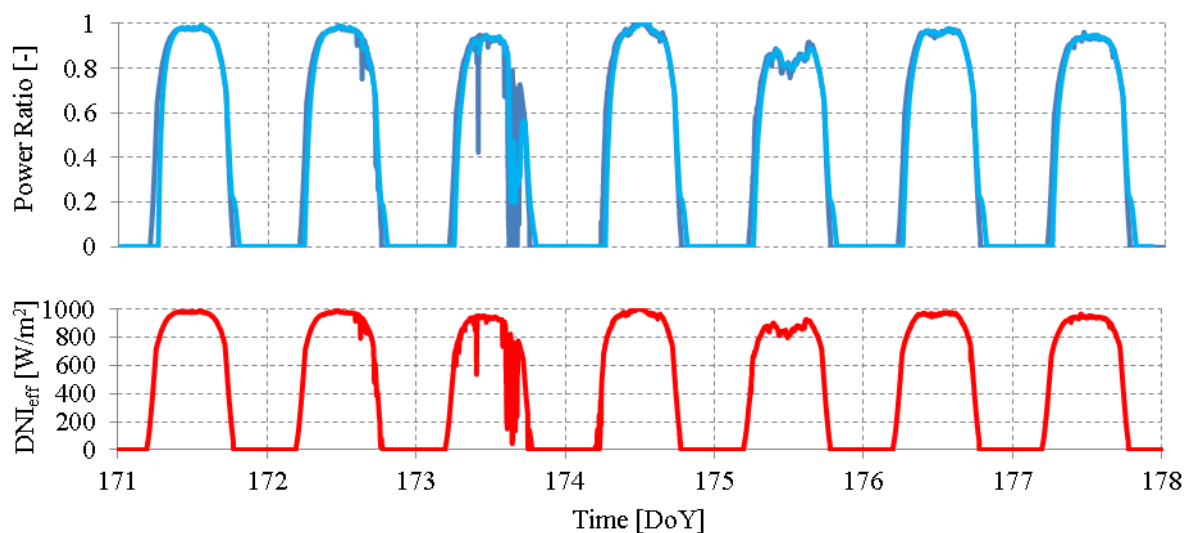


Figure 7.3 Summer week (20th to 26th of June).

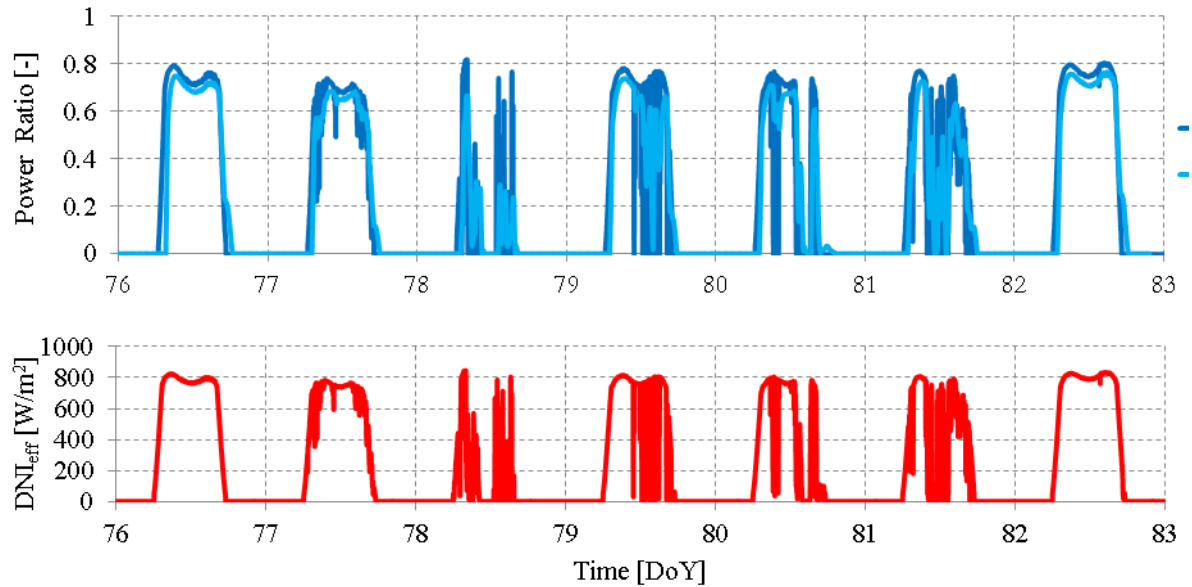


Figure 7.4 Spring week (17th to 23th of March).

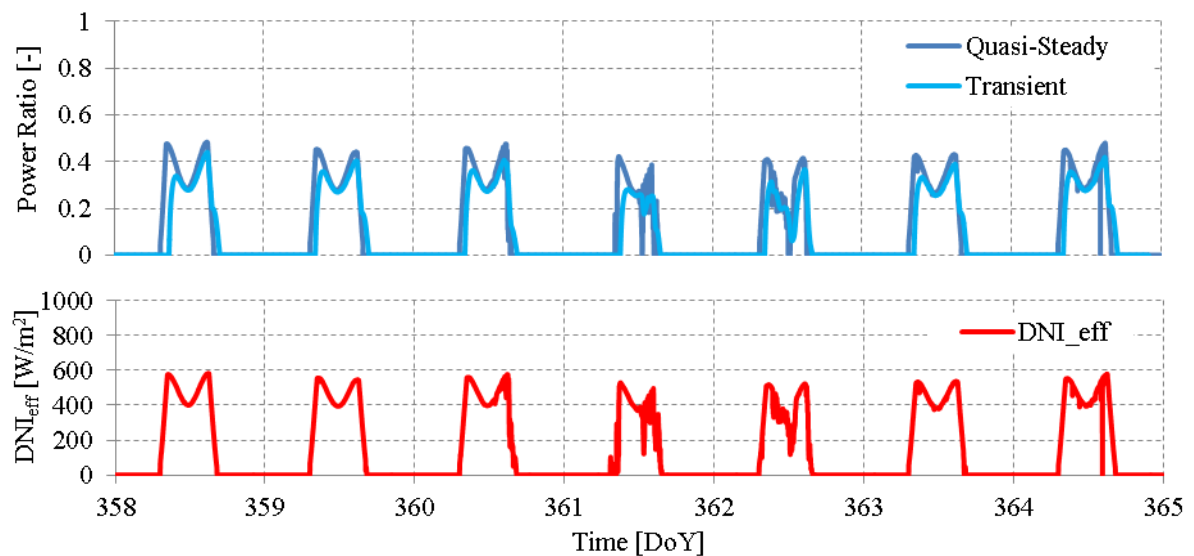


Figure 7.5 Winter week (24th to 30st of December).

In agreement with the clear-sky day analysis, the energetic comparison between the quasi-steady approach and the transient model is enlightened by the integral power ratio values. In agreement with the results referred to clear-sky day, the quasi-steady approach produces an overestimation of the electricity output. The overestimation value is 3.6%, 5.2% and 10.5% for summer, spring and winter weeks respectively. The lower value of the overestimation derived from the relevant presence of cloudy days in the selected weeks that are characterized by a lower difference between the outputs of the two models.

7.1.5 Annual Electricity yield

To conclude the energy performance evaluation, a whole year is simulated and the ratio between the quasi-steady model and the transient model is approximately equal to 0.9.

This value agrees with the results presented in [1], in addition, it is independently obtained in terms of both solar field and power block assumptions, thus validating further the methodology approach.

Considering that, the CSP plants are located in desert or semi-desert area, the presence of cloudy days would have a low probability thus leading to a small effect in energetic prediction. This last consideration seems to indicate how the major research effort has to be pointed to the development of a more detailed start-up modelling that could be important to enhance the knowledge about annual energy yield of linear CSP.

7.2 Bibliography

- [1] Hirsch T, Fabian Feldhoff J, Schenk H. Start-up modeling for annual CSP yield calculations. *J Sol Energy Eng Trans ASME* 2012;134.
- [2] Hirsch T, Schenk H. Dynamics of oil-based parabolic trough plants - a detailed transient simulation model- 2010.
- [3] National Renewable Energy Laboratory. National Solar Radiation Data Base: 1991-2005 Update: Typical Meteorological Year 3 2008;2013.
- [4] Department of Energy (DOE). EnergyPlus Energy Simulation Software: Weather Data 2012.
- [5] Burkholder F, Kutscher CF. Heat Loss Testing of Schott's 2008 PTR70 Parabolic Trough Receiver National Renewable Energy Laboratory; 2009.
- [6] Kutscher C, Burkholder F, Kathleen Stynes J. Generation of a parabolic trough collector efficiency curve from separate measurements of outdoor optical efficiency and indoor receiver heat loss. *J Sol Energy Eng Trans ASME* 2012;134.
- [7] Manzolini G, Giotri A, Saccilotto C, Silva P, Macchi E. Development of an innovative code for the design of thermodynamic solar power plants part A: Code description and test case. *Renew Energy* 2011;36:1993-2003.
- [8] Forristall RE. Heat Transfer Analysis and Modeling of a Parabolic Trough Solar Receiver Implemented in Engineering Equation Solver National Renewable Energy Laboratory; 2003.
- [9] Manzolini G, Giotri A, Saccilotto C, Silva P, Macchi E. A numerical model for off-design performance prediction of parabolic trough based solar power plants. *J Sol Energy Eng Trans ASME* 2012;134.
- [10] Patnode AM. Simulation and performance evaluation of parabolic trough solar power plants 2006.
- [11] Binotti M. Linear Fresnel reflectors : study of the technology and steps toward optimization 2013.
- [12] Lippke F. Simulation of the part-load behavior of a 30 MWe SEGS plant 1995.
- [13] Rheinlander, J. Erbes, M.R., Bergmann, S. Simulation of Solar Field Start-Up in a PTC-CSP Plant 2010.

8 Conclusion and Future Developments

8.1 Conclusions

The PhD work dealt with the study of transient response of indirect linear concentrating power plants. The main aim of the research consisted in the development of simulation models able to assess the behavior of linear CSP in different operating conditions. An important part of the research was devoted to the computation of energetic performance with a “quasi-steady approach” that represents the state-of-art of the yearly performance modelling. This section highlights the capability of this kind of approach to obtain reliable results that can be used in techno-economical evaluations of different CSP technologies. In addition, this part of PhD work was proposed in order to introduce common concepts related to “CSP world” that were recalled in the other parts of the thesis.

Once the “quasi-steady approach” was described, the transient effects of solar field was analyzed through the coding of a specific model able to predict the response of solar field subject to characteristic conditions as, for example, the passage of a cloud or the morning warm-up. A precise model was developed to size the hydraulic network and to evaluate the characteristic dimensions of the piping components that play a fundamental role in the transient response of the system. Once a parabolic trough solar field test-case (ca. 250000 m²) was selected, the effect of moving square disturbance was studied. With the aim of considering the behavior without applying any regulations to single loop (i.e. no control valves are present on the loop), the total HTF mass flow and the defocusing fraction of solar field remain the only two control parameters. The total HTF mass flow was considered to be proportional to the effective impinging DNI with different minimum values (i.e. 25% of nominal mass flow, 50% and 75%), in order to identify the best strategy to face the cloud disturbance. From the analysis of the response to the cloud passage, an interesting result is that maintaining a constant HTF mass flow leads to a safe operation of the solar field. The main advantages of this strategy are the high level of simplicity and the absence of defocused energy but, it is worth to notice that this conclusion is limited to indirect linear CSP plant whilst the thermo-hydraulic complexity of DSG plant is recognized to imply control issues that make mandatory the adoption of control valves on each loop.

A further part of the study was the implementation of a MATLAB[®] model that is able to predict both the cloud movement vector starting from a set of ground GHI measured data and the opacity matrix of the cloud. The model was tested with data from the “Plataforma Solar de Almeria” and the author’s feeling is that the addition of some low cost GHI sensors placed along solar field perimeter could help the prediction of cloud front movement before it reaches the parabolic trough mirrors. This kind of information could help the plant operator to adapt the control parameters optimizing the plant performance and in particular, it is author’s conclusion that the cloud movement prediction could be of fundamental interest mainly for DSG plants that are known to be more subjects to impinging solar energy disturbances.

The last part of the work was the addition of main transient effects in a model able to evaluate the yearly energetic output of a linear CSP plant. The thermo-hydraulic model, in a simplified version, was coupled with a polynomial based modeling approach of the power block. An annual simulation was performed and the obtained results are compared with the electricity output derived from a “quasi-steady state” model. The comparison shows that the quasi-steady model overestimates the energetic output approximately of a 10%. This result is in agreement with other studies obtained independently by other European research groups thus validating the main procedure.

Because the figures of yearly electric energy is in accordance to previous studies that implement a simple lumped-capacitance model, the author’s feeling is that a complete transient model of solar field could be substituted with a “quasi-steady approach” integrated with correction parameters.

8.2 Future Developments

The topics treated in this thesis can be the starting point for further analyses in the field of linear CSP technology. As regards the quasi-steady approach, it is a common idea in the scientific community that this approach is well consolidated and it does not require further research about the main line of the procedure. The main open-line of research is the study of the modelling equations of the single components mainly the turbine; in particular the correct identification of turbine in part-load presents some open spaces for additional research. A personal conclusion of the author is that the quasi-steady approach will be used in future for the prediction of annual energetic yield of CSP because of its fast implementation and good accuracy level, sufficient to have a first idea of the analyzed solutions. GECOS group [1] has undertaken an intensive research activity in analyzing CSP solutions, that are different in both the concentrator technology and the power block section (i.e. Supercritical direct cycle, ORC), from a technical and an economic point of view. In addition to the two articles presented in Chapter “Quasi-steady analysis” it is worth to remember these articles published in peer-reviewed journals or presented at International Conferences [2,3].

As regards possible future developments of this thesis they can be outlined by the following list:

- *Dynamic model of power block section:* as a first approximation, the power block was modelled with a polynomial based steady-state approach. The dynamic model of the main power section components (i.e. heat exchangers, steam turbine) represents a further step towards an exhaustive implementation of a linear CSP plant model. A detailed sizing analysis, in particular pointing to the steam turbine, will be necessary to identify the boundaries of the modelling. In addition, an accurate study about the steam turbine ramp up model can be of crucial importance as underlined by [4].

- *Thermal energy storage system:* the addition of thermal storage system decouples solar energy production from electricity. Among the possible solutions, the thermocline technology was object of a preliminary study and a MATLAB[®] tool was implemented. This choice follows the trend of TES research that identifies the thermocline technology as a promising alternative to the two-tanks system as reported by [5-7]. Due to the same programming language used, this further step should be quite straightforward.

In Figure 7.1, the axial temperature profile of a thermocline tank with the characteristics described in [8] is presented. From the figure below the thermocline zone is easily identifiable.

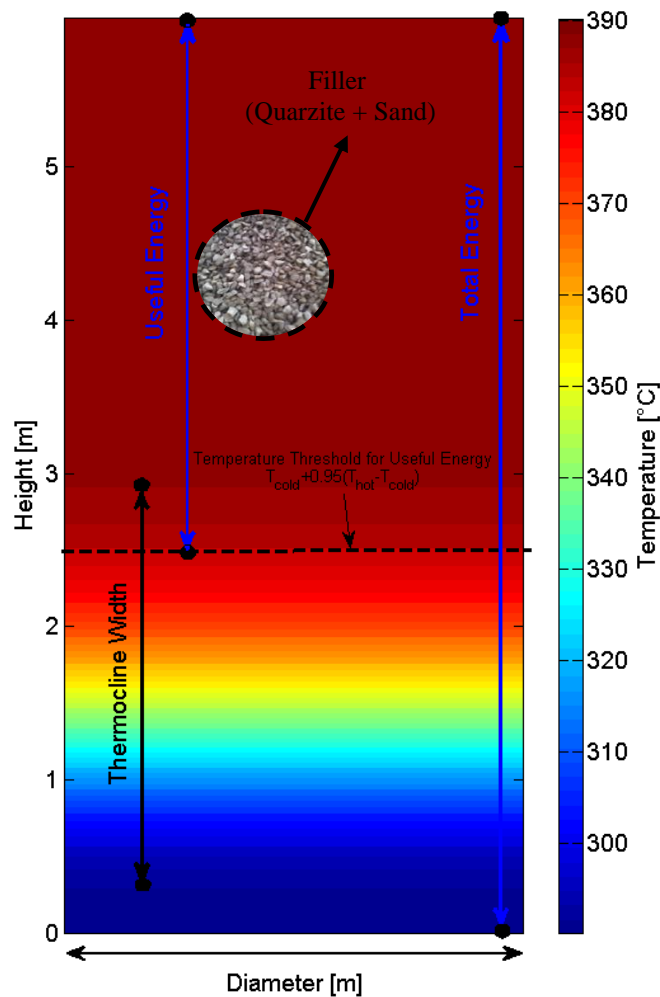


Figure 7.1 Temperature contour of the thermocline tank studied in [8]. The filler material is a mixture of quartzite and sand, HTF is a mixture of molten salts (HITEC).

- *Direct steam generation:* due to the complex physical phenomena induced by the phase transition, the study of transient behavior of DSG solar field is a challenging topics that shows characteristic effect completely different from the situation of HTF indirect plant [9] and [10] and for that reason, this could be a mid-term goal.

- *Addition of more complex control strategies:* in Chapter 5 the solar field behavior was studied without the implementation of mass flow controls. Particularly, a possible modelling improvement can be represented by the addition of mass flow control strategies. The use of a single control valve on each loops increases the degrees of freedom of the system thus allowing a more flexible operation of the solar field.
- *Switching to a different programming language:* as described in the dedicated chapter, the transient model was written in MATLAB[®]. As reported in the previous list elements, the addition of control strategies and power block dynamic modelling would require a more specific program language. CSP research community has been showing an increasing attention to Modelica[®] [11], a non-proprietary and object-oriented language that is used for the dynamic simulation of complex physical systems.

8.3 Bibliography

- [1] GECOS. Politecnico di Milano: Group of Energy Conversion Systems 2013.
- [2] Rinaldi F, Binotti M, Giotri A, Manzolini G. Comparison of linear and point focus collectors in solar power plants. SolarPACES 2013 2013.
- [3] Binotti M, Giotri A, Astolfi M, Colombo L, Macchi E, Manzolini G. Partial admission vs sliding pressure applied to DSG solar plant based on linear Fresnel reflector. SolarPACES 2011 2011.
- [4] Spelling J, Jocker M, Martin A. Annual performance improvement for solar steam turbines through the use of temperature-maintaining modifications. Solar Energy 2012;86:496-504.
- [5] Casati E, Galli A, Colonna P. Thermal energy storage for solar-powered organic Rankine cycle engines. Solar Energy 2013;96:205-219.
- [6] Flueckiger SM, Iverson BD, Garimella SV, Pacheco JE. System-level simulation of a solar power tower plant with thermocline thermal energy storage. Appl Energy 2014;113:86-96.
- [7] Flueckiger SM, Yang Z, Garimella SV. Review of Molten-Salt Thermocline Tank Modeling for Solar Thermal Energy Storage. Heat Transfer Eng 2013;34:787-800.
- [8] Pacheco JE, Showalter SK, Kolb WJ. Development of a molten-salt thermocline thermal storage system for parabolic trough plants. TRANSACTIONS-AMERICAN SOCIETY OF MECHANICAL ENGINEERS JOURNAL OF SOLAR ENERGY ENGINEERING 2002;124:153-159.
- [9] Pye JD, Morrison GL, Behnia M. Unsteady effects in direct steam generation in the CLFR 2007;10:02-2007.
- [10] Birnbaum J, Feldhoff JF, Fichtner M, Hirsch T, Jocker M, Pitz-Paal R, et al. Steam temperature stability in a direct steam generation solar power plant. Solar Energy 2011;85:660-668.
- [11] Modelica and the Modelica Association. Modelica website 2013.

9 Appendix

This appendix gives additional information that are cited in the chapters of the thesis. The topics treated in the following are not necessary to the complete understanding of the work of the thesis but it is only intended to provide additional information useful to go into the treated topics.

9.1 Sun Position

The first step to simulate the yearly performance of a CSP plant is the calculation of the sun vector during time. The sun position, commonly defined by the Zenith angle (θ_z) and the Azimuth angle (γ), is the first info needed to compute the optical performance of concentrating systems as introduced in Chapter 2. The necessary inputs for the sun position calculation are the time, the Standard Time Zone (STZ) and the geographical coordinate of the plant location expressed by latitude (ϕ) and longitude (ϕ_{LONG}) angle.

A lot of models for the sun position calculation, with different levels of accuracy, can be found in literature [1,2]. It is important to underline that to determine the annual energy yield of CSP plants, a simplified algorithm [3,4], outlined by the equations (9.1)-(9.8), can be adopted. The main procedure to define “sun position” is reported below:

$$\begin{array}{l} \text{Declination} \\ (\text{°}): \end{array} \quad \delta = 23.45 \cdot \sin\left(360 \frac{284 + n}{365}\right) \quad (9.1)$$

Equation of Time (min):

$$\begin{aligned} E_n = 229.18 \cdot & \left(0.000075 + 0.001868 \cdot \cos\left(360 \frac{n-1}{365}\right) - 0.03277 \right. \\ & \cdot \sin\left(360 \frac{n-1}{365}\right) - 0.014615 \cdot \cos\left(2 \cdot 360 \frac{n-1}{365}\right) - 0.04080 \\ & \left. \cdot \sin\left(2 \cdot 360 \frac{n-1}{365}\right) \right) \end{aligned} \quad (9.2)$$

$$\begin{array}{l} \text{STZ meridian longitude} \\ (\text{°}): \end{array} \quad \phi_{LONG} = STZ \cdot 15 \quad (9.3)$$

$$\begin{array}{l} \text{Solar Time (h)} \\ 15: \end{array} \quad t_s = t - \frac{(\phi_{STD} - \phi_{LONG})}{15} + \frac{E_n}{60} \quad (9.4)$$

$$\text{Hour Angle (°):} \quad \omega = (t_s - 12) \cdot 15 \quad (9.5)$$

$$\begin{array}{l} \text{Zenith angle} \\ (\text{°}): \end{array} \quad \theta_z = \text{acos}(\cos\phi \cdot \cos\delta \cdot \cos\omega + \sin\phi \cdot \sin\delta) \quad (9.6)$$

¹⁵ Longitudes are negative westward from Greenwich and positive eastward from Greenwich

$$\begin{aligned} \text{Solar Altitude } (\text{°}): \quad \alpha_s &= 90 - \theta_z \text{ (if } \alpha_s < 0 \rightarrow \alpha_s = 0) \end{aligned} \quad (9.7)$$

$$\begin{aligned} \text{Azimuth } (\text{°})^{16}: \quad \begin{cases} \gamma = 180 - a \sin \left(-\frac{\cos \delta \cdot \sin \omega}{\cos \alpha_s} \right) & \text{if } \cos \omega > \frac{\tan \delta}{\tan \phi} \\ \gamma = 360 + a \sin \left(-\frac{\cos \delta \cdot \sin \omega}{\cos \alpha_s} \right) & \text{if } \cos \omega \leq \frac{\tan \delta}{\tan \phi} \end{cases} \quad (9.8) \\ \text{(if } \gamma > 360 \rightarrow \gamma = \gamma - 360) \end{aligned}$$

In the abovementioned equations n represents the day of the year (from 1 to 365), while t is the local standard time.

9.2 Ratio between aperture area and real area of Parabolic Trough

The mathematical proof to calculate the ratio between the aperture area and the real mirrored surface of parabolic trough is reported. In Figure 9.1 a parabolic mirror is shown; in particular the length “W” identifies the mirror aperture, f is the focal length and ϕ is the rim angle.

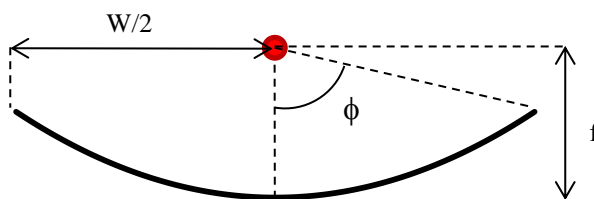


Figure 9.1 Geometrical PT sketch with shape parameters represented.

In accordance with the figure above, the analytical function that represents a generic parabola in a Cartesian reference system (x - y) is expressed by:

$$f(x) = y = \frac{1}{4f} x^2 \quad (9.9)$$

In order to obtain an analytical solution of the mirrored surface of a parabolic trough, it is sufficient to calculate the length of the parabolic profile shown in Figure 9.1.

The general way to calculate the length of a generic curve is expressed by Equation (9.10):

¹⁶ Azimuth is measured clockwise from North $\gamma_{North} = 0$; Azimuth goes from 0° to 360° , if $\gamma > 360 \rightarrow \gamma = \gamma - 360^\circ$

$$l = \int \sqrt{1 + (f'(x))^2} dx \quad (9.10)$$

Once the aperture of parabola is known, the length of the parabolic segment can be calculated by the definite integral as follows:

$$l = \int_{-\frac{W}{2}}^{\frac{W}{2}} \sqrt{1 + \left(\frac{1}{2f}x\right)^2} dx = \int_{-\frac{W}{2}}^{\frac{W}{2}} \sqrt{1 + ax^2} dx \quad (9.11)$$

A brief solution procedure is outlined in the following steps [5]:

1. Reminding the resolution approach named “Integration in Parts” expressed below:

$$\int f(x)g'(x)dx = f(x)g(x) - \int f'(x)g(x)dx \quad (9.12)$$

It is possible to obtain the following form of the integral:

$$\int \sqrt{1 + ax^2}(1)dx = x\sqrt{1 + ax^2} - \int 2ax^2(1 + ax^2)^{-\frac{1}{2}}dx \quad (9.13)$$

2. To solve the right-hand integral, the same solving method is applied obtaining the final results of the length of a generic parabola segment:

$$l_{gen} = \frac{1}{2}x\sqrt{1 + ax^2} + \frac{\text{Log}[\sqrt{ax} + \sqrt{1 + ax^2}]}{2\sqrt{a}} \quad (9.14)$$

or in the alternative form (reminding the definition of the hyperbolic sine)¹⁷

$$l_{gen} = \frac{1}{2}x\sqrt{1 + ax^2} + \frac{\text{ArcSinh}[\sqrt{ax}]}{2\sqrt{a}} \quad (9.15)$$

In relation to Figure 9.1 and to Equation (9.11), the length of the parabolic segment shown is:

$$l_{PT} = \frac{1}{4} \left(W\sqrt{4 + aW^2} + \frac{4\text{ArcSinh}\left[\frac{\sqrt{a}W}{2}\right]}{\sqrt{a}} \right) \quad (9.16)$$

The ratio between the reflective and the aperture area is expressed by:

¹⁷ $\text{ArcSinh}(x) = \text{Log}[x + \sqrt{1 + x^2}]$

$$RAR = \frac{(W\sqrt{4 + aW^2} + \frac{4\text{ArcSinh}[\frac{\sqrt{a}W}{2}]}{\sqrt{a}})}{4W} \quad (9.17)$$

Referencing to the characteristics of ET-150 parabolic trough concentrator ($W=5.76$ m and $f=1.716$ m), a RAR value of 1.107 is obtained.

9.3 Characteristic incidence angles for LFR

In this section, some useful relations to calculate the characteristic incidence angles for PT and LFR are presented. The geometrical proof to obtain the main relation among characteristic angles, shown in Figure 9.2, is presented below.

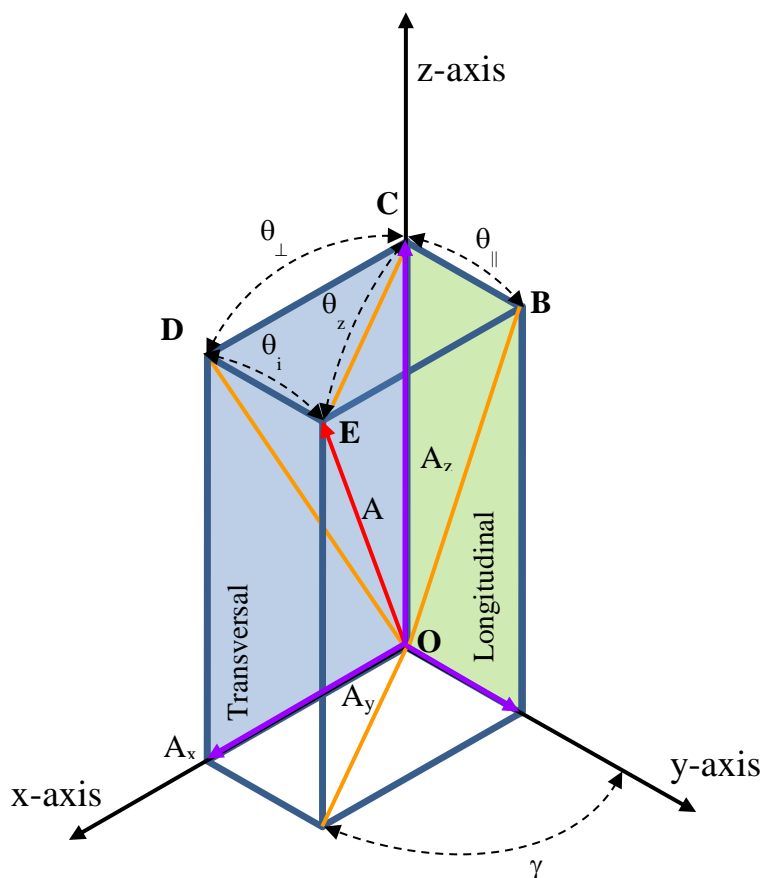


Figure 9.2 Angles definition of a concentrating reflector with horizontal N-S orientation

The unit vector \vec{A} identifies the sunray and it is possible to express its directional cosines A_x , A_y and A_z , with the following relations, function of the sun position (zenith angle and azimuth angle):

$$A_x = A \cos(90 - \vartheta_z) \cos(90 - \gamma) = \sin(\vartheta_z) \sin(\gamma) \quad (9.18)$$

$$A_y = A \cos(90 - \vartheta_z) \cos(\gamma) = \sin(\vartheta_z) \cos(\gamma) \quad (9.19)$$

$$A_z = \cos(\vartheta_z) \quad (9.20)$$

As regards the relation existing among the directional cosines in the Euclidean three dimensional space, the following equation can be written:

$$A_x^2 + A_y^2 + A_z^2 = 1 \quad (9.21)$$

Considering the right triangle BOC the $\vartheta_{||}$ can be related to the sun position as follows:

$$\tan(\vartheta_{||}) = \frac{A_y}{A_z} = \frac{\sin(\vartheta_z) \cos(\gamma)}{\cos(\vartheta_z)} \quad (9.22)$$

With the same consideration applied to the right triangle COD the ϑ_{\perp} angle can be expressed:

$$\tan(\vartheta_{\perp}) = \frac{A_x}{A_z} = \frac{\sin(\vartheta_z) \sin(\gamma)}{\cos(\vartheta_z)} \quad (9.23)$$

Considering the right triangle EOD the ϑ_i angle can be found:

$$\sin(\vartheta_i) = \frac{A_y}{A} = \sin(\vartheta_z) \cos(\gamma) \quad (9.24)$$

For sake of simplicity, the relation described above are referred to a N-S orientation and with no tilt angle. A more general treatise can be obtained using a change of the reference system with the application of a 3D rotation.

In addition to the expressions of the most important incidence angles, two characteristic relations, commonly referenced in literature, are presented. Considering equation (9.22) and dividing it by A_z leads to:

$$\frac{A_x^2}{A_z^2} + \frac{A_y^2}{A_z^2} + 1 = \frac{1}{A_z^2} \quad (9.25)$$

Substituting the previously found relations of $\tan^2(\vartheta_{||})$ and $\tan^2(\vartheta_{\perp})$ and using the Pythagorean trigonometric identity¹⁸, the following equation can be obtained that links together the zenith angle ϑ_z , $\vartheta_{||}$ and ϑ_{\perp} :

$$\tan^2(\vartheta_z) = \tan^2(\vartheta_{||}) + \tan^2(\vartheta_{\perp}) \quad (9.26)$$

Regarding the factorization of the LFR IAM presented in Chapter 2, it is worth to notice that the choice of ϑ_i and ϑ_{\perp} implies another interesting relation (considering the triangle ODE the segment OD is equal to $\cos(\vartheta_i)$ and analyzing the right triangle ODC, it is straightforward to obtain:

$$\cos(\vartheta_z) = \cos(\vartheta_i)\cos(\vartheta_{\perp}) \quad (9.27)$$

9.4 Heat transfer fluid properties

Synthetic oils are the more common heat transfer fluid used in CSP plants. The commercial solution for high capacity power plants has a maximum temperature of the heat source approximately 390°C. The level of temperature limits the choice of the HTF that can be used in the solar field and, as regards the HTF suppliers, Solutia [6] and Dow Chemicals [7] provide two very similar HTFs for the most of the parabolic trough CSP plant in the world, named Therminol VP-1 [8] and DowTherm-A [9] respectively.

The heat transfer fluid considered in this work is Therminol VP-1 that is a mixture of diphenyl ($C_{12}H_{10}$) and diphenyl oxide ($C_{12}H_{10}O$) [8,9]. The HTF fluid properties, used in this work, are expressed in polynomial form as shown in Table 9.1.

Table 9.1 Thermophysical properties of Therminol VP-1

<i>Therminol VP-1 Properties</i>						
Property	Relation Form	Coefficients				
		a	b	c	d	e
ρ [kg/m ³]	$aT + bT^2 + cT^3 + d$	-0.90797	7.8116e-4	-2.367e-6	1083.25	-
k[W/mK]	$aT + bT^2 + cT^3 + dT^4 + e$	-8.19477e-5	-1.92257e-7	2.5034e-11	-7.2974e-15	0.137743
ν [mm ² /s]	$e^{\left(\frac{a}{T+b}+c\right)}$	544.149	114.43	-2.59578	-	-
cp [kJ/kgK]	$aT + bT^2 + cT^3 + dT^4 + e$	0.002414	5.9591e-6	-2.9879e-8	4.4172e-11	1.498

An alternative technology implements the use of a molten salts mixture (60% NaNO₃, 40% KNO₃). The unique example of this kind of linear CSP plant is the Archimede plant.

¹⁸ $\sin^2\alpha + \cos^2\alpha = 1$

In Table 9.2 the thermophysical properties of the molten salts mixture used in CSP application are provided.

Table 9.2 Thermophysical properties of molten salts mixture.

<i>Molten Salt Properties</i>					
Property	Relation Form	Coefficients			
		a	b	c	d
ρ [kg/m ³]	$aT + b$	-0.636	2090	-	-
k[W/mK]	$aT + b$	1.9e-4	0.443	-	-
μ [mPas]	$aT + bT^2 + cT^3 + d$	-0.120	2.281e-4	-1.474e-7	22.714
c_p [kJ/kgK]	$aT + b$	0.172	1443.0	-	-

9.5 Available Pipe Dimension

As regards the commercially available pipe, in the following tables (Table 9.2 and Table 9.3), the inner diameter and the thickness are shown.

Table 9.2 Pipe thickness commercially available

Nominal													
pipe	A	B	C	D	E	F	G	H	I	J	K	L	M
2.5	2.11	3.05	5.16	7.01	9.53	14.02							
3	2.11	3.05	5.49	7.62	11.13	15.24							
4	2.11	3.05	3.96	4.78	6.02	8.56	11.13	13.49	17.12				
6	2.77	3.40	4.78	7.11	10.97	14.27	18.26	21.95					
8	2.77	3.76	6.35	7.04	8.18	10.31	12.70	15.09	18.26	20.62	22.23	23.01	
10	3.40	4.19	4.78	6.35	7.80	9.27	12.70	15.09	18.26	21.44	25.40	28.58	
12	3.96	4.57	6.35	8.38	9.53	10.31	12.70	14.27	17.48	21.44	25.40	28.58	33.32
14	4.78	6.35	7.92	9.53	11.13	12.70	15.09	19.05	23.83	27.79	31.75	35.71	
16	4.78	6.35	7.92	9.53	12.70	14.35	21.44	26.19	30.96	36.53	40.49		
18	4.78	6.35	7.92	9.53	11.13	12.70	14.27	19.05	23.83	29.36	34.93	39.67	45.24
20	5.54	6.35	9.53	12.70	15.09	20.62	26.19	32.54	38.10	44.45	50.01		
22	6.35	9.53	12.70	22.23	28.58	34.93	41.28	47.63	53.98				
24	6.35	9.53	12.70	14.27	17.48	24.61	30.96	38.89	46.02	52.37	59.54		
26	7.92	9.53	12.70										
28	7.92	9.53	12.70	15.88									
30	7.92	9.53	12.70	15.88									
32	7.92	9.53	12.70	15.88	17.48								
34	7.92	9.53	12.70	15.88	17.48								
36	7.92	9.53	12.70	15.88	19.05								
42	9.53	12.70	15.88	19.05									
48	9.53	12.70	15.88	19.05									

Table 9.3 Pipe inner diameter commercially available

Nominal													
pipe	A	B	C	D	E	F	G	H	I	J	K	L	M
2.5	68.8	66.9	62.7	59.0	54.0	45.0							
3	84.7	82.8	77.9	73.7	66.6	58.4							
4	110.1	108.2	106.4	104.7	102.3	97.2	92.0	87.3	80.1				
6	162.7	161.5	158.7	154.1	146.3	139.7	131.7	124.4					
8	213.5	211.6	206.4	205.0	202.7	198.5	193.7	188.9	182.5	177.8	174.6	173.1	
10	266.2	264.7	263.5	260.4	257.5	254.5	247.7	242.9	236.5	230.2	222.3	215.9	
12	315.9	314.7	311.2	307.1	304.8	303.2	298.5	295.3	288.9	281.0	273.1	266.7	257.2
14	346.0	342.9	339.8	336.6	333.3	330.2	325.4	317.5	307.9	300.0	292.1	284.2	
16	396.8	393.7	390.6	387.4	381.0	377.7	363.5	354.0	344.5	333.3	325.4		
18	447.6	444.5	441.4	438.2	434.9	431.8	428.7	419.1	409.5	398.5	387.4	377.9	366.7
20	496.9	495.3	489.0	482.6	477.8	466.8	455.6	442.9	431.8	419.1	408.0		
22	546.1	539.8	533.4	514.4	501.7	489.0	476.3	463.6	450.9				
24	596.9	590.6	584.2	581.1	574.6	560.4	547.7	531.8	517.6	504.9	490.5		
26	644.6	641.4	635.0										
28	695.4	692.2	685.8	679.5									
30	746.2	743.0	736.6	730.3									
32	797.0	793.8	787.4	781.1	777.8								
34	847.8	844.6	838.2	831.9	828.6								
36	898.6	895.4	889.0	882.7	876.3								
42	1047.8	1041.4	1035.1	1028.7									
48	1200.2	1193.8	1187.5	1181.1									

9.6 Bibliography

- [1] Blanco-Muriel M, Alarcón-Padilla DC, López-Moratalla T, Lara-Coira M. Computing the solar vector. *Sol Energy* 2001;70:431-441.
- [2] Reda I, Andreas A. Solar position algorithm for solar radiation applications. *Solar Energy* 2004;76:577-589.
- [3] Duffie JA, Beckman WA. *Solar Engineering of Thermal Processes* Wiley: Hoboken, NJ; 2006.
- [4] Patnode AM. *Simulation and performance evaluation of parabolic trough solar power plants* 2006.
- [5] Bramanti M, Pagani C, Salsa S. *Calcolo infinitesimale e algebra lineare. Seconda edizione.*Zanichelli 2004.
- [6] Solutia. *Solutia (Global leader in Performance Materials and Specialty Chemicals - Website-)* 2013.
- [7] Dow Chemical Corporate. *Dow Chemical Corporate's Website* 2013.
- [8] Solutia. *Therminol Heat Transfer Fluids, Heat Transfer Fluid Products* 2012;2012.
- [9] Dow Chemical Corporate. *DOWTHERM™ | Heat Transfer Fluids | The Dow Chemical Company* 2012;2012.